UNIVERSITY OF OKLAHOMA

GRADUATE COLLEGE

SHAPE SENSITIVITY ANALYSIS FOR THREE-DIMENSIONAL MULTI-SCALE CRACK PROPAGATION PROBLEMS USING THE BRIDGING SCALE METHOD

A DISSERTATION

SUBMITTED TO THE GRADUATE FACULTY

in partial fulfillment of the requirements for the

Degree of

DOCTOR OF PHILOSOPHY

By

YUNXIANG WANG
Norman, Oklahoma
2014

SHAPE SENSITIVITY ANALYSIS FOR THREE-DIMENSIONAL MULTI-SCALE CRACK PROPAGATION PROBLEMS USING THE BRIDGING SCALE METHOD

A DISSERTATION APPROVED FOR THE
SCHOOL OF AEROSPACE AND MECHANICAL ENGINEERING

BY

Dr. Kuang-Hua Chang, Chair

Dr. Peter J. Attar

Dr. Kurt C. Gramoll

Dr. Kanthasamy K. Muraleetharan

Dr. Prakash Vedula

ACKNOWLEDGEMENTS

I would like to start by acknowledging my advisor and mentor, Dr. Kuang-Hua Chang, for his guidance and support during my graduate research. He has been completely selfless in sharing with me the fruits of his wisdom. I have benefited immensely from his passion for research and his deep understanding of this challenging and interesting field. This dissertation would not have been possible without the time and patience that he generously invested in commenting on and revising the manuscript.

I am also thankful to my dissertation committee members Dr. Peter J. Attar, Dr. Kurt C. Gramoll, Dr. Kanthasamy K. Muraleetharan, and Dr. Prakash Vedula for spending their valuable time on reviewing my dissertation.

My appreciation also goes to the AME School and the Graduate College for the financial support during my studies at OU. I am grateful to Dr. Peter J. Attar, Dr. Kuang-Hua Chang, Dr. Farrokh Mistree, Dr. M. Cengiz Altan, Dr. Mrinal C. Saha, Dr. Alfred G. Striz, and Dr. J. David Baldwin for their professional lectures that provided me with useful academic knowledge and techniques for both my graduate research and my future career. I also want to thank all my friends and colleagues for the generous help that they offered in various aspects of my life in Norman.

Last but not least, I would like to express the deepest appreciation to my parents for raising me with love, and to my wife Lan Ji for her constant encouragement and unconditional support over the past four years.

TABLE OF CONTENTS

LIST OF FIGURES

LIST OF TABLES

LIST OF KEY SYMBOLS

b_i = *i*th design variable

$\mathbf{b}$ = vector of design variables

$\mathbf{b}^0$ = current design

C = averaged crack tip location

$\mathbf{d}$ = vector of FE modal displacements

$\mathbf{f}$ = vector of interatomic forces

$\mathbf{f}_{l,m,0}^{imp}$ = impedance boundary forces upon atom (l,m,0)

h_a = equilibrium atomic distance

h_e = length of a 1-D finite element

$H^{\mathrm{m}}(\Omega)$ = Sobolev space of order m

$\mathbf{K}$ = stiffness matrix

m_A = atomic mass

$\mathbf{M}$ = consistent FE mass matrix

$\mathbf{M}_A$ = diagonal mass matrix containing atomic masses

$\mathbf{N}$ = matrix of shape functions

$N_I(\mathbf{x}_\alpha)$ = shape function of node I evaluated at the initial position $\mathbf{x}_\alpha$ of atom α

P = centro-symmetry parameter

$\boldsymbol{P}$ = vector of P parameters

$\mathcal{P}$ = first Piola–Kirchhoff stress

$\mathbf{q}$ = vector of atomic displacements computed in MD simulation

$\bar{\mathbf{q}}$ = atomic virtual displacements

t = time
Δt, Δt_m = FE time step size and MD time step size
t_T = termination time
$\boldsymbol{u}$, $\mathbf{u}$ = continuous and discrete coarse scale displacement fields
$\bar{\boldsymbol{u}}$, $\bar{\mathbf{u}}$ = continuous and discrete coarse scale virtual displacement fields
U = potential energy of the system
$\boldsymbol{v}$, $\mathbf{v}$ = continuous and discrete fine scale displacement fields
$\boldsymbol{V}$ = design velocity field
$\mathcal{V}$ = crack propagation speed
$\tilde{\mathcal{V}}$ = predicted crack speed
$\mathbf{x}$ = spatial coordinate
$\mathbf{x}_\alpha$ = initial location of atom α
$\mathbf{z}$, $\boldsymbol{z}$ = discrete and continuous displacement fields
$\bar{\mathbf{z}}$, $\bar{\boldsymbol{z}}$ = discrete and continuous virtual displacement fields
Z, $\hat{Z}$ = function spaces for displacement fields and virtual displacement fields
$\boldsymbol{\varepsilon}$ = strain
ρ = constant mass density
θ, $\boldsymbol{\theta}$ = time history kernel and time history kernel matrix
$\boldsymbol{\sigma}$ = Cauchy stress
Ω_2 = domain of the FE only region
τ = shape design variable that plays the role of design time
ψ = performance measure
Φ = interatomic potential energy

ABSTRACT

During the past two decades, a variety of concurrent multi-scale simulation methods have been developed, such as the bridging scale method, in which MD simulation is performed only at localized areas of interest, while the response of rest of the domain is solved by using finite element method (FEM). This thesis presents a shape sensitivity analysis approach for multi-scale crack propagation problems based on the bridging scale method. The objective is to reveal the impact of macroscopic shape change on the speed of crack growth at microscopic level. Two major challenges exist in shape sensitivity analysis of coupled atomistic/continuum crack propagation problems, namely the discrete nature of the MD simulation and the non-differentiability of the performance measure of crack propagation speed. In this thesis, the shape sensitivity expressions are derived using direct differentiation method by taking material derivative of a continuum variational formulation of the bridging scale. To get around the discontinuity issue in continuum shape design due to the discrete nature of the MD simulation, the design velocity fields are defined in a way that the shape of the MD region does not change. The derived shape sensitivity formulation can be used to analytically compute the sensitivity coefficients of structural responses at the atomistic level. In addition, a performance measure that quantifies the speed of crack is established to support the sensitivity calculation for crack propagation speed. To overcome the non-differentiability of crack speed in design space, a hybrid method that combines analytical sensitivity analysis and regression analysis is developed. The proposed analytical sensitivity approach and hybrid method are implemented numerically in a nano-beam example, and the accuracy is verified using overall finite difference results.

The analytical sensitivity expressions in this thesis are formulated based on a rigorous mathematical foundation, and is generalized for three-dimensional structures with arbitrary geometric shape. In calculating the sensitivity of crack speed, the hybrid method with regression analysis is much more efficient than overall finite difference. The major contributions of this thesis are: first, it demonstrates the feasibility of shape design of coupled atomistic/continuum systems for the first time; and second, the proposed sensitivity approach accurately predicts the correlation between macroscopic shape change and microscopic crack propagation speed, and therefore establishes the foundation of multi-scale residual-life-based structural optimization without involving traditional fracture mechanics theory.

CHAPTER 1

INTRODUCTION

1.1 Background and Motivation

Fatigue of mechanical systems subject to repeated cyclic loading has been one of the primary concerns in structural design. When the initial crack propagates and reaches a critical size, localized damage occurs, which eventually leads to failure of the structural component. However, the mere presence of crack does not condemn a structure to be unsafe. In fact, it has been a common practice to periodically inspect critical structural components in order to identify presence of cracks, monitor crack growth, and predict useful remaining service life – or residual life. On the other hand, it now becomes possible in many cases to simulate crack propagation and hence estimate residual life using mechanics-based analysis techniques. More importantly, by investigating the impact of geometric shape change on crack growth speed, engineers are able to enhance the durability and maximize the service life of structural components through shape design optimization.

To understand crack propagation and predict residual life, traditional engineering simulation methods have made extensive use of continuum level modeling via empirical constitutive relations and numerical methods such as extended finite element method (XFEM). However, continuum based theories cannot give a fracture criterion from a physical point of view, and therefore are not capable of accounting for all experimentally observed characteristics of crack propagation. For example, it is well known that a crack grows in different patterns along different orientations within a crystal lattice, whereas continuum mechanics views material as continuous and homogenous. In addition, the resolution of a numerical method is limited to the size of the continuum element for which the constitutive relation employed remains valid. This may lead to a result of significant variation due to factors such as mesh size and prescribed crack growth size. For example, it has been shown in [1] that the predicted residual life of a structural component can differ up to 90% between finite element models of coarse and fine meshes, which poses difficulties and uncertainties to residual-life-based structural design.

In order to alleviate such uncertainties, computational methods that can better capture the physical behavior of cracks are desirable. Most often, physical phenomena at atomistic level, such as a fracture, can be simulated using atomistic simulation methods, such as molecular dynamics (MD). During the past few decades, due to the availability of accurate interatomic potentials for a wide range of materials and the rapid progression of computational power, MD simulation techniques advanced greatly and have become prominent as a tool for describing the dynamics of the material at localized and highly nonlinear regions, where the continuum assumption ceases to be valid. However, the length and time scales that can be probed using MD are still fairly limited. Even with the world’s largest computer to-date, MD simulation is generally impractical for structures with length scales larger than a few microns due to the enormous number of degrees of freedom required to be solved. Therefore, atomistic simulations cannot be used alone for solving macroscopic systems, and it then becomes logical to combine atomistic and continuum descriptions of a problem in some manner, while confining the former into localized regions where atomistic level dynamics are important.

It is precisely for bridging the gap between dynamic atomistic and continuum simulations that concurrent multi-scale simulation techniques are developed. These methods have recently become both popular and necessary due to the development of nano-technology. Their ability to examine atomistic-scale material behavior in great detail also makes them suitable for simulating dynamic crack propagation. On one hand, the nonlinear behavior near the crack tip can be accurately captured by the atomistic simulation; on the other hand, the overall computation expense can be significantly reduced by performing atomistic simulation only within localized areas of interest. Therefore, multi-scale simulations appear to be promising for allowing researchers to gain new insight into dynamic crack propagation and fatigue problems. Once these methods are extended to practical applications, it is possible to eliminate the need of traditional fracture mechanics theory developed decades ago that depends largely on assumptions and empirical constants. In the meantime, structural design based on multi-scale simulations can be carried out to prolong the residual life of structural components with better accuracy.

1.2 Literature Review

Atomistic Simulations of Dynamic Crack Propagation

The origin of virtually all fracture phenomena lies at atomistic scale. A macroscopic fracture process can only be understood if the mechanisms on smaller length scales are properly taken into account. The classical theories of continuum mechanics have been the basis of most theoretical and computational tools, forming the foundation for numerical approaches such as the finite element method (FEM). However, at atomistic level, while the material inhomogeneity reaches a length scale comparable to the overall size of the physical phenomena, the basic assumption of continuum theories – materials can be treated without explicitly considering the underlying microstructure – does not hold any more, and hence the continuum description of materials becomes questionable. In contrast, atomistic modeling provides a general and fundamental description of material properties and deformation processes. Atomistic methods are essentially first-principles-based approaches that do not depend on any phenomenological assumption; therefore, they are capable of capturing nano-scale physical mechanisms such as the propagation of cracks.

Atomistic simulation of dynamic crack propagation is a modern development since last several decades due to the advances in computational power. Numerous studies have been reported that investigate crack growth behavior and related physical phenomena (such as dislocation emission, brittle to ductile transition, etc.) at microscopic level using atomistic methods. Here we mention only a few representative studies. For example, a large-scale molecular dynamics simulation using more than one billion atoms was performed by Abraham et al. [2] to reveal the underlying physics of ductile material failure and work-hardening in crystal samples. Gordon et al. [3] examined near-crack-tip deformation in iron and iron alloy single crystals under pure mode-I loading by employing the molecular statics technique; the influence of Ni and Cr solutes on the failure mechanisms of micro-cracks in single crystals of pure iron was studied. Gao et al. [4] carried out molecular dynamics simulations using a self-adaptive time step algorithm in order to understand dynamic crack propagation on different slip planes of BCC iron, and found that the slip plane significantly affects crack propagation speed. Simulations of brittle-to-ductile transition in silicon single crystals were performed by Sen et al. [5] using a first-principles-based atomistic model. Ersland et al. [6] reported a full three-dimensional (3-D) molecular dynamics study of penny-shaped embedded cracks, which showed that the original circular crack geometry can change shape gradually upon loading. A molecular dynamics simulation of nano-scale fatigue damage in nickel and copper single crystals was carried out by Potirniche et al. [7].

Among various atomistic methods, molecular dynamics is the most popular and widely applicable simulation technique. In a MD simulation, the equations of motion of a system of atoms or molecules are solved, resulting in the dynamical trajectories of all particles in the system. Though powerful in revealing atomistic level material behavior, molecular dynamics is still limited in the time and length scales that can be modeled. For example, only systems with a few billion atoms can be simulated even with today’s most powerful computers, whereas a cubic centimeter of solid material already contains more than 10^{23} atoms. Therefore, as shown in Fig. 1.1a, MD has been exclusively aimed at atomistic physics so far, and systems analyzed using MD are mostly at micro or nano scale.

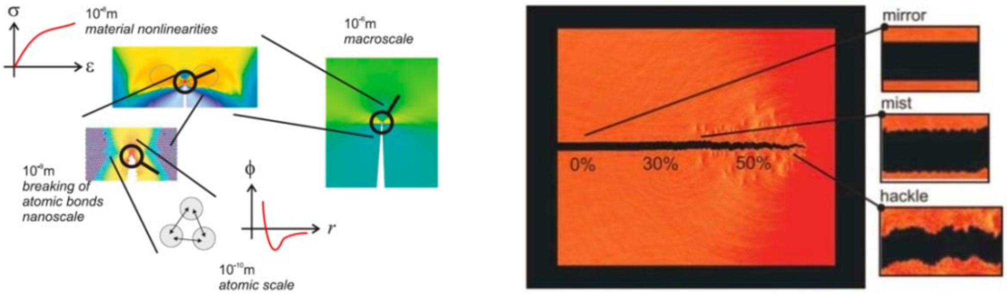

(a) (b)

Figure 1.1 (a) Different length scales associated with dynamic fracture [8]. (b) “Mirror-mist-hackle” transition in dynamic crack instability [9]

Compared to other categories of fracture behaviors, brittle fracture is particularly attractive in the field of MD simulation. This is because in brittle materials, cracks generally propagate at speeds of kilometers per second, corresponding to time and length scales of nanometers per picoseconds (10^{-12}s), which is readily accessible with molecular dynamics. Most MD simulations of dynamic crack propagation in brittle materials are focused on understanding the important physical phenomena in brittle fracture, such as crack limiting speed (maximum speed that a crack can attain) [10,11] and dynamic crack instability (crack face morphology changes from “mirror” to “mist” to “hackle” as crack speed increases, as shown in Fig. 1.1b) [9,12,13]. Recent progress also include investigations of the correlation between atomistic simulation results and continuum theories [13,14]; for example, it is found that atomistic models of brittle fracture reproduce the predictions of linear elastic continuum theory only when harmonic interaction is assumed. In terms of system size, several large-scale MD simulations of brittle crack propagation with more than one billion atoms have been reported since the year of 2000 [2,15,16].

To introduce more about this field, in Appendix A we briefly review the basics of continuum fracture mechanics theories and the results of a series of MD simulations of brittle fracture from literature. The comparison between MD simulation results and existing theories is also discussed in Appendix A.

Multi-scale Simulation Methods

During the past two decades, extensive work has been carried out by different research groups in developing concurrent multi-scale simulation methods that couples dynamic atomistic and continuum simulations. Abraham et al. [17] developed the macroscopic, atomistic, ab initio dynamics (MAAD) method, in which tight binding (TB), molecular dynamics and finite element (FE) simulations run simultaneously in different regions of the computational domain and dynamically exchange necessary information among each other. A related method named coarse-grained molecular dynamics (CGMD) was reported by Rudd and Broughton [18]. The CGMD method removes TB from the original MAAD method and couples only FE and MD. Both MADD and CGMD require the finite element mesh to be graded down to atomistic scale. In the quasi-continuum method proposed by Tadmor et al. [19], atomistic degrees of freedom are selectively removed from the problem by interpolating from a subset of representative atoms, and the atomistic-to-continuum link is achieved by using the Cauchy–Born rule, which assumes that the continuum energy density can be computed using an atomistic potential. Recently, Wagner and Liu [20] developed the bridging scale method (BSM) that decomposes the total displacement into orthogonal coarse and fine scales. Xiao and Belytschko [21] developed the bridging domain multi-scale method, in which an overlapping subdomain consisting of both the molecules and continuum is used to treat the boundary of the atomistic simulation. Shiari et al. [22] proposed a finite temperature coupled atomistic/continuum discrete dislocation (CADD) method to study the nano-indentation process as a function of temperature and rate of indenting. To and Li [23] developed the perfectly matched multi-scale simulation (PMMS), which connects MD and quasi-continuum simulations with a perfectly matched layer.

Among the recently developed multi-scale methods, the bridging scale method by Wagner and Liu [20] offers many distinct advantages. In bridging scale method, the finite element analysis (FEA) is performed everywhere in the domain, while the molecular dynamics simulation is confined into localized areas. The unwanted atomistic degrees of freedom outside the MD region can be eliminated and mathematically accounted for in the form of an impedance boundary condition applied upon the boundary of the MD simulation. In contrast to many concurrent multi-scale methods, the finite elements used in the bridging scale method do not need to be meshed down to atomic scale; therefore, the time step size for FEA is no longer restricted by the smallest, atomic-sized elements in the mesh. The time history kernel (THK) in the impedance force formulation is a compact matrix whose size depends only on the minimum number of degrees of freedom in each unit cell. By utilizing the periodicity of atomic structures, standard Laplace and Fourier transform techniques can be applied in deriving the impedance force for various lattice structures and for multi-dimensional structural problems. The accuracy of the bridging scale method has been demonstrated with one-dimensional (1-D) and two-dimensional (2-D) wave propagation problems [20,24].

Some of the concurrent multi-scale methods have been employed in simulating dynamic crack propagation in coupled atomistic/continuum systems. For instance, Xiao and Belytschko [21] used the bridging domain method to simulate the growth of an edge crack on a carbon grapheme sheet; Rafii-Tabar et al. [25] investigated the brittle crack propagation in a 2-D Ag plate using a generic multi-scale modeling approach; Chen et al. [26] studied different fracture modes of crack propagation in a center-cracked specimen using a multi-scale field theory. The bridging scale method also has been applied to 2-D mode-I and mode-II, and 3-D mode-I dynamic crack propagation problems [24,27,28].

It is worth mentioning, however, that due to the limitation of computation power, even the multi-scale methods are still currently impractical for structures with system sizes at macroscopic level. In fact, only few MD or multi-scale studies have been reported on simulating the behavior of existing components, which are exclusively MEMS (Micro-electro-mechanical systems) or NEMS (Nano-electro-mechanical systems) devices. For example, using the CGMD method, Rudd [29] simulated the vibration of a micro-scale resonator (Fig. 1.2) of size 0.008×0.015×0.2 μm^3 for about 2 million time steps (corresponding to 10^{-9} seconds) with a supercomputer.

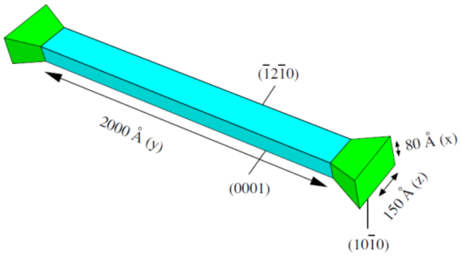

Figure 1.2 A micro-scale resonator with length 0.2 μm [29]

Design Sensitivity Analysis for Structural Dynamics

Structural design is a procedure to improve the performance of a structure by changing its parameters (design variables). As an important step in structural design, design sensitivity analysis (DSA) computes the rate of performance change with respect to the changes of design variables. It is used to provide sensitivity coefficients to optimization algorithms for determining direction towards an optimum design. For structural systems constructed of trusses, beams, membranes, shells and elastic solids, there are five kinds of design variables – material, sizing, configuration, shape and topology design variable, as illustrated in Fig. 1.3. For example, for the truss structure shown in Fig 1.3a, material design variables can be the mass density or Young's modulus, while sizing design variables are the cross-sectional areas of individual truss members; configuration design variables are related to the orientations of components in built-up structures (Fig. 1.3b); shape design variables describe the length of a 1-D structure or the geometric shape of 2-D and 3-D structures (Fig. 1.3c); and topology design variables determine the layout of the structure (Fig. 1.3d).

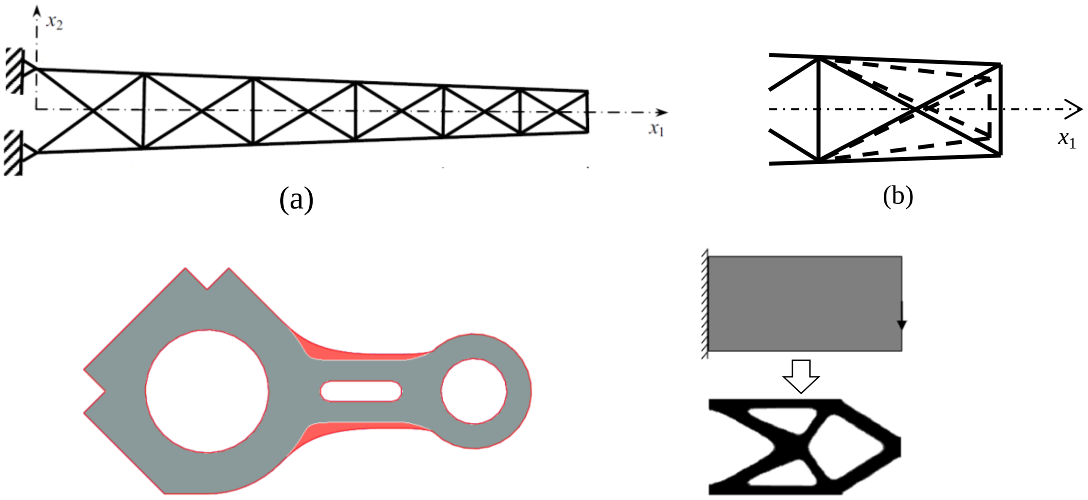

(a) (b)

(c) (d)

Figure 1.3 Illustration of design variables in different categories, (a) a built-up structure in which material properties and cross-sectional areas of the truss members can be changed [30], (b) configuration design by adjusting the orientations and lengths of truss members, (c) shape design for a 2-D engine connecting rod [1], and (d) topology optimization of a solid beam [31]

The formulation of design sensitivity analysis can vary significantly depending on which kind of design variables are being considered and whether the formulation is developed based on a discrete or continuum concept. Substantial literature has merged into the field of design sensitivity analysis and its applications, and a comprehensive introduction of various sensitivity analysis approaches for static and dynamic responses of both linear and nonlinear structural systems can be found in [32]. In this thesis, we focus on continuum shape sensitivity analysis of structural dynamics, which has received a smaller amount of attention in the literature compared to most other topics in this field. Kim et al. [33] reported a continuum shape sensitivity analysis approach for transient dynamic structural problems, which was implemented in the design optimization of a vehicle bumper subject to an impact load. A brief introduction to shape design sensitivity analysis is given in Chapter 2 of this thesis.

Recently, several research results were proposed on design sensitivity analysis of dynamic multi-scale simulations based on the bridging scale method. Kim et al. [34] reported a discrete-analytical multi-scale adjoint design sensitivity analysis method for 1-D and 2-D bridging scale problems. Wang and Chang [35] developed a continuum-based sensitivity analysis method for 2-D multi-scale problems based on a variational formulation of bridging scale. However, rather than shape design, these works focused only on material/sizing design variables, such as atomic mass, interatomic potential function parameters and the thickness of a 2-D sheet.

1.3 Objectives and Scope

In this thesis, we aim at developing a shape sensitivity analysis approach for multi-scale crack propagation problems based on the bridging scale method, in order to reveal the impact of macroscopic shape change on the speed of crack growth at microscopic level. One unique challenge in continuum shape design for coupled atomistic/continuum systems is the discrete nature of the MD simulation. Starting from a continuum variational formulation, we will derive the coupled multi-scale sensitivity expressions in a fully generalized three-dimensional setting, which can be used to analytically compute the sensitivity coefficients of structural responses, such as the displacements of atoms and FE nodes. Particular emphasis will be placed on sensitivity analysis of dynamic crack propagation, for which we need to define an adequate performance measure that quantifies the speed of crack based on atomic displacements. To overcome the non-differentiability of the performance measure of crack speed, a hybrid method that combines analytical sensitivity analysis and finite difference method will be proposed, in which the sensitivity of crack speed is calculated through regression analysis based on analytical sensitivity results. The accuracy of the proposed analytical sensitivity analysis approach and the hybrid method will be demonstrated in a 3-D nano-beam example.

As discussed earlier, neither molecular dynamics nor multi-scale simulations are currently applicable to macroscopic applications. Therefore, this thesis will focus more on methodology development than designing physical devices. Instead of using a real-word structure, we will build a simple nano-scale model for our numerical example, and focus only on brittle crack propagation among various types of fractures. Moreover, as with many MD simulations reported [2,8,12,13], we will adopt a simple interatomic potential function with normalized units to model a generic ‘brittle’ material rather than specific materials. Our objective is to concentrate on theoretical derivation and discussion, and validate the proposed sensitivity analysis approach using an example problem that reveals the generic features of fracture common to a large class of real physical systems.

This thesis attempts for the first time to perform shape sensitivity analysis on coupled atomistic/continuum structural models. Since first-principles-based calculation is employed to capture atomistic level dynamics near the crack tips, it becomes possible to understand the impact of macroscopic shape change on microscopic crack propagation without the necessity of incorporating continuum fracture mechanics theories.

1.4 Outline of the Thesis

The rest of the thesis is organized as follows:

In Chapter 2, we present a brief introduction to shape design sensitivity analysis. In addition to basic concepts and fundamental elements, a simple one-dimensional example will be used to explain various sensitivity analysis approaches for both static and dynamic problems.

In Chapter 3, we review the fundamental theory of the bridging scale method, including the derivation of the time history kernel and the impedance boundary condition. Details of the theory will be explained using a simple one-dimensional lattice. Implementation aspects of bridging scale method for crack propagation problems will also be discussed. A three-dimensional nano-beam example will be introduced to demonstrate the method.

In Chapter 4, we develop a continuum shape sensitivity analysis approach for bridging scale method, based on which the sensitivity of structural responses can be computed. The discontinuity issue in shape DSA of coupled atomistic/continuum systems will be discussed. The analytical sensitivity expressions will be derived in a continuum setting based on the variational formulation of bridging scale. The nano-beam example will be used to verify the accuracy of the calculated sensitivity coefficients of structural responses.

In Chapter 5, we establish a performance measure that quantifies crack propagation speed for sensitivity analysis. The differentiability of crack speed with respect to shape design variables will be discussed from both theoretical and numerical perspectives. The nonlinearity of the performance measure in design space will be illustrated via the nano-beam example.

In Chapter 6, we propose a hybrid sensitivity analysis method to evaluate the sensitivity of crack propagation speed. The sensitivity coefficient of crack speed is computed through polynomial regression analysis based on the analytical sensitivity coefficients of structural responses. Using the nano-beam example, we will carry out a what-if study to demonstrate the feasibility and accuracy of the hybrid method.

In Chapter 7, we conclude this thesis and identify the scope for future research.

Detailed discussions on a number of important topics are included in appendices. Appendix A reviews the basics of classical fracture mechanics theory, as well as a series of molecular dynamics simulations of brittle fracture. Appendix B introduces the formulation of the adjoint variable method. Appendix C gives detailed derivation of the time history kernel for a 1-D atomic lattice. Appendix D demonstrates the derivation of the impedance boundary condition for generalized 3-D atomic structures. Appendix E explains the discretization of the coarse scale outside the MD region. Appendix F introduces the variational formulation for bridging scale method. Appendix G discusses the material derivative of the coarse scale outside the MD region. Appendix H provides detailed steps of the regression analysis used in hybrid method.

CHAPTER 2

SHAPE DESIGN SENSITIVITY ANALYSIS

– A TUTORIAL EXAMPLE

2.1 Introduction

Structural analysis solves the mathematical model of a physical problem. Compared to a differential equation, an energy-based variational formulation is more natural and general in governing the deformation of the structure. For example, the variational equation for a general static structural problem can be formulated based on the principle of virtual work, as

$$a(\boldsymbol{z},\bar{\boldsymbol{z}}) = \ell(\bar{\boldsymbol{z}}), \ \forall \bar{\mathbf{z}} \in Z \tag{2.1a}$$

$$Z = \left\{ \boldsymbol{z} \in \left[H^m(\Omega) \right]^3 \middle| \, \boldsymbol{z} = \boldsymbol{z}_\Gamma \ \text{on} \ \mathbf{x} \in \Gamma^h \right\} \tag{2.1b}$$

where $a(\boldsymbol{z},\bar{\boldsymbol{z}})$ and $\ell(\bar{\boldsymbol{z}})$ are known as the energy bilinear form and load linear forms, respectively, in which $\boldsymbol{z}$ denotes the displacement field to be solved, and $\bar{\boldsymbol{z}}$ stands for the virtual displacement. In addition, $\mathbf{x}$ represents spatial coordinate, Γ^h denotes the essential boundary, and $\boldsymbol{z}_\Gamma$ is the displacement at the essential boundary. Note that both the displacement solution $\boldsymbol{z}$ and the virtual displacement $\bar{\boldsymbol{z}}$ belong to the space of kinematically admissible displacements Z, in which H^m is the Sobolev space of order m.

For an arbitrary-shaped structure, it is generally impossible to obtain the analytical solution of the variational equation (Eq. 2.1). Therefore, an approximation approach is necessary, such as the finite element method. The finite element method approximates the structural domain as a simple geometry set, and establishes the equilibrium conditions for individual elements. The structural problem can then be modeled with a global system of matrix equations. For example, by discretizing the variational equation using shape functions, the finite element matrix equation for a linear elastic structure under static load can be obtained as

$$\mathbf{K}\mathbf{z} = \mathbf{F} \tag{2.2}$$

where **z** is the nodal displacement vector to be solved, **F** is the external nodal force vector, and **K** is called the stiffness matrix. Note that the displacement solution **z** (bold faced + non-italic) in Eq. 2.2 is a column vector that consists of all degrees of freedom of all finite element nodes to be solved, whereas the continuous displacement field $\boldsymbol{z}$ (bold faced + italic) in Eq. 2.1 is a vector whose size depends on the dimension of the problem (e.g., $\boldsymbol{z}$ is a 3×1 vector for three dimensional problems), while each component in vector $\boldsymbol{z}$ is a function of spatial location **x**.

The objective of structural design is to enhance the performance of a structure by changing its parameters. Examples of performance measure in engineering fields include stress, self-weight, stiffness, vibration level, fatigue life, etc. Parameters that can be adjusted during the design process are called design variables, which can be classified based on their characteristics. Various types of design variables have been introduced in Chapter 1 and illustrated in Fig. 1.3.

It is apparent that Eqs. 2.1 and 2.2 are dependent on design variables. For example, the stiffness matrix **K** in Eq. 2.2 varies with the shape or material property of the structure. Consequently, the response of the structure, such as the displacement solution **z**, and hence the performance measures that depend on structural response will change with design variables. When improving or optimizing the performance of the structure by adjusting the design variables, one essential step is design sensitivity analysis, which is used to compute the sensitivity (or design sensitivity, sensitivity coefficient, gradient) of the performance measures with respect to design variables – in other words, the rate of performance measure change with respect to design variable changes. Sensitivity analysis results reveal the relative importance of various design variables to the overall performance of the system, and thus help engineers decide the direction and amount of design change needed to improve the performance towards an optimum design.

As mentioned in the previous chapter, the formulation of design sensitivity analysis can vary significantly depending on which kind of design variables are being considered. For example, in continuum sensitivity analysis, the formulations that treat sizing/material and shape design variables are fundamentally different. This thesis is aimed at shape design sensitivity analysis. For 1-D problems, the only shape design variable is length; for 2-D and 3-D structures, shape sensitivity analysis is concerned with the relation between a variation in geometric shape of a solid domain and the resulting variation in structural performance.

In general, three approaches can be employed in design sensitivity analysis: the approximation, discrete, and continuum approaches. In the approximation approach, design sensitivity is obtained using overall finite difference by rerunning structural analysis at a perturbed design. On the other hand, the discrete and continuum methods analytically formulate the sensitivity calculation. In the discrete method, design sensitivity is obtained by taking design derivatives of the discrete governing equation. If the design derivative of the stiffness matrix is obtained analytically, it is a *discrete-*

analytical method; if the derivative is obtained using finite difference, then the method is called a *semianalytical* method – the most employed approach other than overall finite difference. In the continuum approach, the design derivative of the continuum variational equation is taken before discretization. If the structural problem and sensitivity equations are solved in a continuum setting, then it is called a *continuum-continuum* method; if the continuum sensitivity equation is solved through discretization (such as using FEA), this method is called a *continuum-discrete* method.

The sensitivity analysis methods mentioned above are listed in Fig. 2.1. These methods will be explained in subsequent sections using a simple one-dimensional structure for both static and dynamic problems. Note that in this thesis, the continuum-discrete approach will be applied to carry out shape sensitivity analysis for dynamic multi-scale problems.

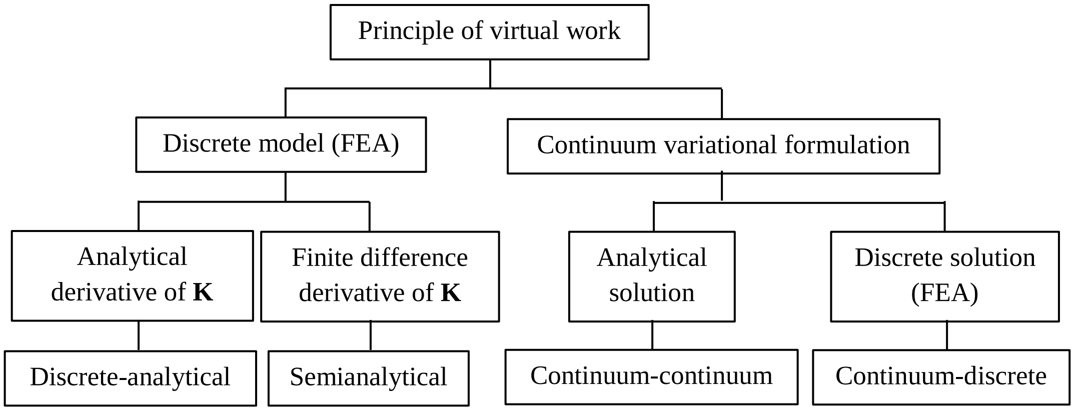

Figure 2.1 Different approaches for design sensitivity analysis

2.2 Simple Bar Example – Static Problem

In this section, a simple static problem is introduced to explain the concept of shape sensitivity analysis and to demonstrate various approaches that can be used to obtain the design sensitivity. As illustrated in Fig. 2.2, the physical structure to be studied is a one-dimensional bar under uniformly distributed load *f* (such as self-weight), and with Young's modulus *E*, uniform cross-sectional area *A*, and length *l*. Our objective is to find the sensitivity of displacement *z*(*x*) with respect to *l*, especially the sensitivity of the displacement at the tip of the bar (*x* = *l*).

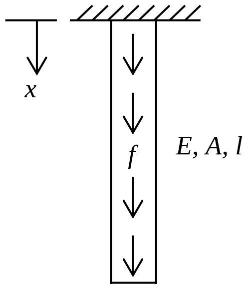

Figure 2.2 Static one-dimensional bar example

2.2.1 Structural Analysis

The governing differential equation of the bar being stretched can be written from the force equilibrium of an infinitesimal element, yielding

$$-\left(EAz_{,1}\right)_{,1} = f \tag{2.3}$$

with boundary conditions

$$z(0) = 0\,;\;\; z_{,1}(l) = 0 \tag{2.4}$$

where the subscript comma denotes differentiation with respect to the spatial coordinate, i.e., $z_{,1} = \partial z/\partial x$. Solving the differential equation gives the solution to the structural problem; that is

$$z(x) = -\frac{f}{2EA}x^2 + \frac{fl}{EA}x \tag{2.5}$$

Thus the value of the performance measure – displacement at the tip of the bar – can be obtained as

$$z(l) = \frac{f\,l^2}{2EA} \tag{2.6}$$

Note that only a handful of structural problems can be formulated and solved analytically. In general, structural problems are solved by using the finite element method. The formulation of FEM usually starts from the principle of virtual work, as will be illustrated next.

According to the principle of virtual work, we derive the variational equation of the structural problem by multiplying both sides of Eq. 2.3 with an arbitrary virtual displacement $\bar{z}$ and then integrate over the domain $x = [0, l]$, giving

$$\int_0^l EAz_{,1}\bar{z}_{,1}dx - \left(EAz_{,1}\bar{z}\right)\Big|_0^l = \int_0^l f\,\bar{z}dx \tag{2.7}$$

where integration by part is used once. Both z and $\bar{z}$ belong to the space of kinematically admissible displacement

$$Z = \left\{ z \in H^1(0,l) \mid z(0) = 0 \right\} \tag{2.8}$$

where H^1 is the first order Sobolev space. Since the boundary terms in Eq. 2.7 can be eliminated by considering $\bar{z}(0) = 0$ and applying the natural boundary condition $z_{,1}(l) = 0$, the following variational equation is obtained for the bar problem

$$a(z,\bar{z}) = \int_0^l EAz_{,1}\bar{z}_{,1}dx = \int_0^l f\,\bar{z}dx = \ell(\bar{z}) \tag{2.9}$$

which holds for all $\bar{z} \in Z$.

Finite Element Analysis

Consider discretizing the bar using two truss elements, each with length $l/2$, as shown in Fig. 2.3.

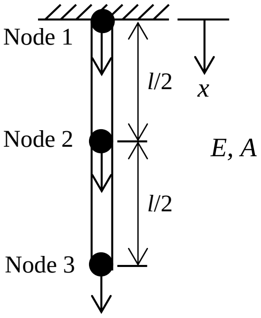

Figure 2.3 Finite element model of the 1-D bar structure. Two truss elements are used to discretize the structural domain

In this example, linear interpolation is used to describe the displacement field between nodal points. For example, the displacement between Node 1 and Node 2 can be written as

$$z_{FEA}(x)=\begin{bmatrix}N_1 & N_2\end{bmatrix}\cdot\begin{bmatrix}z_1\\ z_2\end{bmatrix}=\begin{bmatrix}2x/l & 1-2x/l\end{bmatrix}\cdot\begin{bmatrix}z_1\\ z_2\end{bmatrix};\quad 0\le x\le l/2 \tag{2.10}$$

where N_1 and N_2 are shape functions, while z_1 and z_2 represent nodal displacements.

Discretizing the left and right hand sides of the variational equation (Eq. 2.9) using shape functions gives

$$\int_0^l EAz_{,1}\bar{z}_{,1}dx \overset{discretize}{=} \begin{bmatrix}\bar{z}_1\\ \bar{z}_2\\ \bar{z}_3\end{bmatrix}^T\cdot\frac{2EA}{l}\begin{bmatrix}1 & -1 & 0\\ -1 & 2 & -1\\ 0 & -1 & 1\end{bmatrix}\cdot\begin{bmatrix}z_1\\ z_2\\ z_3\end{bmatrix}=\bar{\mathbf{z}}_g\mathbf{K}_g\mathbf{z}_g \tag{2.11a}$$

$$\int_0^l f\,\bar{z}dx \overset{discretize}{=} \begin{bmatrix}\bar{z}_1\\ \bar{z}_2\\ \bar{z}_3\end{bmatrix}^T\cdot\begin{bmatrix}fl/4\\ fl/2\\ fl/4\end{bmatrix}=\bar{\mathbf{z}}_g\mathbf{F}_g \tag{2.11b}$$

where $\mathbf{K}_g$ is called the generalized global stiffness matrix. $\mathbf{z}_g$, $\bar{\mathbf{z}}_g$, and $\mathbf{F}_g$ are global displacement, virtual displacement, and force vectors, respectively. Note that the distributed load f has been converted into point loads acting upon the nodal points.

Since the left hand sides of Eqs. 2.11a and 2.11b are equal to each other, the global finite element matrix equation can be obtained by eliminating the arbitrary virtual displacement $\bar{\mathbf{z}}_g$, as

$$\mathbf{K}_g\mathbf{z}_g = \frac{2EA}{l}\begin{bmatrix} 1 & -1 & 0 \\ -1 & 2 & -1 \\ 0 & -1 & 1 \end{bmatrix} \cdot \begin{bmatrix} z_1 \\ z_2 \\ z_3 \end{bmatrix} = \begin{bmatrix} fl/4 \\ fl/2 \\ fl/4 \end{bmatrix} = \mathbf{F}_g \tag{2.12}$$

which cannot be solved due to the singularity of $\mathbf{K}_g$. By applying the boundary condition $z_1 = 0$, we can remove z_1 from Eq. 2.12, giving

$$\mathbf{Kz} = \frac{2EA}{l}\begin{bmatrix} 2 & -1 \\ -1 & 1 \end{bmatrix} \cdot \begin{bmatrix} z_2 \\ z_3 \end{bmatrix} = \begin{bmatrix} fl/2 \\ fl/4 \end{bmatrix} = \mathbf{F} \tag{2.13}$$

where

$$\mathbf{K} = \frac{2EA}{l}\begin{bmatrix} 2 & -1 \\ -1 & 1 \end{bmatrix} \tag{2.14}$$

is called the reduced global stiffness matrix, which is nonsingular. Solving the reduced global matrix equation (Eq. 2.13) gives nodal displacement solution

$$\mathbf{z} = \begin{bmatrix} z_2 \\ z_3 \end{bmatrix} = \begin{bmatrix} \dfrac{3fl^2}{8EA} \\ \dfrac{fl^2}{2EA} \end{bmatrix} \tag{2.15}$$

based on which the displacement at an arbitrary location in the domain $x = [0, l]$ can be interpolated using shape functions, as

$$z_{FEA}(x) = \begin{cases} \begin{bmatrix} 2x/l & 1-2x/l \end{bmatrix} \cdot \begin{bmatrix} z_1 \\ z_2 \end{bmatrix}, & 0 \le x \le l/2 \\ \begin{bmatrix} 2(x-l/2)/l & 1-2(x-l/2)/l \end{bmatrix} \cdot \begin{bmatrix} z_2 \\ z_3 \end{bmatrix}, & l/2 < x \le l \end{cases} \tag{2.16}$$

It is of note that the finite element displacement solution $z_{FEA}(x)$ matches the analytical solution (Eq. 2.5) only at nodal points, i.e., $z_2 = z(l/2)$ and $z_3 = z(l)$. This is because linear shape functions are used for interpolation in Eq. 2.16, whereas the analytical solution to the problem is a quadratic function of x.

2.2.2 Shape Design Sensitivity Analysis

As discussed earlier, shape sensitivity analysis computes the rate of performance measure change with respect to the change of shape design variables. In this section, we demonstrate the sensitivity approaches listed in Fig. 2.1 with the simple bar example.

One important concept in shape design is the *design velocity field*. When shape design variables vary, the geometric shape of the structural boundary, and hence the location of material points inside the structural domain must change accordingly. The design velocity field governs the movement of material points both on the boundary and inside the structural domain, providing a systematic scheme that maps the location of material points from original design to updated design.

Consider a structural domain Ω with its boundary Γ as a continuous medium at the initial design $\tau = 0$ as shown in Fig. 2.4 (solid line). Suppose only one parameter τ defines the transformation $\boldsymbol{T}$ that changes the structural domain from Ω to Ω_τ (dashed line). The transformation mapping $\boldsymbol{T}$ that represents this process can be defined as [32]

$$\boldsymbol{T} : \mathbf{x} \rightarrow \mathbf{x}_\tau(\mathbf{x}), \mathbf{x} \in \Omega \tag{2.17}$$

where $\mathbf{x}$ denotes a material point.

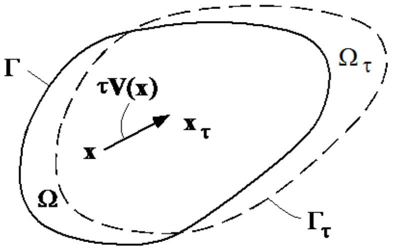

Figure 2.4 Changing of structural domain

The design velocity field $\boldsymbol{V}$ that governs material movement due to a design change is defined as

$$\boldsymbol{V}(\mathbf{x},\tau)\equiv\frac{d\mathbf{x}_\tau}{d\tau}=\frac{d\boldsymbol{T}(\mathbf{x},\tau)}{d\tau} \tag{2.18}$$

where τ plays the role of design time (or design iteration in practice). In the neighborhood of initial design τ = 0, assuming a regularity hypothesis and ignoring higher-order terms, $\boldsymbol{T}$ can be approximated by

$$\boldsymbol{T}(\mathbf{x},\tau)=\boldsymbol{T}(\mathbf{x},0)+\tau\frac{d\boldsymbol{T}(\mathbf{x},0)}{d\tau}+O(\tau^2)\approx\mathbf{x}+\tau\boldsymbol{V}(\mathbf{x}) \tag{2.19}$$

where $\mathbf{x}\equiv\boldsymbol{T}(\mathbf{x},0)$ and $\boldsymbol{V}(\mathbf{x})\equiv\boldsymbol{V}(\mathbf{x},0)$. Note that only the linear term is retained in Eq. 2.19, and τ is determined by the design change.

For the 1-D bar problem, the only shape design variable is length l. For simplicity, we define a linear design velocity field for shape sensitivity analysis; that is

$$V(x)=\frac{x}{l}\delta l \tag{2.20}$$

as illustrated in Fig. 2.5. This linear design velocity field implies that when the bar is elongated, each material point on the current bar moves downwards proportionally to its x coordinate. For instance, the midpoint $x = l/2$ moves to $x = (l + \delta l)/2$ after the design change. Note that during implementation, δl is usually set to 1 for convenience.

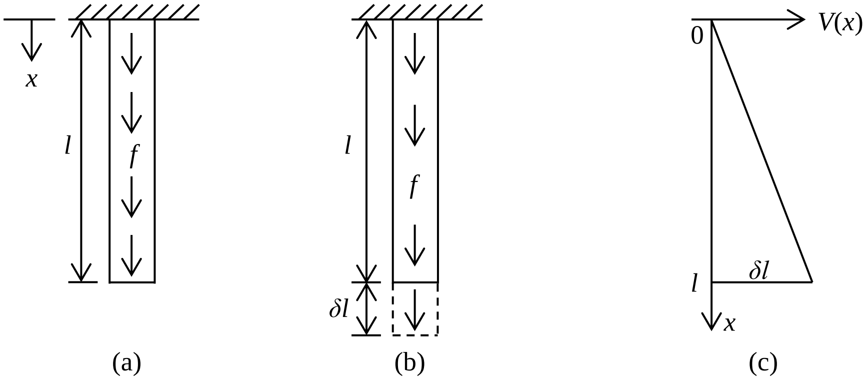

Figure 2.5 Linear design velocity field defined for the simple bar example, (a) structure before design change, (b) structure after design change with length increment *δl*, and (c) linear design velocity field

In the previous section, the displacement at the tip of the bar has been solved using both continuum (analytical) and discrete (FEA) structural analysis approaches. For this simple example, since the solution $z(l)$ is explicitly dependent on design variable l, the sensitivity of $z(l)$ with respect to l can be obtained directly by taking derivative of Eq. 2.6, as

$$\frac{d\,z(l)}{dl} = \frac{f\,l}{EA} \tag{2.21}$$

However, in most cases, a structural performance measure does not explicitly depend on design, and therefore, the sensitivity information needs to be computed using sensitivity analysis methods, as to be introduced in the following sections.

2.2.2.1 Overall Finite Difference Method

Different values of design variables yield different structural analysis results, and hence different values of the performance measure. The easiest way of computing the design sensitivity is by evaluating the performance measure at different stages in the design process. Let $\psi(\mathbf{b})$ denote a general performance measure that depends on design

$$\mathbf{b} = \begin{bmatrix} b_1 & b_2 & \cdots & b_k \end{bmatrix}^T \tag{2.22}$$

which is a vector comprised of all k design variables. The sensitivity of $\psi(\mathbf{b})$ with respect to the ith design variable b_i can be approximated through overall finite difference, as

$$\frac{d\psi}{db_i} \approx \frac{\psi\left(\mathbf{b}^0 + \Delta b_i\right) - \psi\left(\mathbf{b}^0\right)}{\Delta b_i} \tag{2.23}$$

which is also called the forward difference method. Note that $\mathbf{b}^0$ represents the current design, while Δb_i stands for a small prescribed perturbation made to design variable b_i.

For the simple bar example, if the displacement is solved using FEA, then in overall finite difference method, we first solve the displacement of a perturbed structural problem

$$\mathbf{K}(l + \Delta l)\mathbf{z} = \mathbf{F}(l + \Delta l) \tag{2.24}$$

Then, the sensitivity coefficient of the performance measure can be approximated as

$$\frac{d\psi}{db_i} = \frac{dz_3}{dl} \approx \frac{z_3(l + \Delta l) - z_3(l)}{\Delta l} = \frac{\dfrac{f(l + \Delta l)^2}{2EA} - \dfrac{fl^2}{2EA}}{\Delta l} = \frac{2fl + f\Delta l}{2EA} \tag{2.25}$$

where $z_3(l + \Delta l)$ denotes the displacement solution at Node 3 for the perturbed structure with bar length $l + \Delta l$ solved using FEA. As can be seen, as the design perturbation Δl approaches zero, the overall finite difference result (Eq. 2.25) converges to the exact sensitivity value calculated in Eq. 2.21.

Although attractive and popular due to its simplicity, the overall finite difference method suffers major disadvantages. First of all, $k + 1$ structural analyses need to be carried out to compute the sensitivity with respect to all k design variables, which makes this method computationally expensive for large scale problems that involve many design variables. Moreover, the determination of the perturbation size Δb_i greatly affects the sensitivity result. As shown in Fig. 2.6, when the behavior of the performance measure ψ is nonlinear in design space, the design sensitivity approximated using overall finite difference method can be inaccurate if the perturbation size is too large. On the other hand, when a very small perturbation is used, the impact of numerical truncation errors becomes significant. As a result, it is difficult to determine a design perturbation size that works for all problems.

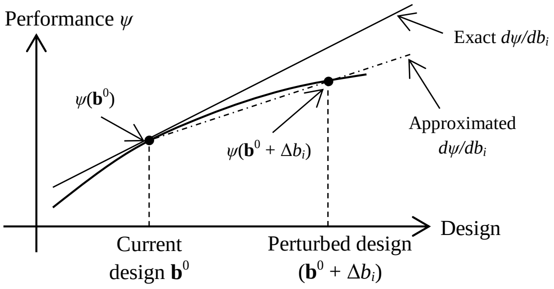

Figure 2.6 Influence of perturbation size in overall finite difference method

2.2.2.2 Discrete Method

When a structural problem is discretized in finite dimensional space, as shown with the finite element method in Section 2.2.1, discrete sensitivity analysis methods can be used to compute the sensitivity of performance for the discretized problem. Consider a linear elastic finite element matrix equation

$$\mathbf{K}(\mathbf{b})\mathbf{z} = \mathbf{F}(\mathbf{b}) \tag{2.26}$$

where the stiffness matrix **K** and the force vector **F** are both functions of design **b**. The total derivative of a performance measure ψ with respect to design variable b_i can be expressed analytically using the chain rule of differentiation, as

$$\frac{d\psi}{db_i} = \frac{\partial \psi}{\partial b_i} + \frac{\partial \psi}{\partial \mathbf{z}} \frac{d\mathbf{z}}{db_i} \tag{2.27}$$

Note that since the expressionfor ψ with respect to b_i and $\mathbf{z}$ is known from its definition, the only unknown in Eq. 2.27 is the $d\mathbf{z}/db_i$ term, which can be computed using either the *direct differentiation method* (DDM) or the *adjoint variable method* (AVM). In this thesis, we focus on the former (which is chosen to be implemented in our numerical example) when demonstrating the sensitivity calculation. The formulation of the adjoint variable method can be found in Appendix B.

Direct Differentiation Method

The direct differentiation method evaluates the implicit dependence of $\mathbf{z}$ on design $\mathbf{b}$ by differentiating the structural equation (Eq. 2.26); that is

$$\mathbf{K}(\mathbf{b})\frac{d\mathbf{z}}{db_i}+\frac{\partial \mathbf{K}(\mathbf{b})}{\partial b_i}\mathbf{z}=\frac{\partial \mathbf{F}(\mathbf{b})}{\partial b_i} \tag{2.28}$$

Rearranging Eq. 2.28 by leaving only unknown terms on the left hand side gives

$$\mathbf{K}(\mathbf{b})\frac{d\mathbf{z}}{db_i}=\frac{\partial \mathbf{F}(\mathbf{b})}{\partial b_i}-\frac{\partial \mathbf{K}(\mathbf{b})}{\partial b_i}\mathbf{z} \tag{2.29}$$

which is sometimes referred to as the *sensitivity equation* or *sensitivity expression*. Note that the displacement solution $\mathbf{z}$ on the right hand side has been obtained through structural analysis (Eq. 2.15). Solving Eq. 2.29 for $d\mathbf{z}/db_i$ by inverting the nonsingular reduced stiffness matrix $\mathbf{K}(\mathbf{b})$ yields

$$\frac{d\mathbf{z}}{db_i}=\mathbf{K}^{-1}(\mathbf{b})\left[\frac{\partial \mathbf{F}(\mathbf{b})}{\partial b_i}-\frac{\partial \mathbf{K}(\mathbf{b})}{\partial b_i}\mathbf{z}\right] \tag{2.30}$$

Substituting the result into Eq. 2.27 then gives the sensitivity of ψ with respect to b_i, as

$$\frac{d\psi}{db_i}=\frac{\partial \psi}{\partial b_i}+\frac{\partial \psi}{\partial \mathbf{z}}\mathbf{K}^{-1}(\mathbf{b})\left[\frac{\partial \mathbf{F}(\mathbf{b})}{\partial b_i}-\frac{\partial \mathbf{K}(\mathbf{b})}{\partial b_i}\mathbf{z}\right] \tag{2.31}$$

The direct differentiation method has been extensively used in structural sensitivity analysis due to its straightforward derivations. Consider the simple bar problem as an example. Using direct differentiation method, we can evaluate the sensitivity of z_3 with respect to l by applying Eq. 2.31 to the reduced finite element matrix equation (Eq. 2.13), as

$$\begin{aligned}\frac{dz_3}{dl} &= \frac{\partial z_3}{\partial l} + \frac{\partial z_3}{\partial \mathbf{z}}\mathbf{K}^{-1}\left[\frac{\partial \mathbf{F}}{\partial l} - \frac{\partial \mathbf{K}}{\partial l}\mathbf{z}\right] \\ &= 0 + \begin{bmatrix} 0 & 1 \end{bmatrix} \cdot \frac{l}{2EA}\begin{bmatrix} 1 & 1 \\ 1 & 2 \end{bmatrix} \cdot \left\{ \begin{bmatrix} f/2 \\ f/4 \end{bmatrix} + \frac{2EA}{l^2}\begin{bmatrix} 2 & -1 \\ -1 & 1 \end{bmatrix}\begin{bmatrix} \dfrac{3fl^2}{8EA} \\ \dfrac{fl^2}{2EA} \end{bmatrix} \right\} = \frac{fl}{EA}\end{aligned} \tag{2.32}$$

which is consistent with the exact solution in Eq. 2.21.

Note that in adjoint variable method, we create an adjoint structure in order to solve for the $(\partial\psi/\partial\mathbf{z})\mathbf{K}^{-1}(\mathbf{b})$ term in Eq. 2.31 directly (shown in Appendix B). The adjoint variable method gives the same sensitivity result as the direct differentiation method. In practice, we choose between DDM and AVM by considering computation efficiency. Generally, for static problems, if the number of performance measures is larger than that of the design variables, then the direct differentiation method is preferable; otherwise, the adjoint variable method will be more efficient. The comparison between DDM and AVM will be explained in detail in Appendix B.

It is also worthy of note that in discrete method, the calculation of design sensitivity (Eq. 2.31) requires differentiating $\mathbf{K}(\mathbf{b})$ and $\mathbf{F}(\mathbf{b})$ with respect to design. If the derivatives $\partial\mathbf{K}(\mathbf{b})/\partial b_i$ and $\partial\mathbf{F}(\mathbf{b})/\partial b_i$ can be analytically calculated from the explicit expressions of the $\mathbf{K}(\mathbf{b})$ and $\mathbf{F}(\mathbf{b})$, then this approach is called a *discrete-analytical* method. However, in general, the explicit expression of $\mathbf{K}$ in terms of design variables may not be available in FEA, especially when a commercial code, such as ANSYS, is used. In those cases, instead of solving $\partial\mathbf{K}(\mathbf{b})/\partial b_i$ explicitly, the design derivative can be approximated using finite difference method, as

$$\frac{\partial\mathbf{K}(\mathbf{b})}{\partial b_i} \approx \frac{\mathbf{K}(\mathbf{b}^0 + \Delta b_i) - \mathbf{K}(\mathbf{b}^0)}{\Delta b_i} \tag{2.33}$$

and this approach is called a *semianalytical* method.

2.2.2.3 Continuum Method

In contrast to the discrete methods, a continuum sensitivity analysis approach uses a continuous displacement field rather than nodal displacements to characterize structural deformation. The continuum sensitivity equations – written in the form of integrals – are obtained by taking design derivative of the continuum variational equation before any discretization takes place.

In continuum shape sensitivity analysis, the physical domain is considered as a continuous medium that changes with design. Therefore, the concept of design velocity field (discussed earlier) and material derivative from continuum mechanics are utilized to obtain a computable expression that relates variations in structural shape to the performance measures.

Material Derivative

Here we first introduce the concept of material derivative used in continuum shape sensitivity analysis. Suppose $\boldsymbol{z}$ is the solution to the structural problem in current domain Ω, the material derivative of $\boldsymbol{z}$ is defined as [32]

$$\dot{\boldsymbol{z}} \equiv \frac{d}{d\tau} \boldsymbol{z}_\tau(\mathbf{x} + \tau\boldsymbol{V}(\mathbf{x}))\Big|_{\tau=0} = \lim_{\tau=0}\left[\frac{\boldsymbol{z}_\tau(\mathbf{x} + \tau\boldsymbol{V}(\mathbf{x})) - \boldsymbol{z}(\mathbf{x})}{\tau}\right] \tag{2.34}$$

where $\boldsymbol{V}(\mathbf{x})$ is the design velocity field introduced in Eq. 2.18. Note that the material derivative of $\boldsymbol{z}$ can be separated into two contributions, as

$$\begin{aligned}\dot{\boldsymbol{z}} &= \lim_{\tau=0}\left[\frac{\boldsymbol{z}_\tau(\mathbf{x})-\boldsymbol{z}(\mathbf{x})}{\tau}\right]+\lim_{\tau=0}\left[\frac{\boldsymbol{z}_\tau(\mathbf{x}+\tau\boldsymbol{V}(\mathbf{x}))-\boldsymbol{z}_\tau(\mathbf{x})}{\tau}\right] \\ &= \boldsymbol{z}'(\mathbf{x})+\nabla\boldsymbol{z}\boldsymbol{V}(\mathbf{x})\end{aligned} \tag{2.35}$$

More specifically, material derivative $\dot{\boldsymbol{z}}(\mathbf{x})$ reveals how the displacement at location $\mathbf{x}$ changes with design, while the measuring point $\mathbf{x}$ moves with the design velocity field. On the other hand, partial derivative $\boldsymbol{z}'(\mathbf{x})$ indicates the difference between displacements before and after design change, measured at the same location. $\nabla\boldsymbol{z}$ represents the gradient of displacement at current design.

Taking the simple bar model as an example, the analytical solution z has been given in Eq. 2.5, based on which the displacement solution associated with a new design with bar length $l + \delta l$ can be easily obtained as

$$z_\tau(x) = -\frac{f}{2EA}x^2+\frac{f(l+\delta l)}{EA}x \tag{2.36}$$

If we focus on the displacement at the midpoint $x = l/2$, then the partial derivative $z'(l/2)$ can be evaluated as

$$z'(l/2)=\lim_{\delta l=0}\left[\frac{z_\tau(l/2)-z(l/2)}{\delta l}\right]=\lim_{\delta l=0}\left[\frac{\left(\frac{3fl^2}{8EA}+\frac{fl\delta l}{2EA}\right)-\left(\frac{3fl^2}{8EA}\right)}{\delta l}\right]=\frac{fl}{2EA} \tag{2.37}$$

where the parameter τ in Eq. 2.35 is replaced by δl in this practical case.

The displacement gradient can be calculated as

$$\nabla z(l/2)=z_{,1}(l/2)=\frac{fl}{2EA} \tag{2.38}$$

and the design velocity at the midpoint is $V(l/2) = 1/2$ according to the linear velocity field defined in Eq. 2.20. Finally, the material derivative at $x = l/2$ is defined as

$$\dot{z}(l/2) = \lim_{\delta l = 0}\left[\frac{z_\tau((l+\delta l)/2) - z(l/2)}{\delta l}\right] = \lim_{\delta l = 0}\left[\frac{\dfrac{3f(l+\delta l)^2}{8EA} - \dfrac{3fl^2}{8EA}}{\delta l}\right] = \frac{3fl}{4EA} \tag{2.39}$$

which is equal to the sum of $z'(l/2)$ and $\nabla z(l/2)\cdot V(l/2)$.

Now we introduce the material derivative of domain functions. Let Ψ be a functional defined as an integral over the current domain Ω

$$\Psi = \iint_\Omega f(\mathbf{x})d\Omega \tag{2.40}$$

then the material derivative of Ψ at Ω can be calculated as [32]

$$\dot{\Psi} = \iint_\Omega \left[f'(\mathbf{x}) + \nabla f(\mathbf{x})^T \boldsymbol{V} + f(\mathbf{x})div\boldsymbol{V}\right]d\Omega \tag{2.41}$$

where

$$f'(\mathbf{x}) \equiv \frac{d}{d\tau} f_\tau(\mathbf{x})\Big|_{\tau=0} = \lim_{\tau=0}\left[\frac{f_\tau(\mathbf{x}) - f(\mathbf{x})}{\tau}\right] \tag{2.42}$$

and $div\boldsymbol{V}$ is the divergence of $\boldsymbol{V}$, defined as $div\boldsymbol{V} = \partial\mathbf{V}/\partial x + \partial\mathbf{V}/\partial y + \partial\mathbf{V}/\partial z$ for a general 3-D scenario. For the 1-D simple bar example, $divV = \partial V/\partial x = 1/l$.

Continuum Shape Sensitivity Analysis

We now use the simple bar example to illustrate the continuum sensitivity analysis methods. Based on the variation formulation of the problem, we will use the direct differential method to compute the sensitivity of displacement with respect to length *l*. (Note that adjoint variable method also can be used in continuum sensitivity analysis [32].)

To start with, take material derivative of both sides of the variational equation (Eq. 2.9) using Eq. 2.41, giving

$$\begin{aligned}
\overset{\bullet}{\left[\int_0^l EAz_{,1}\bar{z}_{,1}dx\right]} &= \int_0^l \left(EAz_{,1}\bar{z}_{,1}\right)' dx + \int_0^l div\left(EAz_{,1}\bar{z}_{,1}V\right)dx \\
&= \int_0^l \left(EAz'_{,1}\bar{z}_{,1} + EAz_{,1}\bar{z}'_{,1}\right)dx + \int_0^l div\left(EAz_{,1}\bar{z}_{,1}V\right)dx \\
&= \int_0^l \left[EA\left(\dot{z} - z_{,1}V\right)_{,1}\bar{z}_{,1} + EAz_{,1}\left(\dot{\bar{z}} - \bar{z}_{,1}V\right)_{,1}\right]dx + \int_0^l \left(EAz_{,11}\bar{z}_{,1}V + EAz_{,1}\bar{z}_{,11}V + EAz_{,1}\bar{z}_{,1}V_{,1}\right)dx \qquad (2.43a) \\
&= \int_0^l \left[EA\dot{z}_{,1}\bar{z}_{,1} - EA\left(z_{,1}V\right)_{,1}\bar{z}_{,1} - EAz_{,1}\left(\bar{z}_{,1}V\right)_{,1}\right]dx + \int_0^l \left(EAz_{,11}\bar{z}_{,1}V + EAz_{,1}\bar{z}_{,11}V + EAz_{,1}\bar{z}_{,1}V_{,1}\right)dx \\
&= \int_0^l \left[EA\dot{z}_{,1}\bar{z}_{,1} - EAz_{,1}\bar{z}_{,1}V_{,1}\right]dx
\end{aligned}$$

and

$$\begin{aligned}
\overset{\bullet}{\left[\int_0^l f\bar{z}dx\right]} &= \int_0^l \left(f\bar{z}\right)' dx + \int_0^l div\left(f\bar{z}V\right)dx \\
&= \int_0^l \left(f'\bar{z} + f\bar{z}'\right)dx + \int_0^l \left(f_{,1}\bar{z}V + f\bar{z}_{,1}V + f\bar{z}V_{,1}\right)dx \qquad (2.43b) \\
&= -\int_0^l f\bar{z}_{,1}Vdx + \int_0^l \left(f\bar{z}_{,1}V + f\bar{z}V_{,1}\right)dx \\
&= \int_0^l f\bar{z}V_{,1}dx
\end{aligned}$$

Note that in derivation of Eq. 2.43a, $\dot{\bar{z}} = 0$ has been applied, which implies that the virtual displacement does not change with design. In addition, *f'* =0 is used in deriving Eq. 2.43b, which in general means that the applied load does not change with design. For the simple bar example, *f'* =0 implies that the distributed load *f* (self-weight) is also applied to the extended portion of the bar, as shown in Fig. 2.5b.

Since the right hand sides of Eqs. 2.43a and 2.43b are equal to each other, we obtain the continuum sensitivity expression

$$\int_0^l \left[EA\dot{z}_{,1}\bar{z}_{,1} - EAz_{,1}\bar{z}_{,1}V_{,1}\right]dx = \int_0^l f\bar{z}V_{,1}dx \qquad (2.44)$$

which can be rearranged as

$$\int_0^l EA\dot{z}_{,1}\bar{z}_{,1}dx = \int_0^l f\,\bar{z}V_{,1}dx + \int_0^l EAz_{,1}\bar{z}_{,1}V_{,1}dx \tag{2.45}$$

so that all terms on the right hand side are known except for $\bar{z}$.

Note that if the continuum sensitivity expression (Eq. 2.45) is solved as a continuum problem, then it is called the *continuum-continuum* method. On the other hand, if it is solved by discretization in the same way that discrete structural problems are solved, then this method is referred to as the *continuum-discrete* method. In fact, only very simple problems – such as the simple bar example – can be solved analytically using the continuum-continuum method. For the bar example, the design sensitivity can be obtained by solving Eq. 2.45 for $\dot{z}$ through integration by part, as

$$\int_0^l -EA\dot{z}_{,11}\bar{z}dx + EA\dot{z}_{,1}\bar{z}\Big|_0^l = \int_0^l f\,\bar{z}V_{,1}dx - \int_0^l EAz_{,11}\bar{z}V_{,1}dx + EAz_{,1}\bar{z}V_{,1}\Big|_0^l \tag{2.46}$$

Note that with boundary conditions $\bar{z}(0)=0$, $\dot{z}_{,1}(l)=0$, and $z_{,1}(l)=0$, the boundary terms in Eq. 2.46 can be eliminated, yielding

$$\int_0^l \bar{z}\cdot\left[-EA\dot{z}_{,11} + EAz_{,11}V_{,1} - fV_{,1}\right]dx = 0 \tag{2.47}$$

which holds for all $\bar{z}\in Z$. Therefore, the sensitivity differential equation can be obtained as

$$EA\dot{z}_{,11} = EAz_{,11}V_{,1} - fV_{,1} \tag{2.48}$$

which can be solved with boundary conditions $\dot{z}(0)=0$, $\dot{z}_{,1}(l)=0$, giving

$$\dot{z} = -\frac{f}{EAl}x^2 + \frac{2f}{EA}x \tag{2.49}$$

The sensitivity of the displacement at the tip can then be calculated as

$$\dot{z}(l) = \frac{fl}{EA} \tag{2.50}$$

which is identical to the result obtained using discrete methods.

Alternatively, Eq. 2.45 can be solved by discretization using finite element shape functions. This approach is called the continuum-discrete method since differentiation is taken at the continuum domain and is then followed by discretization. To start with, the virtual displacement $\bar{z}$, displacement solution z, and material derivative $\dot{z}$ in Eq. 2.45 are discretized using shape functions as in Eq. 2.16, giving a global matrix equation

$$\begin{bmatrix} \bar{z}_1 \\ \bar{z}_2 \\ \bar{z}_3 \end{bmatrix}^T \cdot \frac{2EA}{l} \begin{bmatrix} 1 & -1 & \\ -1 & 2 & -1 \\ & -1 & 1 \end{bmatrix} \cdot \begin{bmatrix} \dot{z}_1 \\ \dot{z}_2 \\ \dot{z}_3 \end{bmatrix} = \begin{bmatrix} \bar{z}_1 \\ \bar{z}_2 \\ \bar{z}_3 \end{bmatrix}^T \cdot \begin{bmatrix} fl/4 \\ fl/2 \\ fl/4 \end{bmatrix} \cdot \frac{1}{l} + \begin{bmatrix} \bar{z}_1 \\ \bar{z}_2 \\ \bar{z}_3 \end{bmatrix}^T \cdot \begin{bmatrix} -3fl/4 \\ fl/2 \\ fl/4 \end{bmatrix} \cdot \frac{1}{l} \quad (2.51)$$

where the nodal displacements solved in FEA (Eq. 2.15) have been substituted for z_1, z_2 and z_3. Note that the partial derivative terms ($\bar{z}_{,1}, z_{,1}$ and $\dot{z}_{,1}$) in Eq. 2.45 are discretized by taking derivative of the shape functions in Eq. 2.16.

Apparently, both sides of Eq. 2.51 can be divided by $[\bar{z}_1 \quad \bar{z}_2 \quad \bar{z}_3]$ to remove the virtual displacement terms. Moreover, the equation can be reduced by applying the boundary condition $\dot{z}_1 = 0$, yielding

$$\frac{2EA}{l} \begin{bmatrix} 2 & -1 \\ -1 & 1 \end{bmatrix} \cdot \begin{bmatrix} \dot{z}_2 \\ \dot{z}_3 \end{bmatrix} = \begin{bmatrix} fl/2 \\ fl/4 \end{bmatrix} \cdot \frac{1}{l} + \begin{bmatrix} fl/2 \\ fl/4 \end{bmatrix} \cdot \frac{1}{l} \quad (2.52)$$

which can be solved for the material derivative of nodal displacements, as

$$\begin{bmatrix} \dot{z}_2 \\ \dot{z}_3 \end{bmatrix} = \begin{bmatrix} \dfrac{3fl}{4EA} \\ \dfrac{fl}{EA} \end{bmatrix} \quad (2.53)$$

where $\dot{z}_3$ is the sensitivity of the displacement at the tip with respect to the length of the bar.

2.2.2.4 Comments on Sensitivity Analysis Approaches

So far the sensitivity analysis approaches listed in Fig. 2.1 have been demonstrated using the simple bar example. Unlike overall finite difference method, the discrete-analytical and the continuum methods provide analytical sensitivity information without recourse to the uncertainty of perturbation size. (Finite difference is necessary for calculating $\partial\mathbf{K}/\partial\mathbf{b}$ in the semianalytical method.) More importantly, it is clear that either Eq. 2.29 or Eq. 2.52 is physically the same as the original structural problem Eq. 2.13, but with a different 'applied load' on the right hand side, which is usually referred to as the *fictitious load*. Therefore, solving the sensitivity equation is much more efficient than rerunning structure analysis at a perturbed design (required in overall finite difference). This is because the decomposition of the stiffness matrix (which involves a large amount of commutation cost) has been performed in structure analysis, while solving the sensitivity equation is equivalent to solving an additional loading condition.

Note that when a commercial FEA code is used, the derivative of the stiffness matrix is generally unavailable, and, as discussed earlier, the $\partial\mathbf{K}/\partial\mathbf{b}$ term in discrete method is usually obtained through finite difference. However, in continuum-discrete method, the fictitious load (right hand side of Eq. 2.45) can be evaluated outside the FEA code using the result data (such as nodal displacements $\mathbf{z}$), and therefore it is neither necessary to differentiate the stiffness matrix $\mathbf{K}$, nor to use any matrix multiplication procedure to calculate $\left(\partial\mathbf{K}/\partial\mathbf{b}\right)\cdot\mathbf{z}$. Moreover, the continuum method provides a general and unified structural sensitivity analysis capability, so that it is possible to develop one design sensitivity analysis system that works with a number of well-established analysis methods, such as FEA, the boundary element method, and the mesh free method.

As can be seen, for the simple bar example, the continuum-discrete method yields the same sensitivity result as the discrete method. In general, for the discrete and continuum-discrete methods to be equivalent, several conditions must be satisfied [32]. For example, the same shape functions used in FEA must be used to discretize the continuum sensitivity equation; an exact integration, instead of a numerical integration, must be used in generating the FE stiffness matrix and in evaluating the continuum sensitivity expression. It is worth mentioning that in many cases, some of these conditions are not easy to satisfy, especially when a commercial FEA code is used.

Finally, for each of the approaches listed in Fig. 2.1, both the direct differentiation method and the adjoint variable method can be employed to compute the design sensitivity information of a general performance measure. For static problems, we choose between the two methods by comparing the number of performance measures with that of the design variables.

2.3 Simple Bar Example – Dynamic Problem

This section demonstrates how sensitivity analysis approaches discussed in Section 2.2 can be used for dynamic structural problems. The basic concepts and derivations are similar to those described in the last section. Both discrete and continuum approaches will be discussed using the simple bar example.

2.3.1 Structural Analysis

For a general dynamic structural problem, the variational formulation can be obtained based on the Hamilton's principle, as

$$\int_0^{t_T} \left[d(\boldsymbol{z}_{,tt}, \bar{\boldsymbol{z}}) + a(\boldsymbol{z}, \bar{\boldsymbol{z}}) \right] dt = \int_0^{t_T} \ell(\bar{\boldsymbol{z}}, t) dt \tag{2.54}$$

with initial conditions

$$\boldsymbol{z}(\mathbf{x}, 0) = \boldsymbol{z}^0(\mathbf{x}) \text{ and } \boldsymbol{z}_{,t}(\mathbf{x}, 0) = \boldsymbol{z}^0_{,t}(\mathbf{x}) \tag{2.55}$$

where the subscript '$,t$' denotes the derivative with respect to time, and t_T is the terminal time of the dynamic problem. Note that the solution of Eq. 2.54 belongs to the function space Z in Eq. 2.1b. If damping effect is not considered, the kinetic energy bilinear form $d(\boldsymbol{z}_{,tt}, \bar{\boldsymbol{z}})$ in Eq. 2.54 can be written as

$$d(\boldsymbol{z}_{,tt}, \bar{\boldsymbol{z}}) = \int_\Omega \rho \bar{\boldsymbol{z}}^T \boldsymbol{z}_{,tt} d\Omega \tag{2.56}$$

where ρ is the mass density, and Ω represents the structural domain. Moreover, in dynamic problems, the load applied can be a function of time; that is

$$\int_0^{t_T} \ell(\bar{\boldsymbol{z}}, t) dt = \int_0^{t_T} \int_\Omega \boldsymbol{f}(t) \bar{\boldsymbol{z}} d\Omega dt \tag{2.57}$$

Note that Eq. 2.54 holds for all kinematically admissible virtual displacements $\bar{\boldsymbol{z}}$ that belong to the function space in Eq. 2.1b and satisfy the additional conditions

$$\bar{\boldsymbol{z}}(\mathbf{x}, 0) = \bar{\boldsymbol{z}}(\mathbf{x}, t_T) = 0 \tag{2.58}$$

Similar to that discussed in Section 2.2.1, the variational formulation for dynamic problems can be discretized using finite element shape functions to obtain the dynamic finite element matrix equation; that is

$$\mathbf{M}(\mathbf{b})\mathbf{z}_{,tt} + \mathbf{K}(\mathbf{b})\mathbf{z} = \mathbf{F}(\mathbf{b}, t) \tag{2.59}$$

with initial conditions $\mathbf{z}(0)=\mathbf{z}^0$ and $\mathbf{z}_{,t}(0)=\mathbf{z}_{,t}^0$. Note that $\mathbf{M}(\mathbf{b})$ is the reduced finite element mass matrix.

Taking the simple bar structure as an example, if a uniformly distributed mass density ρ is assumed, the dynamic variational equation for the bar

$$\int_0^{t_T}\left[\int_0^l \rho z_{,tt}\bar{z}dx+\int_0^l EAz_{,1}\bar{z}_{,1}dx\right]dt=\int_0^{t_T}\left\{\int_0^l f\,\bar{z}dx\right\}dt \tag{2.60}$$

can be discretized as

$$\begin{aligned}&\int_0^{t_T}\left\{\begin{bmatrix}\bar{z}_1\\ \bar{z}_2\\ \bar{z}_3\end{bmatrix}^T\cdot\frac{\rho}{12}\begin{bmatrix}2l & l & 0\\ l & 4l & l\\ 0 & l & 2l\end{bmatrix}\cdot\begin{bmatrix}z_{1,tt}\\ z_{2,tt}\\ z_{3,tt}\end{bmatrix}+\begin{bmatrix}\bar{z}_1\\ \bar{z}_2\\ \bar{z}_3\end{bmatrix}^T\cdot\frac{2EA}{l}\begin{bmatrix}1 & -1 & 0\\ -1 & 2 & -1\\ 0 & -1 & 1\end{bmatrix}\cdot\begin{bmatrix}z_1\\ z_2\\ z_3\end{bmatrix}\right\}dt\\ &=\int_0^{t_T}\left\{\begin{bmatrix}\bar{z}_1\\ \bar{z}_2\\ \bar{z}_3\end{bmatrix}^T\cdot\begin{bmatrix}fl/4\\ fl/2\\ fl/4\end{bmatrix}\right\}dt\end{aligned} \tag{2.61}$$

which must hold for all virtual displacements that satisfies Eq. 2.8 and Eq. 2.58. Thus the dynamic differential equation can be obtained as

$$\begin{aligned}&\mathbf{M}_g(l)\mathbf{z}_{g,tt}+\mathbf{K}_g(l)\mathbf{z}_g\\ &=\frac{\rho}{12}\begin{bmatrix}2l & l & 0\\ l & 4l & l\\ 0 & l & 2l\end{bmatrix}\cdot\begin{bmatrix}z_{1,tt}\\ z_{2,tt}\\ z_{3,tt}\end{bmatrix}+\frac{2EA}{l}\begin{bmatrix}1 & -1 & 0\\ -1 & 2 & -1\\ 0 & -1 & 1\end{bmatrix}\cdot\begin{bmatrix}z_1\\ z_2\\ z_3\end{bmatrix}=\begin{bmatrix}fl/4\\ fl/2\\ fl/4\end{bmatrix}=\mathbf{F}_g(l)\end{aligned} \tag{2.62}$$

which can be reduced by applying z_1(t) = 0, as

$$\mathbf{M}(l)\mathbf{z}_{,tt}+\mathbf{K}(l)\mathbf{z}=\frac{\rho}{12}\begin{bmatrix}4l & l\\ l & 2l\end{bmatrix}\cdot\begin{bmatrix}z_{2,tt}\\ z_{3,tt}\end{bmatrix}+\frac{2EA}{l}\begin{bmatrix}2 & -1\\ -1 & 1\end{bmatrix}\cdot\begin{bmatrix}z_2\\ z_3\end{bmatrix}=\begin{bmatrix}fl/2\\ fl/4\end{bmatrix}=\mathbf{F}(l) \tag{2.63}$$

Equation 2.63 can be solved for nodal displacements with a specific initial condition. Note that since the load f in Eq. 2.63 is not time-dependent, a non-zero initial displacement or velocity needs to be defined to excite the motion of the bar.

In practice, Eq. 2.63 is solved by using numerical time integration. For example, if an explicit time integration algorithm is employed, then within each time step, the displacement **z** at the current time step is known from the last iteration; therefore, the acceleration $\mathbf{z}_{,tt}$ can be computed for the current time step, and then used to update the velocity $\mathbf{z}_{,t}$, and hence displacement **z** for the next time step, until the solution **z** is obtained for all time steps from $t = 0$ to $t = t_T$.

2.3.2 Discrete Sensitivity Analysis

In this section we discuss shape sensitivity analysis for a general dynamic problem using the discrete method. Direct differentiation method will be demonstrated for sensitivity calculation.

Consider a general performance measure for a dynamic problem, as

$$\psi = g(\mathbf{b}, \mathbf{z}(t_T)) + \int_0^{t_T} G(\mathbf{b}, \mathbf{z})dt \tag{2.64}$$

Differentiating the performance measure with respect to design variable b_i gives

$$\frac{d\psi}{db_i} = \frac{\partial g}{\partial b_i} + \frac{\partial g}{\partial \mathbf{z}}\frac{d\mathbf{z}(t_T)}{db_i} + \int_0^{t_T}\left[\frac{\partial G}{\partial b_i} + \frac{\partial G}{\partial \mathbf{z}}\frac{d\mathbf{z}}{db_i}\right]dt \tag{2.65}$$

Note that $d\mathbf{z}(t_T)/db_i$ and $d\mathbf{z}/db_i$ are implicit dependences to be solved in sensitivity analysis.

In direct differentiation method, we differentiate Eq. 2.59 with respect to b_i, giving

$$\mathbf{M}\left(\frac{d\mathbf{z}}{db_i}\right)_{,tt} + \frac{\partial \mathbf{M}}{\partial b_i}\mathbf{z}_{,tt} + \mathbf{K}\frac{d\mathbf{z}}{db_i} + \frac{\partial \mathbf{K}}{\partial b_i}\mathbf{z} = \frac{\partial \mathbf{F}}{\partial b_i} \tag{2.66}$$

Moving all explicit terms to the right to obtain the dynamic sensitivity expression, as

$$\mathbf{M}\left(\frac{d\mathbf{z}}{db_i}\right)_{,tt} + \mathbf{K}\frac{d\mathbf{z}}{db_i} = \frac{\partial \mathbf{F}}{\partial b_i} - \frac{\partial \mathbf{M}}{\partial b_i}\mathbf{z}_{,tt} - \frac{\partial \mathbf{K}}{\partial b_i}\mathbf{z} \tag{2.67}$$

Note that the sensitivity expression can be solved with initial conditions

$$\left.\frac{d\mathbf{z}}{db_i}\right|_{t=0} = 0\,; \quad \left.\left(\frac{d\mathbf{z}}{db_i}\right)_{,t}\right|_{t=0} = 0 \tag{2.68}$$

which implies that the initial displacement and velocity do not change with design variable b_i. In practice, the sensitivity expression (Eq. 2.67) can be solved using the same time integration algorithm as with the analysis of the original structure (Eq. 2.59). Within each time step, all terms on the right hand side of Eq. 2.67 are known, since $\mathbf{z}_{,tt}$ and $\mathbf{z}$ have been solved using Eq. 2.59. Once the solution $d\mathbf{z}/db_i$ is obtained from $t = 0$ to $t = t_T$, it can be substituted into Eq. 2.65 to evaluate the design sensitivity of the performance measure. It is worth mentioning that when explicit time integration is used, the computation cost of solving the sensitivity equation (Eq. 2.67) may not be less than that of the analysis of the original structure (Eq. 2.59), which reduces the merit of the sensitivity computation compared to overall finite difference method.

Adjoint variable method also applies to dynamic problems. The formulation of adjoint variable method for the dynamic bar example can be found in Appendix B, which shows that a dynamic adjoint problem needs to be solved to obtain the value of the adjoint variable through time. Moreover, the adjoint problem is a terminal-value problem that needs to be solved backwards in time from $t = t_T$ to $t = 0$. Therefore, unlike DDM, in which the dynamic sensitivity equation (Eq. 2.67) can be solved in parallel with response analysis (Eq. 2.59), the adjoint problem cannot be solved simultaneously with the response analysis, which significantly complicates the computation associated with dynamic sensitivity analysis. Therefore, for dynamic problems, the direct differentiation method is generally preferable to the adjoint variable method in terms of computation efficiency. Details of the comparison between DDM and AVM for dynamic problems are discussed in Appendix B.

2.3.3 Continuum Sensitivity Analysis

In this section, we employ the direct differentiation method to demonstrate continuum shape sensitivity analysis for dynamic problems using the simple bar example.

Taking material derivative of Eq. 2.60 gives

$$\int_0^{t_T}\left\{\int_0^l\left[\rho\dot{z}_{,tt}\bar{z}+\rho z_{,tt}\bar{z}V_{,1}\right]dx+\int_0^l\left[EA\dot{z}_{,1}\bar{z}_{,1}-EAz_{,1}\bar{z}_{,1}V_{,1}\right]dx\right\}dt=\int_0^{t_T}\int_0^l f\bar{z}V_{,1}dxdt \quad (2.69)$$

which is the dynamic sensitivity expression that can be solved using integration by part (continuum-continuum approach). For the sake of brevity, we show detailed derivation only for the continuum-discrete approach.

Discretize the continuum sensitivity expression (Eq. 2.69) using shape functions (Eq. 2.16) yields

$$\begin{aligned}
&\int_0^{t_T}\left\{\begin{bmatrix}\bar{z}_1\\ \bar{z}_2\\ \bar{z}_3\end{bmatrix}^T\cdot\frac{\rho}{12}\begin{bmatrix}2l & l & 0\\ l & 4l & l\\ 0 & l & 2l\end{bmatrix}\cdot\begin{bmatrix}\dot{z}_{1,tt}\\ \dot{z}_{2,tt}\\ \dot{z}_{3,tt}\end{bmatrix}+\begin{bmatrix}\bar{z}_1\\ \bar{z}_2\\ \bar{z}_3\end{bmatrix}^T\cdot\frac{\rho}{12}\begin{bmatrix}2l & l & 0\\ l & 4l & l\\ 0 & l & 2l\end{bmatrix}\cdot\begin{bmatrix}z_{1,tt}\\ z_{2,tt}\\ z_{3,tt}\end{bmatrix}\cdot\frac{1}{l}\right.\\
&\left.+\begin{bmatrix}\bar{z}_1\\ \bar{z}_2\\ \bar{z}_3\end{bmatrix}^T\cdot\frac{2EA}{l}\begin{bmatrix}1 & -1 & \\ -1 & 2 & -1\\ & -1 & 1\end{bmatrix}\cdot\begin{bmatrix}\dot{z}_1\\ \dot{z}_2\\ \dot{z}_3\end{bmatrix}-\begin{bmatrix}\bar{z}_1\\ \bar{z}_2\\ \bar{z}_3\end{bmatrix}^T\cdot\frac{2EA}{l}\begin{bmatrix}1 & -1 & \\ -1 & 2 & -1\\ & -1 & 1\end{bmatrix}\cdot\begin{bmatrix}z_1\\ z_2\\ z_3\end{bmatrix}\cdot\frac{1}{l}\right\}dt \quad (2.70)\\
&=\int_0^{t_T}\left\{\begin{bmatrix}\bar{z}_1\\ \bar{z}_2\\ \bar{z}_3\end{bmatrix}^T\cdot\begin{bmatrix}fl/4\\ fl/2\\ fl/4\end{bmatrix}\cdot\frac{1}{l}\right\}dt
\end{aligned}$$

where $[z_1 \;\; z_2 \;\; z_3]^T$ and $[z_{1,tt} \;\; z_{2,tt} \;\; z_{3,tt}]^T$ are known terms that have been solved in response analysis.

Rearranging Eq. 2.70 gives

$$\begin{aligned}\int_0^{t_T}\begin{bmatrix}\bar{z}_1\\ \bar{z}_2\\ \bar{z}_3\end{bmatrix}^T\cdot\left\{\frac{\rho}{12}\begin{bmatrix}2l & l & 0\\ l & 4l & l\\ 0 & l & 2l\end{bmatrix}\cdot\begin{bmatrix}\dot{z}_{1,tt}\\ \dot{z}_{2,tt}\\ \dot{z}_{3,tt}\end{bmatrix}+\frac{\rho}{12}\begin{bmatrix}2l & l & 0\\ l & 4l & l\\ 0 & l & 2l\end{bmatrix}\cdot\begin{bmatrix}z_{1,tt}\\ z_{2,tt}\\ z_{3,tt}\end{bmatrix}\cdot\frac{1}{l}\right.\\ \left.+\frac{2EA}{l}\begin{bmatrix}1 & -1 & \\ -1 & 2 & -1\\ & -1 & 1\end{bmatrix}\cdot\begin{bmatrix}\dot{z}_1\\ \dot{z}_2\\ \dot{z}_3\end{bmatrix}-\frac{2EA}{l}\begin{bmatrix}1 & -1 & \\ -1 & 2 & -1\\ & -1 & 1\end{bmatrix}\cdot\begin{bmatrix}z_1\\ z_2\\ z_3\end{bmatrix}\cdot\frac{1}{l}-\begin{bmatrix}fl/4\\ fl/2\\ fl/4\end{bmatrix}\cdot\frac{1}{l}\right\}dt=0\end{aligned} \tag{2.71}$$

which holds for all kinematically admissible virtual displacements $\bar{\mathbf{z}}$ that satisfies $\bar{\mathbf{z}}(0)=\bar{\mathbf{z}}(t_T)=0$. Therefore, the sensitivity differential equation takes the form

$$\begin{aligned}&\frac{\rho}{12}\begin{bmatrix}2l & l & 0\\ l & 4l & l\\ 0 & l & 2l\end{bmatrix}\cdot\begin{bmatrix}\dot{z}_{1,tt}\\ \dot{z}_{2,tt}\\ \dot{z}_{3,tt}\end{bmatrix}+\frac{2EA}{l}\begin{bmatrix}1 & -1 & \\ -1 & 2 & -1\\ & -1 & 1\end{bmatrix}\cdot\begin{bmatrix}\dot{z}_1\\ \dot{z}_2\\ \dot{z}_3\end{bmatrix}\\ &=\begin{bmatrix}fl/4\\ fl/2\\ fl/4\end{bmatrix}\cdot\frac{1}{l}-\frac{\rho}{12}\begin{bmatrix}2l & l & 0\\ l & 4l & l\\ 0 & l & 2l\end{bmatrix}\cdot\begin{bmatrix}z_{1,tt}\\ z_{2,tt}\\ z_{3,tt}\end{bmatrix}\cdot\frac{1}{l}+\frac{2EA}{l}\begin{bmatrix}1 & -1 & \\ -1 & 2 & -1\\ & -1 & 1\end{bmatrix}\cdot\begin{bmatrix}z_1\\ z_2\\ z_3\end{bmatrix}\cdot\frac{1}{l}\end{aligned} \tag{2.72}$$

which can be reduced as

$$\begin{aligned}&\frac{\rho}{12}\begin{bmatrix}4l & l\\ l & 2l\end{bmatrix}\cdot\begin{bmatrix}\dot{z}_{2,tt}\\ \dot{z}_{3,tt}\end{bmatrix}+\frac{2EA}{l}\begin{bmatrix}2 & -1\\ -1 & 1\end{bmatrix}\cdot\begin{bmatrix}\dot{z}_2\\ \dot{z}_3\end{bmatrix}\\ &=\begin{bmatrix}fl/2\\ fl/4\end{bmatrix}\cdot\frac{1}{l}-\frac{\rho}{12}\begin{bmatrix}4l & l\\ l & 2l\end{bmatrix}\cdot\begin{bmatrix}z_{2,tt}\\ z_{3,tt}\end{bmatrix}\cdot\frac{1}{l}+\frac{2EA}{l}\begin{bmatrix}2 & -1\\ -1 & 1\end{bmatrix}\cdot\begin{bmatrix}z_2\\ z_3\end{bmatrix}\cdot\frac{1}{l}\end{aligned} \tag{2.73}$$

and then solved with initial conditions $\dot{\mathbf{z}}(0)=0$ and $\dot{\mathbf{z}}_{,t}(0)=0$. As can be seen, for the simple bar example, Eq. 2.73 is equivalent to the sensitivity expression obtained using the discrete method (Eq. 2.67). The solution $\dot{\mathbf{z}}(t)$ can be substituted into Eq. 2.65 to calculate the sensitivity of the performance measure.

Note that in Chapter 4, we will use an approach similar to that demonstrated in this section (shape sensitivity analysis + continuum-discrete approach + direct differentiation method + dynamic scenario) to perform analytical shape sensitivity analysis for dynamic multi-scale problems.

CHAPTER 3

MULTI-SCALE SIMULATION OF DYNAMIC CRACK PROPAGATION

3.1 Overview

This chapter introduces the multi-scale simulation technique that is used throughout the thesis. As mentioned in Chapter 1, we choose the bridging scale method, among the newly developed methods, for our simulation of dynamic crack propagation. In Section 3.2, a brief introduction to molecular dynamics will be given first. Section 3.3 explains the fundamental theory of the bridging scale method using a one-dimensional atomic lattice. The result of a simple one-dimensional bridging scale example problem will also be demonstrated. The formulation of the bridging scale method for higher dimensional problems will be reviewed in Section 3.4. In Section 3.5, the implementation aspects for dynamic crack propagation problems will be discussed. A three-dimensional nano-beam example will be introduced in Section 3.6 for demonstration of the method.

3.2 Basics of Molecular Dynamics

Molecular dynamics has been widely applied to simulate the behavior of material systems at atomistic level. In an MD simulation, molecules or atoms are treated as a system of interacting material particles, while the goal is to calculate the motion of each atom in the material, characterized by atomic displacement, velocity, and acceleration. Each atom in the system is considered as a classical particle that obeys Newton’s laws of mechanics. Denoting the displacement of atom *i* as $\mathbf{q}_i$, the trajectory of the atom can be determined by numerically solving the Newton's equations of motion

$$m_i \frac{d^2\mathbf{q}_i}{dt^2} = -\frac{dU(\mathbf{q})}{d\mathbf{q}_i} \tag{3.1}$$

where m_i is the atomic mass, and *U* is the sum of the potential energy of all atoms, which depends on the positions of atom *i* and all other atoms in the system. The right-hand side of Eq. 3.1 corresponds to the gradient of the potential energy, which can be thought of as the interatomic force.

The potential energy in molecular dynamics approximates the electronic effects in real materials. Other than atomic structural information, the interatomic potential is the most fundamental input into MD simulations. Numerous potential functions with different levels of accuracy have been proposed, each having its disadvantages and strengths. However, so far there is no single potential function that is suitable for all materials. In this thesis, the potential function chosen to be implemented in our MD simulation is the Lennard-Jones (LJ) 6-12 potential [36], which is one of the simplest and most widely used potentials for modeling brittle fracture [2,8-10,12,14,23,26,27,36,37]. The LJ 6-12 potential takes the form

$$\Phi(r) = 4\varepsilon\left(\left(\frac{\sigma}{r}\right)^{12} - \left(\frac{\sigma}{r}\right)^{6}\right) \tag{3.2}$$

where *r* is the distance between two atoms; σ is the collision diameter (the distance at which $\Phi(r) = 0$); and ε denotes the bonding/dislocation energy – the minimum of Eq. 3.2 that occurs for an atomic pair in equilibrium. In our numerical examples, the parameters for LJ 6-12 will be defined in scaled units as in [2,8-10,12,14,23,26,27], i.e., σ and ε are set to unity while atomic mass is chosen as $m_A = 1$ for all atoms. Although the choice of normalized units cannot lead to quantitative representations of the behavior of a particular material, it allows us to draw generic conclusions about the fundamental and material-independent mechanisms in brittle fracture.

The MD interatomic force can be evaluated by differentiating $\Phi(r)$ with respect to r, as

$$f(r) = -\frac{\partial \Phi(r)}{\partial r} = 48\frac{\varepsilon\sigma^{12}}{r^{13}} - 24\frac{\varepsilon\sigma^{6}}{r^{7}} \tag{3.3}$$

Note that the equilibrium distance (at which $f(r) = 0$) between two neighboring atoms is $h_a = 2^{1/6}\sigma$. The force and potential energy for LJ 6-12 are plotted in Fig. 3.1. The interaction coefficient k can be obtained by taking second-order derivative of the potential function with respect to r and then evaluate at equilibrium distance $r = h_a$, as

$$k = \frac{\partial^2 \Phi(r)}{\partial r^2}\Big|_{r=h_a} = \left(\frac{624\varepsilon\sigma^{12}}{r^{14}} - \frac{168\varepsilon\sigma^{6}}{r^{8}}\right)\Big|_{r=h_a} = 36(4)^{\frac{1}{3}}\frac{\varepsilon}{\sigma^2} \tag{3.4}$$

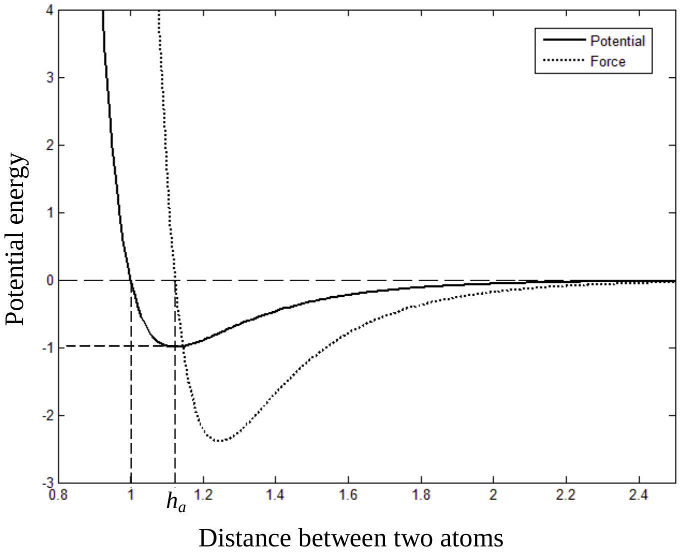

Figure 3.1 Force and potential energy for the LJ 6-12 potential

Note that Eq. 3.1 represents a system of coupled second-order nonlinear differential equations, which can be solved numerically by discretizing the equations in time. There exist many time integration schemes that are frequently used in molecular dynamics implementations. In this thesis, we adopt the *Verlet algorithm* (also known as the *explicit central difference algorithm*) for numerical time integration, in which the positions of atoms are updated as

$$\boldsymbol{v}(t+\Delta t_m) = \boldsymbol{v}(t) + \frac{1}{2}\left(\mathbf{a}(t) + \mathbf{a}(t+\Delta t_m)\right)\Delta t_m \tag{3.5a}$$

$$\mathbf{q}(t+\Delta t_m) = \mathbf{q}(t) + \boldsymbol{v}(t)\Delta t \ + \frac{1}{2}\mathbf{a}(t)\Delta t_m^2 \tag{3.5b}$$

where $\boldsymbol{v}$ and $\mathbf{a}$ represent atomic velocities and accelerations, respectively, and Δt_m is the MD time step size. In general, the time step size for MD simulation can be determined based on atomic vibration frequency. For a harmonic oscillator that approximates the interatomic interaction in a given atomic lattice at equilibrium, the oscillation frequency can be estimated as

$$v^* = \frac{1}{2\pi}\sqrt{\frac{k}{m_A}} \tag{3.6}$$

In order to accurately model the rapid vibration of atoms, the MD time step needs to be chosen much smaller than $1/v^*$ [8]. For the LJ 6-12 potential, based on the normalized parameters σ, ε and m_A defined above, the value of $1/v^*$ for a one-dimensional atomic lattice is found to be around 0.831 (in normalized time unit).

3.3 Bridging Scale Method – A Tutorial 1-D Problem

Proposed by Wagner and Liu [20] in 2003, the bridging scale method has been mainly used for concurrently coupling atomistic and continuum simulations. The theory of bridging scale method has been developed in a fully generalized three-dimensional setting, and the impedance boundary force – the key to achieve multi-scale coupling – has been numerically calculated in multiple dimensions for different lattice structures. In this section, the basic formulation of bridging scale method will be briefly reviewed, and will be illustrated with a simple 1-D example. Detailed derivations and associated discussions can be found in [20,24,27,28].

3.3.1 Bridging Scale Fundamentals

As depicted in Fig. 3.2, the bridging scale method is based on the fundamental idea of decomposing the total atomic displacement field **z** into coarse and fine scales, as

$$\mathbf{z} = \mathbf{u} + \mathbf{v} \tag{3.7}$$

where the coarse scale **u** can be represented by a set of basis functions (such as finite element shape functions), and fine scale **v** is the part of the total solution whose projection onto the coarse scale basis function is zero.

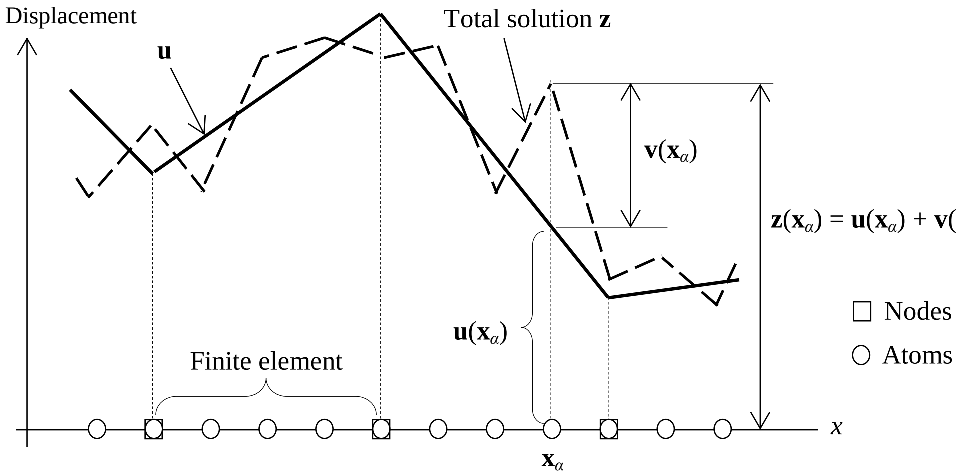

Figure 3.2 One-dimensional illustration of bridging scale coarse-fine decomposition

The coarse scale in bridging scale method is defined as

$$\mathbf{u}(\mathbf{x}_\alpha) = \sum_I N_I (x_\alpha)\mathbf{d}_I \tag{3.8}$$

where $N_I(\mathbf{x}_\alpha)$ is the shape function of node I evaluated at the initial position $\mathbf{x}_\alpha$ of atom α, and $\mathbf{d}_I$ represents FE nodal displacements. The fine scale $\mathbf{v}$ is the part of the total displacement that the coarse scale cannot represent. It is defined to be the projection of the coarse scale subtracted from the total solution $\mathbf{z}$. One of the possible approaches in selecting the projection operator is to minimize the mass-weighted square of the fine scale, while noticing that the total solution $\mathbf{z}$ is equivalent to the MD solution $\mathbf{q}$, as

$$J = \sum_\alpha m_\alpha \left(\mathbf{q}_\alpha - \sum_I N_I^\alpha \mathbf{w}_I \right)^2 \tag{3.9}$$

where m_α is the mass of atom α and $\mathbf{w}_I$ are the temporary nodal degrees of freedom. Solving for $\mathbf{w}$ by minimizing the error J yields

$$\mathbf{w} = \mathbf{M}^{-1}\mathbf{N}^T\mathbf{M}_A\mathbf{q} \tag{3.10}$$

where $\mathbf{M} = \mathbf{N}^T\mathbf{M}_A\mathbf{N}$ denotes the coarse scale consistent mass matrix, and $\mathbf{M}_A$ is a diagonal matrix with atomic masses on the diagonal. $\mathbf{N}$ is a matrix containing the values of the finite element shape functions evaluated at all atomic positions within the domain. The fine scale $\mathbf{v}$ can then be represented as

$$\mathbf{v} = \mathbf{q} - \mathbf{N}\mathbf{w} = \mathbf{q} - \mathbf{P}\mathbf{q} \tag{3.11}$$

where $\mathbf{P} = \mathbf{N}\mathbf{M}^{-1}\mathbf{N}^T\mathbf{M}_A$ is the projection matrix. Finally, the total displacement $\mathbf{z}$ can be written as the sum of coarse and fine scales; that is

$$\mathbf{z} = \mathbf{N}\mathbf{d} + \mathbf{q} - \mathbf{P}\mathbf{q} = \mathbf{N}\mathbf{d} + \mathbf{Q}\mathbf{q} \tag{3.12}$$

where $\mathbf{Q} = \mathbf{I} - \mathbf{P}$. The term $\mathbf{Pq}$ in Eq. 3.12 is called the bridging scale.

3.3.2 Multi-scale Equations of Motion

To obtain the coupled MD and FE equations of motion, a multi-scale Lagrangian $\mathcal{L}$ is first constructed as

$$\mathcal{L}(\mathbf{z},\mathbf{z}_{,t}) = \mathcal{K}(\mathbf{z}_{,t}) - V(\mathbf{z}) \tag{3.13}$$

According to Eq. 3.12, the total solution $\mathbf{z}$ can be decomposed into $\mathbf{d}$ and $\mathbf{q}$, and the kinetic energy $\mathcal{K}(\mathbf{z}_{,t}) = \frac{1}{2}\mathbf{z}_{,t}{}^{T}\mathbf{M}_{A}\mathbf{z}_{,t}$ can also be written in terms of $\mathbf{d}_{,t}$ and $\mathbf{q}_{,t}$, giving

$$\mathcal{L}(\mathbf{d},\mathbf{d}_{,t},\mathbf{q},\mathbf{q}_{,t}) = \frac{1}{2}\mathbf{d}_{,t}{}^{T}\mathbf{M}\mathbf{d}_{,t} + \frac{1}{2}\mathbf{q}_{,t}{}^{T}\mathcal{M}\mathbf{q}_{,t} - U(\mathbf{d},\mathbf{q}) \tag{3.14}$$

where $U(\mathbf{d},\mathbf{q})$ is the interatomic potential energy and $\mathcal{M}$ is the fine scale mass matrix. In deriving Eq. 3.14, the cross terms $\mathbf{d}_{,t}$ and $\mathbf{q}_{,t}$ have been removed due to the orthogonality of the bridging scale [20].

The multi-scale equations of motion can be obtained from the Lagrangian by following the relations

$$\frac{d}{dt}\left(\frac{\partial \mathcal{L}}{\partial \mathbf{d}_{,t}}\right) - \frac{\partial \mathcal{L}}{\partial \mathbf{d}} = 0 \tag{3.15a}$$

$$\frac{d}{dt}\left(\frac{\partial \mathcal{L}}{\partial \mathbf{q}_{,t}}\right) - \frac{\partial \mathcal{L}}{\partial \mathbf{q}} = 0 \tag{3.15b}$$

which lead to the coupled equations of motion

$$\mathbf{M}_{A}\mathbf{q}_{,tt} = \mathbf{f}(\mathbf{q}) \tag{3.16a}$$

$$\mathbf{M}\mathbf{d}_{,tt} = \mathbf{N}^{T}\mathbf{f}(\mathbf{z}) \tag{3.16b}$$

Note that the fine scale equation of motion (Eq. 3.16a) is simply the MD equation of motion, which can be solved with a standard MD solver. Equation 3.16b is the finite element equation of motion, in which **M** is defined to be a consistent mass matrix. When the sizes of the finite elements are large compared to atomic spacing, the FE mass matrix can be written as an integral over the FE domain **Ω** [20], as

$$\mathbf{M} = \iint_{\Omega} \rho \mathbf{N}(\mathbf{X})^{T} \mathbf{N}(\mathbf{X}) d\Omega \tag{3.17}$$

which is the consistent mass matrix used in standard finite element method, where ρ represents an evenly distributed mass density evaluated based on the atomic mass and the space occupied by each atom. Hence, a standard FE solver can be used to find the solution to Eq. 3.16b. The coupling between the two equations is through the coarse scale internal force $\mathbf{N}^T\mathbf{f}(\mathbf{z})$, which is a function of the MD interatomic force **f**.

3.3.3 Elimination of Fine Scale outside the MD Region

Instead of solving molecular dynamics for the entire domain in structural analysis, in bridging scale method, we confine the MD simulation into only a small portion of the domain, while solving the response of the rest of the domain using finite element analysis. Taking the one-dimensional bridging scale structure shown in Fig. 3.3 as an example, the molecular dynamics simulation is only performed in the MD region (*Region 1*), while the finite element analysis exists everywhere (*Region 1* + *Region 2*). In *Region 2,* the coarse scale degrees of freedom are represented by finite element interpolation, while the fine scale degrees of freedom are eliminated. An impedance force that mimics the effect of the eliminated fine scale in *Region 2* is imposed at the boundary of the MD area.

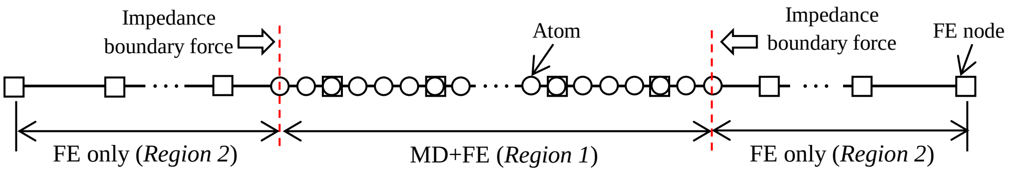

Figure 3.3 A 1-D bridging scale structure

To develop the impedance boundary condition for the MD region, it is assumed that different interatomic potentials are used for *Region 1* and *Region 2*. Since *Region 1* is usually a locally interesting physical domain such as the area near a crack tip, it is necessary to use an anharmonic (or nonlinear) potential (such as LJ 6-12) to accurately capture the interaction between atoms. However, in *Region 2*, where the relative displacements of atoms and the rotation of the atomic lattice are usually small, a harmonic potential – linearized from the anharmonic potential function – can be used to represent the interatomic force as a linear function of the displacements. In other words, while an anharmonic potential will be used for the MD simulation in *Region 1*, a harmonic force will be assumed during the process of eliminating the *Region 2* atomistic degrees of freedom.

The first step in deriving the impedance boundary condition is to linearize the MD equation of motion (Eq. 3.16a). For the atoms in *Region 2*, linearizing the force **f**(**z**) at **v** = 0 while noticing the equality of **q** and **z** yields

$$\mathbf{M}_A \mathbf{q}_{,tt} = \mathbf{M}_A \mathbf{u}_{,tt} + \mathbf{M}_A \mathbf{v}_{,tt} = \mathbf{f}(\mathbf{u}) + \mathbf{K}\mathbf{v} \tag{3.18}$$

where

$$\mathbf{K} = \frac{\partial \mathbf{f}}{\partial \mathbf{z}} \Big|_{\mathbf{v}=0} \tag{3.19}$$

Note that the complete anharmonic force has been decomposed as

$$\mathbf{f}(\mathbf{z}) = \mathbf{f}(\mathbf{u}) + \mathbf{K}\mathbf{v} \tag{3.20}$$

The derivation of the impedance boundary condition requires working with the fine scale equation of motion exclusively. Therefore, to decompose the MD equation of motion into coarse and fine scale components, Eq. 3.18 is separated by considering the coarse and fine scales respectively, as

$$\mathbf{M}_A \mathbf{u}_{,tt} = \mathbf{f}(\mathbf{u}) \tag{3.21a}$$

$$\mathbf{M}_A \mathbf{v}_{,tt} = \mathbf{K}\mathbf{v} \tag{3.21b}$$

The decomposition above is based on the assumption that the fine scale equation of motion can be written neglecting the contributions from the coarse scale. This assumption can be justified by the orthogonality of coarse and fine scales, as well as the fact that the coarse scale has a larger time scale than the fine scale in bridging scale simulations [20].

Now we elucidate the derivation of the impedance boundary force using a simple 1-D atomic lattice. (The extension to higher dimensional cases will be discussed later in this chapter.) Assume a one-dimensional structure consists of a chain of atoms with mass m_A, as shown in Fig. 3.4a, where atoms are connected by nonlinear springs with interaction coefficient k (Eq. 3.4). Each atom is labeled with index l that denotes its spatial position, while the $l = 0$ atom represents the boundary of the MD area. Our goal is to develop a boundary force (acting on the $l = 0$ atom) that mimics the fine scale dynamic effect of the $l > 0$ (*Region 2*) atoms, as shown in Fig. 3.4b. The fine scale degrees of freedom of the $l > 0$ atoms will be eliminated by solving or replacing them in terms of the $l \le 0$ (*Region 1*) degrees of freedom. More specifically, the fine scale displacement of the $l = 1$ atom will be solved for in terms of that of the $l = 0$ atom.

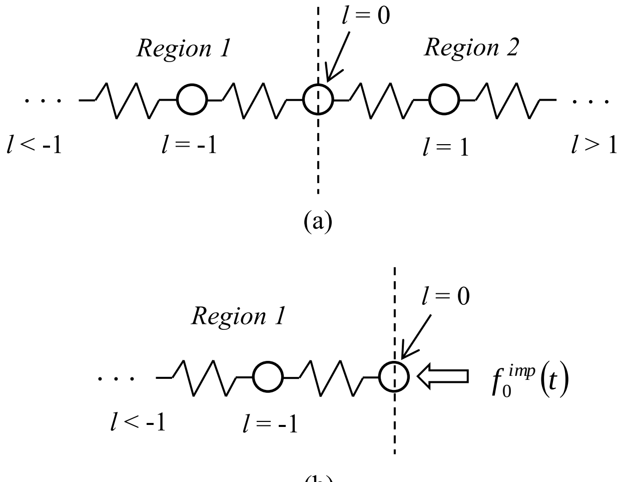

Figure 3.4 (a) Original 1-D atomic system, (b) *Region 2* fine scale eliminated by introducing the impedance boundary force $f_0^{imp}(t)$

The key idea in deriving the impedance force is to utilize the periodicity of the atomic structure so that standard technique of discrete Fourier transform can be applied. To start with, we rewrite the fine scale equation of motion (Eq. 3.21b) for any atom within *Region 2* of the 1-D lattice, as

$$v_{l,tt}(t) = \sum_{l'=l-1}^{l+1} m_A^{-1} K_{l-l'} v_{l'}(t) \tag{3.22}$$

where the stiffness matrices *K* relates the displacements of the neighboring atoms beside atom *l* to the atomic forces acting on it. For a 1-D lattice, the stiffnesses are given by scalars, as

$$K_1 = k \tag{3.23a}$$

$$K_0 = -2k \tag{3.23b}$$

$$K_{-1} = k \tag{3.23c}$$

Note that we assume only nearest neighbor interactions when writing Eq. 3.22.

For the MD boundary atom ($l = 0$), Eq. 3.22 becomes

$$v_{0,tt}(t)=\sum_{l'=-1}^{1} m_A^{-1} K_{-l'} v_{l'}(t) \;=\sum_{l'=-1}^{0} m_A^{-1} K_{-l'} v_{l'}(t)+m_A^{-1} K_{-1} v_1(t) \;=\sum_{l'=-1}^{0} m_A^{-1} K_{-l'} v_{l'}(t)+m_A^{-1} f_0^{imp}(t) \quad (3.24)$$

where

$$f_0^{imp}(t)=K_{-1} v_1(t) \quad (3.25)$$

is the impedance boundary force to be developed (Fig. 3.4b). Note that the effect of the *Region 2* fine scale degrees of freedom on the MD boundary atom (implied by the v_1 term) is involved in the impedance force.

To solve for v_1 in terms of v_0, discrete Fourier transform and Laplace transform need to be performed on the linearized fine scale equation of motion of the *Region 2* atoms (Eq. 3.22). Detailed derivation steps can be found in Appendix C. The resulting impedance boundary force takes the form

$$f_0^{imp}(t)=\int_0^t \theta(t-\tau) v_0(\tau) d\tau \quad (3.26)$$

where

$$\theta\,(t)=\mathcal{L}^{-1}(\Theta(s))=\frac{2k}{t} J_2\left(2\sqrt{\frac{k}{m_A}}t\right) \quad (3.27)$$

is called the time history kernel (plotted in Fig. 3.5), in which J_2 stands for the second-order Bessel function. As can be seen, in contrast to Eq. 3.25, the impedance force in Eq. 3.26 depends only on the fine scale dynamics of the boundary atom at l = 0.

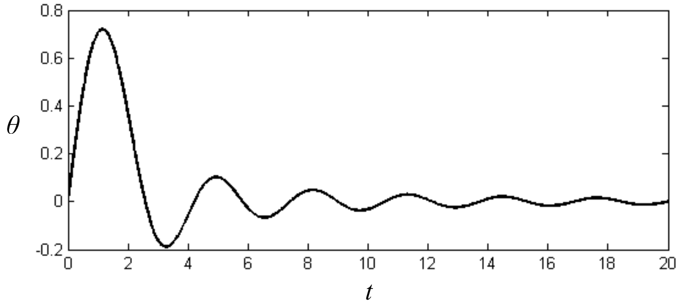

Figure 3.5 1-D time history kernel

Note that the coarse scale equation of motion (Eq. 3.21a) can also be rewritten for the $l = 0$ atom, as

$$u_{0,tt} = m_A^{-1} f_0(\mathbf{u}) \tag{3.28}$$

where $f_0(\mathbf{u})$ is the coarse scale component of the interatomic force acting on the boundary atom, which depends on the coarse scale solution **u** in both *Region 1* and *Region 2*.

Substituting the expression of the impedance boundary force (Eq. 3.26) into the fine scale equation of motion for the boundary atom (Eq. 3.24) and combining the result with Eq. 3.28 gives

$$m_A q_{0,tt}(t) = f_0(\mathbf{q},\mathbf{u}) + \int_0^t \theta(t-\tau) v_0(\tau) d\tau \tag{3.29}$$

where the fine scale displacement $v_0(\tau)$ can be obtained by

$$v_0(\tau) = q_0(\tau) - u_0(\tau) \tag{3.30}$$

Therefore, for a simple 1-D lattice as shown in Fig. 3.3, the final form of the coupled MD and FE equations of motion can be written as

$$\mathbf{M}_A \mathbf{q}_{,tt} = \mathbf{f}(\mathbf{q}) \tag{3.31a}$$

$$m_A q_{0,tt}(t) = f_0(\mathbf{q},\mathbf{u}) + \int_0^t \theta(t-\tau) v_0(\tau) d\tau \tag{3.31b}$$

$$\mathbf{M}\mathbf{d}_{,tt} = \mathbf{N}^T \mathbf{f}(\mathbf{z}) \tag{3.31c}$$

Note that Eq. 3.31a will be solved for all non-boundary atoms, while Eq. 3.31b governs the dynamics of the two atoms at the MD boundary. The interatomic force $\mathbf{f}(\mathbf{q})$ can be derived from any nonlinear interatomic potential function.

3.3.4 Coarse Scale Internal Force

In the coarse scale equation of motion (Eq. 3.31c), the coupling force $\mathbf{N}^T\mathbf{f}(\mathbf{z})$ originates due to the separation of coarse and fine scales. Inside the MD region, since the total solutions (**z** = **u** + **v**) of the atoms are available, the internal force acting upon the FE nodes can be directly evaluated. However, in *Region 2*, the interatomic forces $\mathbf{f}(\mathbf{z})$ are no longer available due to the elimination of the fine scale degrees of freedom, and hence the Cauchy-Born rule [19] is utilized to approximate the $\mathbf{N}^T\mathbf{f}(\mathbf{z})$ term.

In Cauchy-Born rule, it is assumed that the lattice underlying any continuum point will deform homogeneously according to the continuum deformation gradient, while continuum stress and stiffness measures can be obtained directly from interatomic potentials. Based on this concept, the nodal force acting on a *Region 2* FE node *I* can be calculated as

$$\left(\mathbf{N}^T\mathbf{f}\right)_I = -\sum_{\alpha} \mathcal{P}^T\left(\mathbf{x}_\alpha\right)\frac{\partial N_I\left(\mathbf{x}_\alpha\right)}{\partial \mathbf{x}}\Delta V_\alpha \tag{3.32}$$

where ΔV_α is the space occupied by atom α, and $\mathcal{P}$ represents the first Piola-Kirchoff stress defined as

$$\mathcal{P}(\mathbf{x}_\alpha) = \frac{\partial W_\alpha}{\partial \mathbf{F}_\alpha^T} \tag{3.33}$$

where W_α is the potential energy density, and $\mathbf{F}_\alpha$ is the deformation gradient at atom α, which can be computed as

$$\mathbf{F}_\alpha = \mathbf{I} + \frac{\partial \mathbf{u}\left(\mathbf{x}_\alpha\right)}{\partial \mathbf{x}} = \mathbf{I} + \sum_I \mathbf{d}_I\left(\frac{\partial N_I\left(\mathbf{x}_\alpha\right)}{\partial \mathbf{x}}\right)^T \tag{3.34}$$

In practice, the summation in Eq. 3.32 can be replaced by an integral, just as in Eq. 3.17:

$$\left(\mathbf{N}^T\mathbf{f}\right)_I \approx -\int_V \boldsymbol{\mathcal{P}}^T\left(\mathbf{x}\right)\frac{\partial N_I\left(\mathbf{x}\right)}{\partial \mathbf{x}}dV \tag{3.35}$$

which, in numerical implementation, can be approximated by a weighted sum of the function values at a discrete set of quadrature points at locations $\mathbf{x}_q$, as

$$\left(\mathbf{N}^T\mathbf{f}\right)_I \approx -\sum_q \boldsymbol{\mathcal{P}}^T\left(\mathbf{x}_q\right)\frac{\partial N_I\left(\mathbf{x}_q\right)}{\partial \mathbf{x}}w_q \tag{3.36}$$

where w_q is the weight of the quadrature point $\mathbf{x}_q$ [20].

Now a simple example will be used to illustrate the Cauchy-born rule. Consider a 1-D element in *Region 2* with two nodes i and j. As shown in Fig. 3.6, the element contains h_e/h_a atoms, where h_e represents element length. Our goal is to calculate the internal force acting on node j due to the deformation of the element. Note that the displacements of the atoms in the element are unknown due to the elimination of the fine scale outside the MD area.

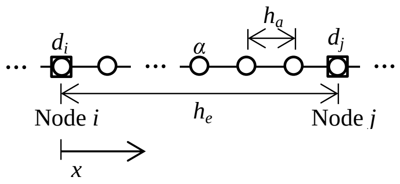

Figure 3.6 A 1-D element with two nodes

According to the Cauchy-born rule, the atomic lattice is assumed to deform homogeneously with the continuum; therefore, using Eq. 3.34, we first calculate the deformation gradient at the location of atom α within the element, as

$$F_\alpha = 1 + d_i\frac{\partial N_i\left(x_\alpha\right)}{\partial x} + d_j\frac{\partial N_j\left(x_\alpha\right)}{\partial x} = 1 + \left(d_j - d_i\right)/h_e \tag{3.37}$$

with linear shape functions

$$N_i = 1 - x/h_e\,; \quad N_j = x/h_e \tag{3.38}$$

Note that d_i and d_j indicate nodal displacements. The potential energy within the space occupied by atom α can then be calculated under small deformation assumption, as

$$\Phi = (1/2)\cdot k \cdot (F_\alpha h_a - h_a)^2 \tag{3.39}$$

which comes from the fact that two atomic bonds are connected to atom α (nearest neighbor interaction assumed), and meanwhile the potential energy of each bond is shared by two atoms.

By taking derivative of the energy density at atom α

$$W_\alpha = \frac{\Phi}{h_a} = \frac{kh_a(F_\alpha - 1)^2}{2} \tag{3.40}$$

with respect to the deformation gradient F_α, the Piola-Kirchoff stress at x_α can be obtained as

$$\mathcal{P}(x_\alpha) = \frac{\partial W_\alpha}{\partial F_\alpha} = kh_a(F_\alpha - 1) = kh_a(d_j - d_i)/h_e \tag{3.41}$$

which is the same for all atoms in the element due to homogeneous deformation. Thus, the internal force acting on node j due to the deformation of element ij can be calculated using Eq. 3.32; that is

$$(\mathbf{N}^T\mathbf{f})_j = -\sum_{\alpha=1}^{h_e/h_a} \mathcal{P}(x_\alpha)\frac{\partial N_j(x_\alpha)}{\partial x}\Delta V_\alpha = -\frac{h_e}{h_a}\cdot\left\{[kh_a(d_j - d_i)/h_e]\cdot\frac{1}{h_e}\cdot h_a\right\} = -kh_a(d_j - d_i)/h_e \tag{3.42}$$

3.3.5 Staggered Time Integration Scheme

The coupled equations of motion (Eqs. 3.31a ~ 3.31c) obtained at the end of Section 3.3.3 indicate a necessity of exchanging information between MD and FE simulations. In numerical implementation, a staggered time integration method based on the Verlet algorithm is used to update the MD and FE quantities simultaneously through time. The

MD simulation is advanced with time step size Δt_m, while the time step for finite element analysis is Δt, with a relation $\Delta t = m\Delta t_m$. Apparently, the time step size for FE simulation is a multiple of Δt_m, indicating that a small time step size is only necessary in solving the MD equation of motion.

Over each FE time step Δt, the molecular dynamics simulation is advanced first by Δt_m for m MD time steps. Note that as implied in Eq. 3.31b, the acceleration calculation for the boundary atoms in each MD time step requires information from the FE simulation near the boundary. Since the FE nodal displacements are only solved for each Δt, an interpolation method is used to approximate the coarse scale boundary displacements and velocities at each MD time step by assuming that the FE acceleration remains constant throughout one single FE time step Δt.

During each MD time step Δt_m, the accelerations of all atoms in the MD area are obtained via a time integration method as follows:

$$\mathbf{u}_\Gamma^{[j+1]} = \mathbf{u}_\Gamma^{[j]} + \mathbf{u}_{\Gamma,t}^{[j]}\Delta t_m + \frac{1}{2}\mathbf{u}_{\Gamma,tt}^{n}\Delta t_m^2 \tag{3.43a}$$

$$\mathbf{u}_{\Gamma,t}^{[j+1]} = \mathbf{u}_{\Gamma,t}^{[j]} + \mathbf{u}_{\Gamma,tt}^{n}\Delta t_m \tag{3.43b}$$

$$\mathbf{q}^{[j+1]} = \mathbf{q}^{[j]} + \mathbf{v}_{MD}^{[j]}\Delta t_m + \frac{1}{2}\mathbf{a}_{MD}^{[j]}\Delta t_m^2 \tag{3.43c}$$

$$\mathbf{a}_{MD}^{[j+1]} = \mathbf{M}_A^{-1}\mathbf{f}\left(\mathbf{q}^{[j+1]}, \mathbf{u}_\Gamma^{[j+1]}, \mathbf{h}^{[j+1]}\right) \tag{3.43d}$$

$$\mathbf{v}_{MD}^{[j+1]} = \mathbf{v}_{MD}^{[j]} + \frac{1}{2}\left(\mathbf{a}_{MD}^{[j+1]} + \mathbf{a}_{MD}^{[j]}\right)\Delta t_m \tag{3.43e}$$

where $\mathbf{q}$, $\mathbf{v}_{MD}$ and $\mathbf{a}_{MD}$ are the displacements, velocities and accelerations of the atoms, respectively. $\mathbf{h}$ represents the time history quantities. $\mathbf{u}_\Gamma$, $\mathbf{u}_{\Gamma,t}$, and $\mathbf{u}_{\Gamma,tt}$ are coarse scale displacements, velocities and accelerations near the boundary updated at each MD time step. Note that those coarse scale quantities include the information of the atom right at the boundary (*l* = 0) as well as the atoms within one cutoff radius outside the MD region (*l* = 1), which are referred to as 'ghost atoms'. The displacements of the ghost atoms are assumed to be equal to the coarse scale displacements and can be obtained by interpolating corresponding FE nodal displacements. The bracket notation [*j*] is used to donate the quantities at each MD time step (e.g., [*j*] is short for the time step *n* + *j*/*m*), and the superscript *n* represents the *n*th FE time step.

Once the MD simulation of *m* MD time steps for the *n*th FE time step is completed, the MD quantities at the time step *n*+1 (*n*+*m/m*) will be used to compute the FE accelerations at the time step *n*+1. A similar integration method is used to update FE displacements **d**, velocities $\mathbf{v}_{FE}$ and accelerations $\mathbf{a}_{FE}$:

$$\mathbf{d}^{n+1} = \mathbf{d}^{n} + \mathbf{v}_{FE}^{n}\Delta t + \frac{1}{2}\mathbf{a}_{FE}^{n}\Delta t^{2} \tag{3.44a}$$

$$\mathbf{a}_{FE}^{n+1} = \mathbf{M}^{-1}\mathbf{N}^{T}\mathbf{f}\left(\mathbf{N}\mathbf{d}^{n+1} + \mathbf{Q}\mathbf{q}^{n+1}\right) \tag{3.44b}$$

$$\mathbf{v}_{FE}^{n+1} = \mathbf{v}_{FE}^{n} + \frac{1}{2}\left(\mathbf{a}_{FE}^{n} + \mathbf{a}_{FE}^{n+1}\right)\Delta t \tag{3.44c}$$

Once the FE simulation goes from time step *n* to *n*+1, the information of the ghost atoms are interpolated using shape functions. These coarse scale boundary quantities will then be used in the next time step for updating the MD quantities.

3.3.6 1-D Numerical Example

In this section, we show dynamic bridging scale simulation for a simple 1-D structure based on the implementation details discussed above. More information about this example problem can be found in our earlier work [39]. As illustrated in Fig. 3.7, the bilaterally symmetric computation domain contains forty linear finite elements;

meanwhile, the MD simulation is confined into a small domain in the middle, which is comprised of 151 atoms. The equilibrium distance between atoms is $h_a = 0.05$, while each finite element contains ten atoms. Due to the nature of the 1-D problem, all atoms and FE nodes can move only along the x direction. The MD time step size is chosen to be 0.0075, and ten MD times steps are run within each FE time step.

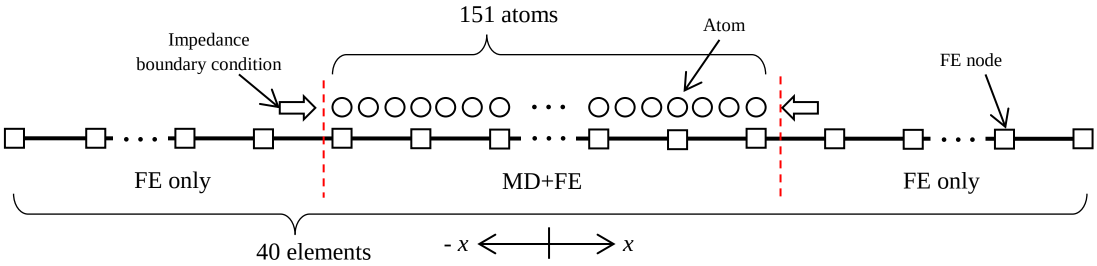

Figure 3.7 A one-dimensional bridging scale problem

As shown in Fig. 3.8a, the initial displacement for this example problem is created by superimposing a high frequency wave onto a truncated Gaussian pulse (Fig. 3.8b) [39]. Note that the displacement in x direction is denoted by the vertical axis in Fig. 3.8 and the following figures in this section. Figure 3.9 illustrates how the initial displacement is implemented on the 1-D bridging scale structure in Fig. 3.7. Only the $+x$ plane is plotted due to symmetry.

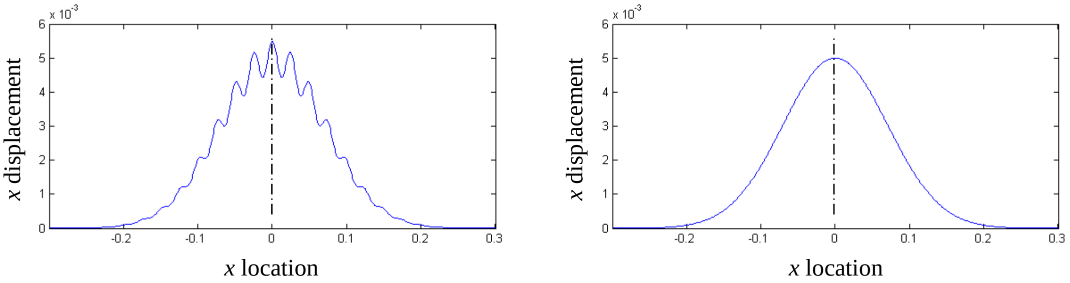

Figure 3.8 (a) Initial displacement of the 1-D bridging scale problem within [-0.3,0.3], and (b) truncated Gaussian pulse

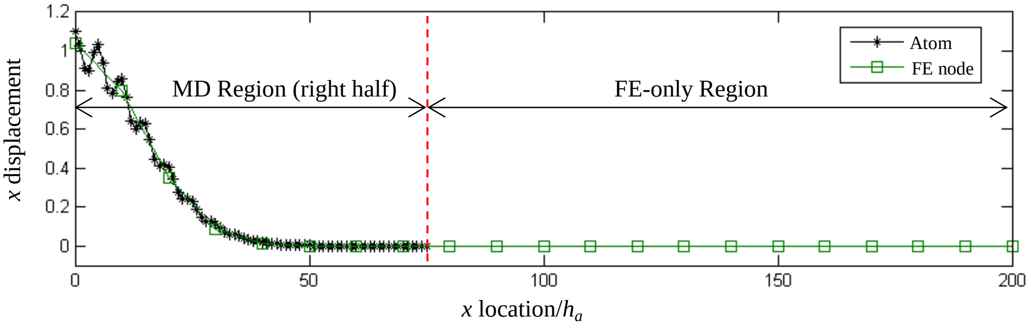

Figure 3.9 Initial condition implemented on 1-D bridging scale structure

Figure 3.10a gives the result of the bridging scale simulation at t = 150. As can be seen, the initial wave passes out of the MD region properly, including the high frequency component. By comparing the simulation result with the result of a full MD simulation (which in this case can be thought of as the exact solution), we can see clearly that the dynamic behavior of the wave has been successfully captured by the bridging scale simulation.

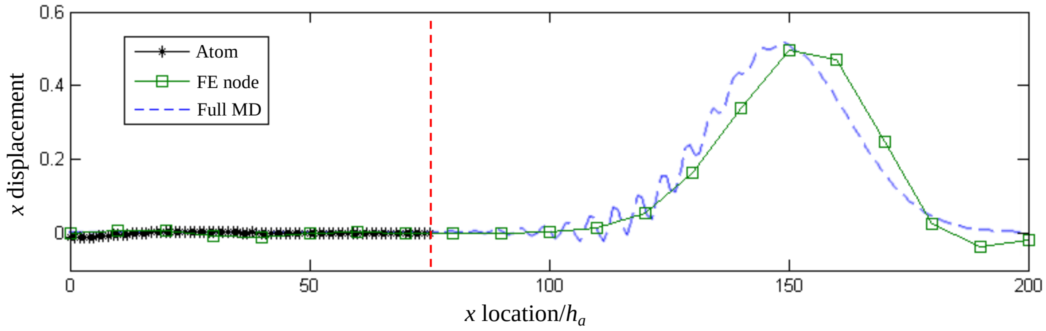

(a)

Figure 3.10 Results of the 1-D bridging scale example problem, (a) with impedance boundary condition, and (b) without impedance boundary condition

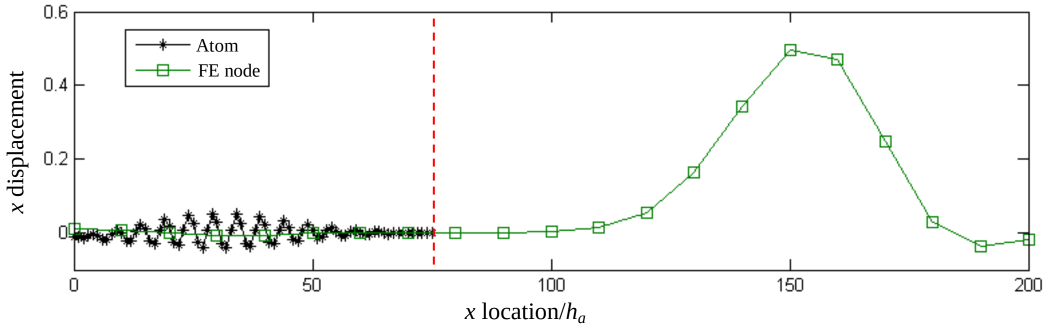

(b)

Figure 3.10 Results of the 1-D bridging scale example problem, (a) with impedance boundary condition, and (b) without impedance boundary condition (cont'd)

To demonstrate the significance of the impedance boundary condition in bridging scale method, Fig. 3.10b shows the bridging scale simulation result in which the MD region is directly coupled to the FE-only region, i.e., the impedance boundary force is not applied. Apparently, since the wavelength of the high frequency component of the initial wave is considerably smaller than that can be captured by the continuum FE region, the wave is thus reflected at the interface, which can result in spurious heat generation in the MD region and a contamination of the simulation. Therefore, it is clear that in bridging scale method, the impedance boundary condition plays an important role in dissipating high frequency wave emitted from the MD region.

3.4 Bridging Scale Method for Higher Dimensions

For 2-D and 3-D structures, the basic concepts of the bridging scale method still apply – the FEA exists everywhere, the MD simulation is confined into a localized domain, and an impedance force is imposed to the boundary of the MD area, as shown in Fig. 3.11.

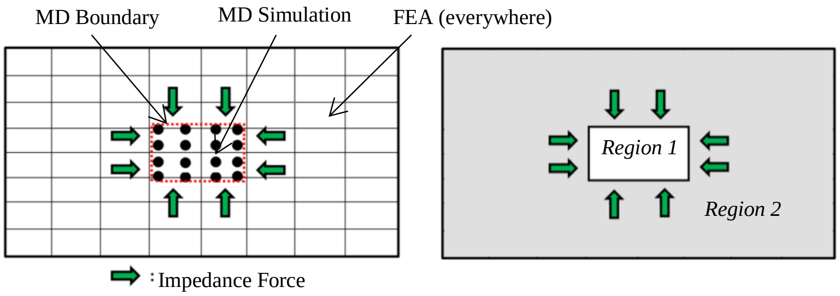

Figure 3.11 Scheme of a 2-D or 3-D bridging scale domain

In this thesis, we focus on 3-D multi-scale problems. The majority of the formulation introduced in the 1-D scenario discussed in Sections 3.3.1 ~ 3.3.3 can also be used for 3-D problems, i.e., the coarse/fine decomposition (Eq. 3.12); multi-scale equations of motion (Eq. 3.16) and linearization of the MD equation of motion (Eq. 3.21). The major difference between 1-D and 3-D bridging scale formulations lies in the derivation of the impedance boundary condition (and hence the equation of motion for MD boundary atoms (Eq. 3.31b)) and the implementation of coarse scale internal force outside the MD region, both of which will be discussed in this section.

For 3-D bridging scale problems, the impedance boundary condition, including the time history kernel, is dependent on the atomic lattice structure. As illustrated in Fig. 3.12, the atomic structure to be utilized in our 3-D numerical example represents a perfect FCC (face centered cubic) crystal (such as Cu, Au, Ag) oriented along the (001) direction.

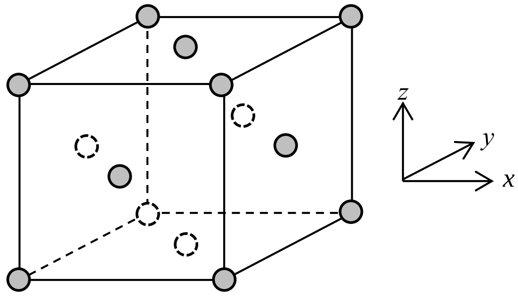

Figure 3.12 A unit cell from the FCC atomic lattice to be used in 3-D numerical example

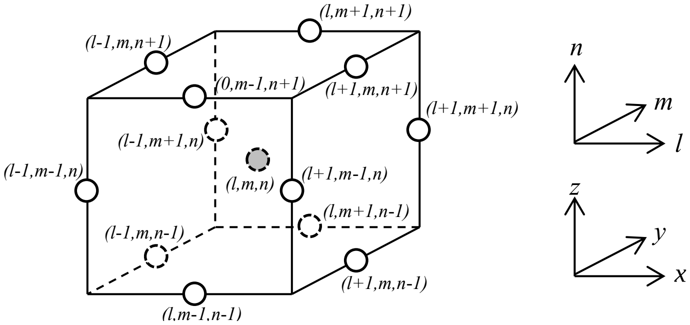

Figure 3.13 An atom (*l*, *m*, *n*) with its neighboring (interacting) atoms in the FCC lattice

To support the derivation of the impedance boundary condition, as shown in Fig. 3.13, each atom in the 3-D FCC lattice is labeled with three indices – *l*, *m*, and *n* – indicating the positions along the *x*, *y*, and *z* axes, respectively. Note that the unit cell in Fig. 3.13 is shifted by half of the edge length compared to that in Fig. 3.12, so that all nearest neighbors of the atom labeled (*l*,*m*,*n*) can be displayed. In Fig. 3.14, we plot the $m = 1$ layer of the FCC lattice based on the atom numbering convention. Note that each value of *n*, for example, describes a layer of atoms bounded in a given *x*-*y* plane. In deriving the impedance force for the 3-D lattice, the $n = 0$ layer is recognized as the boundary of the MD area.

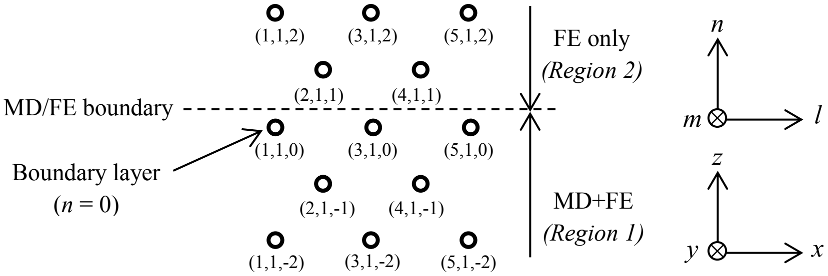

Figure 3.14 The m = 1 layer of a periodic 3D FCC lattice with indices. The dashed line represents the boundary between the MD and the FE-only regions

The derivation of the impedance boundary condition and the time history kernel for the 3-D FCC lattice is detailed in Appendix D. The resulting MD equation of motion for the boundary atoms (n = 0) takes the form

$$\mathbf{M}_A \mathbf{q}_{l,m,0_{,tt}} = \mathbf{f}_{l,m,0}(\mathbf{q},\mathbf{u}) + \mathbf{f}^{imp}_{l,m,0} = \mathbf{f}_{l,m,0}(\mathbf{q},\mathbf{u}) + \sum_{l'=l-l_{crit}}^{l+l_{crit}} \sum_{m'=m-m_{crit}}^{m+m_{crit}} \int_0^t \boldsymbol{\theta}_{l-l',m-m'}(t-\tau)\mathbf{v}_{l',m',0}(\tau)d\tau \quad (3.45)$$

where the time history kernel $\boldsymbol{\theta}$ is a 3×3 matrix. Note that for 3-D bridging scale problems, the equations of motion for non-boundary MD atoms and finite element analysis are the same as with the 1-D case (Eqs. 3.31a and 3.31c).

The diagonal components of the 3-D time history kernel $\boldsymbol{\theta}$ in Eq. 3.45 calculated based on the FCC lattice (Fig. 3.13) and the normalized LJ 6-12 potential are plotted in Fig. 3.15. As can be seen, $\boldsymbol{\theta}_{33}(t)$ is the most important component, while $\boldsymbol{\theta}_{11}(t)$ and $\boldsymbol{\theta}_{22}(t)$ are equal to each other due to symmetry of the lattice in x and y directions.

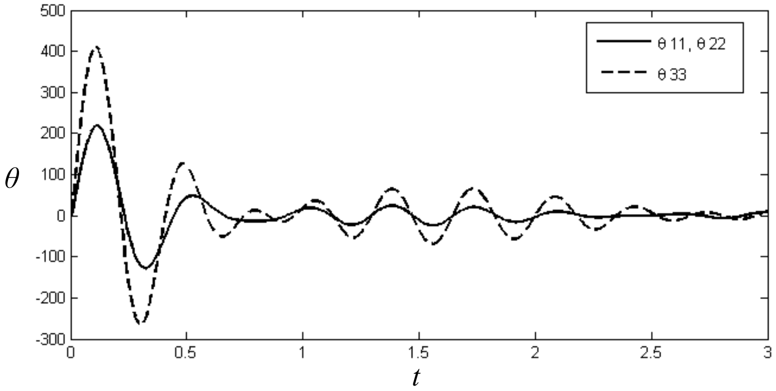

Figure 3.15 Diagonal components of the time history kernel matrix $\boldsymbol{\theta}$

Note that l_{crit} and m_{crit} in Eq. 3.45 are introduced as maximum numbers of neighboring atoms along the x and y directions, respectively, that will be considered during the derivation of the impedance force. It has been shown in [24] that compared to a direct MD/FE coupling, the biggest improvement occurs when the zeroth-order component of the time history kernel is utilized ($l_{crit} = m_{crit} = 0$). Also, it has been discussed in [28] that higher order values of $\boldsymbol{\theta}$(t) corresponding to $l_{crit} > 0$ and $m_{crit} > 0$ are at most 10% of the values shown in Fig. 3.15. Therefore, in this thesis we assume $l_{crit} = m_{crit} = 0$ when calculating the time history kernel matrix.

For higher dimensional problems, the finite element internal forces outside the MD region are also calculated based on the Cauchy-born rule. However, unlike the analytical derivation shown in the 1-D case (Eq. 3.42), the nodal force calculation for 2-D and 3-D problems requires numerical integration. For instance, in our 3-D numerical example, hexahedral eight-node isoparametric elements are used in finite element analysis. To obtain the nodal forces due to the deformation of a given element, the defamation gradient is first calculated at eight quadrature points within the element using Eq. 3.34; then the first Piola-Kirchoff stress at each quadrature point is calculated using Eq. 3.33, where the energy density is evaluated based on the deformation of the 12 atomic bonds surrounding a given atom (assuming FCC lattice and nearest neighbor interaction); finally, the FE nodal forces can be approximated using Eq. 3.36. Details regarding the derivation of the Piola-Kirchoff stress $\mathcal{P}$ and the *Region 2* nodal forces for the 3-D FCC lattice can be found in Appendix E.

Note that if the normalized LJ potential discussed earlier is assumed, then for the FCC lattice, the equivalent interaction coefficient k_e along the x, y, and z directions is calculated as 646.4. The corresponding value of $1/v^*$ is found to be around 0.35 using Eq. 3.6. In our 3-D numerical example, we will use a MD time step size $\Delta t_m = 0.0075$, which is sufficiently small. The FE time step size Δt is not limited to the time scale characterizing atomic vibrations. Due to the larger length and slower time scales associated with the coarse scale, a relatively larger time step can be chosen for FEA.

3.5 Implementation for Crack Propagation Problems

For crack propagation problems, it is important to track the evolution of crack tip location during simulation. In this thesis, to identify the atom right at the crack tip for each time step, we employ the centro-symmetry parameter P defined by Kelchner et al. [40], given by

$$P = \sum_i \left| \mathbf{R}_i + \mathbf{R}_{i+6} \right|^2 \qquad (3.46)$$

where $\mathbf{R}_i$ and $\mathbf{R}_{i+6}$ are vectors corresponding to the six pairs of opposite bonds surrounding a given atom in a FCC crystal. Figure 3.16a illustrates two of the six pairs of bonds around atom α in the FCC lattice used in our numerical example. According to Eq. 3.46, $P = 0$ where the lattice is undisturbed or deformed in a symmetric manner, and

P becomes large near defects or free surfaces. For example, Fig. 3.16b depicts a scenario in which the four nearest neighbors above atom α have been pulled far away so that atom α becomes a surface atom.

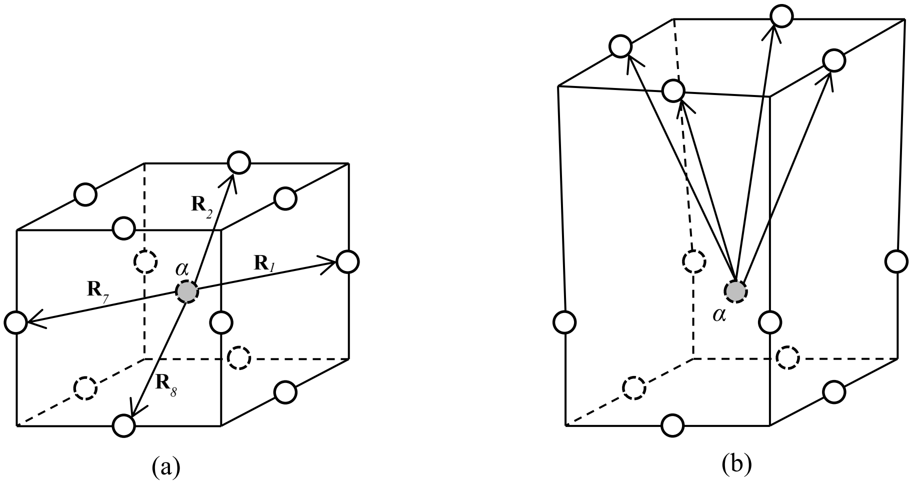

Figure 3.16 (a) An atom α within a FCC lattice, (b) deformed lattice, in which atom α becomes a surface atom

The centro-symmetry parameter is proven to be a useful metric to visualize nano-scale defects in molecular dynamics studies for 3-D FCC crystals reported by Potirniche et al. [7]. Moreover, it is found that the *P* parameters of surface atoms are in most cases much larger than those of atoms near defects such as dislocations or stacking faults [40]. Therefore, for a particular interatomic potential model, a critical value of *P* can be defined to distinguish all the atoms located on free surfaces of the crack, i.e., an atom with *P* parameter greater than the critical value will be identified as a crack surface atom. When a crack grows, for example, horizontally in a specimen shown in Fig. 3.17a, the crack tip position can be determined by finding the *x* location of the crack interior surface atom with the maximum *x* coordinate [8,41,42]. Typically, a curve that depicts the crack tip positions obtained in this way versus time will look similar to that given in Fig. 3.17b, i.e., the crack tip location remains constant for a certain period of time, after which it suddenly jumps to the next atom.

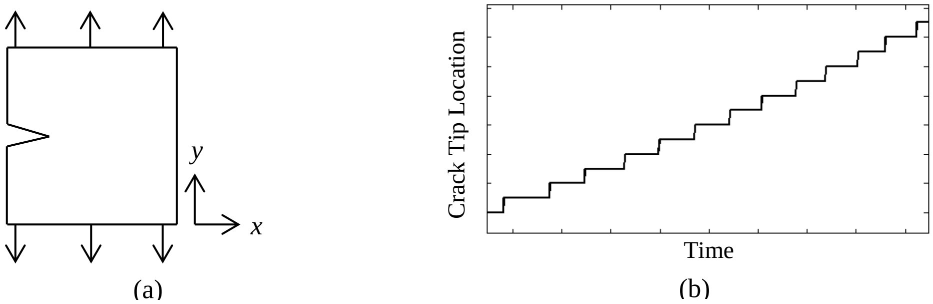

Figure 3.17 (a) A specimen with a horizontal edge crack. (b) A typical crack tip location history curve

Note that the centro-symmetry parameter is not the only way available to identify the crack tip. Alternate approaches have also been widely used in atomistic studies, such as the local potential energy criterion [41] and the crack tip bond length criterion [43]. Note that whichever method we choose, the resulting crack tip location curve is always piecewise constant in time domain as illustrated in Fig. 3.17b.

3.6 Numerical Example: Part 1

In this section, we implement the bridging scale simulation method for a three-dimensional multi-scale dynamic crack propagation problem. The 3-D FCC lattice shown in Fig. 3.12 will be used to model the atomic structure. Other implementation details are similar to those discussed in [20,24,27,28]. For example, the initial temperature of the system is set to 0K; all components of the time history kernel matrix are set to zero after 800 time steps; LJ 6-12 potential with normalized units is used; and only nearest neighbors are considered when calculating interatomic interactions. The simulation code is developed using Matlab [44] and implemented on a DELL T7500 workstation with Intel® Xeon® processor E5603 (clock speed 1.6 GHz).

3.6.1 Simulation Model

The structure under consideration is a nano scale solid beam depicted schematically in Fig. 3.18. As can be seen, the beam has a uniform cross section along the thickness (*y* direction), and is symmetric in *x*-*z* plane with respect to the mid-plane (dashed axis in Fig. 3.18b). The size of the geometry is $136\sqrt{2}\,h_a \times 2\sqrt{2}\,h_a \times 138\sqrt{2}\,h_a$ (in *x*, *y*, *z* directions, respectively) in normalized units. For bridging scale simulation, the beam is modeled with finite elements everywhere, while the MD region is confined to a rectangular area at the bottom. Specifically, the entire domain contains 782 hexahedral eight-node isoparametric finite elements (two layers along the thickness). The 340 elements within the MD region are of the same regular shape, with width $8\sqrt{2}\,h_a$, height $6\sqrt{2}\,h_a$, and thickness $\sqrt{2}\,h_a$. In the FE-only region, the elements are trapezoidal in *x*-*z* plane with the same height of $6\sqrt{2}\,h_a$, whereas their dimensions in *x* direction are subject to the curved shape of the boundary. The MD domain is comprised of 82,583 atoms in total, with 5 layers of atoms in *y* direction. A pre-defined horizontal edge crack of length $12\sqrt{2}\,h_a$ is created in the MD area by blocking the interaction between two adjacent layers of atoms.

During simulation, the structure is fixed at the bottom and pulled at the top face by a displacement boundary condition shown in Fig. 3.19. This boundary displacement corresponds to a strain in *z* direction that grows from zero to approximately 2.5% at $t = 6{,}000\Delta t_m$, after which it keeps stretching the beam at a lower strain rate to prevent the crack faces from contacting each other. To mimic a plane-strain configuration, a periodic boundary condition is applied in the y direction, i.e., the solution at $y = y_0$ is equal to the solution at $y = y_0 + t_h$, where t_h is the thickness of the beam. Following [28], ten MD time steps are run for each FE time step.

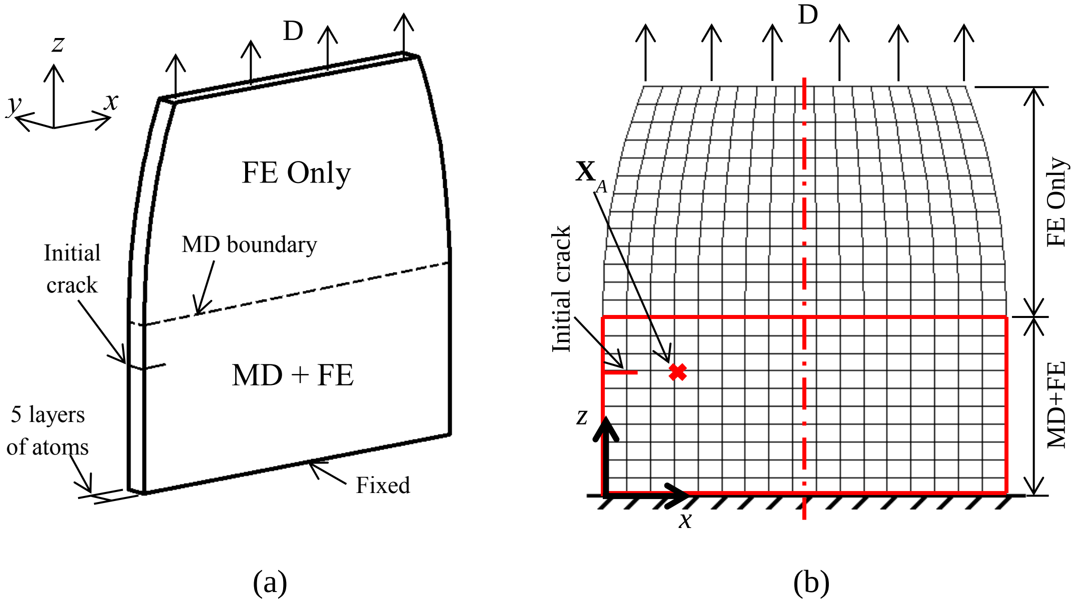

Figure 3.18 3-D nano scale beam model, (a) schematic illustration, and (b) FE mesh in - x-z plane

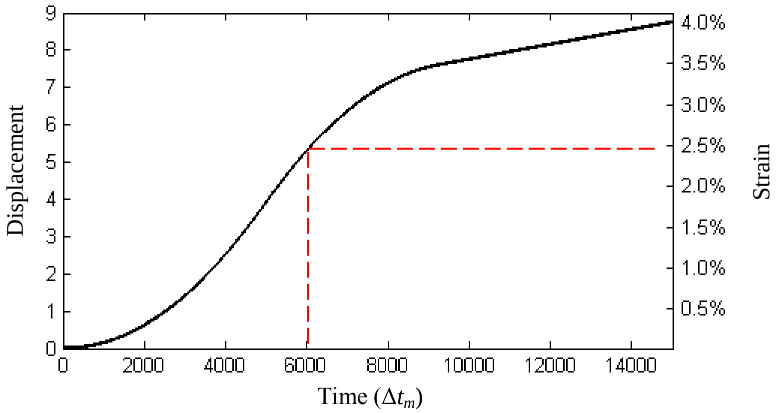

Figure 3.19 Displacement boundary condition applied to the top face of the beam

3.6.2 Simulation Result

Figure 3.20 gives the snapshots of the bridging scale simulation result up to t = 15,000Δt_m. As can be seen, the displacement applied at the top of the beam propagated smoothly into the MD area, causing the initial crack to propagate in a mode I fashion. The solutions of all atoms and FE nodes were consistent along the thickness (y), and no displacement was observed in y direction, indicating that the plane strain condition was applied correctly. The computation time for the bridging scale simulation was about 24 hours.

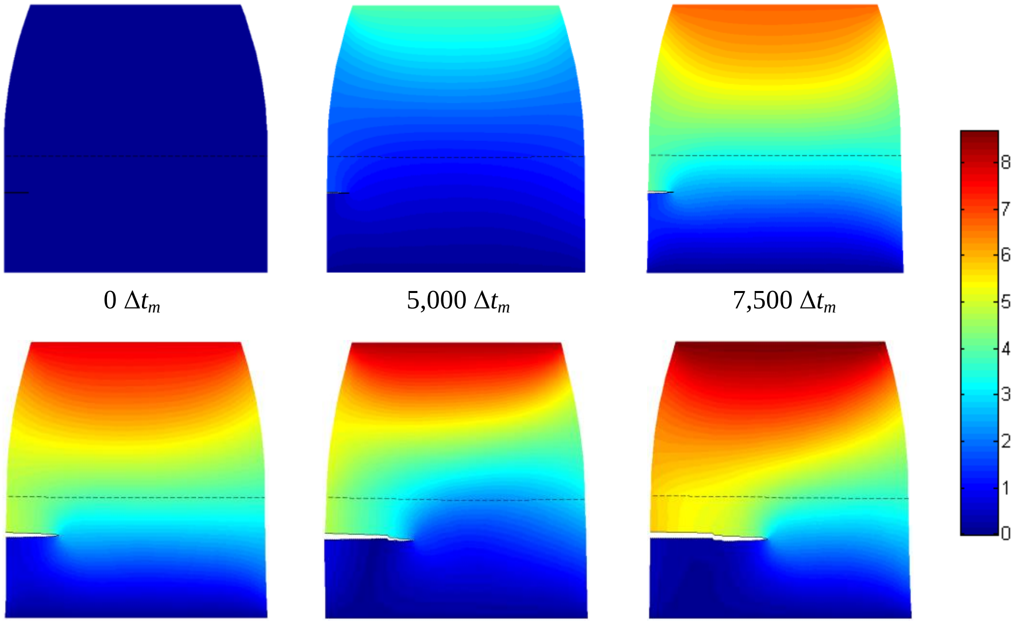

0 Δt_m 5,000 Δt_m 7,500 Δt_m

10,000 Δt_m 12,500 Δt_m 15,000 Δt_m

Figure 3.20 Bridging scale simulation results at various time steps. Contours of z direction displacements shown

As discussed in Section 3.5, we take advantage of the centro-symmetry parameter P to recognize the atoms located on crack surfaces. For the 3-D FCC lattice and the normalized LJ 6-12 potential used in our simulation, we found empirically that $P > 2$ serves as an effective criterion. Figure 3.21a shows a 3-D snapshot of the simulation result within the MD area at $t = 15{,}000\Delta t_m$, where atoms are plotted with colors representing their z direction displacements. A zoomed-in view of the atoms near the crack tip is given in Fig. 3.21b, with $P > 2$ atoms highlighted in black. Apparently, the crack surface atoms are successfully identified, and the crack tip atom is simply the one with maximum x coordinate. The resulting crack tip location history curve is plotted in Fig. 3.22, indicating that the crack started to grow at around $t = 7{,}000\Delta t_m$ and remained an approximately constant propagation speed until the end of the simulation.

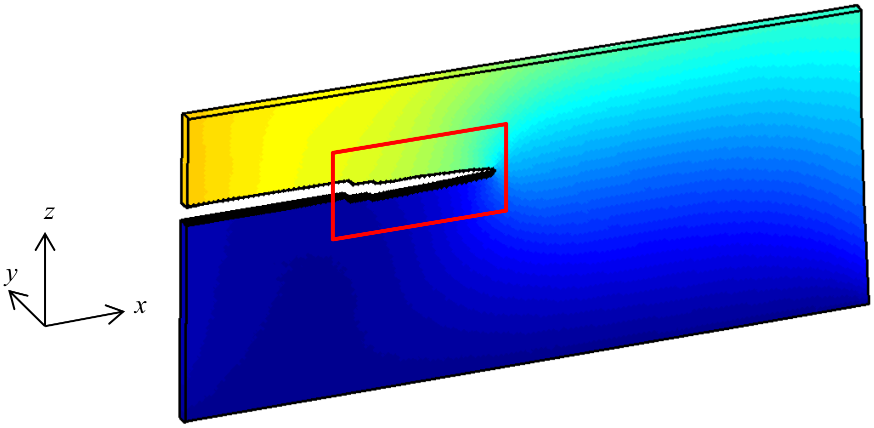

(a)

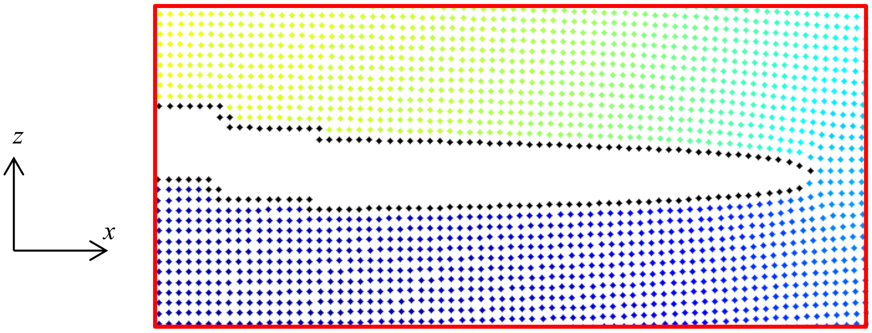

(b)

Figure 3.21 Bridging scale simulation result within the MD area (a) 3-D snapshot at $t = 15{,}000\Delta t_m$, and (b) zoomed-in view near the crack tip with crack surface atoms highlighted

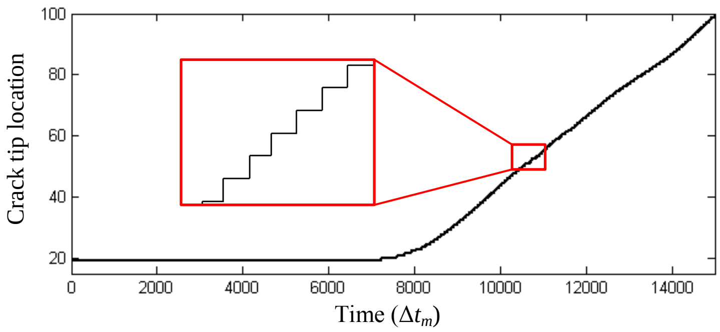

Figure 3.22 Crack tip location history curve

3.6.3 Physical Interpretation

To examine the physics behind the dynamic response of the structure, we first plot in Fig. 3.23 the z displacements of the nodal points at $y = t_h/2$ within the mid-plane (dotted line in Fig. 3.18b) at time steps 2,400Δt_m and 2,800Δt_m. As can be seen, within the 400 MD time steps, the macroscopic wave due to the boundary displacement traveled approximately 35 normalized units along the –z direction. The speed of the macroscopic wave can be calculated as

$$c = 35/(400 \times 0.0075) = 11.7 \tag{3.47}$$

which is very close to the theoretical longitudinal wave speed c_l = 12 [8] for the FCC lattice and LJ potential used in our simulation.

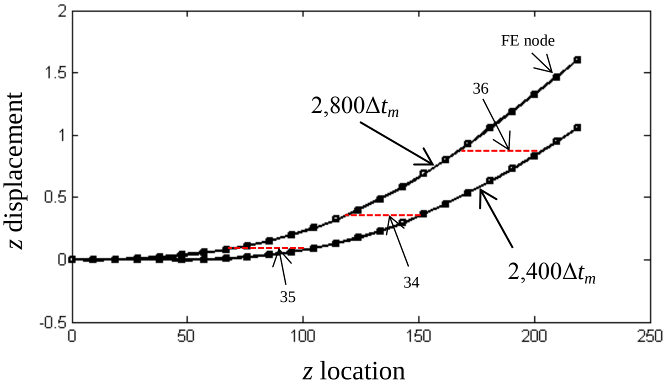

Figure 3.23 z displacement distribution along z direction at time steps 2,400Δt_m and 2,800Δt_m

To take a closer look at the microscopic level dynamics, we focus on the *z* direction displacement history (displacement vs. time) of the atom located at $\mathbf{X}_A$ shown in Fig. 3.18b. As can be seen from Fig. 3.24a, atom $\mathbf{X}_A$ remained stationary until the macroscopic wave arrived at around $t = 2{,}500\Delta t_m$, after which it moved upward with the continuum. At around $t = 9{,}000\Delta t_m$, due to the growth of the crack, the bonds right above atom $\mathbf{X}_A$ broke, and atom $\mathbf{X}_A$ became a surface atom. Therefore, regardless of the majority of the domain still being stretched, atom $\mathbf{X}_A$ went downwards with the lower crack surface right after $t = 9{,}000\Delta t_m$, and finally moved according to the macroscopic vibration of the lower crack surface. If we zoom in the displacement curve, we can see in Fig. 3.24b that the microscopic wave due to atomic vibration is superimposed on the macroscopic wave. Because of the coupling of atomic vibrations in three dimensions, the microscopic vibration frequency observed from the *z* displacement curve is not uniform throughout the entire simulation; however, as shown in Fig. 3.24c, the shortest vibration period is found to be $48\Delta t_m$, corresponding to a frequency of 2.78, which is very close to 2.86 – the vibration frequency calculated in Section 3.4. This also implies that the time step size used is sufficiently small to capture the high frequency microscopic wave in our MD simulation.

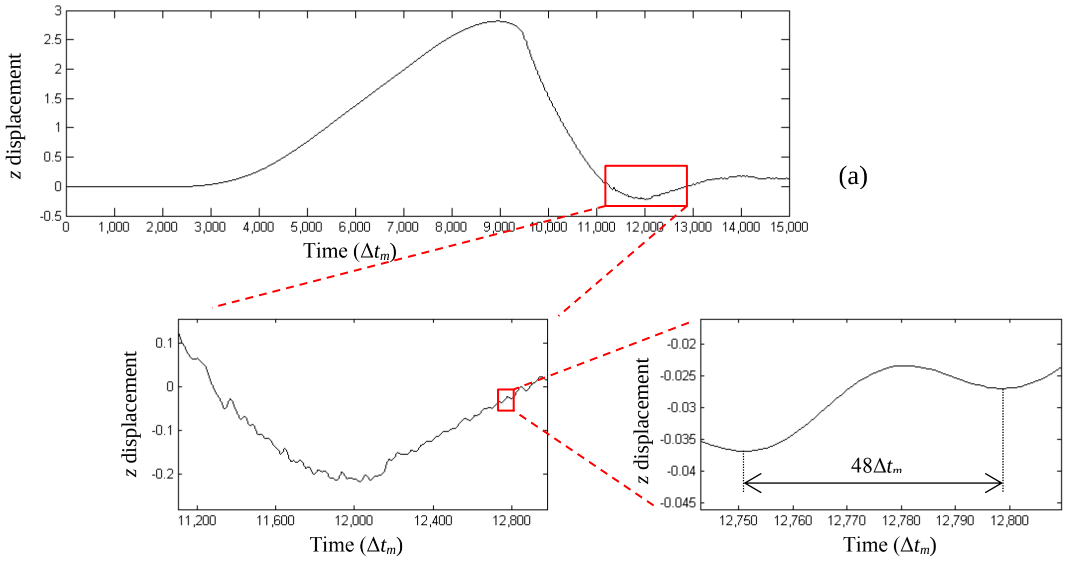

(b) (c)

Figure 3.24 z displacement history of atom $\mathbf{X}_A$

Now we examine the behavior of the crack. As can be seen from Fig. 3.22, the initial crack started to propagate at around $t = 7{,}000\Delta t_m$. Since the LJ potential models a generic brittle material, during most of the simulation period, the crack propagated in a straight line and left “mirror” cleaved surfaces. However, it is also noticed that the crack was roughened at around $t = 10{,}500\Delta t_m$, as shown in Fig. 3.25a, which is due to the instability behavior of brittle crack propagation. In order to better understand the underlying physics, we measure the crack propagation speed right before $t = 10{,}500\Delta t_m$ by averaging the crack tip locations from $9{,}500\Delta t_m$ to $10{,}500\Delta t_m$ using least square fitting (Fig. 3.25b), and the calculated local crack speed turns out to be 1.76, which corresponds to about 32% of the Rayleigh wave speed $c_R = 5.6$ [8] for the FCC crystal modeled in our simulation. This is in good agreement with the experimental and simulation results reported in literature [8,9], i.e., dynamic instability in brittle crack propagation occurs when the crack propagation speed approaches one third of the Rayleigh wave speed c_R. This instability behavior roughened the crack surface near $t =$

$10{,}500\Delta t_m$, meanwhile slowed down crack speed along the x direction. After t = $11{,}000\Delta t_m$ and up to t = $15{,}000\Delta t_m$, the crack propagation speed never reached one third of the Rayleigh speed again due to the reduced strain rate at the top of the beam after t = $8{,}000\Delta t_m$; as a result, crack surfaces again became flat.

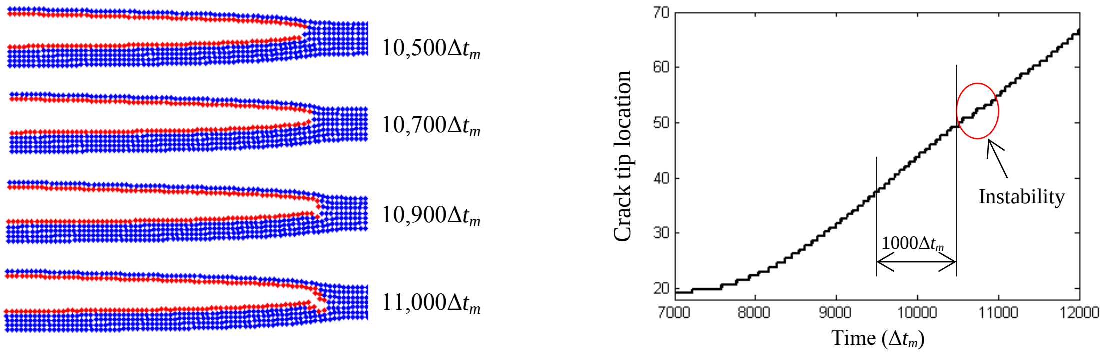

(a) (b)

Figure 3.25 Instability of brittle crack propagation. (a) Crack surface roughened at instability, where atoms near the crack are plotted in blue, except for crack surface atoms being highlighted in red. (b) Calculation of crack speed before instability

According to the observations and discussions above, it is clear that the bridging scale simulation accurately captured the essential physics of brittle crack propagation. The macroscopic displacement at the boundary propagated smoothly into the MD area across the MD/FE boundary, while the longitudinal wave speed measured in simulation matches the theoretical value. At microscopic level, the highest z displacement oscillation frequency measured in simulation is close to the calculated z direction natural vibration frequency of the FCC atomic lattice. Furthermore, the crack speed measured at dynamic instability is consistent with the data published in literature.

CHAPTER 4

ANALYTICAL SHAPE SENSITIVITY ANALYSIS FOR BRIDGING SCALE METHOD

4.1 Overview

The basic concepts of shape sensitivity analysis have been introduced in Chapter 2. In the current chapter, we apply continuum shape sensitivity analysis to dynamic multi-scale problems based on the bridging scale method introduced in Chapter 3. By taking material derivative of the bridging scale variational equations (to be presented in Section 4.3), continuum sensitivity expressions will be derived analytically in a fully generalized 3-D setting.

For bridging scale problems, the most basic and straightforward performance measures are the dynamic responses of the structure, i.e., the displacements, velocities and accelerations of all atoms and FE nodal points in the domain. These performances measures can be referred to as analytical performance measures, since their sensitivity coefficients can be obtained analytically by solving the sensitivity expressions.

In this chapter, we first introduce shape design parameterization and the calculation of design velocity field for general structures. Section 4.3 presents the variational formulation developed for the bridging scale method, which is the starting point of continuum shape sensitivity analysis. A discussion on the discontinuity problem in shape DSA of coupled atomistic/continuum systems will be given in Section 4.4. In Section 4.5, the multi-scale shape sensitivity expressions will be derived in a continuum setting based on the variational formulation. Implementation aspects of sensitivity analysis will be briefly discussed in Section 4.6. Finally, in Section 4.7, the nano-beam example introduced in the previous chapter will be used to verify the accuracy of the sensitivity coefficients of structural responses calculated using the proposed analytical sensitivity analysis approach.

4.2 Design Parameterization and Calculation of Design Velocity Field

Shape design variables govern the geometric shape of the structural boundary, usually represented by parametric curves and surfaces for 2-D and 3-D applications, respectively. Consider the shape design for an engine connecting rod [1] shown in Fig. 4.1. The design boundary (red lines) consists of two cubic Bezier curves at each end and a horizontal line in the middle. Upper and lower design boundaries are symmetric with respect to the centerline.

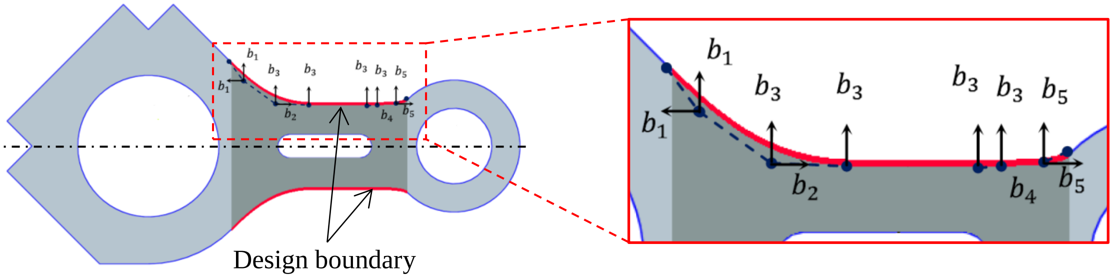

Figure 4.1 Engine connecting rod [1]

Note that Bezier curve is one of the common formats of planar parametric curves. It is represented geometrically by the position of its control points (or control polygon), which determine the shape of the curve with Bernstein basis polynomial. Mathematically, a Bezier curve is defined as [45]

$$\mathbf{C}(u) = \sum_{i=0}^{n} \mathbf{p}_i B_{i,n}(u), u \in [0,1] \tag{4.1}$$

where u is the parametric coordinate of the curve, $\mathbf{p}_i$ represents the ith control point, $n+1$ is the total number of control points, and $B_{i,n}(u)$ is the Berstain polynomial, defined as

$$B_{i,n}(u) = \binom{n}{i} u^i (1-u)^{n-i} \tag{4.2}$$

As illustrated in Fig. 4.2, any perturbation of the position of the control points will result in the change of the geometric shape of the Bezier curve.

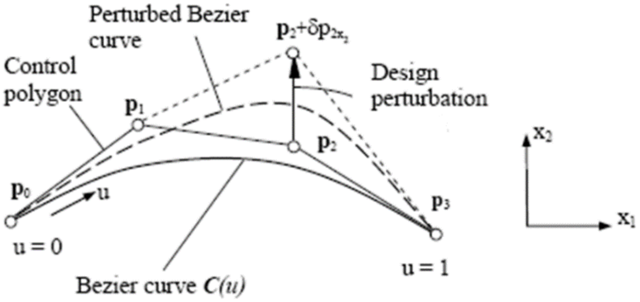

Figure 4.2 A cubic Bezier curve and its variation due to design change [46]

For the connecting rod example, the locations of the control points of the Bezier curves are selected as design variables (b_1 ~ b_5), as shown in Fig. 4.1. The shaded area represents the design domain – the structural domain that will be affected by design variables.

During shape design, the design velocity field is calculated first at the design boundary. The mapping $\boldsymbol{T}$ is characterized by the parametric equations employed for representing the design boundary (such as Eq. 4.1). Therefore, the boundary velocity field can be calculated by varying the parametric equations of the design boundary through changes of design variables. For example, for a 2-D design boundary, the boundary velocity field with respect to the ith design variable b_i can be written as

$$\boldsymbol{V}_i(u) = \delta\mathbf{C}(u;\mathbf{b}) = \frac{\partial\mathbf{C}}{\partial b_i}\delta b_i \tag{4.3}$$

where δb_i is usually set to 1 for convenience in practice.

If finite element method is employed for structural analysis, the finite element nodes at the original design boundary will have to move to the new geometric boundary. The movement, i.e., boundary velocity field, can be calculated by plugging the parametric coordinate u at the nodes (e.g., u_j for node j) along the boundary curve into Eq. 4.3; that is

$$\boldsymbol{V}_i^j(u_j) = \delta\mathbf{C}(u_j;\mathbf{b}) = \frac{\partial\mathbf{C}}{\partial b_i}\delta b_i \tag{4.4}$$

To illustrate the movement of boundary nodes according to the boundary velocity field, a 2-D structural domain with design boundary parameterized using a cubic Bezier curve is depicted in Fig. 4.3. As can be seen, the boundary nodes (n_1 ~ n_6) move with the boundary curve due to the position change of control point $\mathbf{p}_2$ (moved upward by δp_{2x_2}).

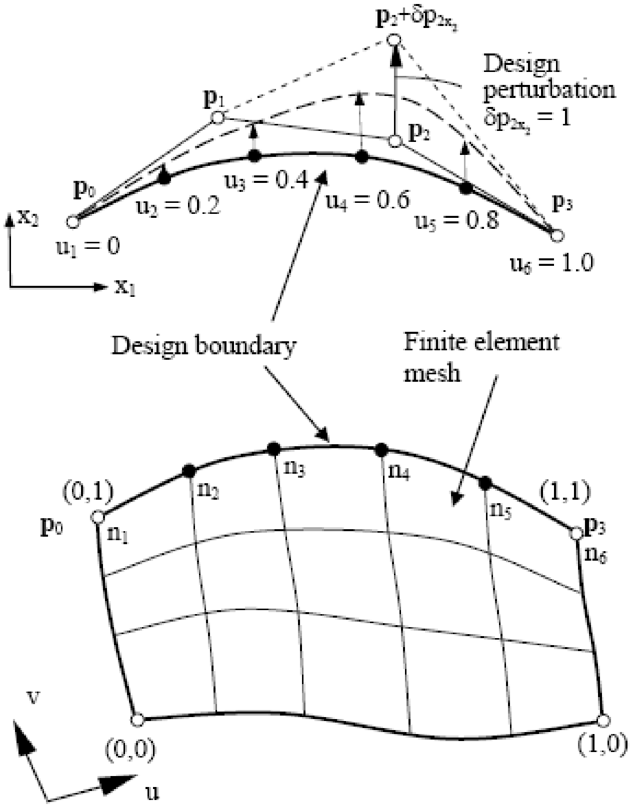

Figure 4.3 A 2-D model with design boundary parameterized using a Bezier curve. Boundary nodes move due to the location change of control point $\mathbf{p}_2$ [46]

The change of structural boundary also causes the movement of material points in the domain of the structure, which is characterized by so called domain velocity field. After a shape design change, instead of re-meshing the domain using a mesh generator (which may result in the change of topology of the finite element mesh), the location of the finite element nodes needs to be updated according to the domain velocity field. Several approaches of calculating the domain velocity field are available, such as the Isoparametric Mapping Method [47] and the Boundary Displacement Method [48], which have been well documented and will not be repeated in this section.

Note that when defining design velocity fields for a general structural domain, several theoretical and practical requirements need to be satisfied. For example, the design velocity field should depend linearly on the variation of shape design parameters; also, it must retain the topology of the original finite element mesh without causing any mesh distortion; moreover, the finite element nodes at the boundary must stay on the boundary for all shape changes [48].

4.3 Variational Formulation for Bridging Scale Method

As discussed earlier in Chapter 2, continuum shape sensitivity analysis requires taking material derivative of a continuum variational governing equation in integral form. In this section, we briefly introduce the continuum variational formulation developed for the bridging scale method, which has been reported in our previous work [35]. Detailed derivation of the variational formulation can also be found in Appendix F of this thesis.

In bridging scale method, the total solution $\boldsymbol{z}(\mathbf{x}, t)$ is defined as the sum of coarse scale $\boldsymbol{u}(\mathbf{x}, t)$ and fine scale $\boldsymbol{v}(\mathbf{x}, t)$, as introduced in Eq. 3.1; that is

$$\boldsymbol{z}(\mathbf{x},t)=\boldsymbol{u}(\mathbf{x},t)+\boldsymbol{v}(\mathbf{x},t) \tag{4.5}$$

where the displacement fields are thought to be continuous functions at first glance. In order to introduce the bridging scale, the structure domain needs to be described using atoms. Therefore, discrete functions $\mathbf{z}$, $\mathbf{u}$ and $\mathbf{v}$, which have values only at atomic positions, are defined to represent the atomic displacement fields. Note that the coarse scale can also be thought of as a continuous field $\boldsymbol{u}$, since it can be interpolated at points in between atoms with FE shape functions; while $\mathbf{u}$ is simply a discrete version of $\boldsymbol{u}$, with function values of $\boldsymbol{u}$ at atomic locations. All the continuous and discrete displacement fields above belong to a function space defined as

$$Z = \mathcal{Z} \bigcup Z \tag{4.6a}$$

$$\mathcal{Z} = \left\{ \boldsymbol{z} = \boldsymbol{u} + \boldsymbol{v},\ \ \boldsymbol{u},\boldsymbol{v} \in \left[H^{m}(\Omega) \right]^{3} \mid \boldsymbol{u} = \boldsymbol{u}_{\Gamma}, \boldsymbol{v} = \boldsymbol{v}_{\Gamma} \text{ on } \mathbf{x} \in \Gamma^{h} \right\} \tag{4.6b}$$

$$Z = \left\{ \mathbf{z} = \mathbf{u} + \mathbf{v},\ \ \mathbf{u}, \mathbf{v} \in \mathbf{R}^{3} \mid \mathbf{u} = \mathbf{u}_{\Gamma}, \mathbf{v} = \mathbf{v}_{\Gamma} \text{ on } \mathbf{x} \in \Gamma^{h} \right\} \tag{4.6c}$$

Following the derivations detailed in Appendix F, we achieve the variational equations for both MD simulation and coarse scale FEA, respectively, as

$$\int_{0}^{t_T} \bar{\mathbf{q}}^{T} \mathbf{M}_{A} \mathbf{q}_{,tt}\, dt = \int_{0}^{t_T} \bar{\mathbf{q}}^{T} \left[\mathbf{f}(\mathbf{q}, \mathbf{u}) + \mathbf{F}^{imp} \right] dt \tag{4.7a}$$

and

$$\int_{0}^{t_T} \iiint_{\Omega} \rho(\mathbf{x}) \bar{\boldsymbol{u}}^{T} \boldsymbol{u}_{,tt} d\Omega\, dt = \int_{0}^{t_T} \left[\bar{\mathbf{u}}^{T} \mathbf{f}(\mathbf{z}) - \iiint_{\Omega_2} \bar{\boldsymbol{\varepsilon}}^{T}(\bar{\boldsymbol{u}}) \boldsymbol{\sigma}(\boldsymbol{u}) d\Omega_{2} \right] dt \tag{4.7b}$$

where $\mathbf{F}^{imp}$ is a vector that includes the impedance forces acting on all boundary atoms. $\boldsymbol{\varepsilon}$ and $\boldsymbol{\sigma}$ denote stain and stress, respectively, while $\boldsymbol{\Omega}_2$ represents the FE-only domain. The virtual displacements $\bar{\mathbf{q}}$, $\bar{\boldsymbol{u}}$ and $\bar{\mathbf{u}}$ belong to the function space $\hat{Z}$ defined as

$$\hat{Z} = \hat{\mathcal{Z}} \bigcup \hat{Z} \tag{4.8a}$$

$$\hat{\mathcal{Z}} = \left\{ \bar{\boldsymbol{z}} = \bar{\boldsymbol{u}} + \bar{\boldsymbol{v}},\ \ \bar{\boldsymbol{u}}, \bar{\boldsymbol{v}} \in \left[H^{m}(\Omega) \right]^{3} \mid \bar{\boldsymbol{u}}, \bar{\boldsymbol{v}} = 0 \text{ on } \mathbf{x} \in \Gamma^{h},\ \bar{\boldsymbol{u}}(\mathbf{x},0) = \bar{\boldsymbol{u}}(\mathbf{x},t_T) = \bar{\boldsymbol{v}}(\mathbf{x},0) = \bar{\boldsymbol{v}}(\mathbf{x},t_T) = 0 \right\} \tag{4.8b}$$

$$\hat{Z} = \left\{ \bar{\mathbf{z}} = \bar{\mathbf{u}} + \bar{\mathbf{v}},\ \ \bar{\mathbf{u}}, \bar{\mathbf{v}} \in \mathbf{R}^{3} \mid \bar{\mathbf{u}}, \bar{\mathbf{v}} = 0 \text{ on } \mathbf{x} \in \Gamma^{h},\ \bar{\mathbf{u}}(\mathbf{x},0) = \bar{\mathbf{u}}(\mathbf{x},t_T) = \bar{\mathbf{v}}(\mathbf{x},0) = \bar{\mathbf{v}}(\mathbf{x},t_T) = 0 \right\} \tag{4.8c}$$

Note that the energy equations (Eqs. 4.7a and 4.7b) are obtained in a continuum setting, except for the MD simulation, which is discrete in nature. The energy equations serve as the basis of the continuum shape sensitivity analysis to be introduced later in this chapter. Also, it has been shown in [35] that starting from the variational formulation, the complete set of bridging scale differential equations presented in Chapter 3 can be naturally obtained.

4.4 Discontinuity in Shape DSA of Bridging Scale Problems

Applying the concept of continuum shape sensitivity analysis to bridging scale problems involves unique challenges due to the nature of coupling atomistic/continuum systems. Here we take a 1-D bridging scale structure shown in Fig. 4.4a as an example for illustration. For 1-D problems, the only shape design variable is length, and the shape sensitivity coefficients describe the influence of length change to the displacements of atoms and finite element nodal points in the structure. Note that in bridging scale, coarse scale solutions are continuous in design; hence, derivatives exist. However, for the fine scale, when the length is changed, atoms must be either added or deleted from the system, losing the continuity requirement.

Now we first discuss the derivatives of the coarse scale solutions to reveal the discontinuity issue, and then introduce the method that we propose to overcome the problem.

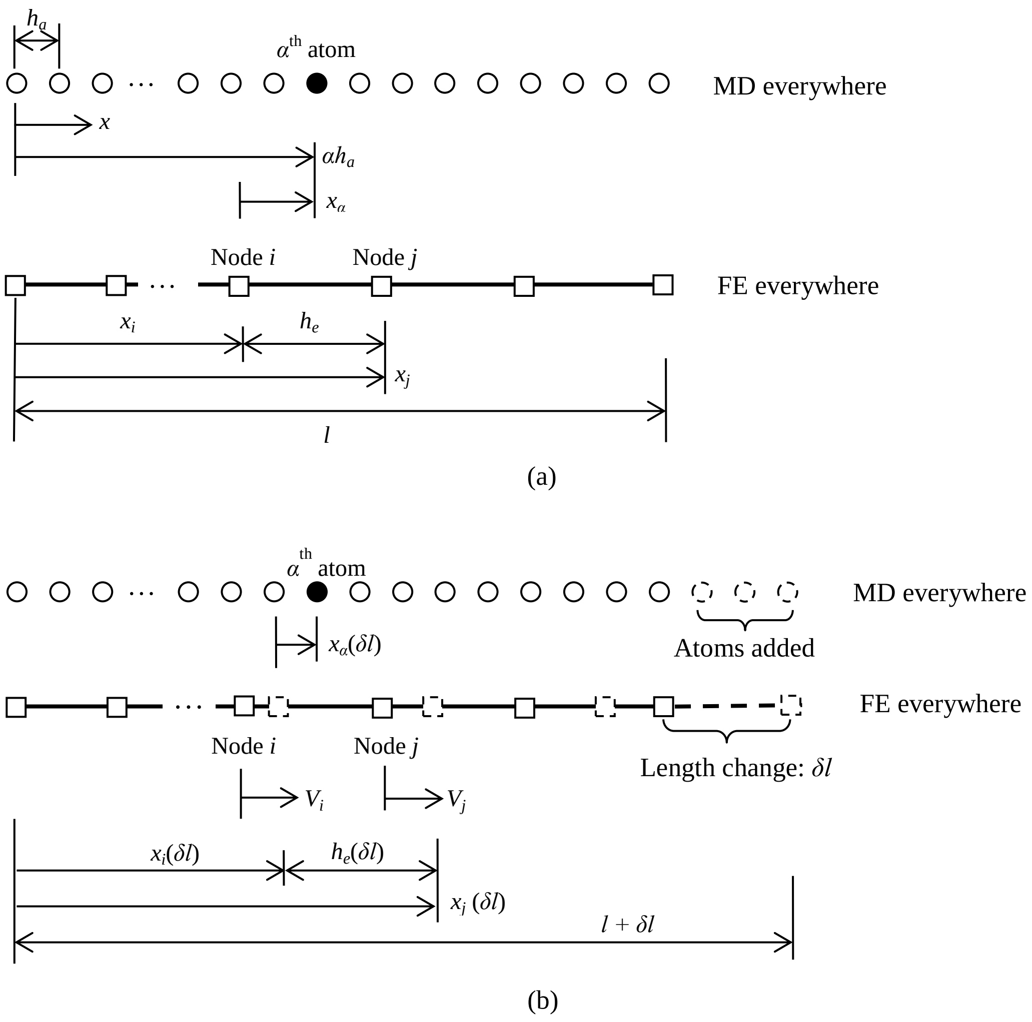

Figure 4.4 1-D bridging scale structure with atom α inside element with nodes i and j. (a) Before design change, and (b) after design change (length changed to $l + \delta l$)

As shown in Fig. 4.4a, the coarse solution of the αth atom, which falls inside the element with end nodes i and j, can be written as

$$u_\alpha = N_i^\alpha d_i + N_j^\alpha d_j \tag{4.9}$$

where d_i and d_j are the displacements at respective nodes i and j, obtained from finite element solutions. N_i^α and N_j^α are linear shape functions of nodes i and j evaluated at x_α, defined as

$$N_i^\alpha = 1 - \frac{x_\alpha}{h_e}, \quad N_j^\alpha = \frac{x_\alpha}{h_e} \tag{4.10}$$

where $x_\alpha = \alpha h_a - x_i$, and h_e denotes the length of the finite elements.

Assume a linear design velocity field for simplicity; i.e., material point (in this case, nodes) moves linearly according to length change δl. The linear design velocity field can be written as

$$V(x) = \frac{x}{l}\delta l \tag{4.11}$$

Hence, as shown in Fig. 4.4b, nodes i and j move to their respective new locations at the perturbed design, as

$$x_i(\delta l) = x_i + V_i = x_i + \frac{x_i}{l}\delta l = x_i\left(1 + \frac{\delta l}{l}\right) \ ; \ \ x_j(\delta l) = x_j\left(1 + \frac{\delta l}{l}\right) \tag{4.12}$$

where, for example, $x_i(\delta l)$ represents the location of node i at the new design with length change δl. Therefore, the element length of the perturbed design becomes $h_e(\delta l) = h_e\,(1+ \delta l/l)$. Since the atomic space h_a is unchanged, the local location of atom α in the same element after design change is

$$x_\alpha(\delta l) = \alpha h_a - x_i\left(1 + \frac{\delta l}{l}\right) \tag{4.13}$$

The derivative of the coarse scale solution at atom α can be obtained as

$$\frac{du_\alpha}{dl} = \frac{\partial N_i^\alpha}{\partial l} d_i + N_i^\alpha \frac{dd_i}{dl} + \frac{\partial N_j^\alpha}{\partial l} d_j + N_j \frac{dd_j^\alpha}{dl} \tag{4.14}$$

where

$$\frac{\partial N_i^\alpha}{\partial l} = \frac{\alpha h_a}{h_e l}, \quad \frac{\partial N_j^\alpha}{\partial l} = -\frac{\alpha h_a}{h_e l} \tag{4.15}$$

Note that Eqs. 4.14 and 4.15 are true only if atom α stays inside the same element before and after the design change; i.e.,

$$x_i \le \alpha h_a \le x_j \quad \text{and} \quad x_i\left(1+\frac{\delta l}{l}\right) \le \alpha h \le x_j\left(1+\frac{\delta l}{l}\right) \tag{4.16}$$

However, it is apparent that any atom that is added or deleted as well as those fall outside their corresponding elements after the design change do not satisfy the requirements of Eq. 4.16. Therefore, the derivative of the coarse solutions of these atoms with respect to the length change does not exist, let alone the fine solutions that are discrete in nature.

In order to overcome this problem, in our numerical example, we define the design velocity field in a way such that the shape of the MD region does not change with design. This is perfectly fine since the domain design velocity can be arbitrarily chosen as long as the velocity field satisfies the continuity and regularity requirements [48]. Moreover, in most multi-scale simulations, the MD region is generally much smaller compared to the entire structural domain; therefore, for 2-D and 3-D multi-scale structures as illustrated in Fig. 3.11, as long as the MD boundary does not overlap with the design boundary, assuming the shape of the MD region is unchanged will not result in any restriction on the modeling of the design problem.

4.5 Continuum Shape Sensitivity Analysis for Bridging Scale Method

In this section, we derive shape sensitivity expressions for the bridging scale method following the continuum-discrete method introduced in Section 2.3.3. Due to the fact that the direct differentiation method is in general more efficient for dynamic problems than the adjoint variable method, in this thesis the former will be employed in sensitivity calculation.

Noting that the displacement solutions ($\mathbf{q}$, $\mathbf{u}$ and $\boldsymbol{u}$) of the variational equations (Eq. 4.7) can be assumed as continuously differentiable functions in design space as in [33], we start by taking material derivative of Eqs. 4.7a and 4.7b, giving

$$\int_0^{t_T} \bar{\mathbf{q}}^T \mathbf{M}_A \dot{\mathbf{q}}_{,tt}\, dt = \int_0^{t_T} \bar{\mathbf{q}}^T \left[\mathbf{f}_{,\mathbf{q}^T}(\mathbf{q},\mathbf{u})\dot{\mathbf{q}} + \mathbf{f}_{,\mathbf{u}^T}(\mathbf{q},\mathbf{u})\dot{\mathbf{u}} + \mathbf{F}^{imp}_{,\mathbf{q}^T}(\mathbf{q},\mathbf{u})\dot{\mathbf{q}} + \mathbf{F}^{imp}_{,\mathbf{u}^T}(\mathbf{q},\mathbf{u})\dot{\mathbf{u}} \right] dt \tag{4.17a}$$

and

$$\begin{aligned} &\int_0^{t_T} \left[\iiint_\Omega \rho \bar{\boldsymbol{u}}^T \dot{\boldsymbol{u}}_{,tt} d\Omega + \iiint_\Omega \rho \bar{\boldsymbol{u}}^T \boldsymbol{u}_{,tt} div \boldsymbol{V} d\Omega \right] dt \\ &= \int_0^{t_T} \Big\{ \bar{\mathbf{u}}^T \mathbf{f}_{,\mathbf{q}^T}(\mathbf{z})\dot{\mathbf{q}} + \bar{\mathbf{u}}^T \mathbf{f}_{,\mathbf{u}^T}(\mathbf{z})\dot{\mathbf{u}} - \iiint_{\Omega_2} \Big[\left(\bar{\boldsymbol{\varepsilon}}^T(\bar{\boldsymbol{u}})\boldsymbol{\sigma}(\boldsymbol{u}) \right)' \\ &+ \nabla \left(\bar{\boldsymbol{\varepsilon}}^T(\bar{\boldsymbol{u}})\boldsymbol{\sigma}(\boldsymbol{u}) \right)^T \boldsymbol{V} + \bar{\boldsymbol{\varepsilon}}^T(\bar{\boldsymbol{u}})\boldsymbol{\sigma}(\boldsymbol{u}) div \boldsymbol{V} \Big] d\Omega_2 \Big\} dt \end{aligned} \tag{4.17b}$$

Note that an evenly distributed mass density is assumed as mentioned in Eq. 3.17, and thus the function $\rho(\mathbf{x})$ in Eq. 4.7b is replaced by a constant ρ in Eq. 4.17b.

According to Eq. 2.35, the first term in the domain integral on the right hand side of Eq. 4.17b can be evaluated as

$$\begin{aligned} \left(\bar{\boldsymbol{\varepsilon}}^T(\bar{\boldsymbol{u}})\boldsymbol{\sigma}(\boldsymbol{u}) \right)' &= \bar{\boldsymbol{\varepsilon}}^T(\bar{\boldsymbol{u}}')\boldsymbol{\sigma}(\boldsymbol{u}) + \bar{\boldsymbol{\varepsilon}}^T(\bar{\boldsymbol{u}})\boldsymbol{\sigma}(\boldsymbol{u}') \\ &= \bar{\boldsymbol{\varepsilon}}^T\left(\dot{\bar{\boldsymbol{u}}} - \nabla \bar{\boldsymbol{u}}^T \boldsymbol{V} \right)\boldsymbol{\sigma}(\boldsymbol{u}) + \bar{\boldsymbol{\varepsilon}}^T(\bar{\boldsymbol{u}})\boldsymbol{\sigma}\left(\dot{\boldsymbol{u}} - \nabla \boldsymbol{u}^T \boldsymbol{V} \right) \\ &= -\bar{\boldsymbol{\varepsilon}}^T\left(\nabla \bar{\boldsymbol{u}}^T \boldsymbol{V} \right)\boldsymbol{\sigma}(\boldsymbol{u}) + \bar{\boldsymbol{\varepsilon}}^T(\bar{\boldsymbol{u}})\boldsymbol{\sigma}(\dot{\boldsymbol{u}}) - \bar{\boldsymbol{\varepsilon}}^T(\bar{\boldsymbol{u}})\boldsymbol{\sigma}\left(\nabla \boldsymbol{u}^T \boldsymbol{V} \right) \end{aligned} \tag{4.18}$$

Note that $\dot{\bar{\boldsymbol{u}}} = 0$ is assumed when deriving Eq. 4.18, which implies that the coarse scale virtual displacement will not change with design.

Substituting Eq. 4.18 into Eq. 4.17b gives

$$\begin{aligned} &\int_0^{t_T} \left[\iiint_\Omega \rho \bar{\boldsymbol{u}}^T \dot{\boldsymbol{u}}_{,tt} d\Omega + \iiint_\Omega \rho \bar{\boldsymbol{u}}^T \boldsymbol{u}_{,tt} div \boldsymbol{V} d\Omega \right] dt = \int_0^{t_T} \Big\{ \bar{\mathbf{u}}^T \mathbf{f}_{,\mathbf{q}^T}(\mathbf{z})\dot{\mathbf{q}} + \bar{\mathbf{u}}^T \mathbf{f}_{,\mathbf{u}^T}(\mathbf{z})\dot{\mathbf{u}} \\ &- \iiint_{\Omega_2} \Big[-\bar{\boldsymbol{\varepsilon}}^T\left(\nabla \bar{\boldsymbol{u}}^T \boldsymbol{V} \right)\boldsymbol{\sigma}(\boldsymbol{u}) + \bar{\boldsymbol{\varepsilon}}^T(\bar{\boldsymbol{u}})\boldsymbol{\sigma}(\dot{\boldsymbol{u}}) - \bar{\boldsymbol{\varepsilon}}^T(\bar{\boldsymbol{u}})\boldsymbol{\sigma}\left(\nabla \bar{\boldsymbol{u}}^T \boldsymbol{V} \right) \\ &+ \nabla \left(\bar{\boldsymbol{\varepsilon}}^T(\bar{\boldsymbol{u}})\boldsymbol{\sigma}(\boldsymbol{u}) \right)^T \boldsymbol{V} + \bar{\boldsymbol{\varepsilon}}^T(\bar{\boldsymbol{u}})\boldsymbol{\sigma}(\boldsymbol{u}) div \boldsymbol{V} \Big] d\Omega_2 \Big\} dt \end{aligned} \tag{4.19}$$

To solve for the material derivatives of atomic displacements, velocities and accelerations, rearrange Eq. 4.17a as

$$\int_0^{t_T} \bar{\mathbf{q}}^T \left[\mathbf{M}_A \dot{\mathbf{q}}_{,tt} - \mathbf{f}_{,\mathbf{q}^T}(\mathbf{q},\mathbf{u})\dot{\mathbf{q}} - \mathbf{f}_{,\mathbf{u}^T}(\mathbf{q},\mathbf{u})\dot{\mathbf{u}} - \mathbf{F}^{imp}_{,\mathbf{q}^T}(\mathbf{q},\mathbf{u})\dot{\mathbf{q}} - \mathbf{F}^{imp}_{,\mathbf{u}^T}(\mathbf{q},\mathbf{u})\dot{\mathbf{u}}\right] dt = 0 \quad (4.20)$$

Since the virtual displacement $\bar{\mathbf{q}}$ is arbitrary, the sensitivity differential equation for the MD simulation can be obtained as

$$\mathbf{M}_A \dot{\mathbf{q}}_{,tt} = \mathbf{f}_{,\mathbf{q}^T}(\mathbf{q},\mathbf{u})\dot{\mathbf{q}} + \mathbf{f}_{,\mathbf{u}^T}(\mathbf{q},\mathbf{u})\dot{\mathbf{u}} + \mathbf{F}^{imp}_{,\mathbf{q}^T}(\mathbf{q},\mathbf{u})\dot{\mathbf{q}} + \mathbf{F}^{imp}_{,\mathbf{u}^T}(\mathbf{q},\mathbf{u})\dot{\mathbf{u}} \quad (4.21)$$

As can be seen, the dynamic responses of atoms depend only implicitly on design. The material derivative terms in Eq. 4.21 are equivalent to partial derivatives with respect to shape design variables. This is because the shape of the MD region is assumed to remain untouched, and therefore the material point (atoms) within the MD region is not moving with shape design changes.

To solve for the material derivative of the coarse scale degrees of freedom, we create finite element mesh over the domain and discretizing Eq. 4.19 using FE shape functions, as

$$\int_0^{t_T} \left(\bar{\mathbf{d}}^T \mathbf{M} \dot{\mathbf{d}}_{,tt} + \bar{\mathbf{d}}^T \dot{\mathbf{M}} \mathbf{d}_{,tt}\right) dt = \int_0^{t_T} \bar{\mathbf{d}}^T \begin{bmatrix} \mathbf{N}^T\left(\mathbf{f}_{,\mathbf{q}^T}(\mathbf{z})\dot{\mathbf{q}} + \mathbf{f}_{,\mathbf{d}^T}(\mathbf{z})\dot{\mathbf{d}}\right) \\ \overset{\bullet}{\mathbf{F}}^{CB} \end{bmatrix} dt \quad (4.22)$$

where

$$\iiint_\Omega \rho \bar{\boldsymbol{u}}^T \boldsymbol{u}_{,tt} div\boldsymbol{V} d\Omega \overset{discretize}{=} \bar{\mathbf{d}}^T \dot{\mathbf{M}} \mathbf{d}_{,tt} \quad (4.23)$$

In Eq. 4.22, **M** stands for the consistent finite element mass matrix (Eq. 3.17), and $\overset{\bullet}{\mathbf{F}}^{CB}$ represents the material derivative of the coarse scale nodal forces obtained by discretizing the integral over the domain Ω_2 on the right hand side of Eq. 4.19 using finite element shape functions. Details regarding the derivation of Eqs. 4.22 and 4.23 are given in appendices. Specifically, the discretization of coarse scale in *Region 2* is explained in detail in Appendix E, while the material derivative of coarse scale (such as the calculation of $\overset{\bullet}{\mathbf{F}}^{CB}$) can be found in Appendix G.

Similarly, the coarse scale sensitivity equation can be obtained by considering the arbitrariness of $\overline{\mathbf{d}}$; that is

$$\mathbf{M}\dot{\mathbf{d}}_{,tt} = \begin{bmatrix} \mathbf{N}^T\left(\mathbf{f}_{,\mathbf{q}^T}(\mathbf{z})\dot{\mathbf{q}} + \mathbf{f}_{,\mathbf{d}^T}(\mathbf{z})\dot{\mathbf{d}}\right) \\ \overset{\bullet}{\mathbf{F}}^{CB} \end{bmatrix} - \dot{\mathbf{M}}\mathbf{d}_{,tt} \tag{4.24}$$

Note that Eqs. 4.21 and 4.24 are the coupled dynamic shape sensitivity expressions for the MD and FE simulations, respectively.

4.6 Implementation Aspects for Sensitivity Analysis

In our numerical implementation, the coupled sensitivity equations derived above (Eqs. 4.21 and 4.24) are solved in parallel with structural analysis (Eqs. 3.31a, 3.31c, and 3.45) using the same time integration method introduced in Section 3.3.5. It is assumed that the initial displacements and velocities for all MD atoms and FE nodes will not change with design, which is physically meaningful. Hence, the initial conditions for the sensitivity equations can be defined as

$$\frac{d\mathbf{q}(0)}{d\mathbf{b}} = 0,\ \frac{d\mathbf{q}_{,t}(0)}{d\mathbf{b}} = 0,\ \frac{d\mathbf{d}(0)}{d\mathbf{b}} = 0,\ \frac{d\mathbf{d}_{,t}(0)}{d\mathbf{b}} = 0 \tag{4.25}$$

During each MD time step, the solution of bridging scale simulation, such as **q** and **d**, are obtained first and then substituted into the sensitivity expressions. Thus, the sensitivity equations can be solved in the same time step, and the results, such as $\dot{\mathbf{q}}$ and

$\dot{\mathbf{d}}$, will be employed as initial conditions to solve the sensitivity equations in the next time step. Note that the direct solutions of the sensitivity expressions (e.g., $\dot{\mathbf{q}}$ and $\dot{\mathbf{d}}$) at each time step are the sensitivity coefficients of structural responses.

The calculated sensitivity coefficients describe quantitatively the rate of performance measure change with respect to the change of shape design variables, and therefore can be used to predict the behavior of the structure at a perturbed design during design process. Consider a general performance measure ψ as an example. The solid curve shown in Fig. 4.5a depicts the change of the performance measure with respect to the *i*th design variable b_i, which is unknown in practice. In structural design, we first calculate the sensitivity coefficient $d\psi/db_i$, which is the slope of the curve at the current design $\mathbf{b}^0$, and then use the 1st-order prediction

$$\bar{\psi}\left(\mathbf{b}^0+\delta b_i\right)=\psi\left(\mathbf{b}^0\right)+\frac{d\psi}{db_i}\delta b_i \tag{4.26}$$

to estimate $\psi(\mathbf{b}^0+\delta b_i)$, which is the actual value of the performance measure at the perturbed design $\mathbf{b}^0+\delta b_i$.

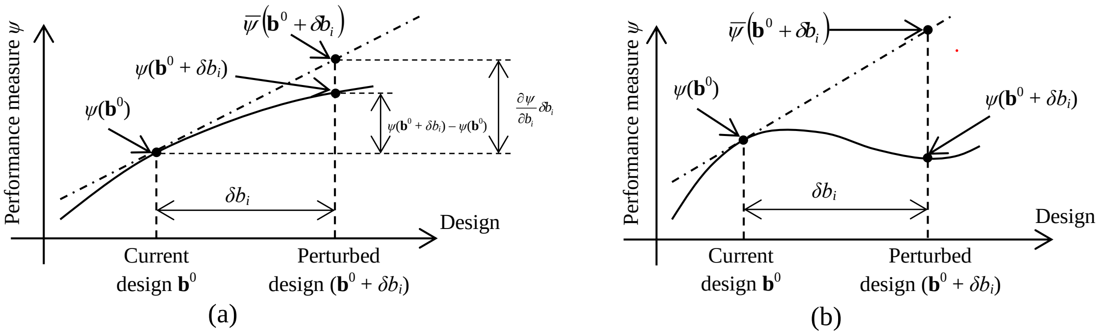

(a) (b)

Figure 4.5 (a) Behavior of performance measure ψ in design space. (b) A performance measure ψ that shows high nonlinearity

In our numerical example, to verify the accuracy of the proposed sensitivity analysis approach, we compare the sensitivity coefficients with overall finite difference result. The accuracy of the 1st-order prediction of performance measure ψ can be quantified using an accuracy index defined as

$$Accuracy\,index = \frac{\overline{\psi}\left(\mathbf{b}^0 + \delta b_i\right) - \psi\left(\mathbf{b}^0\right)}{\psi\left(\mathbf{b}^0 + \delta b_i\right) - \psi\left(\mathbf{b}^0\right)} = \frac{\dfrac{d\psi}{db_i}\delta b_i}{\psi\left(\mathbf{b}^0 + \delta b_i\right) - \psi\left(\mathbf{b}^0\right)} \tag{4.27}$$

where $\psi(\mathbf{b}^0 + \delta b_i)$ can be obtained through re-analysis, i.e., rerunning the simulation at $\mathbf{b} = \mathbf{b}^0 + \delta b_i$. If the accuracy index is close to 100%, or, more rigorously, if the accuracy index converges to 100% as δb_i approaches zero, then the sensitivity coefficient $d\psi/db_i$ is considered to be correct.

As can be seen from Fig. 4.5, the accuracy of the 1st-order prediction depends on not only the accuracy of the calculated sensitivity coefficient, but also the nonlinearity of the performance measure in design space. Therefore, we often use a very small design perturbation δb_i for accuracy verification (Eq. 4.27) in order to avoid the nonlinear effect. On the other hand, during design process, a large perturbation size (or step size) is preferred. However, if, near the current design, the performance measure exhibits high nonlinearity in design space, as shown in Fig. 4.5b, then the perturbation size must be kept very small to ensure an accurate 1st-order prediction; in other words, only very small step sizes can be used in design process.

4.7 Numerical Example: Part 2

In this section, we verify the accuracy of the proposed analytical shape sensitivity analysis method using the nano-beam example introduced in Chapter 3.

4.7.1 Design Parameterization

For the purpose of sensitivity analysis, we model the geometric shape of the curved boundary faces above the MD region on both sides of the nano-beam using parametric Bezier curves with three control points. As illustrated in Fig. 4.6a, the shape of the left boundary face, for example, can be morphed by adjusting the locations of control points P1, P2 and P3. In our study, we define three shape design variables b_1, b_2, and b_3 that correspond respectively to $P2_y$ (y direction coordinate of point P2), $P3_y$ and $P3_x$. At the current design, the locations of the three control points are $(0, 66\sqrt{2}\,h_a)$, $(0, 102\sqrt{2}\,h_a)$ and $(13.6h_a, 138h_a)$ for P1, P2 and P3, respectively. The shape of the right boundary face will vary accordingly during a design change to maintain the symmetry of the beam. The design velocity fields associated with individual design variables are illustrated in Fig. 4.6b. Note that shape changes only take place in the FE-only region, whereas the shape of the MD region will remain untouched as discussed earlier in Section 4.4.

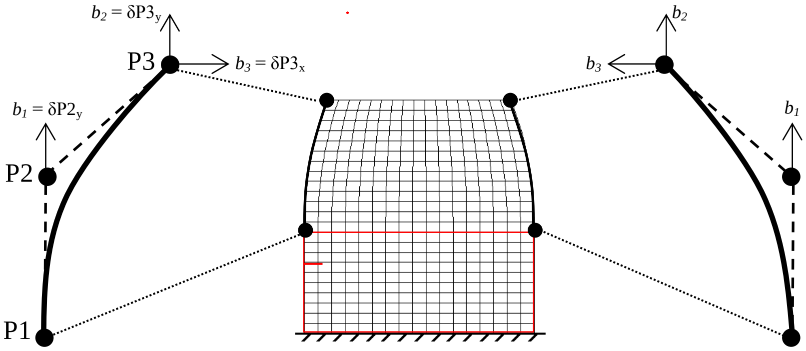

(a)

Figure 4.6 Design parameterization for the nano-beam. (a) Parametric boundary curve, and (b) design velocity fields for individual design variables

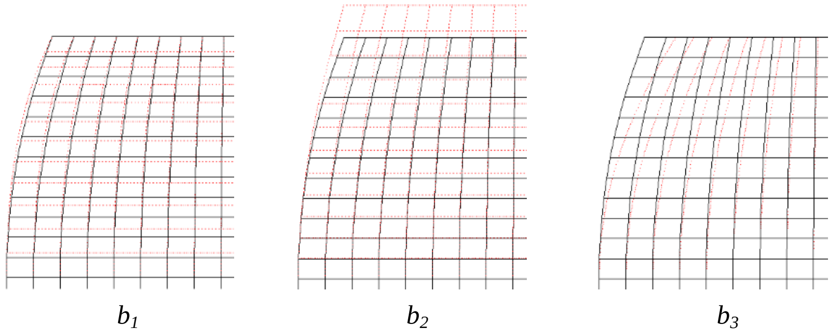

(b)

Figure 4.6 Design parameterization for the nano-beam. (a) Parametric boundary curve, and (b) design velocity fields for individual design variables (cont'd)

4.7.2 Sensitivity Accuracy Verification

We carried out analytical shape sensitivity analysis for the nano-beam example. For bridging scale problems, the simplest analytical performance measures are the responses of the structure, including the displacements, velocities and accelerations of all atoms and FE nodes. For accuracy verification, we arbitrarily pick one atom ($\mathbf{X}_A$ in Fig. 4.7) and one FE node ($\mathbf{X}_N$) from the MD and FE-only regions, respectively, and then examine their accuracy indices (Eq. 4.27) by comparing the sensitivity coefficients with overall finite difference results.

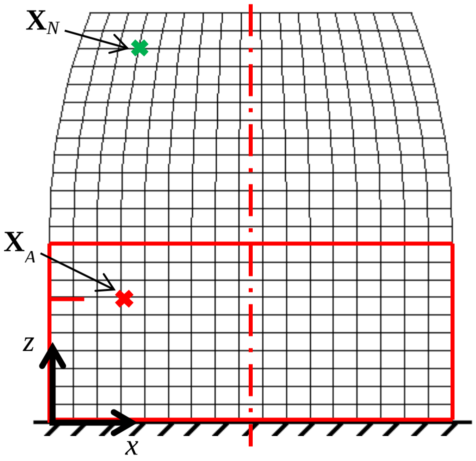

Figure 4.7 Atom $\mathbf{X}_A$ and node $\mathbf{X}_N$ chosen for sensitivity accuracy verification

An accuracy index convergence study is first carried out as shown in Fig. 4.8, in which the accuracy indices of the *z* direction displacement sensitivity coefficients for atom $\mathbf{X}_\mathrm{A}$ with respect to b_2 are plotted versus simulation time for different design perturbations (δb_i in Eq. 4.27) ranging from $\delta b_2 = 0.0001$ to $\delta b_2 = 0.1$, where $\delta b_2 = 0.1$ corresponds to an 0.05% increment of beam length. Note that *z* direction sensitivity coefficients are chosen due to the fact that the deformation of the beam is mainly along the *z* direction. As can be seen from Fig. 4.8, for all time steps plotted, the accuracy index converges to 100% as the perturbation size approaches zero, which implies that the proposed analytical sensitivity analysis method is accurate.

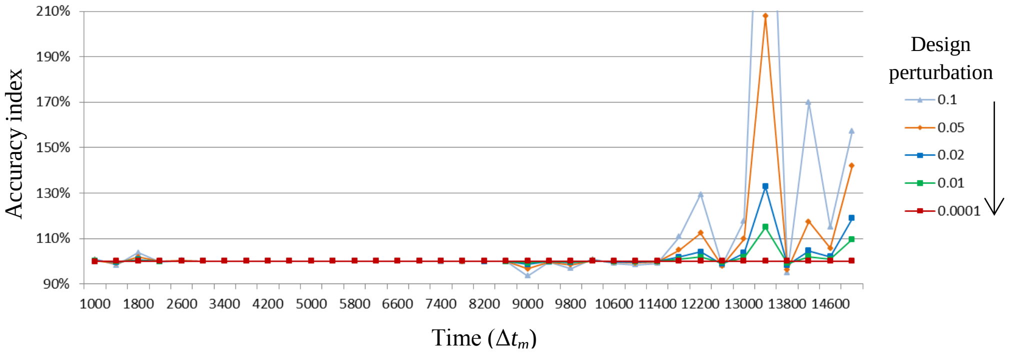

Figure 4.8 Accuracy index convergence study for atom $\mathbf{X}_\mathrm{A}$. Accuracy indices for *z* displacement sensitivity with respect to b_2 plotted

Then we take a closer look at the accuracy of the sensitivity coefficients by listing in Tables 4.1 ~ 4.3 the *z* direction sensitivity coefficients of atom $\mathbf{X}_\mathrm{A}$ with respect to all three design variables. The perturbation size for overall finite difference used in Tables 4.1 ~ 4.3 is $\delta b_i = 0.0001$ – the smallest one plotted in Fig. 4.8. In each table, Column A lists the selected FE time steps. Columns B to D show the structural responses at current design ($\psi(\mathbf{b}^0)$), including displacement $\mathbf{q}$, velocity $\mathbf{v}_{MD}$ and acceleration $\mathbf{a}_{MD}$, at each chosen time step. Columns E to G list the same information at the perturbed design ($\psi(\mathbf{b}^0 + \delta b_i)$) obtained through re-analysis. Columns H to J show differences of the structural responses due to the design change, obtained using overall finite difference (denominator in Eq. 4.27); i.e., Column H = Column E – Column B, etc. The analytically calculated sensitivity coefficients ($d\psi/db_i$) are listed in Columns K to M, and are then compared with the overall finite difference results in Columns H to J, after multiplied by the design perturbation δb_i. The accuracy comparison results (accuracy index) are shown in Columns N to P. As we can see, the sensitivity coefficients are very accurate compared to overall finite difference results. Also, the sensitivity coefficients with respect to design variable b_1 (Columns K to M in Table 4.1) are in general much smaller than those with respect to b_2 and b_3, which means the response of the structure is less sensitive to b_1 than to b_2 and b_3. The sensitivity accuracy verification for node $\mathbf{X}_\mathrm{N}$ with respect to design variable b_2 is given in Table 4.4. In fact, many other atoms and nodes have been tested, and it is found that the sensitivity results for all atoms and FE nodes with respect to all three design variables are generally of the same level of accuracy.

Table 4.1 Accuracy verification of z direction sensitivity coefficients with respect to b_1 for atom $\mathbf{X}_\mathrm{A}$

A	B	C	D	E	F	G	H	I	J	K	L	M	N	O	P
Time Step (Δt_m)	Current Design			Perturbed Design			Overall Finite Difference			Sensitivity Prediction			Accuracy Index		
	$q(\mathbf{b}^0)$	$v_{MD}(\mathbf{b}^0)$	$a_{MD}(\mathbf{b}^0)$	$q(\mathbf{b}^0+\delta b_1)$	$v_{MD}(\mathbf{b}^0+\delta b_1)$	$a_{MD}(\mathbf{b}^0+\delta b_1)$	Δq	Δv_{MD}	Δa_{MD}	DSA q	DSA v_{MD}	DSA a_{MD}	% q	% v_{MD}	% a_{MD}
3,000	3.32E-02	1.54E-02	3.14E-03	3.32E-02	1.54E-02	3.14E-03	-2.99E-09	5.47E-10	-3.86E-10	-2.99E-05	5.47E-06	-3.86E-06	100.000%	100.001%	100.035%
5,000	7.55E-01	7.78E-02	2.25E-03	7.55E-01	7.78E-02	2.25E-03	1.38E-08	2.29E-09	2.92E-10	1.38E-04	2.29E-05	2.92E-06	100.000%	100.001%	100.094%
7,000	1.98E+00	8.19E-02	3.97E-04	1.98E+00	8.19E-02	3.97E-04	4.04E-08	4.54E-10	6.01E-10	4.04E-04	4.54E-06	6.01E-06	100.000%	100.023%	100.044%
9,000	2.81E+00	-5.92E-03	-7.61E-04	2.81E+00	-5.92E-03	-7.61E-04	6.96E-08	2.85E-08	2.61E-09	6.96E-04	2.85E-04	2.62E-05	100.000%	100.001%	100.240%
11,000	2.13E-01	-1.38E-01	5.11E-01	2.13E-01	-1.38E-01	5.11E-01	-3.08E-07	1.64E-06	7.19E-06	-3.08E-03	1.64E-02	7.19E-02	100.001%	100.000%	100.015%
13,000	2.77E-02	1.33E-01	3.05E-01	2.77E-02	1.33E-01	3.05E-01	2.79E-07	1.66E-06	-3.08E-05	2.79E-03	1.66E-02	-3.08E-01	99.999%	100.000%	100.000%
15,000	1.35E-01	1.12E-01	-5.49E-01	1.35E-01	1.12E-01	-5.49E-01	1.83E-07	-3.46E-06	-6.86E-05	1.83E-03	-3.46E-02	-6.86E-01	100.006%	99.995%	100.004%

Table 4.2 Accuracy verification of z direction sensitivity coefficients with respect to b_2 for atom $\mathbf{X}_\mathrm{A}$

A	B	C	D	E	F	G	H	I	J	K	L	M	N	O	P
Time Step	Current Design			Perturbed Design			Overall Finite Difference			Sensitivity Prediction			Accuracy Index		
(Δt_m)	$q(\mathbf{b}^0)$	$v_{MD}(\mathbf{b}^0)$	$a_{MD}(\mathbf{b}^0)$	$q(\mathbf{b}^0+\delta b_2)$	$v_{MD}(\mathbf{b}^0+\delta b_2)$	$a_{MD}(\mathbf{b}^0+\delta b_2)$	Δq	Δv_{MD}	Δa_{MD}	DSA q	DSA v_{MD}	DSA a_{MD}	% q	% v_{MD}	% a_{MD}
3,000	3.32E-02	1.54E-02	3.14E-03	3.32E-02	1.54E-02	3.14E-03	-1.81E-07	-3.83E-08	4.30E-09	-1.81E-03	-3.83E-04	4.30E-05	100.000%	100.000%	99.997%
5,000	7.55E-01	7.78E-02	2.25E-03	7.55E-01	7.78E-02	2.25E-03	-1.00E-06	-3.76E-08	-7.89E-11	-1.00E-02	-3.76E-04	-7.86E-07	100.000%	100.000%	99.619%
7,000	1.98E+00	8.19E-02	3.97E-04	1.98E+00	8.19E-02	3.97E-04	-1.19E-06	-7.50E-09	9.95E-09	-1.19E-02	-7.50E-05	9.95E-05	100.000%	99.999%	99.993%
9,000	2.81E+00	-5.92E-03	-7.61E-04	2.81E+00	-5.92E-03	-7.61E-04	-1.05E-08	5.41E-08	-6.82E-07	-1.05E-04	5.41E-04	-6.82E-03	99.993%	99.992%	99.982%
11,000	2.13E-01	-1.38E-01	5.11E-01	2.13E-01	-1.38E-01	5.11E-01	1.44E-06	-4.54E-06	-2.87E-05	1.44E-02	-4.54E-02	-2.87E-01	99.998%	100.002%	99.973%
13,000	2.77E-02	1.33E-01	3.05E-01	2.77E-02	1.33E-01	3.05E-01	-1.26E-06	-2.16E-06	2.27E-04	-1.26E-02	-2.16E-02	2.27E+00	100.017%	100.034%	100.007%
15,000	1.35E-01	1.12E-01	-5.49E-01	1.35E-01	1.12E-01	-5.49E-01	2.21E-07	-2.63E-07	1.14E-04	2.21E-03	-2.61E-03	1.14E+00	100.096%	99.370%	99.926%

Table 4.3 Accuracy verification of z direction sensitivity coefficients with respect to b_3 for atom $\mathbf{X}_\mathrm{A}$

A	B	C	D	E	F	G	H	I	J	K	L	M	N	O	P
Time Step	Current Design			Perturbed Design			Overall Finite Difference			Sensitivity Prediction			Accuracy Index		
(Δt_m)	$q(\mathbf{b}^0)$	$v_{MD}(\mathbf{b}^0)$	$a_{MD}(\mathbf{b}^0)$	$q(\mathbf{b}^0+\delta b_3)$	$v_{MD}(\mathbf{b}^0+\delta b_3)$	$a_{MD}(\mathbf{b}^0+\delta b_3)$	Δq	Δv_{MD}	Δa_{MD}	DSA q	DSA v_{MD}	DSA a_{MD}	% q	% v_{MD}	% a_{MD}
3,000	3.32E-02	1.54E-02	3.14E-03	3.32E-02	1.54E-02	3.14E-03	-2.30E-08	-8.97E-09	-2.15E-09	-2.30E-04	-8.97E-05	-2.15E-05	100.000%	100.000%	100.003%
5,000	7.55E-01	7.78E-02	2.25E-03	7.55E-01	7.78E-02	2.25E-03	-4.64E-07	-3.72E-08	1.47E-09	-4.64E-03	-3.72E-04	1.47E-05	100.000%	100.000%	100.010%
7,000	1.98E+00	8.19E-02	3.97E-04	1.98E+00	8.19E-02	3.97E-04	-7.98E-07	-1.45E-08	4.28E-10	-7.98E-03	-1.45E-04	4.27E-06	100.000%	100.000%	99.936%
9,000	2.81E+00	-5.92E-03	-7.61E-04	2.81E+00	-5.92E-03	-7.61E-04	-5.54E-07	-1.35E-07	-2.48E-07	-5.54E-03	-1.35E-03	-2.48E-03	100.000%	99.996%	99.829%
11,000	2.13E-01	-1.38E-01	5.11E-01	2.13E-01	-1.38E-01	5.11E-01	2.30E-06	-1.09E-05	-4.94E-05	2.30E-02	-1.09E-01	-4.94E-01	99.994%	100.002%	99.902%
13,000	2.77E-02	1.33E-01	3.05E-01	2.76E-02	1.33E-01	3.05E-01	-1.88E-06	-1.15E-05	2.32E-04	-1.88E-02	-1.14E-01	2.32E+00	100.007%	99.992%	99.996%
15,000	1.35E-01	1.12E-01	-5.49E-01	1.35E-01	1.12E-01	-5.49E-01	-8.54E-07	2.20E-05	4.26E-04	-8.54E-03	2.20E-01	4.26E+00	99.947%	100.035%	99.976%

Table 4.4 Accuracy verification of z direction sensitivity coefficients with respect to b_2 for node $\mathbf{X}_\mathrm{N}$

A	B	C	D	E	F	G	H	I	J	K	L	M	N	O	P
Time Step	Current Design			Perturbed Design			Overall Finite Difference			Sensitivity Prediction			Accuracy Index		
(Δt_m)	$d(\mathbf{b}^0)$	$v_{FE}(\mathbf{b}^0)$	$a_{FE}(\mathbf{b}^0)$	$d(\mathbf{b}^0+\delta b_2)$	$v_{FE}(\mathbf{b}^0+\delta b_2)$	$a_{FE}(\mathbf{b}^0+\delta b_2)$	Δd	Δv_{FE}	Δa_{FE}	DSA d	DSA v_{FE}	DSA a_{FE}	% d	% v_{FE}	% a_{FE}
3,000	1.13E+00	1.12E-01	5.54E-03	1.13E+00	1.12E-01	5.54E-03	-4.46E-07	-2.27E-08	7.66E-10	-4.46E-03	-2.27E-04	7.66E-06	100.000%	100.000%	100.005%
5,000	3.44E+00	1.96E-01	4.87E-03	3.44E+00	1.96E-01	4.87E-03	-8.32E-07	-2.69E-08	1.46E-08	-8.32E-03	-2.69E-04	1.46E-04	100.000%	100.000%	99.998%
7,000	6.05E+00	1.25E-01	-6.78E-03	6.05E+00	1.25E-01	-6.78E-03	-4.15E-07	2.74E-08	9.86E-09	-4.15E-03	2.74E-04	9.86E-05	100.000%	100.001%	100.002%
9,000	7.19E+00	2.67E-02	-4.84E-03	7.19E+00	2.67E-02	-4.84E-03	-1.54E-07	-2.49E-08	-2.31E-08	-1.54E-03	-2.49E-04	-2.31E-04	100.001%	100.000%	99.985%
11,000	7.32E+00	1.04E-02	2.27E-03	7.32E+00	1.04E-02	2.27E-03	-6.59E-07	-8.17E-08	5.32E-08	-6.59E-03	-8.17E-04	5.32E-04	100.000%	99.999%	100.002%
13,000	7.59E+00	2.23E-02	9.30E-03	7.59E+00	2.23E-02	9.30E-03	-1.33E-06	-2.16E-07	-3.89E-07	-1.33E-02	-2.16E-03	-3.89E-03	100.000%	100.004%	100.002%
15,000	8.23E+00	5.73E-02	-4.13E-03	8.23E+00	5.73E-02	-4.13E-03	-1.81E-06	1.03E-07	2.94E-07	-1.81E-02	1.03E-03	2.94E-03	100.001%	99.959%	99.937%

Note that Fig. 4.8 can also be considered as a design perturbation study, which shows how accurate the 1st-order predictions of atomic displacements are, compared to the actual displacements at perturbed designs. As can be seen, the 1st-order predictions are in general less accurate in predicting the responses of atoms at large design perturbations. For example, as shown in Fig. 4.8, when a design perturbation $\delta b_2 = 0.05$ is applied, at some time steps, the error of 1st-order prediction can be as large as 110% (accuracy index is about 210%). Also can be observed from Fig. 4.8 is that the accuracy of the 1st-order predictions starts to deteriorate when crack propagation initiates at around $t = 7{,}000\Delta t_m$.

To explain this deterioration of accuracy, in Fig. 4.9a we zoom in the z displacement history curve of atom $\mathbf{X}_\mathrm{A}$, and then, in the z displacement-time-design space, we plot the z displacements at $\mathbf{X}_\mathrm{A}$ from $t = 11{,}640\Delta t_m$ to $t = 11{,}680\Delta t_m$ at several perturbed designs up to $\delta b_2 = 1$. It is illustrated clearly in Fig. 4.9a how the z displacement of atom $\mathbf{X}_\mathrm{A}$ changes with both time and design, while Fig. 4.9b and 4.9c show respectively the z displacement history at perturbed design $\delta b_2 = 0.5$ and the change of z displacement with design at $t = 11{,}660\Delta t_m$.

By looking at the 3-D surface in Fig. 4.9a along the design direction, the zoomed-in z displacement history curves of atom $\mathbf{X}_\mathrm{A}$ at different perturbed designs are plotted in Fig. 4.10a. It is apparent in Fig. 4.10a that the displacement curve is further and further delayed in time space as the perturbation size grows, resulting in staggered crests of individual curves. In Figs. 4.10b and 4.10c, we compare the 1st-order predictions of z displacements (red dashed line) with the z displacements at perturbed designs obtained through re-analysis (blue dashed line with markers) at two different time steps. As we can see, at $t = 11{,}668\Delta t_m$, when the slopes of individual displacement curves in Fig. 4.10a are relatively uniform, the 1st-order predictions are generally in agreement with the displacements from re-analysis even at large perturbations (Fig. 4.10b). However, at $t = 11{,}653\Delta t_m$, when the slopes of the displacement curves are close to zero, the accuracy of the 1st-order prediction deteriorates quickly as the perturbation size increases (Fig. 4.10c). This is because in dynamic problems, analytical performances such as atomic displacements are measured at individual time steps, and each analytical sensitivity coefficient only predicts the change of performance measure at a fixed time step. For example, the sensitivity coefficient of the *z* displacement of atom $\mathbf{X}_{\mathrm{A}}$ at $t = 100\Delta t_m$ predicts how the *z* displacement of $\mathbf{X}_{\mathrm{A}}$ at that exact time step changes with design. Therefore, if the performance measure history curve is delayed (or advanced) due to a design change, then at the time steps where the curve slope changes drastically (e.g., near the crest and trough of each microscopic oscillation), the performance measure will exhibit highly nonlinear behavior in design space (blue curve in Fig. 4.10c), and hence the 1st-order prediction will lose accuracy at relatively large design perturbations.

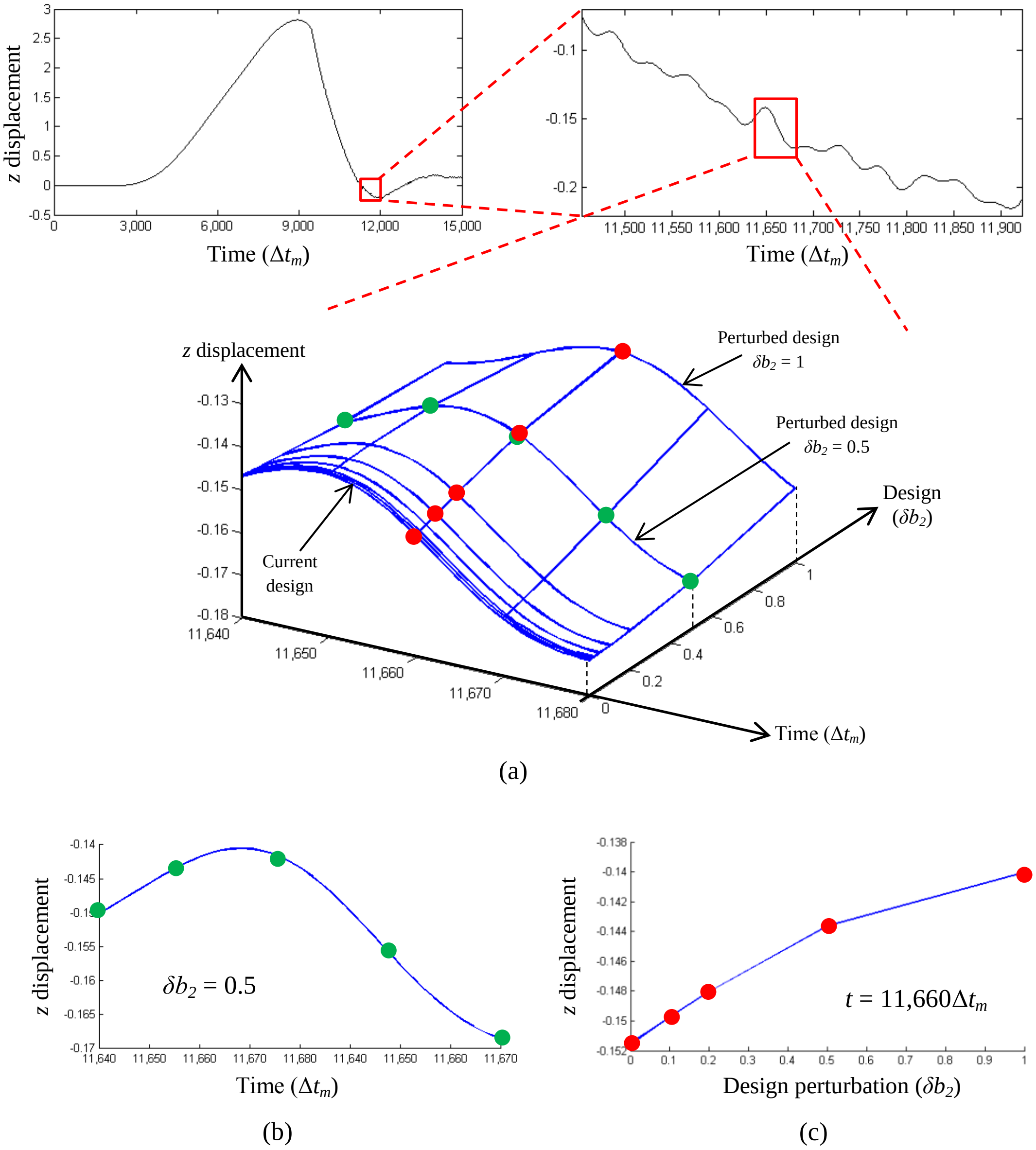

Figure 4.9 z displacement at $\mathbf{X}_A$ in time and design spaces. (a) z displacement surface in 3-D displacement-time-design space, (b) z displacement in time domain at perturbed design $\delta b_2 = 0.5$, and (c) z displacement in design domain at $t = 11{,}660\Delta t_m$

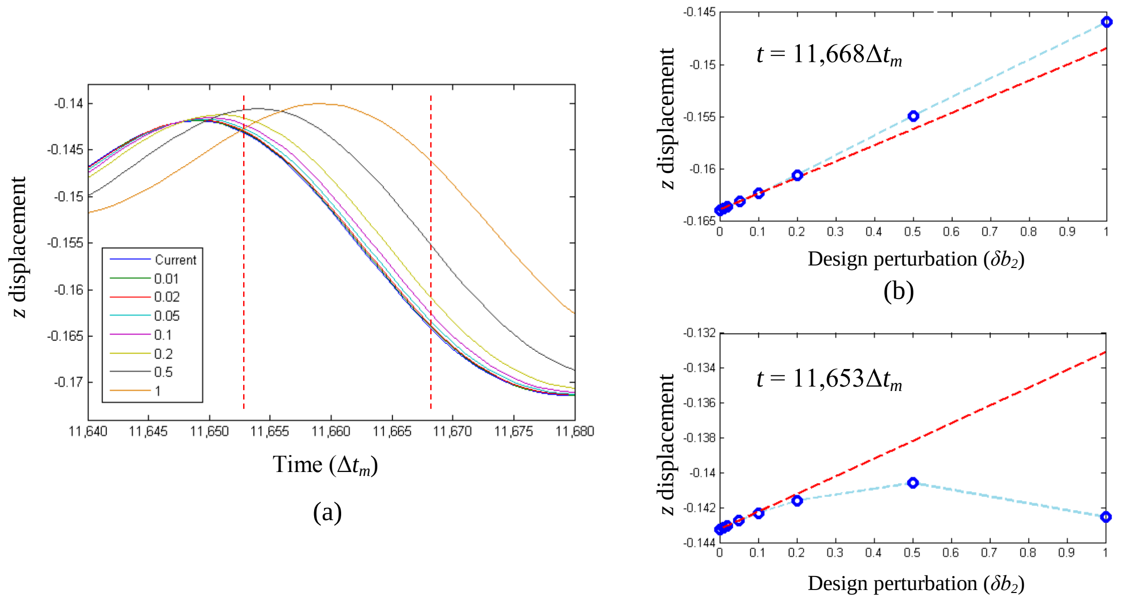

(a)

(b)

(c)

Figure 4.10 Nonlinearity of atomic displacement in design space. (a) *z* displacement history curves of atom $\mathbf{X}_A$ at different perturbed designs, (b) nonlinearity of *z* displacement at t = 11,668Δt_m, and (c) nonlinearity of *z* displacement at 11,653Δt_m

Therefore, it becomes clear that although the sensitivity coefficients of structure responses are accurately calculated, the accuracy of the 1st-order predictions can be affected by the nonlinearity of the performance measures (such as atomic displacements) in design space. As discussed above, the severe nonlinearity observed in Fig. 4.10c is resulted from two factors – high frequency oscillation of the performance measure history curve and delay of the performance measure in time space due to design change. One can readily infer that the less accurate predictions in Fig. 4.8 must be measured near the crests or troughs of the oscillating atomic displacement history curve. Moreover, since the initial temperature of the MD area was set to 0K in our simulation, atoms did not vibrate until microscopic waves were generated by bond breaking due to crack propagation. Consequently, the deterioration of accuracy in Fig. 4.8 is observed only after the initiation of crack growth.

In summary, it has been demonstrated with the nano-beam example that the accuracy indices of the sensitivity coefficients of structural responses converge to 100% as perturbation size approaches zero, indicating the accuracy of the proposed analytical shape sensitivity analysis approach. In the meantime, it is observed that atomic responses show severe nonlinearity in design space, and thus their sensitivity coefficients can only be used to predict very small design perturbations.

CHAPTER 5

PERFORMANCE MEASURE: CRACK PROPAGATION SPEED

5.1 Overview

The analytical sensitivity formulation derived in the previous chapter can be used to compute sensitivity coefficients of analytical performance measures in bridging scale problems, such as atomic and nodal displacements. In fact, most of the common performance measures in practical structural design problems (such as stress, strain, local temperature, etc.) are analytical, and can be expressed explicitly or implicitly in terms of the response of the structure; as a result, the design sensitivity of those performance measures can also be written as analytical functions of the sensitivity coefficients of structural responses. In addition, most performance measures for dynamic problems are usually defined either at a given time instant or as an average over a fixed time period. For example, in a multi-scale problem, we can define the performance measure to be the average stress from 0 sec to 5 sec at the location of a given atom in the domain.

To study how crack propagation will be affected by shape design changes, we must first establish the relation between crack propagation speed and the responses of atoms. Although crack propagation speed has always been a quantity of interest in atomistic simulations, defining a performance measure of crack speed based on atomic responses for sensitivity analysis and structural design can be challenging. This is because after a design change, the crack may propagate to the same location at a different time step, which means we can no longer define the performance measure based on the responses of a few fixed atoms at fixed time steps. Moreover, crack propagation speed inherently involves derivative of crack length increment with respect to time, while the length increment cannot be written explicitly in terms of atomic responses due to the crack tip identification procedure discusses in Section 3.5.

In this chapter, we first establish our sensitivity performance measure of crack propagation speed based on the *P* parameter criterion introduced in Chapter 3. The differentiability of the performance measure in design space will then be discussed from both theoretical and numerical perspectives. In addition, as has been demonstrated in Numerical Example Part 2 (Section 4.7), atomic responses in bridging scale simulations show high nonlinearity in design space; therefore, at the end of this chapter, we will use the same example problem to demonstrate and discuss the nonlinearity of the performance measure of crack propagation speed.

5.2 Performance Measure of Crack Propagation Speed

In Section 3.5, we proposed to use the centro-symmetry parameter *P* as a criterion to identify crack surface atoms and determine crack tip location at each time step. However, it is also found that the crack tip location obtained in this way is discontinuous, or more specifically, piecewise constant in time domain, as shown in Fig. 3.17. This implies that the time derivative of the crack tip location curve is meaningless, and, as a result, the crack tip location itself cannot be considered as a physically meaningful measure of crack propagation speed. Therefore, to quantify the speed of crack propagation, we must take average of the crack tip locations in some ways. One commonly used approach is to first average the crack tip locations over small time intervals, as illustrated in Fig. 5.1, and then evaluate the crack propagation speed by dividing the change in averaged crack tip position (ΔC) by the length of the time interval (D) [8,41,42]. For example, for the crack tip location curve depicted in Fig. 5.1, the crack speed at t_0 can be calculated as

$$v_{t_0} = \frac{\Delta C}{D} = \frac{C_2 - C_1}{D} \tag{5.1}$$

where C_1 and C_2 are averaged crack tip locations of intervals $[t_0 - D, t_0]$ and $[t_0, t_0 + D]$, respectively. In this way, a physically meaningful crack propagation speed can be determined for each short interval. Note that other averaging techniques, such as least square fitting, can also be employed to obtain the average slope of the discontinuous crack tip location curve within a given time interval.

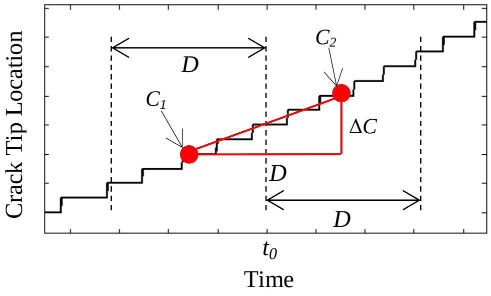

Figure 5.1 Averaging crack tip location over time interval D

The concept described above – taking average of crack tip locations obtained based on the P parameter criterion – can be considered as a logical approach to measure crack propagation speed for atomistic simulations. However, before it can be accepted as a performance measure for structural design, additional requirements need to be taken into account.

For example, a desirable performance measure should be able to provide a clear indication of the change in crack speed due to a design variation, i.e., whether crack propagation is accelerated or slowed down by the design change. Apparently, when the average interval D is small compared to the entire simulation period, the crack speed obtained for a small prescribed interval can be thought of as the speed of crack propagation at the ‘instant’. If the sensitivity of crack speed is positive at some instants, but negative at others, then it becomes difficult to conclude from a grand perspective how we should make design changes in order to slow down crack propagation. In this sense, it is more reasonable to take average of crack tip locations over only one large interval to obtain one single performance measure that quantifies the speed of crack propagation, as long as the crack tip location increases monotonically with roughly a constant slope, i.e., the crack speed does not vary dramatically during simulation. In fact, in most macroscopic scenarios, such as Stage II fatigue crack propagation, the crack speed is close to a constant. Therefore, for our numerical example, we define the performance measure of crack speed as the average of crack tip locations over the entire time period during crack propagation. Certainly, this idea of using only one average interval may not be appropriate when crack speed varies significantly within different simulation periods, in which case it might be necessary to define crack speed separately for individual periods.

Another important criterion for an adequate performance measure is that its sensitivity must be calculable, which, in our case, implies that the design derivative of the performance measure of crack speed must exist. This requirement presents a key challenge in selecting an adequate performance measure for crack propagation speed and its subsequent sensitivity calculation. These important issues will be discussed in the following sections.

In addition, the sensitivity of crack speed should be able to predict the crack propagation speed in a perturbed structure with acceptable accuracy. This means the nonlinearity of crack speed in design space should at least not be as severe as that of atomic responses in our bridging scale example (Section 4.7). The nonlinearity of crack propagation speed and its dependence on the average interval D will be demonstrated using the nano-beam problem at the end of this chapter.

5.3 Differentiability of Crack Propagation Speed

The objective of sensitivity analysis is to find the sensitivity coefficient $d\mathcal{V}/d\mathbf{b}$, which is the derivative of the performance measure of crack propagation speed with respect to shape design variables. Therefore, it is important to first investigate the differentiability of crack propagation speed in design space.

5.3.1 Theoretical Discussion

Consider a simple illustrative crack propagation problem as shown in Fig. 5.2a. Assume that at current design $\mathbf{b}^0$, based on the P parameter criterion, the crack tip at time T_1 is identified to be atom a with x coordinate $x = x_a$, meanwhile atom b at $x = x_b$ and atom c at $x = x_c$ turn into crack tip atoms later at T_2 and T_3, respectively. Figure 5.2b gives the crack tip location curve near the two crack tip jumps at T_2 and T_3, which is theoretically a piecewise constant function in time domain, i.e., the crack tip location remains constant for a period of time and suddenly jumps to the next value (next atom).

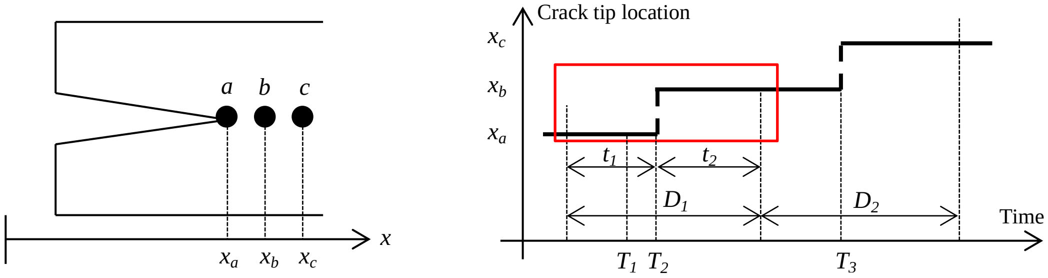

(a) (b)

Figure 5.2 Illustrative crack propagation problem, (a) schematic structure with a horizontal crack, and (b) crack tip location curve near the two crack tip jumps

To demonstrate the differentiability of crack propagation speed, we take the crack tip location curve within the two average intervals D_1 and D_2 shown in Fig. 5.2b for consideration, and, for simplicity, we assume that the lengths of D_1 and D_2 are identical, i.e., $D_1 = D_2 = D$. As discussed in the previous section, the first step of calculating crack speed is to average the crack tip locations within each average interval. According to Eq. 5.1, it is clear that crack propagation speed v will be differentiable in design space as long as the averaged crack tip locations are differentiable functions of design variables.

Therefore, we first discuss the differentiability of C_{D1} – the averaged crack tip location of interval D_1. Figure 5.3a shows the zoomed in crack tip location curve at current design $\mathbf{b}^0$ within interval D_1, where $t_1 + t_2 = D_1 = D$. To take a closer look at the crack tip jump at time instant T_2, we schematically plot the P parameters of all atoms in the system at T_1 and T_2 for illustration. In Fig. 5.3b, the vertical coordinate of each dot inside the boxes represents the value of P parameter of a particular atom in the MD domain at the corresponding instant, and the atoms whose P parameters are greater than the critical value P_{crit} (in other words, crack surface atoms) are highlighted in red.

Apparently, the crack tip jump at T_2 is due to the change of the P parameter of atom b, i.e., P_b is lower than the critical value P_{crit} at T_1, but becomes equal to P_{crit} at T_2.

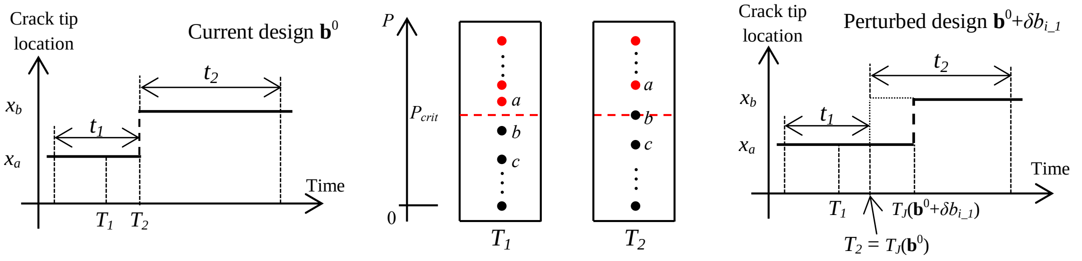

(a) (b) (c)

Figure 5.3 (a) Crack tip location curve at current design $\mathbf{b}^0$, (b) P parameters of atoms at T_1 and T_2, and (c) crack tip location curve at perturbed design $\mathbf{b}^0+\delta b_{i\_1}$

According to Fig. 5.3a, the averaged crack tip location for interval D_1 at current design can be calculated as

$$C_{D1}\left(\mathbf{b}^0\right)=\frac{x_a \times t_1 + x_b \times t_2}{D} \tag{5.2}$$

Now assume a small perturbation δb_{i_1} made to design variable b_i, because of which the crack tip jump delays as shown in Fig. 5.3c. If we define T_J – the moment at which the crack tip jump occurs due to P_b – as a function of shape design variables, then the averaged crack tip location for D_1 can also be written as a function of design. For instance, at perturbed design $\mathbf{b} = \mathbf{b}^0+\delta b_{i\_1}$ (Fig. 5.3c), we have

$$C_{D1}\left(\mathbf{b}^0+\delta b_{i\_1}\right)=\frac{x_a \times \left(t_1 + T_J\left(\mathbf{b}^0+\delta b_{i\_1}\right) - T_J\left(\mathbf{b}^0\right)\right) + x_b \times \left(t_2 - T_J\left(\mathbf{b}^0+\delta b_{i\_1}\right) + T_J\left(\mathbf{b}^0\right)\right)}{D} \tag{5.3}$$

Note that at current design, $T_J\left(\mathbf{b}^0\right) = T_2$. Also, Eq. 5.3 is equivalent to Eq. 5.2 at $\mathbf{b} = \mathbf{b}^0$ ($\delta b_{i\_1} = 0$).

Since x_a, x_b, t_1 and t_2 are all constants, the derivative of Eq. 5.3 at current design $\mathbf{b}^0$ with respect to design variable b_i can be written as

$$
\begin{aligned}
\frac{dC_{D1}}{db_i} &= \lim_{\delta b_i \to 0} \frac{C_{D1}\left(\mathbf{b}^0 + \delta b_i\right) - C_{D1}\left(\mathbf{b}^0\right)}{\delta b_i} \\
&= \lim_{\delta b_i \to 0} \frac{\dfrac{\left[x_a \times \left(t_1 + T_J\left(\mathbf{b}^0 + \delta b_i\right) - T_J\left(\mathbf{b}^0\right)\right) + x_b \times \left(t_2 - T_J\left(\mathbf{b}^0 + \delta b_i\right) + T_J\left(\mathbf{b}^0\right)\right)\right]}{D} - \dfrac{x_a \times t_1 + x_b \times t_2}{D}}{\delta b_i} \\
&= \frac{x_a - x_b}{D} \cdot \lim_{\delta b_i \to 0} \frac{T_J\left(\mathbf{b}^0 + \delta b_i\right) - T_J\left(\mathbf{b}^0\right)}{\delta b_i}
\end{aligned}
\tag{5.4}
$$

which exists only if T_J is a differentiable function of b_i, i.e.,

$$
\lim_{\delta b_i \to 0} \frac{T_J\left(\mathbf{b}^0 + \delta b_i\right) - T_J\left(\mathbf{b}^0\right)}{\delta b_i} = \frac{dT_J}{db_i} \tag{5.5}
$$

Now, in order to demonstrate the differentiability of T_J, we plot P_b in the three dimensional P_b -time-design space, as shown in Fig. 5.4. Note that the P parameter surface of any atom must be a smooth surface that is at least C^1 continuous along both time and design directions, because:

1. The displacement of each atom at any given time instant can be assumed to be differentiable with respect to shape design variables, as argued in [33].
2. The displacement of each atom is a second order differentiable function of time, and therefore is at least C^1 continuous in time domain.
3. The P parameters are continuous and smooth functions of atomic displacements (Eq. 3.46).

In addition, when plotting Fig. 5.4, we assume P_b to be a monotonically increasing function versus time, and a monotonically decreasing function versus design within the plotted time and design domain. This assumption is solely intended for a better illustration and does not cause any loss of generality of our discussion.

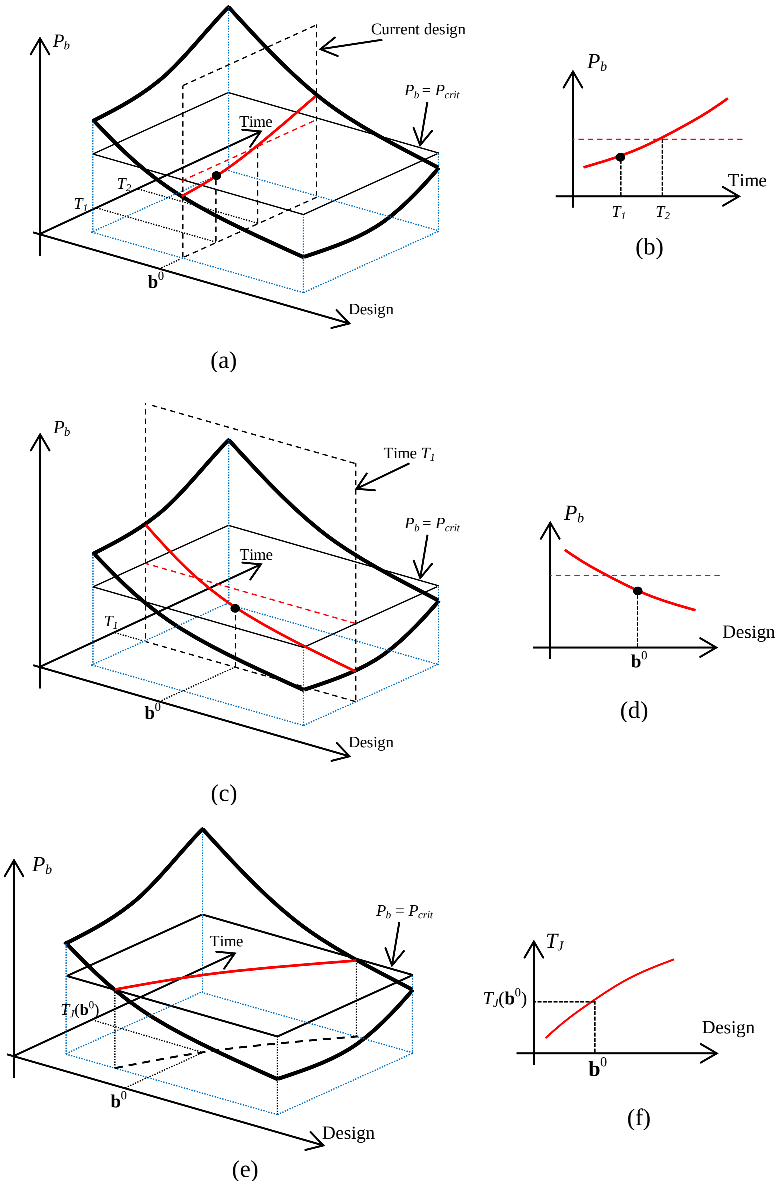

(a) (b)

(c) (d)

(e) (f)

Figure 5.4 The P_b surface in P_b -time-design space. (a) Intersection between the P_b surface and the $\mathbf{b} = \mathbf{b}^0$ plane, (b) P_b vs. time at $\mathbf{b} = \mathbf{b}^0$, (c) intersection between the P_b surface and the $t = T_1$ plane, (d) P_b at $t = T_1$ vs. design, (e) intersection between the P_b surface and the $P_b = P_{crit}$ plane, and (f) T_J vs. design

In Figs. 5.4a, 5.4c and 5.4e, the red curves are intersections between the P_b surface and three planes – the current design plane, the $t = T_1$ plane and the $P_b = P_{crit}$ plane, respectively. Therefore, Figure 5.4b shows the P_b curve in time space at the current design $\mathbf{b}^0$, while Fig. 5.4d shows the P_b curve in design space at time instant T_1. The black dots in Figs. 5.4b and 5.4d denote the same point in the P_b -time-design space – it represents the P parameter of atom b at time T_1 in current design $\mathbf{b}^0$.

Note that the red curve in Fig. 5.4f depicts the relation between the crack tip jump instant T_J (at which $P_b = P_{crit}$) and shape design variable b_i. Since the P_b surface is smooth, the intersection of the P_b surface and the $P_b = P_{crit}$ plane must be a continuous and smooth curve in time-design space as shown in Fig. 5.4f. In other words, T_J is continuously differentiable with respect to b_i. Therefore, according to Eqs. 5.4 and 5.5, C_{D1} is also a continuously differentiable function in design space.

Note that the differentiability of C_{D2} can be proven in the same way. As a result, the crack propagation speed $\mathcal{V} = (C_{D2} - C_{D1})/D$ must be continuously differentiable with respect to shape design variables. The design derivative of $\mathcal{V}$ at current design $\mathbf{b}^0$ is exactly the sensitivity of crack propagation speed being sought.

5.3.2 Differentiability of Crack Speed in Numerical Simulations

Although theoretically the performance measure of crack speed is a differentiable function of design, it may not be the case in numerical simulations, where differential equations are solved through time integration and the solution in time domain is available only at a finite number of time instants (time steps). As illustrated in Figs. 5.5a and 5.5b, for the same illustrative problem discussed above, if time step size Δt_m is used in solving the MD equation of motion, the crack tip location curve (crack tip location vs. time) is no longer piecewise constant, but becomes a discrete function in time domain that has values only at individual time steps (black dots). Moreover, the moment of crack tip jump will be determined as $T_{J\_N}(\mathbf{b}^0)$ and $T_{J\_N}(\mathbf{b}^0+\delta b_{i\_1})$ respectively at current design $\mathbf{b}^0$ and perturbed design $\mathbf{b}^0+\delta b_{i\_1}$. As can be seen, due to the discrete nature of solution in time domain, $T_{J\_N}(\mathbf{b}^0)$ and $T_{J\_N}(\mathbf{b}^0+\delta b_i)$ are inconsistent with analytical crack tip jump instants $T_J(\mathbf{b}^0)$ and $T_J(\mathbf{b}^0+\delta b_{i\_1})$.

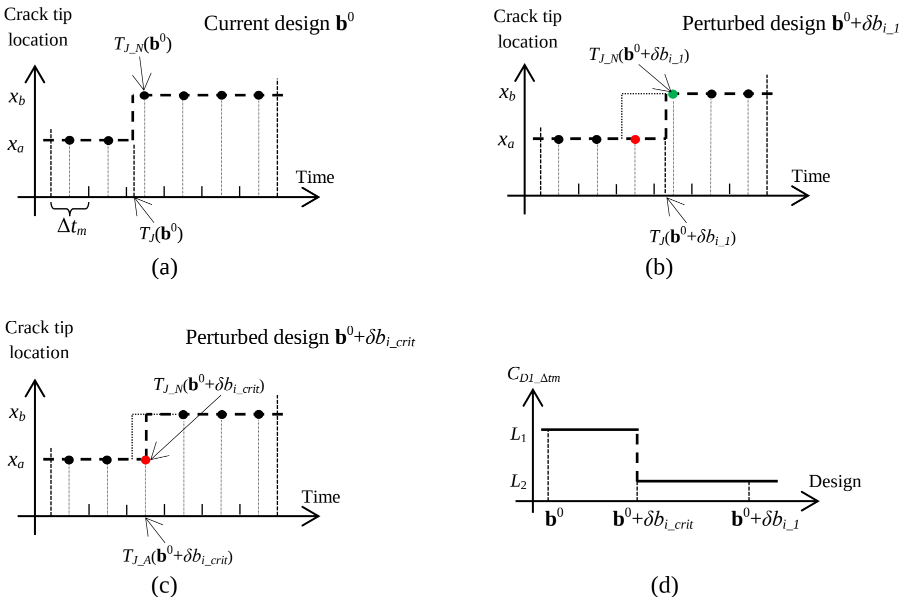

(a) (b) (c) (d)

Figure 5.5 Discrete crack tip location curve within interval D_1 in numerical simulation with time step size Δt_m at (a) current design $\mathbf{b}^0$, (b) perturbed design $\mathbf{b}^0+\delta b_{i\_1}$, (c) perturbed design $\mathbf{b}^0+\delta b_{i\_crit}$, and (d) the discontinuous averaged crack tip location curve in design space

For a better elaboration, as shown in Fig. 5.5c, we assume that at design perturbation δb_{i_crit} ($0 < \delta b_{i\_crit} < \delta b_{i\_1}$), we have $T_{J\_N}(\mathbf{b}^0+\delta b_{i\_crit}) = T_J(\mathbf{b}^0+\delta b_{i\_crit})$, i.e., the crack tip jump happens to occur exactly at the time step indicated by the red dot. One can readily imagine that when a very small design perturbation within $[0, \delta b_{i\_crit})$ is applied, the slight delay of the crack tip jump will not be captured by the relatively larger time step size Δt_m, and therefore T_{J_N} will remain unchanged after the design perturbation. When the design perturbation increases to the critical value δb_{i_crit}, T_{J_N} jumps to the next time step (indicated by the green dot in Fig. 5.5b). Therefore, it is apparent that in numerical simulations, T_{J_N} is discontinuous and hence non-differentiable in design space.

Then we take a look at the differentiability of averaged crack tip location in numerical simulations. According to Figs. 5.5a and 5.5b, with time step size Δt_m, the averaged crack tip location for interval D_1 can be calculated as

$$C_{D1\_\Delta tm}\left(\mathbf{b}^0\right)=\frac{x_a\times 2\times \Delta t_m}{D}+\frac{x_b\times 4\times \Delta t_m}{D}=L_1 \tag{5.6a}$$

at the current design $\mathbf{b}^0$ (Fig. 5.5a) and

$$C_{D1\_\Delta tm}\left(\mathbf{b}^0+\delta b_{i\_1}\right)=\frac{x_a\times 3\times \Delta t_m}{D}+\frac{x_b\times 3\times \Delta t_m}{D}=L_2 \tag{5.6b}$$

at the perturbed design $\mathbf{b}^0+\delta b_{i\_1}$ (Fig. 5.5b). Similar to T_{J_N}, $C_{D1\_\Delta tm}$ will not change at very small design perturbations within $[0, \delta b_{i\_crit})$, while at $\mathbf{b}^0+\delta b_{i\_crit}$ (Fig. 5.5c), the crack tip location at the corresponding time step (red dot) changes from x_b to x_a, resulting in a jump of $C_{D1\_\Delta tm}$. Therefore, as illustrated in Fig. 5.5d, when time step size Δt_m is employed, one jump of averaged crack tip location occurs in between the current design $\mathbf{b}^0$ and the perturbed design $\mathbf{b}^0+\delta b_{i\_1}$. Apparently, the averaged crack tip location curve becomes a discontinuous (piecewise constant) curve in design space.

Now we reduce the time step size to half, as shown in Fig. 5.6. In this case, T_{J_N} is still discontinuous in design space since the time step size is still finite. On the other hand, as the design perturbation size increases from zero to δb_{i_1}, the averaged crack tip location jumps from

$$C_{D1\_\Delta tm/2}\left(\mathbf{b}^0\right)=\frac{x_a\times 4\times \Delta t_m/2}{D}+\frac{x_b\times 8\times \Delta t_m/2}{D}=L_1 \tag{5.7a}$$

at current design $\mathbf{b}^0$ to

$$C_{D1\_\Delta tm/2}\left(\mathbf{b}^0+\delta b_{i\_a}\right)=\frac{x_a\times 5\times \Delta t_m/2}{D}+\frac{x_b\times 7\times \Delta t_m/2}{D}=L_3 \qquad (5.7b)$$

$$C_{D1\_\Delta tm/2}\left(\mathbf{b}^0+\delta b_{i\_b}\right)=\frac{x_a\times 6\times \Delta t_m/2}{D}+\frac{x_b\times 6\times \Delta t_m/2}{D}=L_2 \qquad (5.7c)$$

$$C_{D1\_\Delta tm/2}\left(\mathbf{b}^0+\delta b_{i\_1}\right)=\frac{x_a\times 7\times \Delta t_m/2}{D}+\frac{x_b\times 5\times \Delta t_m/2}{D}=L_4 \qquad (5.7d)$$

at perturbations δb_{i_a}, δb_{i_b}, and finally δb_{i_1}, respectively. As illustrated Fig. 5.6c, this time the averaged crack tip location jumps three times between the current design $\mathbf{b}^0$ and the perturbed design $\mathbf{b}^0+\delta b_{i\_1}$.

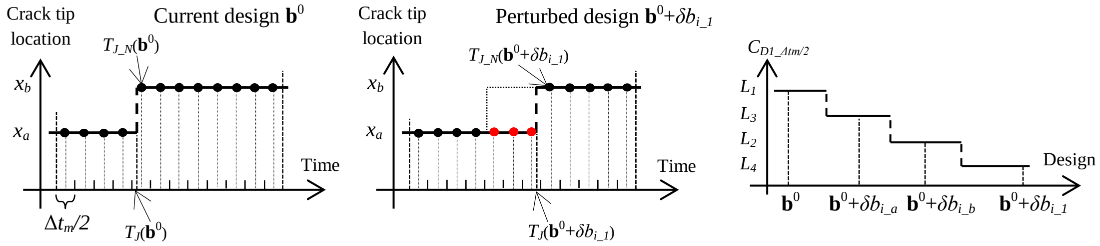

(a) (b) (c)

Figure 5.6 Discrete crack tip location curve in numerical simulation with time step size $\Delta t_m/2$ at (a) current design $\mathbf{b}^0$ and (b) perturbed design $\mathbf{b}^0+\delta b_{i\_1}$, and (c) the discontinuous averaged crack tip location curve in design space

Thus it is clear that when the time domain is discretized in numerical simulations, the averaged crack tip locations C_{D1} and C_{D2} will turn into 'stepped' piecewise constant curves in design space. Moreover, the steps on the curves will be refined as we reduce the time step size. As illustrated in Fig. 5.7, as the time step size approaches zero, the averaged crack tip location C_{D1} converges to the analytical solution, which, as discussed earlier (Eq. 5.3), is a continuously differentiable function of shape design variables.

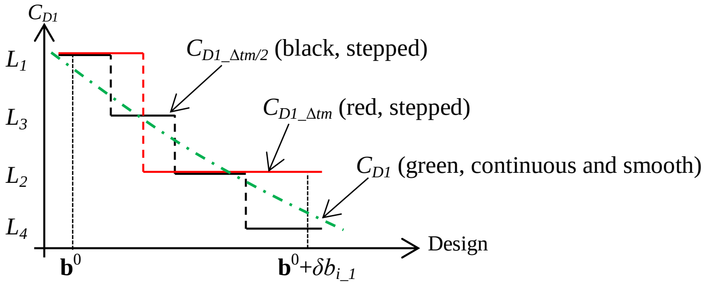

Figure 5.7 Reducing time step size refines averaged crack tip location (C) curve in design space

As a result, as illustrated in Fig. 5.8, in numerical simulations, the crack propagation speed $\mathcal{V} = (C_{D2} - C_{D1})/D$ will also become a ‘stepped’ curve in design space, which will eventually converge to a continuously differentiable function as the time step size becomes infinitely small.

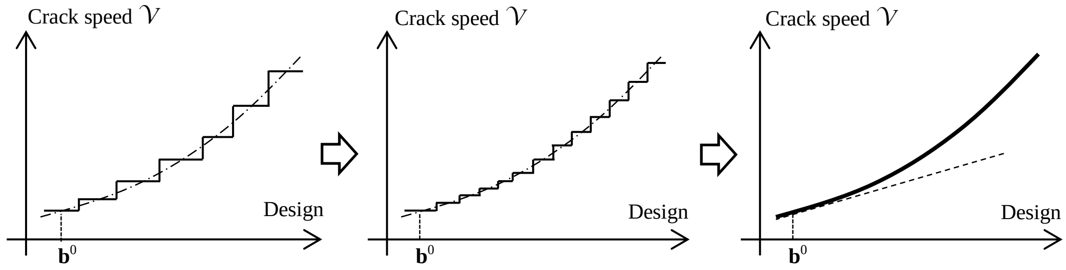

Figure 5.8 Refining the stepped crack speed curve in design space by reducing time step size

In summary, the performance measure that we defined for crack propagation speed is theoretically a differentiable function of shape design variables, but numerically a stepped curve in design space. The calculation of the sensitivity of crack speed will be discussed in the next chapter.

5.4 Numerical Example: Part 3

This section is aimed at investigating the nonlinearity of crack propagation speed in design space using the nano-beam example. More specifically, we are interested in finding the correlation between the average interval size D and the nonlinearity of crack speed.

In Fig. 5.9, we compare the nonlinearity of crack speeds calculated based on different average interval sizes ranging from $200\Delta t_m$ to $3{,}200\Delta t_m$. For example, the subgraph at the top of Fig. 5.9a depicts the crack speed history curve obtained by averaging crack tip locations using an average interval $D = 200\Delta t_m$. The two subgraphs in the first row of Figs. 5.9b and 5.9c reveal how the crack speeds calculated at two selected instants ($8{,}000\Delta t_m$ and $13{,}600\Delta t_m$, circled out) change with shape design variable b_2, respectively, where the data points are obtained by reruning the simulation at several design perturbations ($b_2 = 0.01, 0.02, 0.05, 0.1, 0{,}2, 0.5, 1$). Note that on some of the crack speed vs. design curves (such as the third subgraph in Fig. 5.9b), slight oscillations are observed at small perturbations, which is a numerical issue – the time step size used in our simulation is not small enough to capture the changes of crack tip jumps when the design perturbation is too small. In addition, it can be seen that the last data point of each crack speed history curve (red curves in Fig. 5.9a) is not available. This is because the calculation of the crack speed at $t = t_a$ requires crack tip location data within the interval $[t_a - D, t_a + D]$. Thus, for example, the crack propagation speed at $t = 12{,}800\Delta t_m$ in the subgraph at the bottom of Fig. 5.9a cannot be computed unless we include the data within $[15{,}000\Delta t_m, 16{,}000\Delta t_m]$, which exceeds the duration of our simulation.

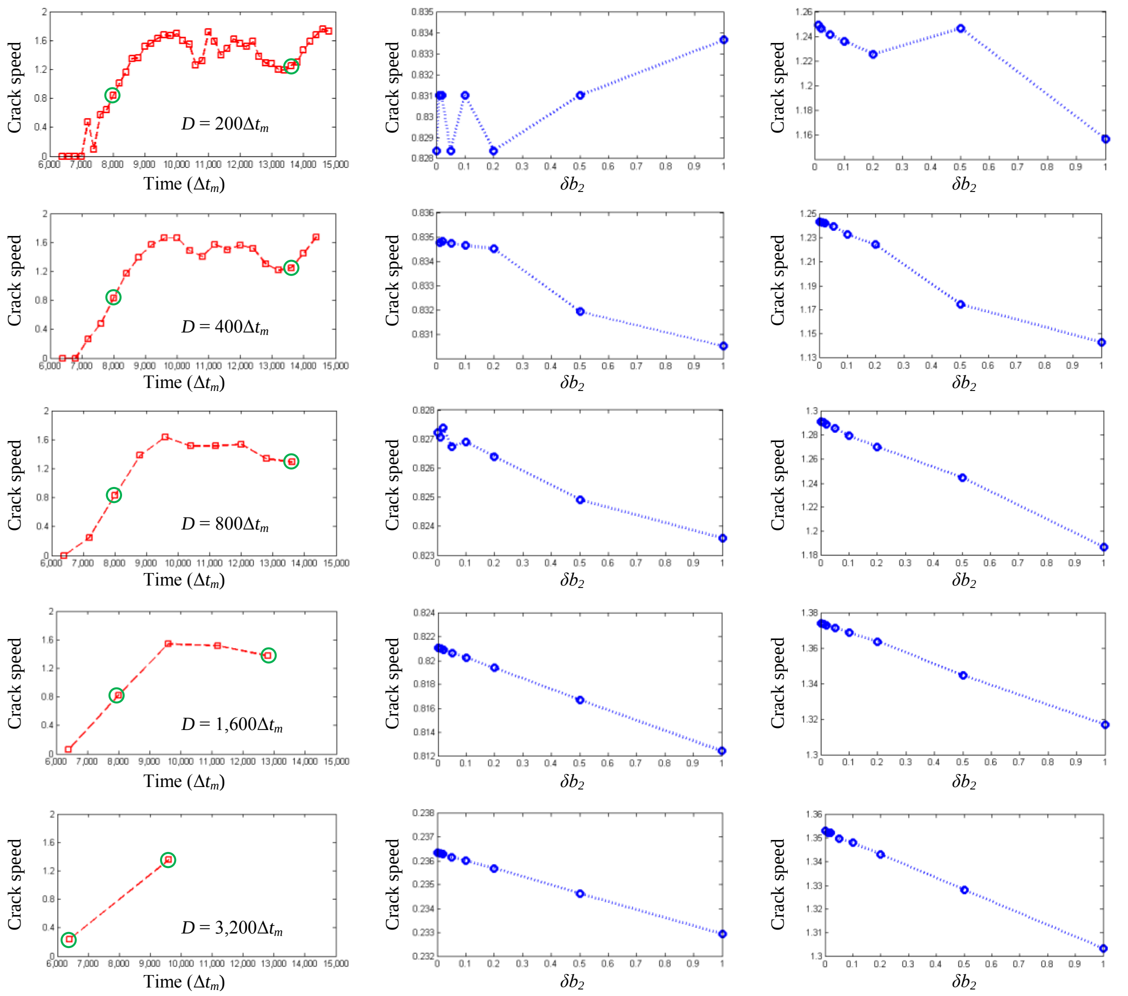

(a) (b) (c)

Figure 5.9 Nonlinearity of crack propagation speeds calculated with different average interval sizes. (a) Crack speed vs. time, (b) crack speed at the first chosen time step vs. design perturbation, and (c) crack speed at the second chosen time step vs. design perturbation

As can be seen from Figs. 5.9b and 5.9c, the nonlinearity of crack speed in design space is in general less severe than that of atomic responses (compared to Fig. 4.10c, for example). More importantly, it is found that the nonlinearity of crack speed can be further reduced by increasing the size of the average interval *D*. In fact, when a large average interval (such as 1,600Δt_m or 3,200Δt_m) is used, the calculated performance measure (crak speed) exibits an almost linear behavior in design space regardless of the high nonlinearity of atomic responses, which is desirable. This is mainly because that at small perturbations in the vicinity of the current design, the delay (or advance) of atomic displacements due to a shape design change is approximately proportional to the size of the design perturebation; therefore, the delay of P parameters and hence the delay of the crack tip location curve is also proportional to design perturebation, which eventually leads to the linear-like behavior of crack speed in design space.

Based on the observations above, for the nano-beam example, we will define the performance measure of crack propagation speed by taking average of all crack tip locations between $t = 9{,}000\Delta t_m$ and $t = 15{,}000\Delta t_m$ (where crack grows with a roughly constant rate), as shown in Fig. 5.10. Since only one interval is considered, we use least square fitting to identify a straight line whose slope can be taken as the crack propagation speed. At current design, the crack speed is calculated to be 1.466.

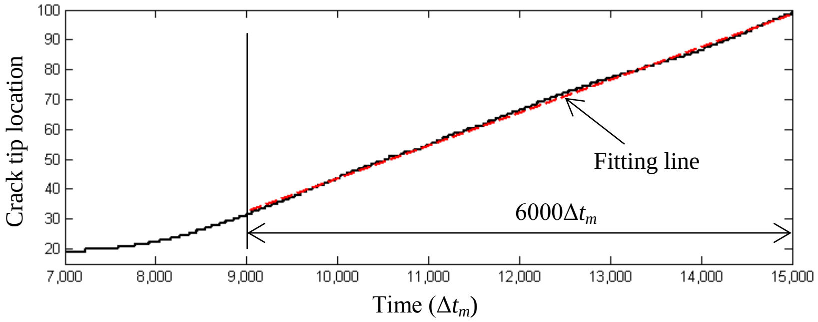

Figure 5.10 Performance measure defined for numerical example. A straight line (red dashed line) is fitted to the crack speed locations within $9{,}000\Delta t_m \sim 15{,}000\Delta t_m$

Note that this performance measure will be used in the next chapter to carry out sensitivity analysis of crack propagation speed for the nano-beam example. Due to the fact that the nonlinearity of crack speed in design space is much less severe than that of atomic responses, the 1st-order prediction of crack speed is expected to be accurate for much larger design perturbations than that of atomic responses, as long as the sensitivity of crack speed can be computed accurately.

CHAPTER 6

HYBRID SENSITIVITY ANALYSIS METHOD FOR CRACK PROPAGATION PROBLEMS

Nomenclature

$\mathcal{V}_T$ = theoretical crack propagation speed. It is a function of deign variables (explicit expression unavailable), and is differentiable in design space.

$\mathcal{V}$ = crack propagation speed calculated in numerical simulation. It is piecewise constant (stepped) in design space. The value of $\mathcal{V}$ with different values of the design variable can be obtained by re-running the simulation (re-analysis) for different perturbed designs.

$\tilde{\mathcal{V}}$ = predicted crack speed. It is a prediction of $\mathcal{V}$ calculated based on analytical sensitivity results. The value of $\tilde{\mathcal{V}}$ with different values of the design variable can be obtained efficiently using analytical sensitivity coefficients (without the necessity of re-analysis).

$\overline{\mathcal{V}}$ = 1st-order prediction of crack propagation speed. It is obtained using the crack speed sensitivity calculated through hybrid method.

$S_{\mathcal{V}T}$ = 'slope' of theoretical crack propagation speed $\mathcal{V}_T$. As a function of design perturbation size δb_i, it represents the slope of the straight line in design space that connects two points – $\mathcal{V}_T$ at current design $\mathbf{b}^0$ and at perturbed design $\mathbf{b}^0 + \Delta b_i$.

$$S_{\mathcal{V}_T}(\Delta b_i) = \left[\mathcal{V}_T(\mathbf{b}^0 + \Delta b_i) - \mathcal{V}_T(\mathbf{b}^0)\right] / \Delta b_i$$

$S_{\mathcal{V}}$ = ‘slope’ of crack propagation speed $\mathcal{V}$. It is similar to $S_{\mathcal{V}T}$, but calculated using crack propagation speed $\mathcal{V}$.

$$S_{\mathcal{V}}(\Delta b_i) = \left[\mathcal{V}(\mathbf{b}^0 + \Delta b_i) - \mathcal{V}(\mathbf{b}^0)\right] / \Delta b_i$$

$S_{\tilde{\mathcal{V}}}$ = ‘slope’ of predicted crack speed $\tilde{\mathcal{V}}$. It is similar to $S_{\mathcal{V}}$, but calculated using predicted crack speed $\tilde{\mathcal{V}}$ at $\mathbf{b}^0 + \Delta b_i$ instead of $\mathcal{V}(\mathbf{b}^0 + \Delta b_i)$.

$$S_{\tilde{\mathcal{V}}}(\Delta b_i) = \left[\tilde{\mathcal{V}}(\mathbf{b}^0 + \Delta b_i) - \mathcal{V}(\mathbf{b}^0)\right] / \Delta b_i$$

$d\mathcal{V}_T/db_i$ = theoretical sensitivity of crack propagation speed with respect to design variable b_i.

$d\mathcal{V}/db_i$ = sensitivity of crack propagation speed with respect to design variable b_i calculated numerically using hybrid method. It is obtained by performing regression analysis based on the ‘slope’ of predicted crack speed $S_{\tilde{\mathcal{V}}}$ (since calculating $S_{\mathcal{V}}$ is computationally prohibitive).

$[0, \Delta b_{i\_reg}]$ = the design perturbation range for regression analysis in hybrid method

$[0, \Delta b_{i\_noise}]$ = the design perturbation range of numerical noise on the $S_{\tilde{\mathcal{V}}}$ curve

6.1 Overview

As has been demonstrated in the previous chapter, the performance measure that we defined for crack propagation speed is theoretically a continuously differentiable function in design space. In this chapter, we denote this theoretical crack propagation speed as $\mathcal{V}_T$. However, due to the discrete nature of MD simulation and the way we identify the location of the crack tip, the formulation of crack speed $\mathcal{V}_T$ cannot be expressed in design in any form, explicitly or implicitly. More importantly, in numerical simulation, since it is impossible to use an infinitely small time step size, the numerically obtained crack speed $\mathcal{V}$ will not be differentiable in design space, and hence the design derivative of crack speed cannot be evaluated directly.

To avoid the non-differentiability issue, in this section, we investigate the feasibility of hybrid sensitivity analysis method in calculating the sensitivity of crack speed based on the discontinuous crack speed curve in design space. In Section 6.2, we first look into the 'standard' hybrid method that directly combines analytical sensitivity analysis and finite difference. After identifying the fundamental drawback of the standard hybrid method, in Section 6.3 we propose an enhanced hybrid method that employs regression analysis to evaluate crack speed sensitivity. In Section 6.4, the accuracy of the hybrid method with regression analysis is verified using the nano-beam example, and its applicability to design will be demonstrated through a what-if study.

6.2 Initial Concept – Standard Hybrid Method

The key idea of the standard hybrid method is to take advantage of both analytical sensitivity analysis and finite difference method as proposed in [49]. First, for each time step, the sensitivity coefficients of the *P* parameters with respect to the *i*th shape design variable b_i can be calculated as

$$\frac{d\boldsymbol{P}}{db_i} = \frac{\partial \boldsymbol{P}}{\partial \mathbf{q}} \cdot \frac{d\mathbf{q}}{db_i} \tag{6.1}$$

where $\boldsymbol{P}$ is a vector that contains the *P* parameter information of all atoms at all time steps, and $d\mathbf{q}/db_i$ represents the sensitivity coefficients of atomic displacements obtained by solving the analytical sensitivity equations. Note that $\partial\boldsymbol{P}/\partial\mathbf{q}$ can be evaluated directly since P parameters are continuous functions of atomic displacements $\mathbf{q}$ (Eq. 3.46).

Next, the increment of $\boldsymbol{P}$ due to a small prescribed design perturbation Δb_i can be calculated using the P parameter sensitivity coefficient; that is

$$\Delta\boldsymbol{P} = \frac{d\boldsymbol{P}}{db_i}\Delta b_i \tag{6.2}$$

The P parameters at perturbed design $\mathbf{b}^0 + \Delta b_i$ can then be approximated by

$$\tilde{\boldsymbol{P}}(\mathbf{b}^0 + \Delta b_i) = \boldsymbol{P}(\mathbf{b}^0) + \Delta\boldsymbol{P} \tag{6.3}$$

Using the P parameter criterion, the position of the crack tip at each time step for the perturbed structure $\mathbf{b}^0 + \Delta b_i$ can be predicted based on the predictions of the P parameters $\tilde{\boldsymbol{P}}(\mathbf{b}^0 + \Delta b_i)$ of associated atoms near the crack tip. Then, the prediction of crack speed at the perturbed design $\tilde{\mathcal{V}}(\mathbf{b}^0 + \Delta b_i)$ can be evaluated by averaging the predicted crack tip locations. Finally, the theoretical sensitivity of crack propagation speed with respect to design variable b_i can be approximated as

$$\frac{d\mathcal{V}_T}{db_i} \approx \frac{\tilde{\mathcal{V}}(\mathbf{b}^0 + \Delta b_i) - \mathcal{V}(\mathbf{b}^0)}{\Delta b_i} \tag{6.4}$$

The procedure above is illustrated in the flowchart shown in Fig. 6.1. As can be seen, the standard hybrid sensitivity analysis method is a combination of analytical sensitivity analysis and finite difference method, while finite difference is only required for computing the sensitivity of crack propagation speed.

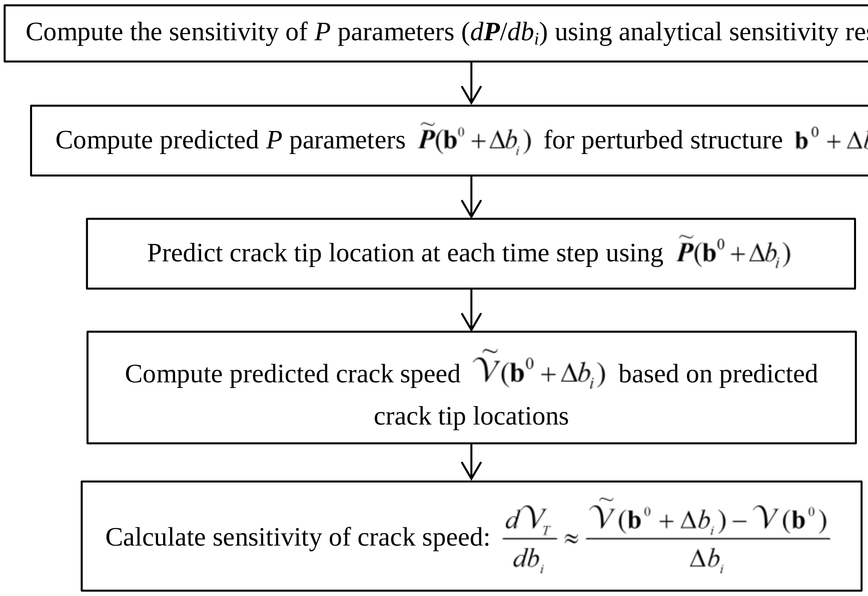

Figure 6.1 Flowchart of standard hybrid method

The scheme of the standard hybrid method is further elaborated in Fig. 6.2. In Fig. 6.2a, the solid curve depicts schematically how the numerically obtained crack speed $\mathcal{V}$ changes with design variable b_i, while the slope of the blue dash-dotted line, assuming exists, represents the sensitivity of crack speed at the current design $\mathbf{b}^0$. If we zoom in near the current design, as discussed in the previous chapter, we should see that the $\mathcal{V}$ curve is piecewise constant (stepped) in design space, as shown in Fig. 6.2b (black solid curve). It is worth mentioning that this black solid curve (crack speed $\mathcal{V}$ vs. design) can only be obtained by rerunning the bridging scale simulation for numerous times at different perturbed designs. In standard hybrid method, to evaluate the sensitivity of crack speed, we first predict the crack propagation speed at a perturbed design ($\tilde{\mathcal{V}}(\mathbf{b}^0+\Delta b_i)$, point *A* on green dashed curve in Fig 6.2b) using analytical sensitivity results, and then calculate the approximation of crack speed sensitivity (red dash-dotted line in Fig. 6.2b) using finite difference (Eq. 6.4).

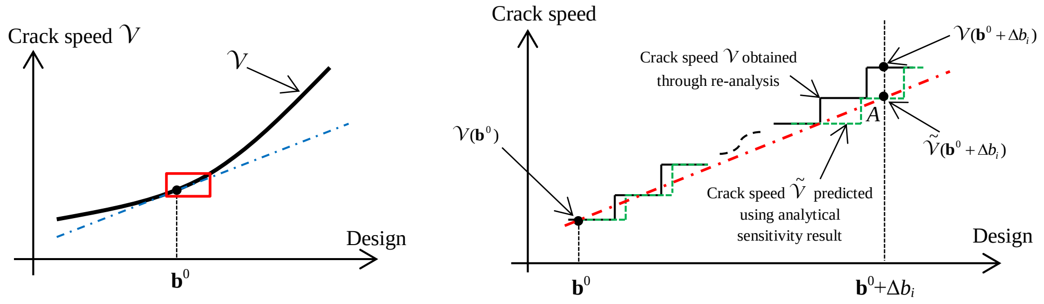

(a) (b)

Figure 6.2 Illustration of standard hybrid method. (a) Crack speed curve in design space, and (b) zoomed-in view with predicted crack speed displayed

The major drawback of this initial concept, or the standard hybrid method, is that the crack speed sensitivity obtained using Eq. 6.4 is strongly dependent on the prescribed design perturbation size Δb_i. Due to the inherent limitation of the finite difference method (discussed in Chapter 2), Δb_i is difficult to determine when the behavior of crack speed in design space is unknown.

One can argue that a convergence study for Eq. 6.4 can be carried out by continuously reducing Δb_i near the current design ($\Delta b_i = 0$) to find out an accurate crack speed sensitivity. To explain the feasibility of this idea, in Fig. 6.3a, we first plot schematically the theoretical crack speed curve – denoted by $\mathcal{V}_T$ – in design space (upper plot), which is continuously differentiable with respect to design variables. The lower plot in Fig. 6.3a depicts the 'slope' of theoretical crack speed; that is

$$S_{\mathcal{V}_T}(\Delta b_i) = \frac{\mathcal{V}_T(\mathbf{b}^0 + \Delta b_i) - \mathcal{V}_T(\mathbf{b}^0)}{\Delta b_i} \tag{6.5}$$

which does not indicate the actual local gradient of $\mathcal{V}_T$ at $\mathbf{b}^0$, but is a function of design perturbation Δb_i that represents the slope of the straight line in design space that connects two points – $\mathcal{V}_T$ at current design $\mathbf{b}^0$ and at perturbed design $\mathbf{b}^0 + \Delta b_i$ (as shown in the upper plot of Fig. 6.3a). As can be seen, $S_{\mathcal{V}T}$ converges to the analytical slope of the theoretical crack speed curve at current design $\mathbf{b}^0$ as the perturbation size Δb_i approaches zero, and this analytical slope is the theoretical crack speed sensitivity $d\mathcal{V}_T/db_i$. However, in numerical simulations, the crack speed $\mathcal{V}$ is a stepped curve in design space, and so is the crack speed $\tilde{\mathcal{V}}$ predicted using analytical sensitivity result, as shown in the upper plot of Fig. 6.3b. Thus, as we reduce perturbation size Δb_i, the 'slope'

$$S_{\tilde{\mathcal{V}}}(\Delta b_i) = \frac{\tilde{\mathcal{V}}(\mathbf{b}^0 + \Delta b_i) - \mathcal{V}(\mathbf{b}^0)}{\Delta b_i} \tag{6.6}$$

(equivalent to Eq. 6.4, except that Δb_i is varying) obtained based on the stepped $\tilde{\mathcal{V}}$ curve oscillates in design space (lower plot of Fig. 6.3b), and will not converge to a constant value. In fact, as shown in the lower plot of Fig. 6.3b, $S_{\tilde{\mathcal{V}}}$ reduces to zero at very small perturbations near the current design.

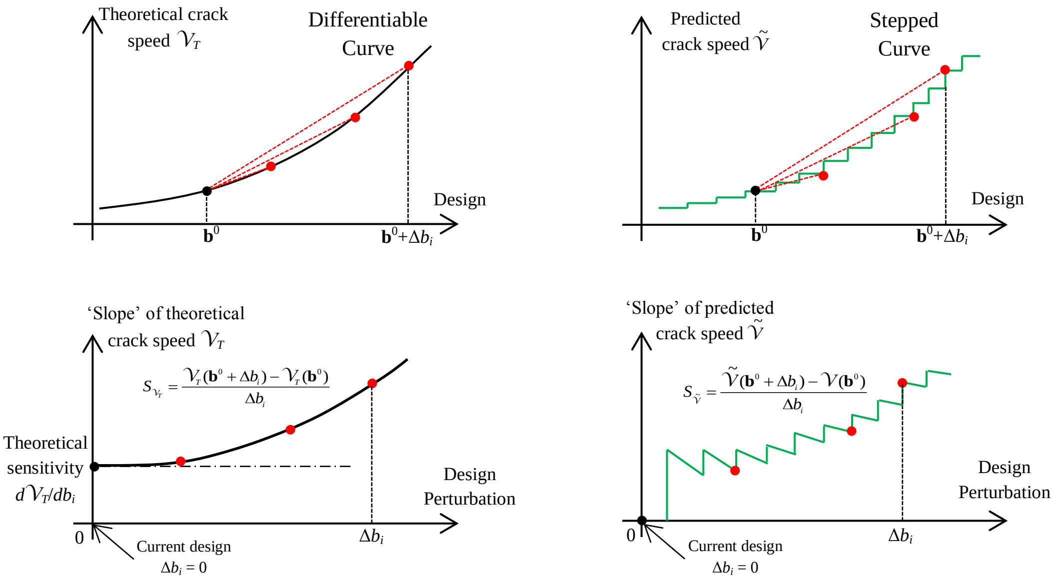

(a) (b)

Figure 6.3 Comparison between smooth and stepped crack speed curves in design space, (a) theoretically differentiable $\mathcal{V}_T$ curve whose 'slope' converges to a constant value (theoretical sensitivity $d\mathcal{V}_T/db_i$), and (b) stepped $\tilde{\mathcal{V}}$ curve whose 'slope' is discontinuous and does not converge

Therefore, it is clear that in our case, the sensitivity of crack propagation speed cannot be evaluated numerically by carrying out convergence study for the 'slope' of predicted crack speed ($S_{\tilde{\mathcal{V}}}$). Hence, an alternative approach is required to approximate the sensitivity of crack propagation speed based on the discontinuous and oscillating $S_{\tilde{\mathcal{V}}}$ curve in design space.

6.3 Hybrid Method with Regression Analysis

Due to the difficulty of determining perturbation size Δb_i in standard hybrid method and the infeasibility of convergence study based on $S_{\tilde{\mathcal{V}}}$, we propose an enhanced hybrid method that employs polynomial regression analysis to approximate crack speed sensitivity using the discontinuous $S_{\tilde{\mathcal{V}}}$ curve. As illustrated in Fig. 6.4, the basic idea is to select a small perturbation range [0, Δb_{i_reg}] near the current design $\mathbf{b}^0$, and fit the $S_{\tilde{\mathcal{V}}}$ (green curve in Fig, 6.4b) within the chosen range with a polynomial curve, while the slope of the polynomial curve at the current design ($\Delta b_i = 0$) is set to zero as illustrated in Fig. 6.4b in order to capture the convergence behavior of $S_{\tilde{\mathcal{V}}}$. Then the vertical intercept of the polynomial curve can be considered as a reasonable approximation of the sensitivity of crack speed, denoted as $d\mathcal{V}/db_i$ in Fig. 6.4b. Note that the $S_{\mathcal{V}}$ curve in Fig. 6.4b is defined in a way similar to Eq. 6.5, but with $\mathcal{V}_T$ replaced by $\mathcal{V}$. Detailed algorithm and procedure of the regression analysis will be introduced later in this chapter using the nano-beam example. The remainder of the current section discusses technical essentials associated with the proposed hybrid method with regression analysis.

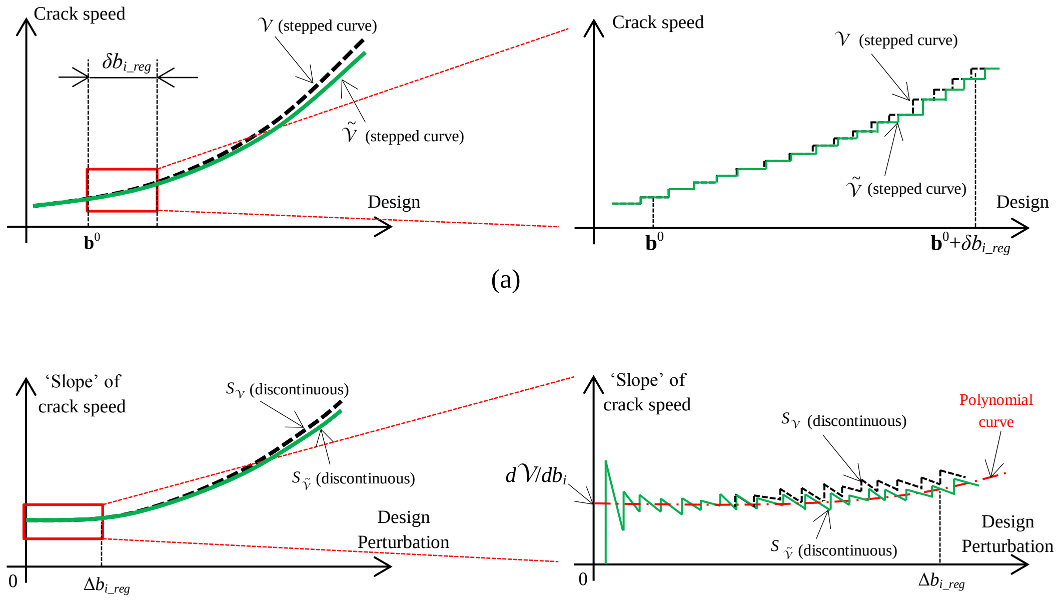

(a)

(b)

Figure 6.4 Illustration of hybrid method with regression analysis. (a) Crack speed curves, and (b) crack speed 'slope' curves

To start, it is important to reiterate that, theoretically, crack propagation speed is differentiable with respect to design variables as demonstrated in Chapter 5, and thus the sensitivity of crack speed exists from theoretical perspective (the 'theoretical sensitivity $d\mathcal{V}_T/db_i$' in the lower plot of Fig. 6.3a.). In numerical simulations, the differentiable crack speed curve $\mathcal{V}_T$ in design space is unattainable, and hence the continuous crack speed 'slope' curve $S_{\mathcal{V}T}$ does not exist. Therefore, the sensitivity of crack speed has to be evaluated numerically based on the discontinuous crack speed 'slope' curve $S_{\mathcal{V}}$. However, calculating either the $\mathcal{V}$ or $S_{\mathcal{V}}$ curve (black dashed curves in Fig. 6.4) through re-analysis is computationally prohibitive. As a result, we propose to perform regression analysis for the $S_{\tilde{\mathcal{V}}}$ curve instead of $S_{\mathcal{V}}$ to obtain the approximated sensitivity $d\mathcal{V}/db_i$, as described at the beginning of this section.

Apparently, compared to the standard hybrid method, the proposed hybrid method with regression analysis requires a large quantity of $S_{\tilde{\mathcal{V}}}$ data within $[0, \Delta b_{i\_reg}]$. As discussed in the previous section, the predicted crack speed $\tilde{\mathcal{V}}$ is obtained based on analytical sensitivity coefficients of atomic responses; therefore, the computation of all $S_{\tilde{\mathcal{V}}}$ data needed for regression analysis (green curve within $[0, \Delta b_{i\_reg}]$ in Fig. 6.4b) is very fast compared to rerunning the bridging scale simulation for overall finite difference (actual CPU time will be given in numerical example).

Moreover, it is clear that the crack speed sensitivity $d\mathcal{V}/db_i$ calculated using the hybrid method is dependent on the range $[0, \Delta b_{i\_reg}]$ chosen for regression analysis. In numerical simulation, at very small design perturbations, the $S_{\tilde{\mathcal{V}}}$ curve will be contaminated by numerical noise caused by the discretization of the time domain (will be demonstrated in our numerical example); therefore, we need to choose [0, Δb_{i_reg}] to be larger than the noise range [0, Δb_{i_noise}] to ensure incorporating adequate useful data for curve fitting. More specifically, in our implementation, we first calculate the $S_{\tilde{\mathcal{V}}}$ data starting from $\Delta b_i = 0$ with a certain interval in design domain until the end of the noise range can be identified through visual inspection, after which we continue computing $S_{\tilde{\mathcal{V}}}$ with increasing Δb_i, until the total range of the calculated $S_{\tilde{\mathcal{V}}}$ data is several times larger than the noise range [0, Δb_{i_noise}]. The perturbation range for regression analysis can then be chosen as $\Delta b_{i\_reg} = N_R \times \Delta b_{i\_noise}$, where N_R is a prescribed multiple. As will be shown in our numerical example, the perturbation range chosen in this manner is able to yield accurate sensitivity of crack propagation speed.

Furthermore, the accuracy of the crack speed sensitivity $d\mathcal{V}/db_i$ is also associated with the accuracy of the 'slope' of predicted crack speed $S_{\tilde{\mathcal{V}}}$ (i.e., whether the green curves in Fig. 6.4b match the black ones) within the chosen range [0, Δb_{i_reg}]. Apparently, although $S_{\tilde{\mathcal{V}}}$ is not expected to always match $S_{\mathcal{V}}$ (obtained from re-analysis), it should be accurate (i.e., close enough to $S_{\mathcal{V}}$) within a small perturbation range near the current design. This is because $S_{\tilde{\mathcal{V}}}$ is computed using $\tilde{\mathcal{V}}$, while $\tilde{\mathcal{V}}$ is predicted based on the 1st-order predictions of atomic displacements, which have been shown in Section 4.7 to be accurate in the vicinity of the current design. In fact, as will be demonstrated and discussed later in this chapter, the 'slope' of predicted crack speed $S_{\tilde{\mathcal{V}}}$ will remain highly accurate for much larger design perturbations than the 1st-order predictions of atomic responses, and this highly accurate range can be large enough to support regression analysis. On the other hand, even when $S_{\tilde{\mathcal{V}}}$ is less accurate at relatively large perturbations within $[0, \Delta b_{i\_reg}]$, the crack speed sensitivity can still be accurately approximated using the proposed hybrid method, as long as the polynomial curve captures the convergence of the $S_{\tilde{\mathcal{V}}}$ curve based on the accurate $S_{\tilde{\mathcal{V}}}$ data near the current design, as illustrated in Fig. 6.5.

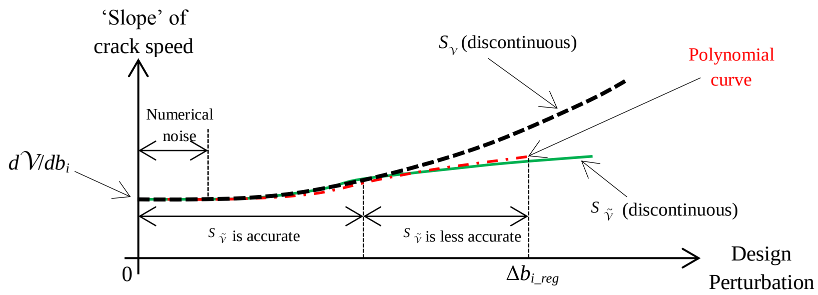

Figure 6.5 Choosing design perturbation range for regression analysis

Now we summarize the complete procedure of the hybrid method with regression analysis as follows:

1. Using analytical sensitivity coefficients of atomic displacements, compute the analytical sensitivity coefficients of P parameters.
2. Compute the 1st-order predictions of P parameters for a perturbed design at $\mathbf{b}^0 + \Delta b_i$.
3. Predict the crack propagation speed $\tilde{\mathcal{V}}$ for the perturbed design based on the P parameter criterion.
4. Calculate the ‘slope’ of predicted crack propagation speed $S_{\tilde{\mathcal{V}}}$ using Eq. 6.6.
5. Repeat steps 2 to 4 for increasing Δb_i from $\Delta b_i = 0$.
6. Visually determine the noise range $[0, \Delta b_{i\_noise}]$, and then define the perturbation

range for regression analysis [0, Δb_{i_reg}] as a multiple of [0, Δb_{i_noise}], i.e., $\Delta b_{i\_reg} = N_R \times \Delta b_{i\_noise}$.

7. Approximate the sensitivity of crack speed though regression analysis based on the $S_{\tilde{V}}$ curve within [0, Δb_{i_noise}].

Note that the analytical shape sensitivity analysis approach developed in Chapter 4 can be used to compute sensitivity coefficients of analytical performance measures, such as structural responses, while the hybrid method proposed in the current chapter is intended for calculating the sensitivity of crack propagation speed. Once the sensitivity of crack speed is obtained, it can be used to predict the crack propagation speed at large design perturbations during design process. The applicability of the hybrid method with regression analysis will be demonstrated in the following section using the nano-beam example.

It is also worth mentioning that in Step 2 of the hybrid method, the calculation of the 1st-order predictions of P parameters requires the sensitivity coefficients of the displacements of a considerable amount of atoms near the crack surfaces. Since crack speed cannot be expressed explicitly in terms of atomic displacements, the displacements of individual atoms near the crack should be treated as separate performance measures. As a result, the number of performance measures need to be considered in analytical shape sensitivity analysis is much greater than the number of shape design variables, which further justifies our use of the direct differentiation method in deriving the analytical sensitivity expressions in Chapter 4.

Finally, it needs to be pointed out that in this chapter, the notation 'Δ' before design variable (for example Δb_i) is used to represent design perturbations related to finite difference or the hybrid method, while the notation ‘δ’ denotes design perturbations associated with 1st-order predictions.

6.4 Numerical Example: Part 4

Based on the performance measure of crack speed defined in Chapter 5, in this section we use the nano-beam example to demonstrate the feasibility and accuracy of the proposed hybrid sensitivity analysis method. The calculation of crack speed sensitivity through regression analysis will be illustrated with details. The justification of the hybrid method will be discussed, and the accuracy of the ‘slope’ of predicted crack speed will be evaluated and compared to that of atomic responses. The accuracy of the crack speed sensitivity calculated using hybrid method will be verified by comparing the 1st-order predictions of crack speed with re-analysis results. Finally, a what-if study will be carried out to demonstrate the applicability of the proposed hybrid method to design.

6.4.1 Crack Speed Sensitivity Calculation Using Hybrid Method

In this section, we use the proposed hybrid method that incorporates polynomial regression curve fitting to approximate the sensitivity of crack propagation speed for the nano-beam example. First, we plot the $S_{\tilde{V}}$ curves with respect to all three design variables individually, as shown in Figs. 6.6a, 6.6b and 6.6c. Note that each curve in Fig. 6.6 is plotted with a 0.0002 interval, i.e., for example, the curve for b_2 is comprised of 1250 data points. Figure 6.6b is also zoomed in at [0.145, 0.155], which shows clearly that the $S_{\tilde{V}}$ curve is discontinues in design space.

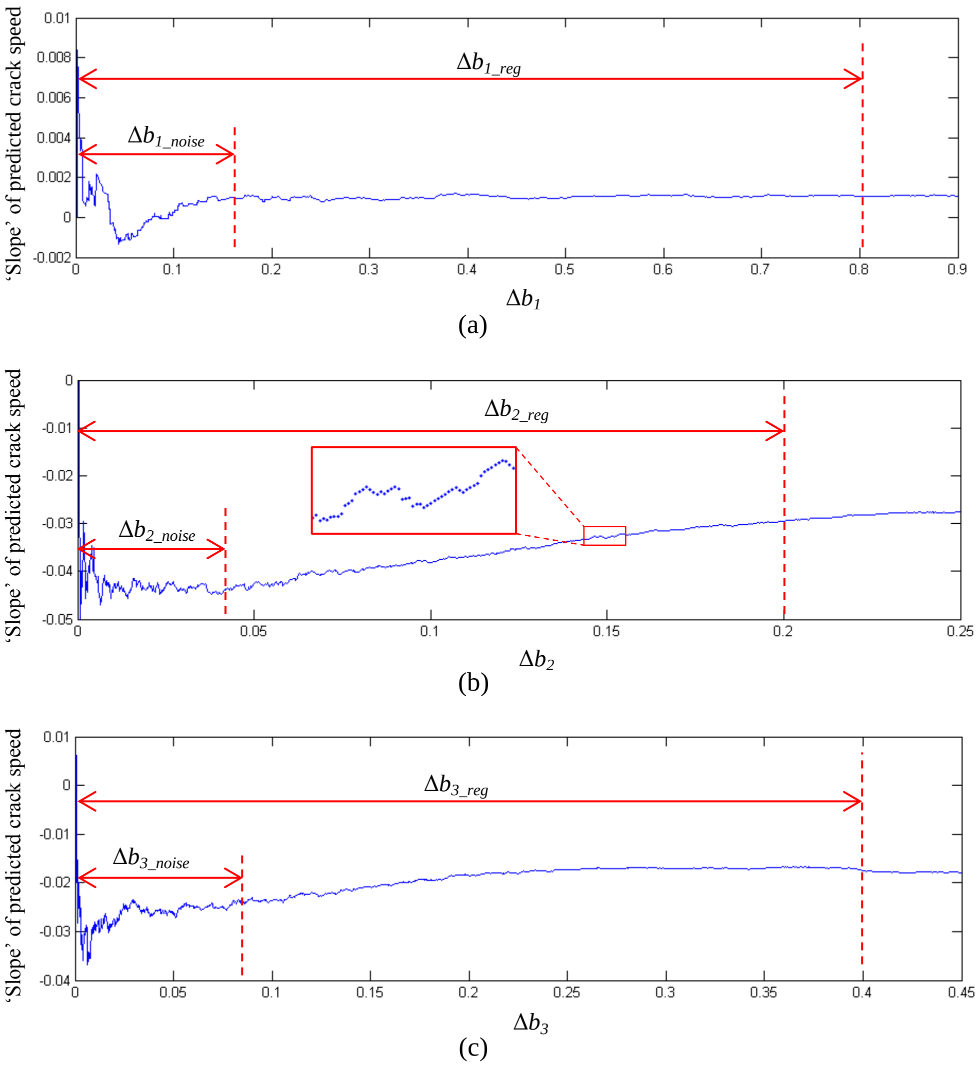

Figure 6.6 'Slope' of predicted crack speed for (a) shape design variable b_1, (b) shape design variable b_2, and (c) shape design variable b_3. The curve for b_2 is zoomed in at [0.145, 0.155]

As can be seen from Fig. 6.6, numerical noise due to time discretization exists at small perturbations on each curve. Note that the noise range for each curve can be easily identified through visual inspection. For this example, we determine the design perturbation range for regression analysis to be five times larger than the noise range, i.e., N_R = 5. One can argue that there seems to be no distinct noise/non-noise boundary on each curve; however, a precise determination of Δb_{i_noise} is not necessary, since the convergence of the $S_{\tilde{V}}$ curves can be captured by the fitting curve as long as enough 'non-noise' data are included in $[0, \Delta b_{i\_reg}]$.

Once the $S_{\tilde{V}}$ curves are obtained, regression analysis can be performed for individual design variables following in the procedure below, with more detailed algorithm and steps documented in Appendix H.

1. Using the method of least-squares, fit a polynomial curve to the $S_{\tilde{V}}$ data within the chosen range, while setting the slope of the fitting curve at $\Delta b_i = 0$ to zero in order to capture the convergence behavior. It is found empirically that a fourth order polynomial curve will generally be adequate in fitting the data within $[0, \Delta b_{i\_reg}]$.
2. Calculate the square of error for each data point using the fitting curve as a reference, and then remove the data points with large error exceeding a deviation threshold. This is to minimize the impact of the noisy data near the current design.
3. Repeat Steps 2 and 3 for the remaining data, until the difference between the vertical intercepts of the fitting curves in the current and the previous iteration is smaller than 1%.
4. The vertical intercept of the current fitting curve can be considered as a reasonable approximation of the sensitivity of crack propagation speed.

The curve fitting results for the three design variables are shown in Fig. 6.7. In each plot, the red curve represents the polynomial estimated in the last iteration. Note that most of the noise (blue dots) has been successfully eliminated from the original data, and the fitting curves accurately capture the trend of convergence of the $S_{\tilde{V}}$

curves. It turns out that the sensitivity of crack speed can be determined after two to four curve fitting iterations for the three shape design variables in our example. Note that the curve fitting results can always be visually verified.

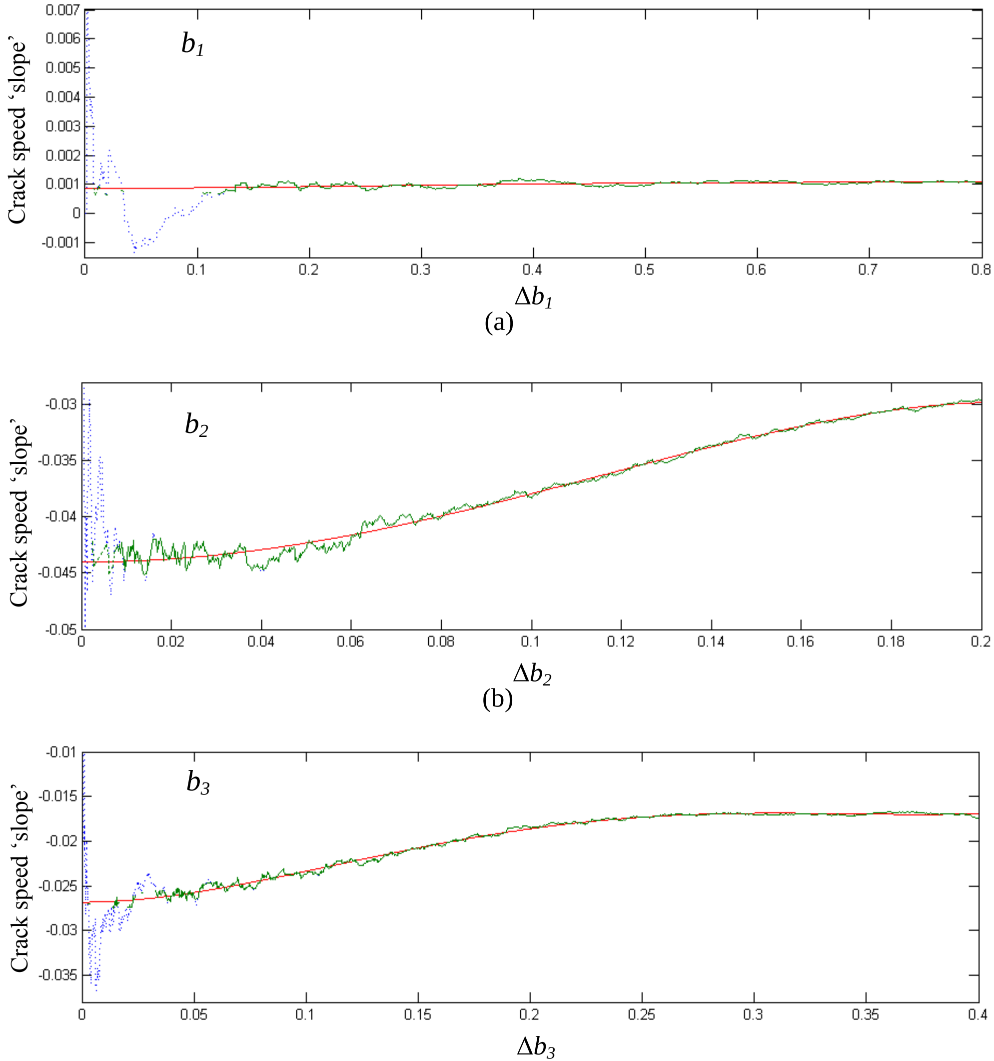

(a)

(b)

(c)

Figure 6.7 Regression analysis results for (a) shape design variable b_1, (b) shape design variable b_2, and (c) shape design variable b_3

The sensitivity coefficients of crack propagation speed obtained for individual design variables are listed in Table 6.1, where the signs of the sensitivity values provide a clear indication that within the simulation period $9{,}000\Delta t_m$ ~ $15{,}000\Delta t_m$, crack propagation will slow down due to an increment of either b_2 or b_3, or a decrement of b_1.

Table 6.1 Sensitivity coefficients of crack propagation speed

Design variable	b_1	b_2	b_3
Crack speed sensitivity	9.7097E-04	-4.3939E-02	-2.6893E-02

It is noteworthy that during regression analysis, the ‘slope’ of predicted crack speed $S_{\tilde{V}}$ needs to be calculated at thousands of perturbations within $[0, \Delta b_{i\_reg}]$. However, since the P parameters are predicted with existing analytical sensitivity results of structural responses, the $S_{\tilde{V}}$ data can be computed very fast. For example, the calculation of the 1,250 data points plotted in Fig. 6.6 for b_2 only takes about 9 minutes (CPU time with the DELL workstation). Hence, the computation time for the $S_{\tilde{V}}$ data for all three design variables is merely a fraction of the time needed for rerunning the bridging scale simulation for even one perturbed design (about 24 hours). Moreover, the computation for regression analysis can be further reduced by using larger intervals when plotting the $S_{\tilde{V}}$ curves. Therefore, the proposed hybrid method is much more efficient than the overall finite difference method, in which the regression analysis for S_{V} requires rerunning simulation for a large set of perturbed designs.

6.4.2 Discussions and Justifications

The sensitivity coefficients of crack propagation speed calculated above can be used to predict the crack speed at larger perturbations during design. The desired scenario is that the 1st-order prediction of crack propagation speed

$$\overline{\mathcal{V}}(\mathbf{b}^0 + \delta b_i) = \mathcal{V}(\mathbf{b}^0) + \frac{d\mathcal{V}}{db_i} \cdot \delta b_i \tag{6.7}$$

can be accurate compared to the crack speed $\mathcal{V}$ obtained from re-analysis at perturbed designs. In general, from design perspective, if the accuracy (accuracy index, Eq. 4.27) of the 1st-order prediction $\overline{\mathcal{V}}$ at a given design perturbation δb_i is between 85% and 115%, then the prediction at δb_i is considered to be acceptable. We hope that the 'accurate range' for $\overline{\mathcal{V}}$ (the design perturbation range in which the accuracy of $\overline{\mathcal{V}}$ is within 85% ~ 115%) to be as large as possible, so that large step sizes can be used during the design process.

Certainly, the accuracy of the 1st-order prediction $\overline{\mathcal{V}}$ is dependent on the nonlinearity of crack propagation speed in design space. In general, when a performance measure is highly nonlinear, its 1st-order prediction can deteriorate quickly as design perturbation size increases. However, it has been shown at the end of Chapter 5 that since crack propagation speed is defined by averaging crack tip locations over a large time interval, the nonlinearity of crack speed is much less severe than that of atomic responses. Therefore, the 1st-order prediction $\overline{\mathcal{V}}$ is expected to remain highly accurate for a much larger design perturbation range compared to the 1st-order predictions of atomic responses, as long as the sensitivity of crack propagation speed is calculated accurately.

Now we discuss whether the hybrid method with regression analysis is a desirable approach that produces accurate sensitivity of crack propagation speed. As can be seen from Fig. 6.7, the polynomial curves obtained through regression analysis are capable of accurately capturing the behavior of the $S_{\tilde{\mathcal{V}}}$ curves near the current design.

Each fitting curve converges quickly within a few iterations. In the meantime, the noisy data are eliminated during regression analysis and thus have only minimum impact on the result of curve fitting. Therefore, this concept of improving standard hybrid method by incorporating regression analysis turns out to be an adequate and efficient way of computing crack speed sensitivity.

The only concern left regarding the hybrid method is the accuracy of the $S_{\tilde{\mathcal{V}}}$ data, i.e., whether the green curves illustrated in Fig. 6.4b are close to the blank ones. Apparently, since the regression analysis performed in Section 6.4.1 is based on $S_{\tilde{\mathcal{V}}}$ rather than $S_{\mathcal{V}}$, the hybrid method cannot be justified unless $S_{\tilde{\mathcal{V}}}$ is accurate compared to $S_{\mathcal{V}}$. For example, if the $S_{\tilde{\mathcal{V}}}$ curve in Fig. 6.6a is accurate only within [0, 0.05] (smaller than the noise range), then the sensitivity calculated using hybrid method will be useless since the regression analysis is performed completely on inaccurate $S_{\tilde{\mathcal{V}}}$ data. Therefore, in order to yield accurate crack speed sensitivity, the $S_{\tilde{\mathcal{V}}}$ data for each design variable must maintain reasonable accuracy (for example, 85% ~ 115% compared to $S_{\mathcal{V}}$) at least for a range of design perturbation that is a few times larger than the noise range [0, Δb_{i_noise}].

To justify the hybrid method with regression analysis, the remainder of this section discusses in detail the accuracy of $S_{\tilde{\mathcal{V}}}$, with support of numerical evidences from the nano-beam example.

6.4.2.1 Accuracy of ‘Slope’ of Predicted Crack Speed

As introduced in Section 6.2 and also illustrated in Fig. 6.8, the ‘slope’ of predicted crack speed $S_{\tilde{V}}$ is calculated using predicted crack speed $\tilde{V}$, while $\tilde{V}$ is evaluated based on the predicted crack tip locations. The predicted crack tip locations are computed using the 1st-order predictions of P parameters ($\tilde{\boldsymbol{P}}$ in Eq. 6.3), which are calculated based on the sensitivity coefficients of atomic responses obtained in analytical sensitivity analysis. Since it has been shown in Section 4.7 that the 1st-order predictions of atomic responses can generally remain accurate for only very small design perturbations due to nonlinearity in design space, it becomes important to investigate whether the ‘slope’ of predicted crack speed $S_{\tilde{V}}$ is able to remain highly accurate for an adequately large design perturbation range to support regression analysis.

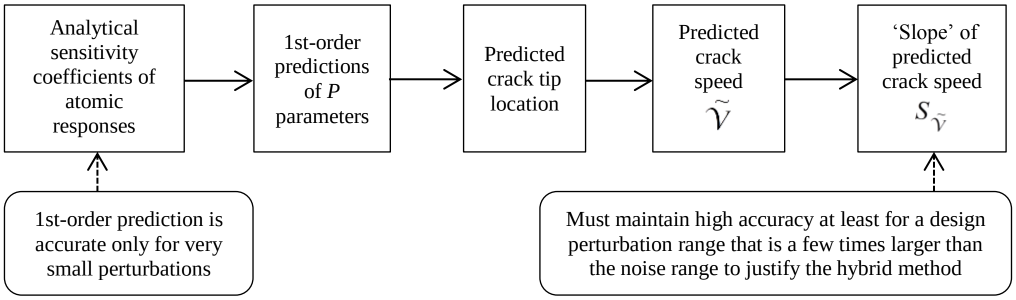

Figure 6.8 Flowchart of the calculation of $S_{\tilde{V}}$

In this section, we sort out the relations among the following: the accuracy of 1st-order predictions of atomic responses, the accuracy of 1st-order predictions of P parameters, the accuracy of predicted crack tip locations, the accuracy of predicted crack speed, and the accuracy of the ‘slope’ of predicted crack speed, through five steps as illustrated in Fig. 6.9. The discussion will be supported by numerical results from the nano-beam example.

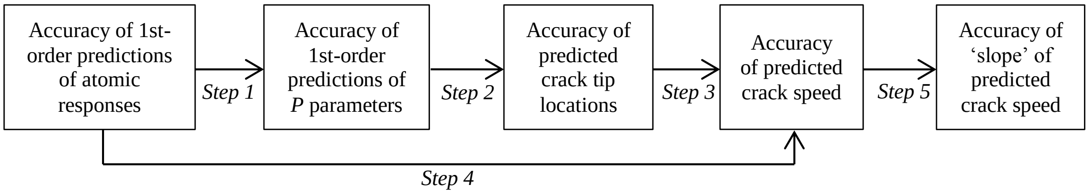

Figure 6.9 Flowchart of the discussion regarding different 'accuracies' involved in hybrid method

Step 1: Atomic Response vs. P Parameter

Provided that the sensitivity coefficients for atomic responses are calculated accurately through analytical shape sensitivity analysis, the accuracy of their 1st-order predictions then depends only on the nonlinearity of atomic responses in design space. According to Eq. 3.46, the P parameters are calculated analytically from atomic responses. More specifically, the P parameter of each atom is a continuous function of the displacements of itself and all 12 nearest neighbors (assuming an FCC lattice). Therefore, it is reasonable to expect that the accuracy of the 1st-order predictions of P parameters should be at the same level as that of the 1st-order predictions of atomic responses.

Now we use the nano-beam example to demonstrate the accuracy of the 1st-order predictions of P parameters. In Table 6.2, we list the sensitivity results of the P parameter of atom $\mathbf{X}_A$ (Fig. 4.7) with respect to three shape design variables at various time steps. Apparently, as with atomic responses, the sensitivity coefficients of P parameters are calculated accurately, since the 1st-order predictions are of excellent accuracy (Columns L ~ N in Table 6.2) at small design perturbation 0.0001.

Table 6.2 Accuracy verification of P parameter sensitivity coefficients for atom $\mathbf{X}_A$. Design perturbation used for calculating the accuracy index is 0.0001

A	B	C	D	E	F	G	H	I	J	K	L	M	N
Time Step	Current Design	Perturbed Design			Overall Finite Difference			Sensitivity Prediction			Accuracy Index		
(Δt_m)	$P(\mathbf{b}^0)$	$P(\mathbf{b}^0+\delta b_1)$	$P(\mathbf{b}^0+\delta b_2)$	$P(\mathbf{b}^0+\delta b_3)$	$\Delta P(b_1)$	$\Delta P(b_2)$	$\Delta P(b_3)$	DSA $P(b_1)$	DSA $P(b_2)$	DSA $P(b_3)$	% $P(b_1)$	% $P(b_2)$	% $P(b_3)$
3,000	3.09E-09	3.09E-09	3.09E-09	3.09E-09	-6.92E-16	-4.57E-15	-5.07E-15	-6.92E-12	-4.57E-11	-5.07E-11	100.020%	100.006%	100.002%
5,000	2.78E-07	2.78E-07	2.78E-07	2.78E-07	5.93E-14	5.27E-13	-1.28E-13	5.93E-10	5.27E-09	-1.28E-09	99.998%	100.001%	99.997%
7,000	9.11E-07	9.11E-07	9.11E-07	9.11E-07	7.34E-14	-5.37E-13	-5.90E-13	7.34E-10	-5.37E-09	-5.90E-09	100.033%	99.996%	99.999%
9,000	1.25E-04	1.25E-04	1.25E-04	1.25E-04	1.23E-09	-3.47E-09	-8.51E-09	1.23E-05	-3.47E-05	-8.51E-05	100.001%	99.996%	99.994%
11,000	5.71E-03	5.71E-03	5.71E-03	5.71E-03	3.20E-07	-8.71E-07	-2.15E-06	3.20E-03	-8.71E-03	-2.15E-02	100.003%	99.993%	99.981%
13,000	4.99E-04	4.99E-04	4.99E-04	4.99E-04	7.77E-09	1.41E-07	-7.68E-09	7.77E-05	1.41E-03	-7.74E-05	99.984%	99.954%	100.794%
15,000	1.45E-04	1.45E-04	1.45E-04	1.44E-04	1.61E-08	1.45E-08	-9.25E-08	1.61E-04	1.44E-04	-9.26E-04	99.989%	99.811%	100.081%

In the meantime, it is also found in the nano-beam example that the nonlinearity of P parameters in design space is in general comparable to that of atomic responses, which is expected. For example, in Fig. 6.10 the P parameter of atom $\mathbf{X}_A$ at $t = 11{,}653\Delta t_m$ is plotted in design space (versus design perturbation δb_2). Note that severe nonlinearity is observed, similar to the nonlinearity of the displacement of the same atom at the same time step (Fig. 4.10c). This implies that the 1st-order predictions of P parameters can remain accurate only for very small design perturbations as with atomic responses.

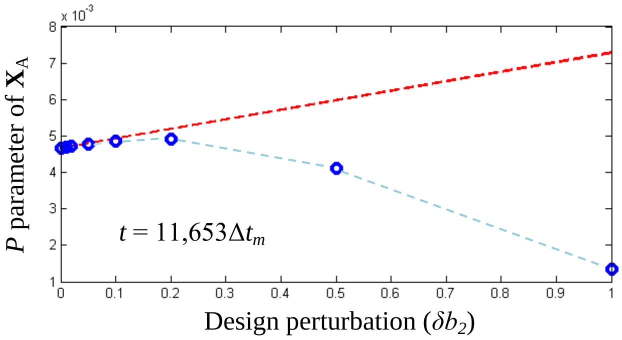

Figure 6.10 Nonlinearity of P parameter of atom $\mathbf{X}_A$ at $t = 11{,}653\Delta t_m$ in design space

Step 2: P Parameter vs. Predicted Crack Tip Location

To explain the relation between the accuracy of the 1st-order predictions of P parameters and that of the predicted crack tip locations, in Fig. 6.11 we plot schematically the P parameters at time T_1 for perturbed design $\mathbf{b}^0 + \Delta b_i$ (obtained from re-analysis), where the 1st-order predictions of the *P* parameters at the same instant are represented by the hollow dots. As can be seen from Fig. 6.11a, even if the predicted *P* parameters are not 100% consistent with those obtained from re-analysis, as long as all hollow dots are on the same side of the red line (P_{crit}) as the corresponding solid ones, the crack tip location at this time step can still be predicted exactly (100% accuracy). On the other hand, if, for example, the *P* parameter of atom *a* at T_1 is extremely close to or right on the red line (Fig. 6.11b), then even a *P* parameter prediction of high accuracy (such as 99.99%) may still result in an inaccurate prediction of crack tip location for that time step. This implies an uncertainty imposed on the relation between the accuracy of the 1st-order predictions of *P* parameters and that of the predictions of crack tip locations; that is:

1. At each time step, even a highly accurate 1st-order prediction of *P* parameters cannot guarantee the accurate prediction of crack tip location.
2. It is also possible that *P* parameter predictions with low accuracy can result in exact predictions of crack tip locations for some time steps, especially in between two adjacent crack tip jumps when the *P* parameters of all atoms are relatively away from the critical value.

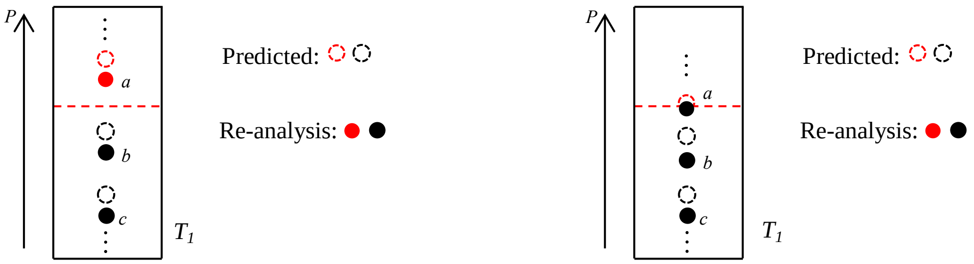

(a) (b)

Figure 6.11 Accuracy of crack tip location prediction when the *P* parameter of atom *a* is (a) away from the critical value and (b) close to the critical value

Step 3: Predicted Crack Tip Location vs. Predicted Crack Speed

As can be easily conceived, when the performance measure of crack speed is defined as an average of crack tip locations over a long time interval that consists a great number of time steps, the impact of inaccurate predictions of crack tip locations caused by either the uncertainty discussed above or the nonlinearity of atomic responses will be minimized.

Taking the nano-beam as an example, we show in Fig. 6.12 the difference between the crack tip location curves for perturbed design $\Delta b_2 = 0.1$ obtained from re-analysis and through prediction using analytical sensitivity results. Note that $\Delta b_2 = 0.1$ can be considered as a relatively large design perturbation for atomic responses due to nonlinearity (discusses in Section 4.7). The point at each time step in Fig. 6.12 is calculated as

$$Diff_C(t) = \tilde{C}^{b_2}(t) - C^{b_2}(t) \tag{6.8}$$

where $C^{b_2}(t)$ is the crack tip location at time t (a multiple of time step size Δt_m) calculated by re-running simulation for perturbed design $\Delta b_2 = 0.1$, while $\tilde{C}^{b_2}(t)$ represents the crack tip location at t predicted using the predicted P parameters in Eq. 6.3, which are computed based on analytical sensitivity results.

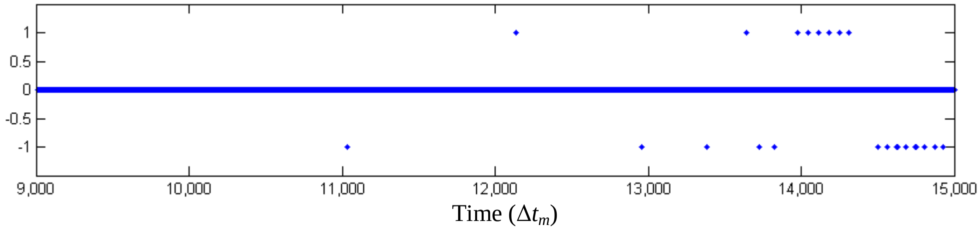

Figure 6.12 Difference between the crack tip location curves obtained from re-analysis and through sensitivity prediction for perturbed design $\Delta b_2 = 0.1$. Time steps within $9{,}000\Delta t_m \sim 15{,}000\Delta t_m$ are plotted

Apparently, in Fig. 6.12, $Diff_C(t)$ = 0 at most time steps, which means $\tilde{C}^{b_2}$ matches $C^{b_2}(t)$. The isolated dots with $Diff_C(t)$ = 1 (or -1) imply that at each of those time steps, the predicted crack tip location is one atom ahead of (or behind) the crack tip location obtained through re-analysis. For the specific case show in Fig. 6.12, the predicted crack tip location $\tilde{C}^{b_2}$ is inaccurate ($Diff_C(t) \neq 0$) at about 40 time steps out of 6,000 within 9,000Δt_m ~ 15,000Δt_m.

Denoting the crack tip locations at the current design as $C^{\mathbf{b}^0}(t)$, the accuracy index of predicted crack tip location

$$Accuracy\ index\ of\ \tilde{C}^{b_2} = \frac{\tilde{C}^{b_2}(t) - C^{\mathbf{b}^0}(t)}{C^{b_2}(t) - C^{\mathbf{b}^0}(t)} \qquad (6.9)$$

for those inaccurate time steps can be, for example, zero or infinity (among many other possible values) when $\tilde{C}^{b_2}(t) = C^{\mathbf{b}^0}(t) \,\&\, C^{b_2}(t) \neq C^{\mathbf{b}^0}(t)$ or $\tilde{C}^{b_2}(t) \neq C^{\mathbf{b}^0}(t) \,\&\, C^{b_2}(t) = C^{\mathbf{b}^0}(t)$, respectively, which is clearly not usable in design. However, after crack propagation speed is calculated based on crack tip locations, the accuracy index of predicted crack speed

$$Accuracy\ index\ of\ \tilde{\mathcal{V}}^{b_2} = \frac{\tilde{\mathcal{V}}^{b_2} - \mathcal{V}^{\mathbf{b}^0}}{\mathcal{V}^{b_2} - \mathcal{V}^{\mathbf{b}^0}} \qquad (6.10)$$

is found to be around 112% for this case, which is acceptable. Note that in Eq. 6.10, $\mathcal{V}^{\mathbf{b}^0}$ and $\mathcal{V}^{b_2}$ are crack propagation speeds obtained by running simulation at the current design and the perturbed deign Δb_2 = 0.1, respectively, while $\tilde{\mathcal{V}}^{b_2}$ stands for the predicted crack speed calculated based on $\tilde{C}^{b_2}(t)$ within the simulation period 9,000Δt_m

~ 15,000Δt_m. Therefore, it becomes clear that the impact of inaccurate predictions of crack tip locations can be minimized during crack speed calculation.

Step 4: Atomic Response vs. Predicted Crack Speed

Based on the three steps discussed above, the predicted crack speed $\tilde{\mathcal{V}}$ is expected to be generally more accurate than atomic responses. In other words, it will remain highly accurate for larger design perturbations than the 1st-order predictions of atomic responses. Now we use the nano-beam example to demonstrate the accuracy of predicted crack speed $\tilde{\mathcal{V}}$ and compare it to the accuracy of the 1st-order predictions of atomic responses.

Figure 6.13 plots the predicted crack speed curves for all three shape design variables in the nano-beam example. In each of the sub-graphs, the green curve is comprised of 5,000 data points of predicted crack speeds $\tilde{\mathcal{V}}$ with interval 0.0002, whereas the blue dots represent crack speeds $\mathcal{V}$ obtained through re-analysis at corresponding perturbed designs. It is apparent that each predicted crack speed curve exhibits ‘stepped’ behavior in design space (zoomed in view for b_2 in Fig. 6.13). Moreover, in general, the predicted crack speed $\tilde{\mathcal{V}}$ data match well with $\mathcal{V}$ (blue dots).

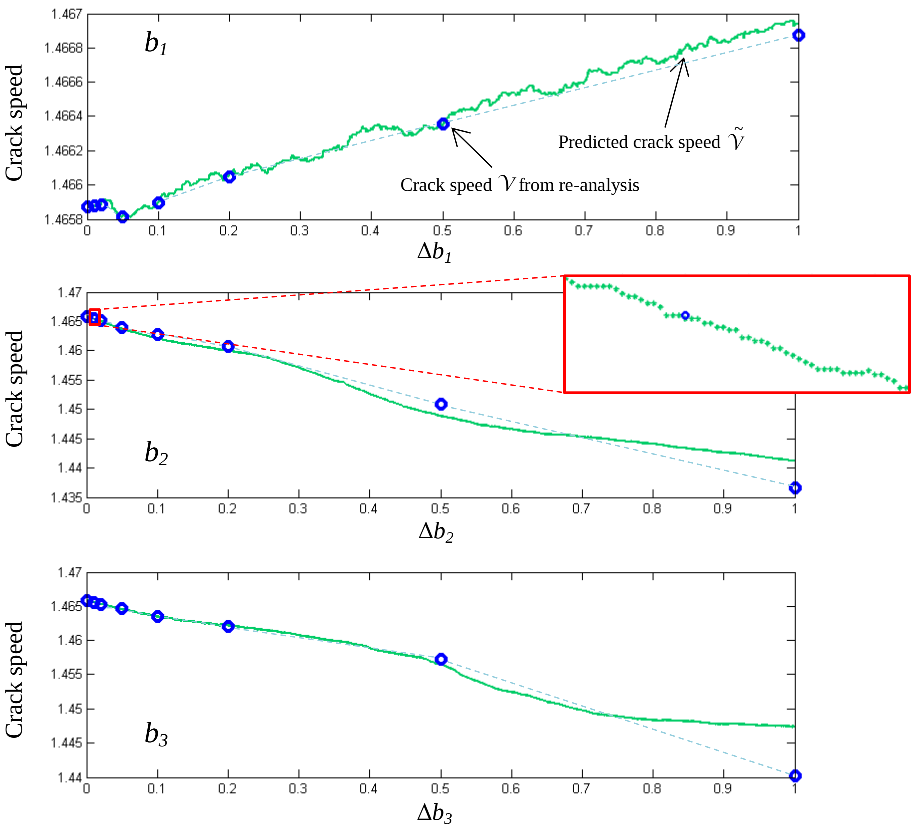

Figure 6.13 Predicted crack speeds in design space for individual design variables. Blue data points represent crack speed $\mathcal{V}$ from re-analysis. Predicted crack speed curve for b_2 is zoomed in at [0.006, 0.017]

The accuracy of the predicted crack speeds is listed in Table 6.3, where the accuracy indices are calculated using Eq. 4.27. As can be seen, up to at least $\Delta b_1 = 1$, $\Delta b_2 = 0.2$ and $\Delta b_3 = 0.5$, the accuracy indices of the predicted crack speeds are between 85% and 115%; within these accurate ranges, the predicted crack speed curves are considerably close to the re-analysis results, especially when compared to the 1st-order predictions of atomic responses. Recall that as shown in Fig. 4.8, the error of the 1st-order predictions of atomic displacements can be as large as 110% (corresponding to accuracy index 210%) for a design perturbation as small as $\delta b_2 = 0.05$ at some time steps. Therefore, it is clear that the predicted crack speed $\tilde{\mathcal{V}}$ can remain highly accurate for much larger design perturbations than the 1st-order predictions of atomic responses.

Table 6.3 Accuracy of predicted crack speed

Design Perturbation (Δb_1)	0.01	0.02	0.05	0.1	0.2	0.3	0.4	0.5	1
Crack speed from re-analysis ($\mathcal{V}$)	1.46588	1.46588	1.46581	1.46590	1.46605	1.46611	1.46627	1.46636	1.46687
Predicted crack speed ($\tilde{\mathcal{V}}$)	1.46588	1.46588	1.46581	1.46590	1.46604	1.46615	1.46633	1.46635	1.46694
Accuracy index	100.00%	100.00%	100.00%	100.00%	98.78%	113.45%	113.49%	98.76%	106.33%

Design variable b_1

Design Perturbation (Δb_2)	0.01	0.02	0.05	0.1	0.2	0.3	0.4	0.5	1
Crack speed from re-analysis ($\mathcal{V}$)	1.46544	1.46509	1.46405	1.46275	1.46069	1.45851	1.45530	1.45090	1.43658
Predicted crack speed ($\tilde{\mathcal{V}}$)	1.46543	1.46501	1.46384	1.46236	1.45996	1.45709	1.45258	1.44884	1.44121
Accuracy index	103.24%	110.47%	111.09%	112.41%	114.05%	119.24%	125.75%	113.74%	84.19%

Design variable b_2

Design Perturbation (Δb_3)	0.01	0.02	0.05	0.1	0.2	0.3	0.4	0.5	1
Crack speed from re-analysis ($\mathcal{V}$)	1.46558	1.46532	1.46464	1.46358	1.46203	1.46071	1.45895	1.45724	1.44023
Predicted crack speed ($\tilde{\mathcal{V}}$)	1.46558	1.46532	1.46456	1.46350	1.46219	1.46075	1.45886	1.45644	1.44741
Accuracy index	100.00%	99.72%	106.23%	103.33%	95.87%	99.22%	101.22%	109.26%	71.98%

Design variable b_3

Also can be observed from Fig. 6.13 and Table 6.3 is that the accurate range of predicted crack speed can vary between individual shape design variables. In fact, the length of the accurate range is related to how sensitive the structural response is with respect to the design variable. More specifically, if the dynamic response of the structure (including crack propagation speed) is less sensitive to a design variable (such as b_1 in the nano-beam example), then for a given design perturbation size, the delay or advance of atomic displacements due to design change will be smaller; consequently, the 1st-order predictions of structural responses (such as atomic displacements), and hence the predicted crack speed for the design variable will be more accurate.

Step 5: Predicted Crack Speed vs. 'Slope' of Predicted Crack Speed

The accuracy of the 'slope' of predicted crack speed is defined as

$$\mathit{accuracy\ \ of}\ S_{\tilde{\mathcal{V}}} = \frac{S_{\tilde{\mathcal{V}}}}{S_{\mathcal{V}}} = \frac{\dfrac{\tilde{\mathcal{V}}\left(\mathbf{b}^0 + \Delta b_i\right) - \mathcal{V}\left(\mathbf{b}^0\right)}{\Delta b_i}}{\dfrac{\mathcal{V}\left(\mathbf{b}^0 + \Delta b_i\right) - \mathcal{V}\left(\mathbf{b}^0\right)}{\Delta b_i}} = \frac{\tilde{\mathcal{V}}\left(\mathbf{b}^0 + \Delta b_i\right) - \mathcal{V}\left(\mathbf{b}^0\right)}{\mathcal{V}\left(\mathbf{b}^0 + \Delta b_i\right) - \mathcal{V}\left(\mathbf{b}^0\right)} \quad (6.11)$$

which indicates the ratio between the 'slope's obtained based on $\tilde{\mathcal{V}}$ and $\mathcal{V}$, i.e., the discrepancy between the blank and green curves in Fig. 6.4b. Note that the expression after the last equal sign in Eq. 6.11 is the same as the definition of the accuracy (accuracy index) of predicted crack speed $\tilde{\mathcal{V}}$, which means the accuracy of the 'slope' of predicted crack speed $S_{\tilde{\mathcal{V}}}$ is equivalent to the accuracy of predicted crack speed $\tilde{\mathcal{V}}$, and hence the accurate range of $S_{\tilde{\mathcal{V}}}$ is identical to that of $\tilde{\mathcal{V}}$. This implies that $S_{\tilde{\mathcal{V}}}$ can also remain highly accurate for much larger design perturbations than the 1st-order predictions of atomic responses. Similar to Fig. 6.13, the comparison between the $S_{\tilde{\mathcal{V}}}$ curves and the $S_{\mathcal{V}}$ data for all three shape design variables in the nano-beam example is shown in Fig. 6.14. As can be seen, the $S_{\tilde{\mathcal{V}}}$ curves match well with $S_{\mathcal{V}}$.

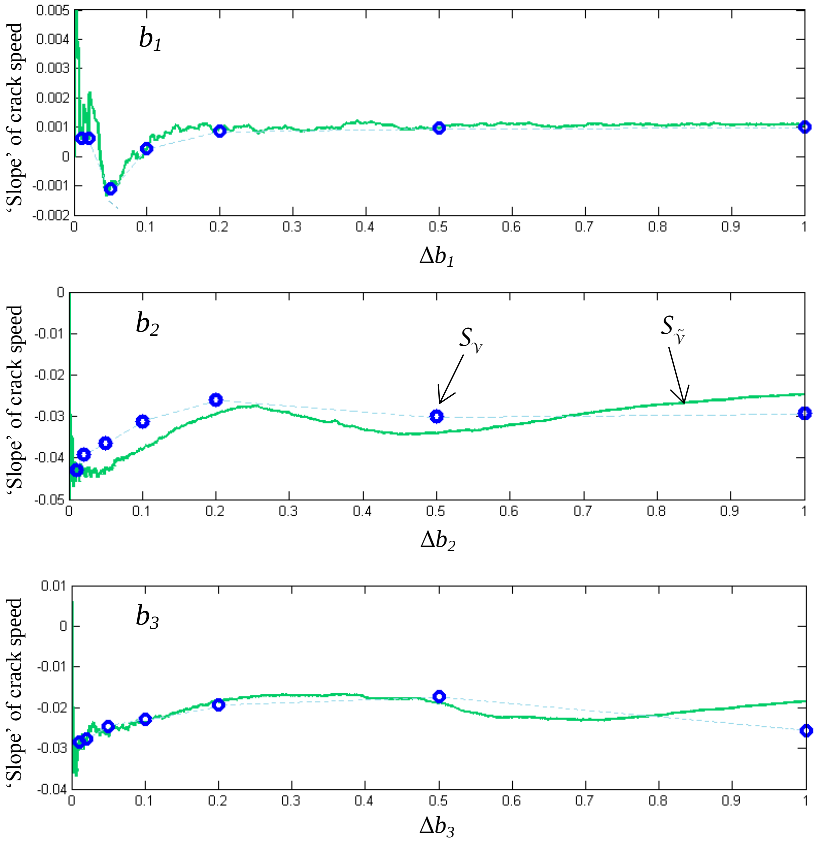

Figure 6.14 Accuracy verification for 'slope' of predicted crack speed ($S_{\tilde{\mathcal{V}}}$) for individual design variables. Blue data points represent $S_{\mathcal{V}}$ obtained from re-analysis

6.4.2.2 Justification of Hybrid Method with Regression Analysis

Now recall the regression analysis carried out in Section 6.4.1. It is important to note that for the nano-beam example, the accurate ranges for $S_{\tilde{\mathcal{V}}}$ (1, 0.2 and 0.5 for b_1, b_2, and b_3, respectively, Table 6.3) are in general much larger than the noise ranges of individual design variables ($\Delta b_{1\_noise} = 0.2$, $\Delta b_{2\_noise} = 0.04$, $\Delta b_{3\_noise} = 0.08$, Fig. 6.6), indicating the feasibility of the hybrid method with regression analysis. In addition, the curve fitting ranges chosen for the three design variables ($\Delta b_{1\_reg} = 0.8$, $\Delta b_{2\_reg} = 0.2$, $\Delta b_{3\_reg} = 0.4$, Fig. 6.7) are all equal or smaller than the accurate ranges, which, according to the discussion in Section 6.3, implies that the crack speed sensitivity calculated using the proposed hybrid method should be accurate.

6.4.3 Accuracy Verification of Crack Speed Sensitivity

In order to verify the accuracy of the crack speed sensitivity coefficients calculated in Section 6.4.1, we compare the 1st-order predictions of crack propagation speeds with re-analysis results. In Fig. 6.15, the blue data points are crack speeds $\mathcal{V}$ obtained through re-analysis, while the red dashed lines represent the 1st-order predictions of crack speeds calculated using Eq. 6.7. Note that the $\overline{\mathcal{V}}(\delta b_i)$ data show in Fig 6.15 and the $\overline{\mathcal{V}}(\mathbf{b}^0+\delta b_i)$ in Eq. 6.7 represent the same quantity.

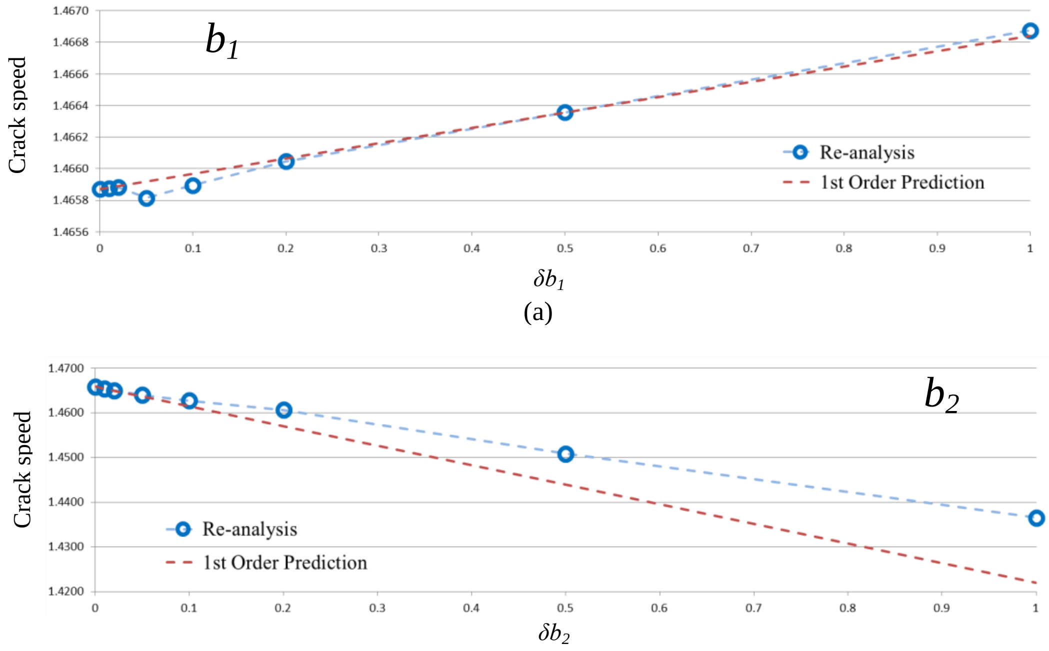

(a)

(b)

Figure 6.15 Accuracy verification of crack speed sensitivity for (a) shape design variable b_1, (b) shape design variable b_2, and (c) shape design variable b_3

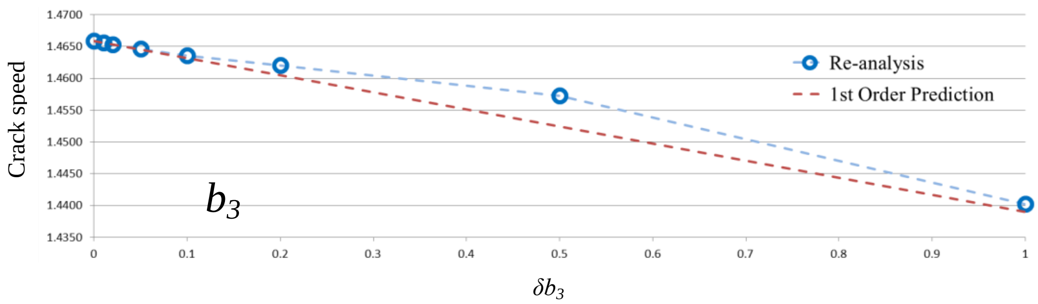

(c)

Figure 6.15 Accuracy verification of crack speed sensitivity for (a) shape design variable b_1, (b) shape design variable b_2, and (c) shape design variable b_3 (cont'd)

As we can see, using the proposed hybrid method with polynomial regression, the sensitivity coefficients of crack speed with respect to all three design variables are accurately computed. In addition, due to the relatively linear behavior of crack speed in design space, the 1st-order predictions of crack speed are accurate for much larger design perturbations than those of atomic responses, which is desirable.

It is worth mentioning that the hybrid method with regression analysis is certainly not the only way to evaluate the sensitivity of crack propagation speed. Alternative approaches can always be employed or developed as long as they are capable of calculating crack speed sensitivity based on the discontinuous crack speed 'slope' curve in design space. However, in this chapter, the hybrid method with regression analysis has been demonstrated to be both efficient and accurate for the nano-beam example.

6.4.4 What-if Study

Based on the crack speed sensitivity calculated using the hybrid method, we carry out a what-if study for the nano-beam example. Our objective is to slow down crack propagation by varying $\delta \mathbf{b} = [\delta b_1, \delta b_2, \delta b_3]^T$, i.e., simultaneously perturbing all three shape design variables. To start with, we plot the sensitivity of crack propagation speed with respect to three design variables in Fig. 6.16. As can be seen, crack speed slows down when b_2 and b_3 are increased, whereas an increment of b_1 accelerates crack propagation.

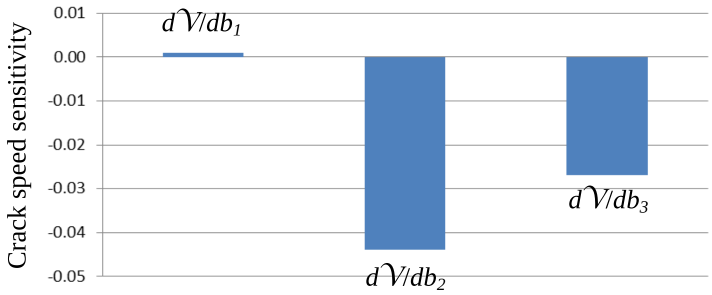

Figure 6.16 Sensitivity coefficients of crack propagation speed with respect to three design variables

With the crack speed sensitivity coefficients, it is possible to find a direction for vector $\delta\mathbf{b}$, along which the crack propagation slows down with a maximum rate, i.e., the crack speed decreases most with a given length of vector $\delta\mathbf{b}$. The normal vector associated with this direction is determined by

$$\mathbf{n} = \frac{-\left[\dfrac{d\mathcal{V}}{db_1} \quad \dfrac{d\mathcal{V}}{db_2} \quad \dfrac{d\mathcal{V}}{db_3}\right]^T}{\sqrt{\left(\dfrac{d\mathcal{V}}{db_1}\right)^2 + \left(\dfrac{d\mathcal{V}}{db_2}\right)^2 + \left(\dfrac{d\mathcal{V}}{db_3}\right)^2}} \tag{6.12}$$

Thus any design change along this direction can be written as

$$\delta\mathbf{b} = \alpha \cdot \mathbf{n} \tag{6.13}$$

where α is a scaling factor.

Based on the discussion above, what-if studies are carried out for a series of perturbations along $\mathbf{n}$ with scaling factors ranging from α = 0.1 to α =1.5. For comparison, the crack speeds $\mathcal{V}$ in perturbed designs are also obtained for individual cases through re-analysis. The results of the what-if studies are shown in Table 6.4. In this table, Columns 3 to 5 list the changes in individual design variables corresponding to the length of $\delta\mathbf{b}$ in each case. For example, the δb_2 for Case 7 (1.279) represents approximately a 0.6% increment of beam length. Column 6 lists the crack propagation speeds predicted in the what-if studies; that is

$$\overline{\mathcal{V}}\left(\mathbf{b}^0+\delta\mathbf{b}\right)=\mathcal{V}\left(\mathbf{b}^0\right)+\frac{d\mathcal{V}}{db_1}\delta b_1+\frac{d\mathcal{V}}{db_2}\delta b_2+\frac{d\mathcal{V}}{db_3}\delta b_3 \qquad (6.14)$$

while Column 7 shows the crack propagation speeds $\mathcal{V}\left(\mathbf{b}^0+\delta\mathbf{b}\right)$ obtained through re-analysis. The accuracy indices are listed in Column 8.

Table 6.4 Accuracy verification for what-if studies

Case No.	Length of $\delta\mathbf{b}$	δb_1	δb_2	δb_3	What-if Study	Re-analysis	Accuracy Index
1	0.1	-1.884E-03	8.528E-02	5.219E-02	1.46072	1.46134	113.67%
2	0.2	-3.769E-03	1.706E-01	1.044E-01	1.45557	1.45782	128.06%
3	0.4	-7.538E-03	3.411E-01	2.088E-01	1.44526	1.45183	146.83%
4	0.6	-1.131E-02	5.117E-01	3.132E-01	1.43496	1.44446	144.37%
5	0.8	-1.508E-02	6.822E-01	4.176E-01	1.42465	1.43282	124.71%
6	1	-1.884E-02	8.528E-01	5.219E-01	1.41435	1.42343	121.40%
7	1.5	-2.827E-02	1.279E+00	7.829E-01	1.38858	1.41560	153.75%

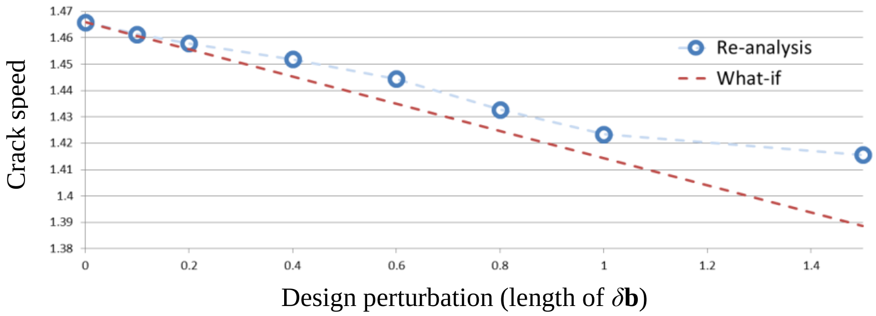

Figure 6.17 Comparison between crack propagation speeds from what-if studies and re-analysis for various design perturbations

The crack propagation speeds listed in Column 6 and Column 7 of Table 6.4 are also plotted in Fig. 6.17. As can be seen, the design direction determined based on sensitivity analysis leads to an intended change in performance measure, i.e., crack propagation slows down when design changes are made along the direction determined by Eq. 6.13. To better illustrate the impact of shape design changes on crack propagation, in Fig. 6.18 we plot the crack tip location curves for the current design and the perturbed designs (obtained through re-analysis) with perturbation scaling factors ranging from 0.1 to 1.5. Note that at around $t = 7{,}700\Delta t_m$ (Area A) – right after the crack started to grow – crack propagation is delayed in perturbed designs. Moreover, as we can see from the zoomed-in view of area B, at later time steps during the simulation, the delay of crack propagation becomes larger, indicating that crack speed is indeed reduced in perturbed designs.

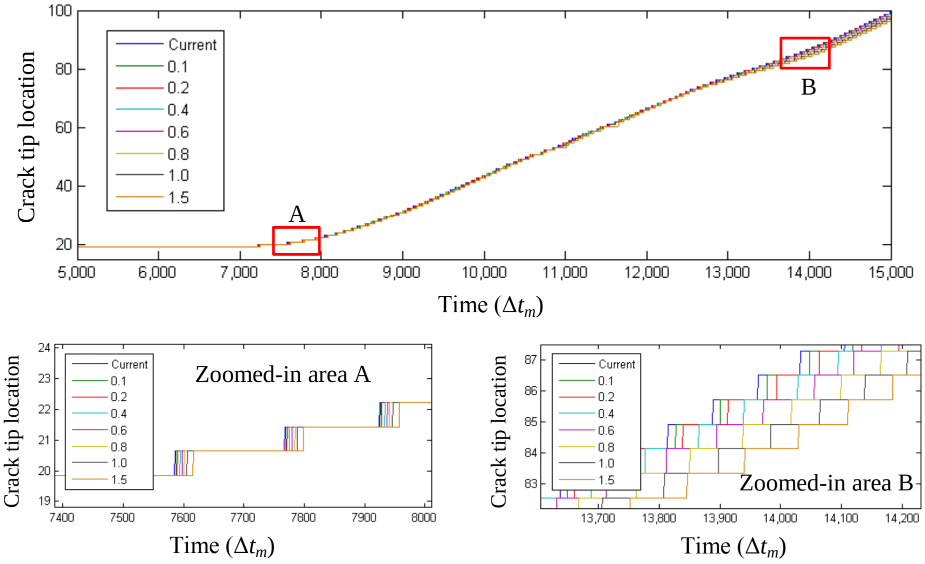

Figure 6.18 Crack tip location curves for perturbed designs with various scaling factors

CHAPTER 7

CONCLUSIONS AND FUTURE WORKS

7.1 Conclusions

In this thesis, a shape sensitivity analysis of multi-scale crack propagation problems, including analytical and hybrid methods, has been presented. The analytical sensitivity expressions were derived from the continuum variational formulation of the bridging scale method. Direct differentiation method was employed due to its efficiency for crack propagation problems that depend highly on the atomistic dynamic responses of the structure. Accuracy of the analytical sensitivity coefficients of structural responses has been verified via a nano-beam example. For crack propagation problems, an adequate performance measure of crack speed was established, and a hybrid sensitivity analysis method that combines analytical sensitivity analysis and finite difference method was developed for calculating the sensitivity of crack speed. The feasibility and accuracy of the hybrid method has been demonstrated through a what-if study using the nano-beam example, which shows that the sensitivity result is effective in support of design decision making.

Two major challenges have been overcome in this thesis: first, since atomic displacement solution is discontinuous due to the discrete nature of MD simulation, we defined design velocity fields in a way that the shape of the MD area does not change. Second, the performance measure of crack speed is theoretically differentiable but numerically discontinuous in design space, and we address this issue by proposing a hybrid method, in which the sensitivity of crack speed is approximated through regression analysis. It has been shown that for crack propagation problems, the hybrid method is much more efficient compared to overall finite difference.

This thesis is the first study that investigates the feasibility of shape sensitivity analysis for coupled atomistic/continuum problems. The derived sensitivity formulation is capable of handling general 3-D geometry. The proposed approach establishes a basis for multi-scale shape optimization of structural components for maximum service life. By employing molecular dynamics simulation near the crack tip, fatigue crack growth can be examined at atomistic level, and residual life can be predicted without using traditional fracture mechanics theory.

7.2 Future Works

Improvements must be made to extend the scope of the current research for practical applications. For example, future works may be focused on relaxing the assumptions and restrictions of both the MD simulation and the bridging scale method. The usage of simple interatomic potential function in this thesis is due to our interest in investigating the generic features of brittle crack propagation. It is certainly possible, however, to study a particular material by defining an LJ potential with parameters that match the material properties, or by replacing the LJ potential with more realistic models, such as an EAM potential [50], to support a broad range of materials and applications. In terms of the bridging scale method, a finite temperature coupling can be accomplished by taking into account the random terms when deriving the time history kernel; higher order time history kernel terms and longer-ranged interatomic interaction can be incorporated to improve accuracy of the simulation; impedance boundary condition for the vertical MD boundaries can be developed, so that the size of the MD simulation can be further reduced to a rectangular area instead of a strip.

The largest concern for the proposed approach to be applied to practical applications lies in the intensive computation required for molecular dynamics simulation. Although the MD domain has been reduced significantly in size by using multi-scale methods, the time scale in practical fatigue problems is much longer than that studied in this work. Nevertheless, the most powerful supercomputer today is about one million times faster than the workstation used for the current research (in terms of floating-point operations per second); therefore, by taking advantage of parallel computing, the proposed sensitivity analysis approach is computationally feasible in supporting the design of micro-scale devices in the near future. With revolutionary advance in computer technology, macroscopic application might be possible within the next decade.

REFERENCES

[1] Edke, M., “Shape Design Sensitivity Analysis and Optimization For 2-D Structural Components under Mixed-mode Fracture Using Extended Finite Element Method and Level Set Method,” Ph.D. Thesis, University of Oklahoma, Norman, OK, 2009.

[2] Abraham, F.F., Walkup, R., Gao, H., Duchaineau, M., Rubia, T. and Seager, M., “Simulating Materials Failure by Using up to One Billion Atoms and the World's Fastest Computer: Work-hardening,” Proceedings of the National Academy of Sciences, 99(9), 5783-5787, 2002.

[3] Gordon, P.A., Neeraj, T., Luton, M.J. and Farkas, D., “Crack-Tip Deformation Mechanisms in α-Fe and Binary Fe Alloys: An Atomistic Study on Single Crystals,” Metallurgical and Materials Transactions A, 38(A), 2191-2302, 2007.

[4] Gao, Y., Lu, C., Tieu, A.K. and Zhu, H.T., “Molecular Dynamics Simulation of Crack Propagation on Different Slip Planes of BCC Iron,” International Conference on Nanoscience and Nanotechnology, 226-229, IEEE, 2008.

[5] Sen, D, Cohen, A., Thompson, A.P., Duin, A.V., Goddard, W.A. and Buehler, M.J., “Direct Atomistic Simulation of Brittle-to-ductile Transition in Silicon Single Crystals,” MRS Proceedings, 1272(PP04-13), Materials Research Society, 2010.

[6] Ersland, C.H., Vatne, I.R. and Thaulow C., “Atomistic Modeling of Penny-shaped and Through-thickness Cracks in BCC Iron,” Modelling and Simulation in Materials Science and Engineering, 20, 075004, 2012.

[7] Potirniche, G.P., Horstemeyer, M.F., Jelinek, B. and Wagner, G.J., “Fatigue Damage in Nickel and Copper Single Crystals at Nanoscale,” International Journal of Fatigue, 27, 1179-1185, 2005.

[8] Buehler, M. J., Atomistic Modeling of Materials Failure, Springer, NY 2008.

[9] Abraham, F.F., Brodbeck, D., Rudge, W.E. and Xu, X., “A Molecular Dynamics Investigation of Rapid Fracture Mechanics,” Journal of the Mechanics and Physics of Solids, 45(9), 1595-1619, 1997.

[10] Abraham, F.F., “How Fast Can Cracks Move? A Research Adventure in Materials Failure Using Millions of Atoms and Big Computers,” Advances in Physics, 52(8), 727-790, 2003.

[11] Buehler, M.J., Abraham, F.F. and Gao, H., “Stress and Energy Flow Field Near a Rapidly Propagating Mode I Crack,” Springer Lecture Notes in Computational Science and Engineering, 143-156, ISBN 3-540-21180-2, 2004.

[12] Abraham, F.F., Brodbeck, D., Rafey, R.A. and Rudge, W.E., “Instability Dynamics of Fracture: A Computer Simulation Investigation,” Physical Review Letter, 73(2), 272-275, 1994.

[13] Buehler, M.J. and Gao, H., “Dynamical Fracture Instabilities due to Local Hyperelasticity at Crack Tips,” Nature, 439, 307-310, 2006.

[14] Buehler, M.J., Abraham, F.F. and Gao, H., “Hyperelasticity Governs Dynamic Fracture at a Critical Length Scale,” Nature, 426, 141-146, 2003.

[15] Abraham, F.F., Walkup, R., Gao, H., Duchaineau, M., Rubia, T. and Seager, M., “Simulating Materials Failure by Using up to One Billion Atoms and the World's Fastest Computer: Brittle Fracture,” Proceedings of the National Academy of Sciences, 99(9), 5788-5792, 2002.

[16] Rountree, C.L., Kalia, R.K., Lidorikis, E., Nakano, A., Brutzel, L.V. and Vashishta, P., “Atomistic Aspects of Crack Propagation in Brittle Materials: Multimillion Atom Molecular Dynamics Simulations,” Annual Review of Materials Research, 32, 377-400, 2002.

[17] Abraham, F. F., Broughton, J., Bernstein, N. and Kaxiras, E., “Spanning the Continuum to Quantum Length Scales in a Dynamic Simulation of Brittle Fracture,” Europhysics Letters, 44(6), 783-787, 1998.

[18] Rudd, R. E. and Broughton, J. Q., “Coarse-grained Molecular Dynamics and the Atomic Limit of Finite Elements,” Physical Review B, 58(10), 5893-5896, 1998.

[19] Tadmor, E., Ortiz, M., and Phillips, R., “Quasicontinuum Analysis of Defects in Solids,” Philosophical Magazine A, 73(6), 1529-1563, 1996.

[20] Wagner, G. J. and Liu, W. K., “Coupling of Atomistic and Continuum Simulations Using a Bridging Scale Decomposition,” Journal of Computational Physics, 190, 249–274, 2003.

[21] Xiao, S. P. and Belytschko, T., “A Bridging Domain Method for Coupling Continua with Molecular Dynamics,” Computer Methods in Applied Mechanics and Engineering, 193, 1645–1669, 2004.

[22] Shiari, B., Miller, R. E. and Curtin, W. A., “Coupled Atomistic/Discrete Dislocation Simulations of Nanoindentation at Finite Temperature,” Journal of Engineering Materials and Technology, 127, 358-368, 2005.

[23] To, A. C. and Li, S., “Perfectly Matched Multiscale Simulations,” Physical Review B, 72, 035414, 2005.

[24] Park, H. S., Karpov, E. G., Klein, P. A. and Liu, W. K., “The Bridging Scale for Two-dimensional Atomistic/Continuum Coupling,” Philosophical Magazine, 85(1), 79-113, 2005.

[25] Rafii-Tabar, H., Hua, L. and Cross, M., “A Multi-scale Atomistic-continuum Modelling of Crack Propagation in a Two-dimensional Macroscopic Plate,” Journal of Physics: Condensed Matter, 10, 2375-2387, 1998.

[26] Chen, J., Wang, X., Wang, H. and Lee, J.D., “Multiscale Modeling of Dynamic Crack Propagation,” Engineering Fracture Mechanics, 77, 736-743, 2010.

[27] Farrell, D.E., Park, H.S. and Liu, W.K., “Implementation Aspects of the Bridging Scale Method and Application to Intersonic Crack Propagation,” International Journal for Numerical Methods in Engineering, 71, 583-605, 2007.

[28] Park, H. S., Karpov, E. G., Klein, P. A. and Liu, W. K., “Three-dimensional Bridging Scale Analysis of Dynamic Fracture,” Journal of Computational Physics, 207, 588-609, 2005.

[29] Rudd, R.E., “Coarse-Grained Molecular Dynamics for Computer Modeling of Nanomechanical Systems,” International Journal for Multiscale Computational Engineering, 2(2), 203-220, 2004.

[30] Twu, S. and Choi, K.K., “Configuration Design Sensitivity Analysis of Built-up Structures Part II: Numerical Method,” International Journal for Numerical Methods in Engineering, 36, 4201-4222, 1993.

[31] http://paulino.cee.illinois.edu/educational.html

[32] Choi, K. K., Kim, N., Structural Sensitivity Analysis and Optimization 1, Springer, NY 2004.

[33] Kim, N.H. and Choi, K.K., “Design sensitivity analysis and optimization of nonlinear transient dynamics,” Mechanics of Structures and Machines, 29(3), 351-371, 2001.

[34] Kim, M.G., Jang, H. and Cho, S., “Adjoint Design Sensitivity Analysis of Reduced Atomic Systems using Generalized Langevin Equation for Lattice Structures,” Journal of Computational Physics, 240, 1-19, 2013.

[35] Wang, Y. and Chang, K.H., “Continuum-based Sensitivity Analysis for Coupled Atomistic and Continuum Simulations for 2-D Applications using Bridging Scale Decomposition,” Structural Multidisciplinary Optimization, 47(6), 867-892, 2013.

[36] Jones, J.E., “On the Determination of Molecular Fields. II. From the Equation of State of a Gas,” Proceedings of the Royal Society of London A, 106(738), 463-477, 1924.

[37] Falk, M.L., “Molecular-dynamics Study of Ductile and Brittle Fracture in Model Noncrystalline Solids,” Physical Review B, 60(10), 1999.

[38] Chang, W.J. and Fang, T.H., “Influence of Temperature on Tensile and Fatigue Behavior of Nanoscale Copper Using Molecular Dynamics Simulation,” Journal of Physics and Chemistry of Solids, 64, 1279-1283, 2003.

[39] Chang, K.H. and Wang,Y., “Sensitivity Analysis for Coupled Atomistic and Continuum Simulations using Bridging Scale Decomposition,” Mechanics Based Design of Structures and Machines, 40, 292-333, 2012.

[40] Kelchner, C.L., Plimton, S.J. and Hamilton, J.C., “Dislocation Nucleation and Defect Structure during Surface Indentation,” Physical Review B, 58(17), 1998.

[41] Gumbsch, P., Zhou, S J. and Holian, B.L., “Molecular Dynamics Investigation of Dynamic Crack Stability,” Physical Review B, 55(6), 1997.

[42] Qin, Z. and Buehler, M.J., “Dynamic Failure of a Lamina Meshwork in Cell Nuclei under Extreme Mechanical Deformation,” BioNanoScience, 1, 14-23, 2011.

[43] Karimi, M., Roarty, T. and Kaplan, T., “Molecular Dynamics Simulations of Crack Propagation in Ni with Defects,” Modelling and Simulation in Materials Science and Engineering, 14, 1409-1420, 2006.

[44] MATLAB, computer software, Ver. 7.12, The MathWorks Inc., Natick, MA, 2011.

[45] Mortenson, M.E., Geometric Modeling, John Wiley and Sons, Inc., NY 1997.

[46] Chang, K.H. and Edke, M., “Manufacturing in Shape Optimization of Structural Components,” Computational Optimization: New Research Developments, edited by Linton, R.F. and Carroll, T.B., Nova Science Publishers, Inc., 2009.

[47] Chang, K.H. and Choi, K.K., "A Geometry-Based Parameterization Method for Shape Design of Elastic Solids," Mechanics Based Design of Structures and Machines, 20(2), 215-252, 1992.

[48] Choi, K.K and Chang, K.H., "A Study of Design Velocity Field Computation for Shape Optimal Design," Finite Elements in Analysis and Design, 15(4), 317-342, 1994.

[49] Chang, K.H., Yu, X. and Choi, K.K., "Shape Design Sensitivity Analysis and Optimization for Structural Durability," International Journal of Numerical Methods in Engineering, 40, 1719-1743, 1997.

[50] Daw, M.S. and Baskes, M.I., "Semiempirical Quantum Mechanical Calculation of Hydrogen Embrittlement in Metals," Physical Review Letters, 50(17), 1285-1288, 1983.

[51] Anderson, T.L., Fracture Mechanics: Fundamentals and Applications, Third Edition, CRC Press, FL 2005.

[52] Freund, L.B., Dynamic Fracture Mechanics, Cambridge University Press, 1990.

[53] Griffith, A.A., "The Phenomenon of Rupture and Flow in Solids," Philosophical Transactions of the Royal Society A, 221, 163-198, 1920.

[54] Irwin, G.R., "Fracture dynamics," Fracturing of Metals, American Society for Metals, 147-166, OH 1948.

[55] Yoffe, E.H., "The Moving Griffith Crack," Philosophical Magazine, 42, 739-750, 1951.

[56] Gao, H., "A Theory of Local Limiting Speed in Dynamic Fracture," Journal of the Mechanics and Physics of Solids, 44(9), 1453-1474, 1996.

[57] Gao, H., "Elastic Waves in a Hyperelastic Solid Near its Plane-strain Equibiaxial Cohesive Limit," Philosophical Magazine Letters, 76(5), 307-314, 1997.

[58] Wagner, G.J., Karpov, E.G. and Liu, W.K., "Molecular Dynamics Boundary Conditions for Regular Crystal Lattices," Computer Methods in Applied Mechanics and Engineering, 193, 1579-1601, 2004.

[59] Weeks, W. T., "Numerical Inversion of Laplace Transforms Using Laguerre Functions," Journal of the Association for Computing Machinery, 13(3), 419-426, 1966.

[60] Wang, Y., "Energy Based Sensitivity Analysis for Coupled Atomistic and Continuum Simulations for 2-D Applications using Bridging Scale Decomposition," M.S. Thesis, University of Oklahoma, Norman, OK, 2012.

APPENDIX A

DYNAMIC FRACTURE IN BRITTLE MATERIALS – CONTINUUM THEORY AND ATOMISTIC SIMULATIONS

In this appendix, theoretical concepts of dynamic brittle fracture at the continuum scale will be reviewed first, followed by the demonstration of a series of MD simulations of dynamic crack propagation with simple potential functions. A systematic comparison between continuum mechanics theories and MD simulation results will be given. For more information, many reviews of continuum fracture mechanics theory are available such as [51,52], and detailed explanations of the MD examples discussed in this appendix can be found in [8].

A1 Basics of Linear Elastic Fracture Mechanics

In linear elastic fracture mechanics (LEFM), it is assumed that the material is continuous, isotropic and linear elastic. The linear elastic fracture mechanics theory serves as the basis of various later developed continuum fracture mechanics theories that are capable of dealing with nonlinear material behavior or dynamic effects. In fact, the continuum theories have made powerful predictions of the material behavior near cracks, and have been proven to be successful and applicable to a wide range of applications. In this section, we review some of the important concepts of linear elastic fracture mechanics, such as the Griffith's criterion, crack tip stress field, crack limiting speed, and dynamic crack instability.

The Griffith Energy Balance

In 1920, Griffith [53] first postulated that a crack starts to grow when the decrease in potential energy due to crack growth equals the energy necessary to create new material surfaces. The Griffith energy balance for an increment of the crack area dA can be expressed under equilibrium conditions, as

$$\frac{dU}{dA} = \frac{dW_P}{dA} + \frac{dW_S}{dA} = 0 \tag{A1}$$

where U, W_P and W_S denote total energy in the system, potential energy supplied by the internal strain energy and external load, and energy required to create new surfaces, respectively. In 1948, Irwin [54] defined an energy release rate

$$G = -\frac{dW_P}{dA} \tag{A2}$$

as a measure of the rate of change in potential energy with the crack area. Crack propagation occurs when the energy release rate reaches a critical value

$$G = 2\gamma_S \tag{A3}$$

where γ_S is the surface energy per unit area.

Stress Field near Crack Tip

There are three types of loading that a crack can experience. As illustrated in Fig. A1a, in mode I loading, the principal load is applied normal to the crack plane; mode II corresponds to in-plane shear loading; mode III refers to out-of-plane shear. A cracked body can be loaded in any one of these modes, or a combination of two or three modes.

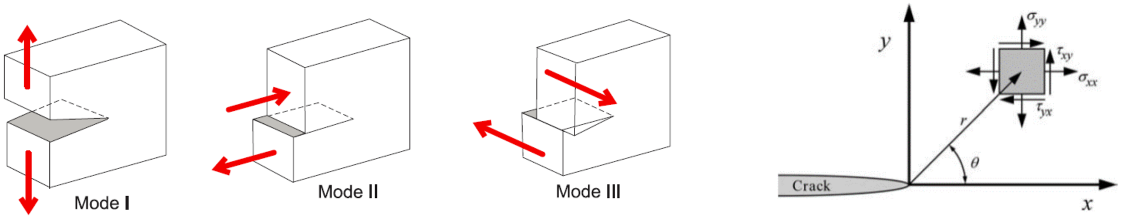

(a) (b)

Figure A1 (a) Three modes of loading [8]. (b) The polar coordinate ahead of a crack tip [51]

Assuming isotropic linear elastic material behavior, it is possible to express the stress field in the vicinity of the crack tip. If we define a polar coordinate system with the origin at the crack tip (Fig. A1b), the stress field near the crack tip for a mode I loading condition can be written as

$$\sigma_{xx}(r,\theta)=\frac{K_I}{\sqrt{2\pi r}}\cos\left(\frac{\theta}{2}\right)\cdot\left[1-\sin\left(\frac{\theta}{2}\right)\sin\left(\frac{3\theta}{2}\right)\right] \tag{A4a}$$

$$\sigma_{yy}(r,\theta)=\frac{K_I}{\sqrt{2\pi r}}\cos\left(\frac{\theta}{2}\right)\cdot\left[1+\sin\left(\frac{\theta}{2}\right)\sin\left(\frac{3\theta}{2}\right)\right] \tag{A4b}$$

$$\tau_{xy}(r,\theta)=\frac{K_I}{\sqrt{2\pi r}}\cos\left(\frac{\theta}{2}\right)\sin\left(\frac{\theta}{2}\right)\cos\left(\frac{3\theta}{2}\right) \tag{A4c}$$

where K_I is called the mode I stress intensity factor. Note that in addition to the static solution, more general solutions that also include the case of moving cracks can be found in [52].

Crack Limiting Speed

Brittle crack grows rapidly in material. In general, a larger applied load leads to faster crack propagation. However, the maximum speed that a crack can attain is limited by an upper bound related to the speed of waves in the elastic media in which the crack propagates. According to the continuum theory, mode I, mode II and mode III cracks are limited by the Rayleigh wave speed c_R, longitudinal wave speed c_l, and shear wave speed c_s, respectively [8]. The physical reason for the limiting speed is the dependence of the energy release rate G on the crack speed. For example, for mode I crack propagation,

$$G \sim 1 - \frac{v}{c_R} \tag{A5}$$

which implies that the energy release rate approaches zero when crack speed v approaches the Rayleigh wave speed.

Dynamic Crack Instability

It has been observed in many experimental and computational studies on rapidly moving cracks in brittle materials that the crack face morphology changes as the crack speed increases – a phenomenon usually referred to as the dynamic instability of cracks. As shown in Fig. 1.1b, up to a critical speed, newly created crack surfaces are mirror flat, whereas at higher speeds, the crack surfaces start to roughen (mist regime) and eventually become very rough (hackle regime). This behavior is found to be universal for a variety of brittle materials including ceramics, glasses and polymers.

During the past few decades, several theoretical explanations of crack instability have been proposed. For example, the linear elastic analyses carried out by Yoffe [55] predicted that the instability speed of cracks is about 73% of the Rayleigh wave speed. However, experiments and numerical simulations have suggested that the actual critical instability speed can be much lower in many materials. Gao [56,57] proposed a model to explain the reduced instability speed based on the concept of hyperelasticity within the framework of nonlinear continuum mechanics, with the central argument that atomic bonding in real materials tends to soften with increasing strain.

Despite important progresses in the past, so far there is still no clear picture of the mechanisms underlying dynamical crack instability. None of the existing theoretical models are able to explain all experimental and numerical results with a universal understanding applicable to a wide range of materials.

A2 Atomistic Simulations

Molecular dynamics simulation of dynamic fracture is becoming increasingly popular due to the rapid advance in computation technology. In contrast to continuum theories, an MD simulation model does not require a priori knowledge about the failure, and therefore is more useful in investigating the most fundamental aspects of dynamic crack propagation. Numerous MD simulations have been carried out to study dynamic fracture in brittle materials, some of which are mentioned in Chapter 1 of this thesis. Many of the reported works are focused on understanding the atomistic physics of crack propagation and its relation to continuum theories. In this section, we present several MD simulations of dynamic fracture that are well documented in [8]. These simulations are performed on two dimensional atomic lattices, where interatomic interactions are modeled with simple potential functions. Our goal is to illustrate the correlation between atomistic simulations and continuum theories in several aspects including crack tip stress field, crack limiting speed, and dynamic instability. It will be demonstrated that nonlinearity plays a governing role in dynamic fracture.

Crack Tip Stress Field and Crack Limiting Speed

In the MD studies to be presented in this section, the LJ 6-12 potential with reduced units (discussed in Section 3.2) will be adopted as the basis to model the interatomic interactions. For example, to study a harmonic system, we define a harmonic potential by expanding the LJ potential function around its equilibrium position and consider only first order terms; that is

$$\Phi(r) = a_0 + \frac{1}{2}k(r - h_a)^2 \tag{A6}$$

where h_a is the equilibrium distance, k is the interaction coefficient defined in Eq. 3.4, and a_0 is a constant parameter set to -1 in harmonic approximation.

The 2-D simulation model is illustrated in Fig. A2. As can be seen, the crack propagates in a triangular hexagonal atomic lattice. To avoid crack branching, the harmonic potential (Eq. A6) is used to model the interactions between atoms (so that atomic bonds will never break), except that a weak fracture layer is introduced by modelling the atomic bonds across the layer using the nonlinear LJ 6-12 potential (Eq. 3.2). During simulation, the model is slowly loaded with a constant strain rate, which induces the propagation of the initial crack along the y direction.

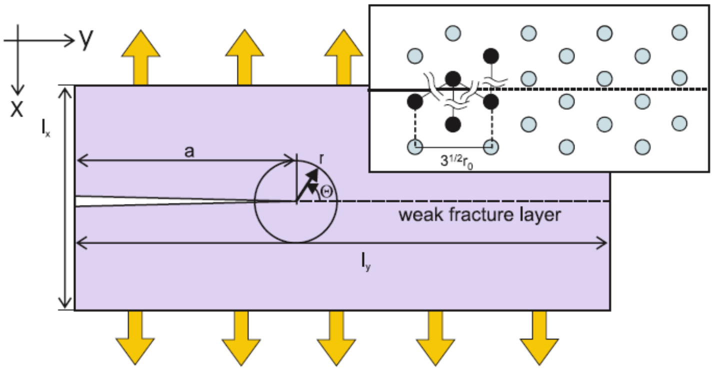

Figure A2 A schematic illustration of the simulation model [8]

The simulation results are shown in Fig. A3, in which the measured angular variation of σ_{xx} is plotted for different crack speeds ranging from 0 to 87% of the Rayleigh speed, and compared with the continuum solution of dynamic crack tip stress field given in [52]. Atomic quantities are evaluated in a small region around a constant radius of $r \approx 11$ (Fig. A2, normalized unit) centered at the crack tip. The continuum theory solution and the simulation results are both normalized with respect to the dynamic stress intensity factor [52].

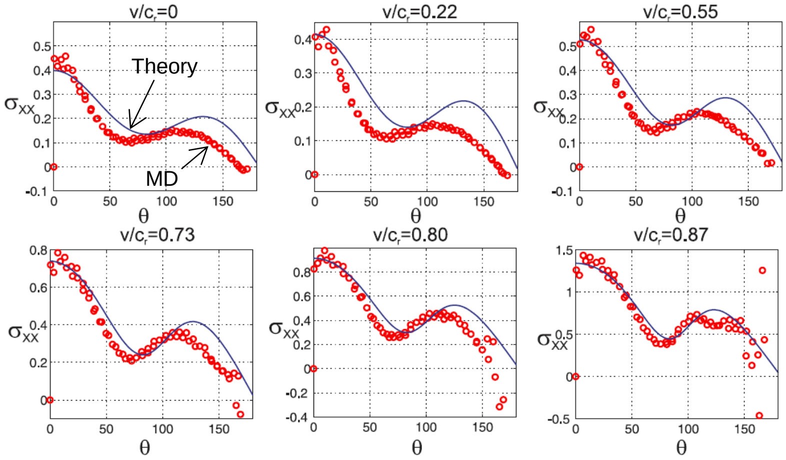

Figure A3 Comparison between σ_{xx} measured in MD simulations and the prediction of the continuum mechanics theory for different crack speeds. The solid curves represent continuum solution, and the red dots are measured in MD simulations [8]

As can be seen, the stress field σ_{xx} measured in MD simulation is generally in agreement with the LEFM solution (same for other quantities such as σ_{yy} and τ_{xy}). It is also found that acceleration effects can severely change the resulting stress fields. If the measurements are taken while the crack accelerates too rapidly, the agreement of measured field and continuum theory prediction can be poor.

The comparison of principal strain field is shown in Fig. A4 for different velocities of $v/c_R \approx 0$, $v/c_R \approx 0.5$, and $v/c_R \approx 1$. Note that the MD result is in good agreement with the continuum theory. It can be seen clearly that the typical trimodal structure of the asymptotic principal strain field develops close to the Rayleigh velocity, in contrast to the bimodal structure at low crack speeds.

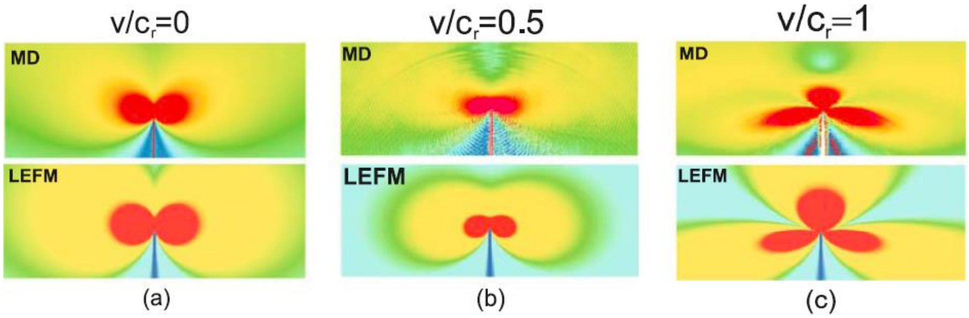

Figure A4 Principal strain field at various crack speeds (a) $v/c_R \approx 0$, (b) $v/c_R \approx 0.5$, (c) $v/c_R \approx 1$ [8]

To study the limiting speed of cracks, the same model in Fig. A2 with a fracture layer is used. A harmonic system is simulated first, in which the atomic bonds across the fracture layer is modeled by the harmonic potential (Eq. A6), but with a snapping distance r_{break} at which the bond breaks. The simulation result demonstrates that, independent of model size, the harmonic system behaves as predicted by linear elastic continuum theories of fracture, i.e., a mode I crack cannot move faster than the Rayleigh wave speed (c_R = 4.8 for the 2-D lattice studied), as shown in Fig. A5.

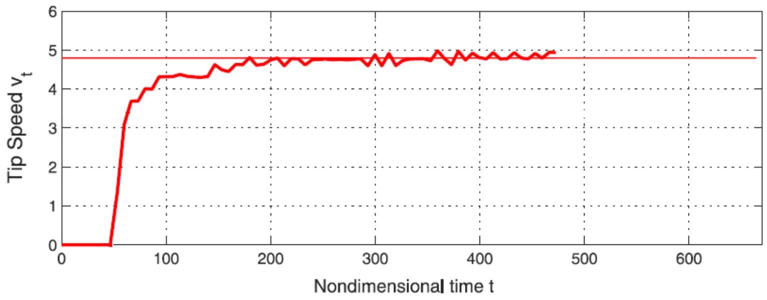

Figure A5 Crack speed history for the harmonic material model in simulation [8]

To reveal the impact of nonlinearity on the speed of crack propagation, the harmonic potential is then replaced by a biharmonic potential in order to model the nonlinear effect. As shown in Fig. A6a, the value of k_1 refers to the large-strain interaction coefficient, and the parameter r_{on} (or $\varepsilon_{\mathrm{on}}$) allows us to tune the size of the nonlinear region near the crack tip. The potential function illustrated in Fig. A6a models an elastic ‘stiffening’ material.

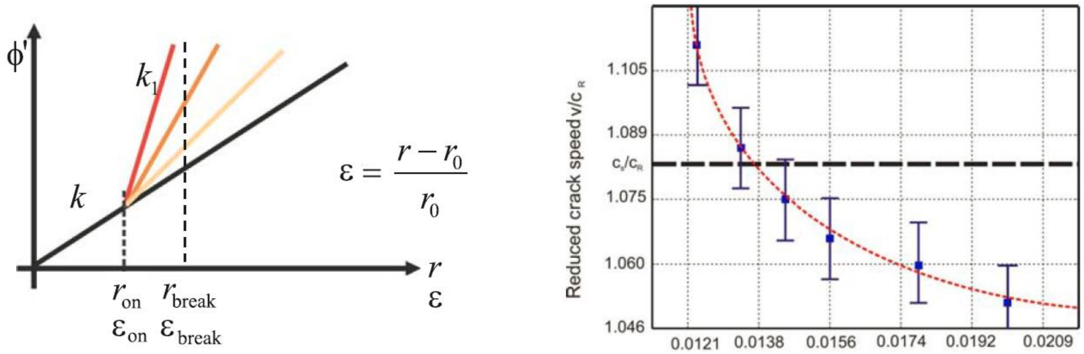

(a) (b)

Figure A6 (a) A biharmonic potential with stiffening effect. (b) Change of reduced limiting crack speed (Limiting crack speed/Rayleigh wave speed c_R) as a function of $\varepsilon_{\mathrm{on}}$ [8]

The simulation results show crack propagation at super-Rayleigh velocities with a local stiffening zone around the crack tip. Figure A6b plots the limiting crack speed as a function of $\varepsilon_{\mathrm{on}}$. As can be seen, the earlier the nonlinear effect is turned on, the larger the limiting speed. For example, when the large-strain interaction coefficient is chosen to be $k_1 = 4k$, with $r_{\mathrm{on}} = 1.1375$ and $r_{bearK} = 1.1483$, the mode I crack can propagate about 20 percent faster than the Rayleigh wave speed of the material, in clear contrast to the linear continuum theory. It is also found that the limiting crack speed is lower than in the harmonic case if a local ‘softening’ effect is modeled. Therefore, it is clear that local nonlinearity around the crack tip can significantly influence the limiting speed of cracks.

Dynamic Crack Instability

To study dynamic crack instability, atomistic models with different potential functions are investigated. An interatomic force function is defined as

$$f(r) = \frac{d\,\Phi}{dr}(r) = k(r - h_a)\left[\exp\left(r\frac{\Xi}{r_{break}} - \Xi\right) + 1\right]^{-1} \qquad \text{(A7)}$$

so that a series of MD simulations can be performed by varying systematically the parameters r_{break} and Ξ. Figure A7 depicts interatomic force versus atomic bond length with different r_{break} and Ξ. As can be seen, the parameter Ξ controls the shape of the interatomic force curve (Fig. A7b). Note that the curve becomes smoother with a smaller Ξ, whereas an infinitely large Ξ leads to a harmonic potential. By performing MD simulations using potential models with different parameters, the impact of the transition from linear elastic to strongly nonlinear material behavior on the instability dynamics of cracks can be understood.

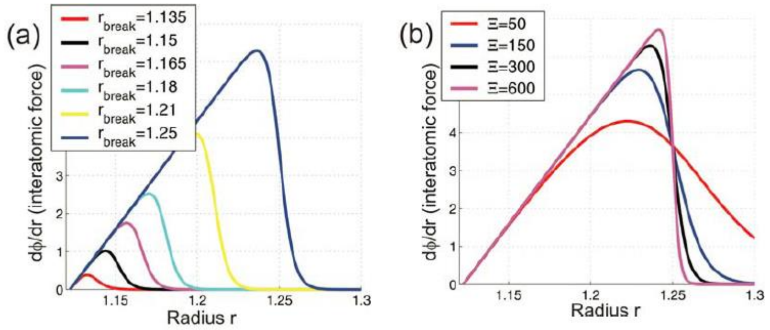

Figure A7 Interatomic force versus atomic bond length for various choices of parameters r_{break} and Ξ [8]

First of all, it is found that for materials with linear elastic properties (harmonic potential, achieved by setting Ξ in Eq. A7 to infinity), a critical instability speed of about 73% of the Rayleigh wave speed can be observed independent of the choice of r_{break}. Apparently, this is in quantitative agreement with the prediction of Yoffe's model [55], in which the nonlinearity of atomic bonds is completely neglected.

Next, the parameters in Eq. A7 are adjusted systematically to model different levels of nonlinearity near the crack tip. In Fig. A8, the prediction by Yoffe's model [55] is shown as the red line, while the predictions by Gao's model [56,57] are plotted as the blue points. As can be seen, for any choice of r_{break} and Ξ, the critical instability speed lies in between the prediction by Gao's model and that by Yoffe's model. Whether it is closer to the former or the latter depends on the choice of r_{break} and Ξ. These results indicate that the critical instability speed depends strongly on the nonlinearity introduced at the crack tip.

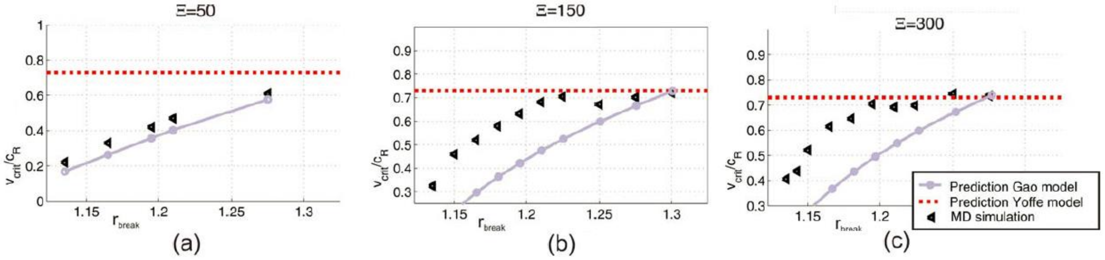

Figure A8 Critical instability speed as a function of r_{break} for different choices of Ξ [8]

Summary

Based on the observations above, it is clear that the predictions by linear elastic fracture mechanics theories can be recaptured in MD simulations when a harmonic potential is used to model the interaction between atoms; in the meantime, the nonlinearity near the crack tip significantly influences the fracture mechanism, and is crucial in producing simulation results that are closer to the behavior of real materials. In this thesis, we use the bridging scale method to simulate crack propagation. Although the majority of the structural domain is modeled using finite elements based on linear elasticity, a fully nonlinear (instead of biharmonic) potential function is used for MD simulation (discussed in Section 3.2) near the crack tip, so that the essential physics of brittle fracture can be capture in our numerical example.

APPENDIX B

ADJOINT VARIABLE METHOD

In this appendix, we explain the adjoint variable method for design sensitivity analysis using the simple bar example introduced in Chapter 2. Both static and dynamic scenarios will be discussed. More information about the adjoint method can be found in [32].

Static Problem

In Section 2.2.2.2, sensitivity analysis is carried out using the discrete method, while the direct differentiation method is employed to calculate the sensitivity coefficient of a general performance measure. It is noteworthy that all terms in Eq. 2.31 can be easily calculated from their definitions, except for the term $(\partial\psi/\partial\mathbf{z})\mathbf{K}^{-1}(\mathbf{b})$, which apparently does not vary during the sensitivity analysis with respect to different design variables. Therefore, the adjoint variable method is developed to compute this term directly by defining it as the adjoint variable $\boldsymbol{\lambda}$:

$$\boldsymbol{\lambda} \equiv \left[\frac{\partial\psi}{\partial\mathbf{z}}\mathbf{K}^{-1}(\mathbf{b})\right]^T = \mathbf{K}^{-1}(\mathbf{b})\frac{\partial\psi}{\partial\mathbf{z}}^T \tag{B1}$$

where the symmetric property of $\mathbf{K}(\mathbf{b})$ has been used. By multiplying both sides of Eq. B1 by $\mathbf{K}(\mathbf{b})$, we obtain the adjoint equation

$$\mathbf{K}(\mathbf{b})\boldsymbol{\lambda} = \frac{\partial\psi}{\partial\mathbf{z}}^T \tag{B2}$$

which represents the same structural problem as with Eq. 2.26, except that the load vector is replaced by $(\partial\psi/\partial\mathbf{z})^T$ – sometimes referred to as the *adjoint load*. Solving the adjoint problem in Eq. B2 and substituting the result into Eq. 2.31 gives the sensitivity of the performance measure, as

$$\frac{d\psi}{db_i} = \frac{\partial \psi}{\partial b_i} + \boldsymbol{\lambda}^T \left[\frac{\partial \mathbf{F}(\mathbf{b})}{\partial b_i} - \frac{\partial \mathbf{K}(\mathbf{b})}{\partial b_i} \mathbf{z} \right] \tag{B3}$$

For the simple bar example, the adjoint problem becomes

$$\mathbf{K}\boldsymbol{\lambda} = \frac{\partial z_3}{\partial \mathbf{z}}^T = \begin{bmatrix} 0 \\ 1 \end{bmatrix} \tag{B4}$$

Note that as shown in Fig. B1, the load vector in Eq. B4 represents a unit point load acting on Node 3 – the location where we measure the performance z_3. The adjoint structure in Eq. B4 can be solved for **λ**, as

$$\boldsymbol{\lambda} = \begin{bmatrix} \frac{l}{2EA} & \frac{l}{EA} \end{bmatrix}^T \tag{B5}$$

which can then be substituted into Eq. 2.31 to obtain the design derivative of the performance measure z_3, as

$$\frac{dz_3}{dl} = \frac{\partial z_3}{\partial l} + \boldsymbol{\lambda}^T \left[\frac{\partial \mathbf{F}}{\partial l} - \frac{\partial \mathbf{K}}{\partial l} \mathbf{z} \right] = 0 + \begin{bmatrix} \frac{l}{2EA} & \frac{l}{EA} \end{bmatrix} \cdot \left\{ \begin{bmatrix} f/2 \\ f/4 \end{bmatrix} + \frac{2EA}{l^2} \begin{bmatrix} 2 & -1 \\ -1 & 1 \end{bmatrix} \cdot \begin{bmatrix} \frac{3fl^2}{8EA} \\ \frac{fl^2}{2EA} \end{bmatrix} \right\} = \frac{fl}{EA} \tag{B6}$$

which is the same as the result obtained by using the direct differentiation method (Eq. 2.32).

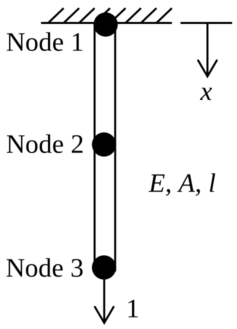

Figure B1 Adjoint structure for the simple bar example

To determine which approach – the direct differentiation method or the adjoint variable method – will be employed, we compare the number of equations to be solved during sensitivity calculation. The direct differentiation method computes sensitivity using the chain rule of differentiation. To calculate the design derivative of each performance ψ_i, Eq. 2.29 must be solved for each design variable b_i. Therefore, k (the number of design variables) matrix equations need to be solved. With all $d\mathbf{z}/db_i$, the sensitivity of each performance can be calculated directly from Eq. 2.31. On the other hand, the adjoint variable method computes sensitivity by constructing and solving the adjoint problem. The adjoint structure in Eq. B2 must be solved for each performance measure ψ_i, while the adjoint solution $\boldsymbol{\lambda}_i$ can be used for all design variables, i.e., the sensitivity of performance ψ_i with respect to each design variable b_i can be calculated directly from Eq. B3. As a result, the number of equations to be solved equals to N_P – the number of performance measures.

Therefore, from computation perspective, in general, if the number of performance measures is larger than that of the design variables ($N_P > k$), then the direct differentiation method is preferable; otherwise, the adjoint variable method will be more efficient.

Dynamic Problem

For dynamic problems, the sensitivity calculation using the direct differentiation method has been demonstrated in Section 2.3.2 (Eqs. 2.64 ~ 2.68). In adjoint variable method, the essence is to replace the unknown terms in Eq. 2.65 with adjoint variables. In case of a general dynamic problem, we start by multiplying both sides of the dynamic finite element matrix equation (Eq. 2.59) by $\boldsymbol{\lambda}^T$ and then integrating over time interval $[0, t_T]$, yielding

$$\int_0^{t_T} \boldsymbol{\lambda}^T \left[\mathbf{M}(\mathbf{b})\mathbf{z}_{,tt} + \mathbf{K}(\mathbf{b})\mathbf{z} - \mathbf{F}(\mathbf{b})\right] dt = 0 \tag{B7}$$

Given that $\boldsymbol{\lambda}$ is defined to be independent of design, we take design derivative of Eq. B7 with respect to b_i, as

$$\int_0^{t_T} \boldsymbol{\lambda}^T \left[\mathbf{M}\left(\frac{d\mathbf{z}}{db_i}\right)_{,tt} + \frac{\partial \mathbf{M}}{\partial b_i}\mathbf{z}_{,tt} + \mathbf{K}\frac{d\mathbf{z}}{db_i} + \frac{\partial \mathbf{K}}{\partial b_i}\mathbf{z} - \frac{\partial \mathbf{F}}{\partial b_i}\right] dt = 0 \tag{B8}$$

Next, the time derivative of $d\mathbf{z}/db_i$ within the integral in Eq. B8 can be eliminated using integration by parts to obtain the following relation

$$\boldsymbol{\lambda}^T \mathbf{M}\left(\frac{d\mathbf{z}}{db_i}\right)_{,t}\Bigg|_0^{t_T} - \boldsymbol{\lambda}^T_{,t}\mathbf{M}\frac{d\mathbf{z}}{db_i}\Bigg|_0^{t_T} + \int_0^{t_T}\left[\boldsymbol{\lambda}^T_{,tt}\mathbf{M}\frac{d\mathbf{z}}{db_i} + \boldsymbol{\lambda}^T\left(\frac{\partial \mathbf{M}}{\partial b_i}\mathbf{z}_{,tt} + \frac{\partial \mathbf{K}}{\partial b_i}\mathbf{z} + \mathbf{K}\frac{d\mathbf{z}}{db_i} - \frac{\partial \mathbf{F}}{\partial b_i}\right)\right] dt = 0 \tag{B9}$$

where the initial terms can be removed by accounting for the initial conditions in Eq. 2.68, giving

$$\boldsymbol{\lambda}(t_T)^T \mathbf{M}\left(\frac{d\mathbf{z}(t_T)}{db_i}\right)_{,t} - \boldsymbol{\lambda}(t_T)^T_{,t}\mathbf{M}\frac{d\mathbf{z}(t_T)}{db_i} + \int_0^{t_T}\left[\left(\boldsymbol{\lambda}^T_{,tt}\mathbf{M} + \boldsymbol{\lambda}^T\mathbf{K}\right)\frac{d\mathbf{z}}{db_i} + \boldsymbol{\lambda}^T\left(\frac{\partial \mathbf{M}}{\partial b_i}\mathbf{z}_{,tt} + \frac{\partial \mathbf{K}}{\partial b_i}\mathbf{z} - \frac{\partial \mathbf{F}}{\partial b_i}\right)\right] dt = 0 \tag{B10}$$

which must hold for all $\boldsymbol{\lambda}$.

Now we define the dynamic adjoint problem as follows

$$\mathbf{M}\cdot\boldsymbol{\lambda}(t_T) = 0 \tag{B11a}$$

$$\mathbf{M}\cdot\boldsymbol{\lambda}(t_T)_{,t}=-\frac{\partial g}{\partial \mathbf{z}}^T \tag{B11b}$$

$$\mathbf{M}\cdot\boldsymbol{\lambda}_{,tt}+\mathbf{K}\cdot\boldsymbol{\lambda}=\frac{\partial G}{\partial \mathbf{z}}^T \tag{B11c}$$

Note that the adjoint problem above is defined in such a way that by substituting the adjoint solution **λ** that satisfies Eq. B11 into Eq. B10, we obtain

$$\frac{\partial g}{\partial \mathbf{z}}\frac{d\mathbf{z}(t_T)}{db_i}+\int_0^{t_T}\frac{\partial G}{\partial \mathbf{z}}\frac{d\mathbf{z}}{db_i}dt=-\int_0^{t_T}\boldsymbol{\lambda}^T\left(\frac{\partial \mathbf{M}}{\partial b_i}\mathbf{z}_{,tt}+\frac{\partial \mathbf{K}}{\partial b_i}\mathbf{z}-\frac{\partial \mathbf{F}}{\partial b_i}\right)dt \tag{B12}$$

where all implicit terms in Eq. 2.65 are expressed by explicit terms and the adjoint variable. Therefore, once the adjoint solution **λ** is obtained by solving the adjoint problem, the sensitivity of the performance measure can be calculated as

$$\frac{d\psi}{db_i}=\frac{\partial g}{\partial b_i}+\int_0^{t_T}\frac{\partial G}{\partial b_i}dt-\int_0^{t_T}\boldsymbol{\lambda}^T\left(\frac{\partial \mathbf{M}}{\partial b_i}\mathbf{z}_{,tt}+\frac{\partial \mathbf{K}}{\partial b_i}\mathbf{z}-\frac{\partial \mathbf{F}}{\partial b_i}\right)dt \tag{B13}$$

Note that in dynamic scenarios, the direct differentiation method always allows the sensitivity equation (Eq. 2.67) to be solved in parallel with response analysis (Eq. 2.59). On the contrary, the adjoint problem in Eq. B11 can be thought of as a terminal-value problem that needs to be solved backwards in time from $t = t_T$ to $t = 0$. Thus, in cases when the performance measure is not a linear function of displacement solution **z**, i.e., when $\partial g/\partial \mathbf{z}$ and $\partial G/\partial \mathbf{z}$ in Eq. B11 are not constants but depend on **z**, the adjoint problem cannot be solved simultaneously with the response analysis. This complicates significantly the calculations associated with dynamic sensitivity analysis. In fact, even if the adjoint problem can be solved simultaneously with the response analysis, the calculation of the time integral term in design sensitivity (Eq. B13) requires either the solution of structural response or the adjoint equation throughout the entire simulation period [0, t_T] to be stored, which places heavy burden to the I/O system.

Therefore, for dynamic problems, as long as the number of design variables is not much greater than that of performance measures, the direct differentiation method is generally preferable to the adjoint variable method.

APPENDIX C

DERIVATION OF TIME HISTORY KERNEL FOR 1-D ATOMIC LATTICE

This appendix demonstrates detailed derivation of the time history kernel for the one-dimensional atomic lattice discussed in Chapter 3. Discrete Fourier Transform and Laplace Transform will be introduced first to support the derivation.

Discrete Fourier Transform and Laplace Transform

The *discrete Fourier transform* (DFT) is used to transform one function into its frequency domain representation. If a function *f* can be defined at all atomic positions *l*, the DFT of *f* is defined as

$$\hat{f}(p) = \mathcal{F}_{l\to p}\{f_l\} \equiv \sum_{l=-L/2+1}^{L/2} f_l e^{-i2\pi pl/L} \tag{C1}$$

where *L* indicates the size of the atomic lattice and *p* can take any integer value between –*L*/2 +1 and *L*/2. For 1-D problems, *L* gives the length of the domain. For multi-dimensional problems, more indices are needed to represent the additional dimensions. The *inverse Fourier transform* (IFT) is defined as

$$f_l = \mathcal{F}^{-1}_{p\to l}\left\{\hat{f}(p)\right\} \equiv \frac{1}{L}\sum_{p=-L/2+1}^{L/2} \hat{f}(p) e^{i2\pi pl/L} \tag{C2}$$

Note that when analytically calculating the time history kernel for a 1-D lattice, it is usually assumed that the discrete Fourier transform is carried out over an infinitely long chain, i.e., $-\infty < L < \infty$. Therefore, instead of taking integer values, the wavenumber *p* is mapped to the real numbers between -π and π, as discussed in [58].

The DFT and IFT for this limiting case take the form

$$\hat{f}(p) = \mathcal{F}_{l\to p}\{f_l\} \equiv \sum_{l=-\infty}^{\infty} f_l e^{-ipl} \tag{C3}$$

$$f_l = \mathcal{F}^{-1}_{p\to l}\left\{\hat{f}(p)\right\} \equiv \frac{1}{2\pi}\int_{-\pi}^{\pi} \hat{f}(p) e^{ipl} dp \tag{C4}$$

The *Laplace transform* (LT) is interpreted as a transformation from the time domain, in which inputs and outputs are functions of time, to the frequency domain. The LT of a function $f(t)$ is defined as

$$F(s) = \mathcal{L}\{f(t)\} \equiv \int_0^{\infty} f(t) e^{-st} dt \tag{C5}$$

while the *inverse Laplace transform* is defined to be

$$f(t) = \mathcal{L}^{-1}\{F(s)\} \equiv \frac{1}{2\pi i}\int_{c-i\infty}^{c+i\infty} F(s) e^{st} ds \tag{C6}$$

Because of the complex expressions involved in bridging scale problems, for 2-D and 3-D problems, the inverse Laplace transform has to be conducted numerically. The method employed is introduced by Weeks et al. [59]. This method utilizes an expansion of the inverse in terms of orthonormal Laguerre functions, yielding excellent accuracy.

The Laplace transform of the time derivative of a function is written as

$$\mathcal{L}\left\{\frac{d^n f(t)}{dt^n}\right\} = s^n F(s) - s^{n-1} f(0) - s^{n-2}\frac{df}{dt}(0) - \cdots - \frac{d^{n-1} f}{dt^{n-1}}(0) \tag{C7}$$

Finally, both the DFT and the LT have convolution properties as follows

$$\mathcal{F}_{l\to p}\left(\sum_{l'=-L/2+1}^{L/2} f_{l-l'} g_{l'}\right) = \hat{f}(p)\hat{g}(p) \tag{C8}$$

$$\mathcal{L}\left\{\int_0^t f(t-\tau) g(\tau) d\tau\right\} = F(s) G(s) \tag{C9}$$

Derivation of Time History Kernel

Following the discussion in Section 3.3.3, the linearized fine scale equation of motion for the boundary atom is obtained in Eq. 3.24, where the $f_0^{imp}(t)$ term is the impedance boundary force to be developed. Note that the effect of the *Region 2* fine scale degrees of freedom (implied by the v_1 term) is included in the impedance force, and our objective is to solve for v_1 in terms of v_0 by using discrete Fourier transform and Laplace transform, so that the fine scale degrees of freedom outside the MD area can be eliminated.

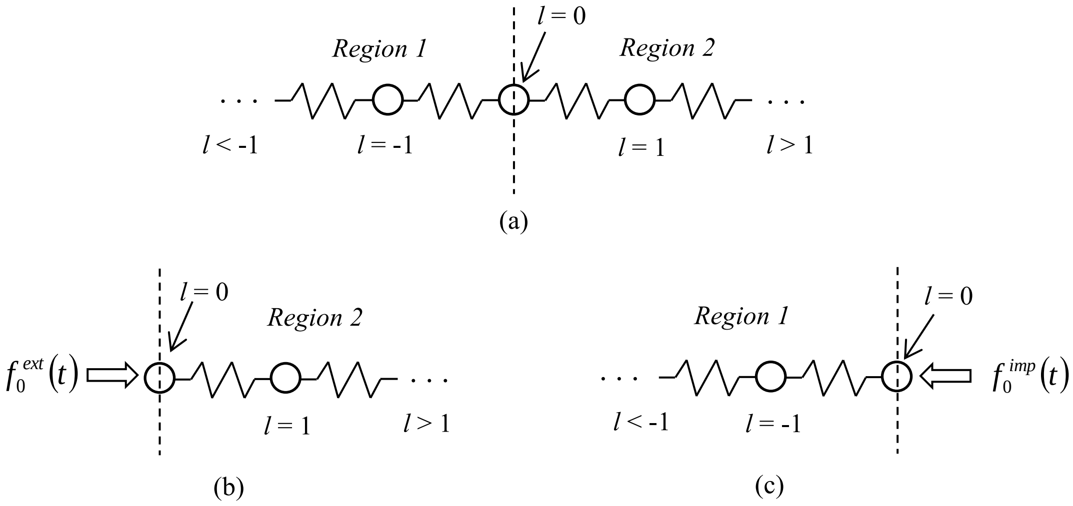

Figure C1 (a) Original 1-D atomic system, (b) $l < 0$ atoms replaced with $f_0^{ext}(t)$, and (c) *Region 2* fine scale eliminated by introducing the impedance boundary force $f_0^{imp}(t)$

As shown in Fig. C1a, the motion of the $l = 0$ atom depends on the displacement of itself and its nearest neighbors ($l = -1$ and $l = 1$). Since the Fourier transforms can be employed only for the atoms within the harmonic region ($l \geq 0$), the $l < 0$ atoms are temporarily removed from the system, and are replaced by an undetermined external force $f_0^{ext}(t)$ that acts only upon the $l = 0$ atom, as shown in Fig. C1b. Therefore, for the $l \geq 0$ atoms, Eq. 3.22 can be rewritten as

$$v_{l,tt}(t) = \sum_{l'=l-1}^{l+1} m_A^{-1} K_{l-l'} v_{l'}(t) + m_A^{-1} f_0^{ext}(t) \tag{C10}$$

Note that $f_0^{ext}(t)$ is introduced merely to support the derivation of the impedance boundary condition, and it is *NOT* the MD boundary force $f_0^{imp}(t)$ (Fig C1c) to be developed.

Taking discrete Fourier transform of Eq. C10 gives

$$\hat{V}_{,tt}(p,t) = \hat{A}(p)\hat{V}(p,t) + m_A^{-1} f_0^{ext}(t) \tag{C11}$$

where *p* corresponds to the spatial index *l*, and $\hat{A}(p)$ is the discrete Fourier transform of $m_A^{-1} K_l$; that is

$$\hat{A}(p) = \sum_{l=-\infty}^{\infty} m_A^{-1} K_l e^{-ipl} = \sum_{l=-1}^{1} m_A^{-1} K_l e^{-ipl} = \frac{2k}{m_A}(\cos p - 1) \tag{C12}$$

Taking Laplace transform of Eq. C11 yields

$$s^2 \hat{V}(p,s) - sv(p,0) - v_{,t}(p,0) = \hat{A}(p)\hat{V}(p,s) + m_A^{-1} F_0^{ext}(s) \tag{C13}$$

where *s* denotes the Laplace transform variables. Rearranging Eq. C13 gives

$$\hat{V}(p,s) = \hat{G}(p,s)\left(m_A^{-1} F_0^{ext}(s) + sv(p,0) + v_{,t}(p,0)\right) \tag{C14}$$

where

$$\hat{G}(p,s) = \left(s^2 - \hat{A}(p)\right)^{-1} = \frac{1}{s^2 - 2k(\cos p - 1)/m_A} \tag{C15}$$

Taking inverse Fourier transform of Eq. C14 gives

$$V_l(s) = G_l(s) m_A^{-1} F_0^{ext}(s) + R_l^d(s) \tag{C16}$$

where $G_l(s)$ is the inverse Fourier transform of $\hat{G}(p,s)$. For example

$$\begin{aligned} G_0(s) &= \frac{1}{2\pi}\int_{-\pi}^{\pi}\hat{G}(p,s)e^{0}dp \\ &= \frac{1}{2\pi}\int_{-\pi}^{\pi}\frac{1}{s^2-2k(\cos p-1)/m_A}dp = \frac{1}{s\sqrt{s^2+4k/m_A}} \end{aligned} \tag{C17}$$

and

$$\begin{aligned} G_1(s) &= \frac{1}{2\pi}\int_{-\pi}^{\pi}\hat{G}(p,s)e^{-ip}dp \\ &= \frac{1}{2\pi}\int_{-\pi}^{\pi}\frac{e^{-ip}}{s^2-2k(\cos p-1)/m_A}dp = \frac{m_A s^2+2k-m_A s\sqrt{s^2+4k/m_A}}{2ks\sqrt{s^2+4k/m_A}} \end{aligned} \tag{C18}$$

Note that the $R_l^d(s)$ term in Eq. C16 is related to the initial conditions in the continuum region, and is considered to be a random displacement that represents the thermally dependent excitations exerted on the MD region by the surrounding coarse scale. In our numerical examples, by assuming the temperature of the surrounding continuum to be 0K, this term can be set to zero.

By writing Eq. C16 for the $l = 0$ and $l = 1$ atoms while neglecting the random term $R_l^d(s)$, the external force $F_0^{ext}(s)$ can be cancelled out, and $V_1(s)$ can then be solved for in terms of $V_0(s)$, as

$$V_1(s) = Q(s)V_0(s) \tag{C19}$$

where

$$Q(s) = G_1(s)G_0^{-1}(s) = \frac{1}{2k}\left(m_A s^2 + 2k - m_A s\sqrt{s^2+4k/m_A}\right) \tag{C20}$$

To obtain the expression of the impedance force, we take Laplace transform of Eq. 3.25, yielding

$$F_0^{imp}(s) = K_{-1}V_1(s) \tag{C21}$$

Substituting Eq. C19 into Eq. C21 gives

$$F_0^{imp}(s) = K_{-1}Q(s)V_0(s) = \Theta(s)V_0(s) \tag{C22}$$

where

$$\Theta(s) = K_{-1}Q(s) = kQ(s) = \frac{1}{2}\left(m_A s^2 + 2k - m_A s\sqrt{s^2 + 4k/m_A}\right) \tag{C23}$$

Hence, the impedance boundary force can be obtained by taking inverse Laplace transform of Eq. C22, giving

$$f_0^{imp}(t) = \int_0^t \theta(t-\tau)v_0(\tau)d\tau \tag{C24}$$

where

$$\theta\ (t) = \mathcal{L}^{-1}(\Theta(s)) = \frac{2k}{t} J_2\left(2\sqrt{\frac{k}{m_A}}t\right) \tag{C25}$$

is called the time history kernel, in which J_2 stands for the second-order Bessel function. It is important to note that an analytical expression of the time history kernel is possible only for a 1-D lattice. For multiple dimensional problems, analytically deriving the impedance boundary condition can be intractable. Therefore, numerical procedures are inevitably involved, as presented in Appendix D.

APPENDIX D

DERIVATION OF IMPEDANCE BOUNDARY CONDITION FOR 3-D ATOMIC LATTICE

This appendix presents the derivation of bridging scale impedance boundary condition, including the time history kernel, in a generalized three dimension scenario. More details and discussions on this subject can be found in [28].

As with the derivation for the 1-D lattice discussed in Chapter 3, the key idea in deriving the impedance force for a 3-D lattice is to utilize the periodicity of the atomic structure so that standard technique of discrete Fourier transform (Appendix C) can be applied. For a better illustration, the 3-D FCC lattice used in our numerical example is depicted in Fig. D1, while Fig. D2 shows the m = 1 layer of the periodic 3-D lattice labeled with indices l, m, and n. It is of note, however, that the derivation to be presented below is general for a variety of lattice structures.

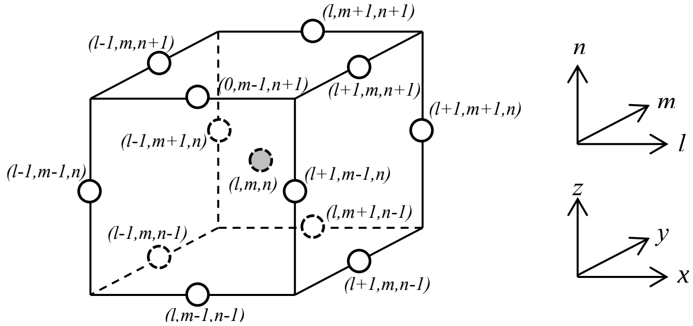

Figure D1 An atom (l, m, n) with its neighboring (interacting) atoms in the FCC lattice

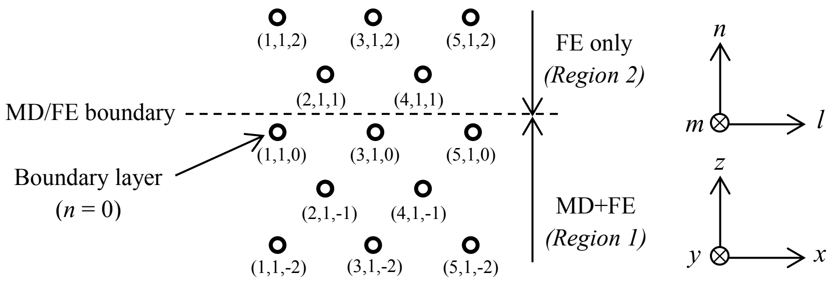

Figure D2 The $m = 1$ layer of a periodic 3D FCC lattice with indices. The dashed line represents the boundary between the MD region and the FE-only region

Note that in Fig. D2, each value of n, for example, describes a layer of atoms bounded in a given x-y plane. Assume that $n = 0$ denotes the boundary layer of the MD region (as shown in Fig. D2). Our goal is to develop an impedance boundary force that mimics the fine scale dynamic effect of the $n > 0$ (*Region 2*) atoms on the remaining system. The fine scale degrees of freedom of the $n > 0$ atoms will be eliminated by solving or replacing them in terms of the $n \leq 0$ (*Region 1*) degrees of freedom. More specifically, the displacements of the $n = 1$ atoms will be solved for in terms of the displacements of the atoms within the $n = 0$ layer.

To start with, the fine scale equation of motion (Eq. 3.21b) for any atom within the harmonic region ($n \geq 0$) can be rewritten, based on the atomic lattice structure, as

$$\mathbf{v}_{l,m,n,tt}(t) = \sum_{l'=l-\mu}^{l+\mu} \sum_{m'=m-\nu}^{m+\nu} \sum_{n'=n-1}^{n+1} \mathbf{M}_A^{-1} \mathbf{K}_{l-l',m-m',n-n'} \mathbf{v}_{l',m',n'}(t) \tag{D1}$$

where the constant stiffness matrices $\mathbf{K}$ relate the displacements of the neighboring atoms around the atom labeled (l, m, n) to the atomic forces acting on it. Writing Eq. D1 for the $n = 0$ atoms yields

$$\begin{aligned}\mathbf{v}_{l,m,0_{,tt}}(t) &= \sum_{l'=l-\mu}^{l+\mu}\ \sum_{m'=m-\nu}^{m+\nu}\ \sum_{n'=-1}^{1}\mathbf{M}_A^{-1}\mathbf{K}_{l-l',m-m',0-n'}\mathbf{v}_{l',m',n'}(t) \\ &= \sum_{l'=l-\mu}^{l+\mu}\ \sum_{m'=m-\nu}^{m+\nu}\ \sum_{n'=-1}^{0}\mathbf{M}_A^{-1}\mathbf{K}_{l-l',m-m',0-n'}\mathbf{v}_{l',m',n'}(t) + \sum_{l'=l-\mu}^{l+\mu}\ \sum_{m'=m-\nu}^{m+\nu}\mathbf{M}_A^{-1}\mathbf{K}_{l-l',m-m',-1}\mathbf{v}_{l',m',1}(t)\end{aligned} \tag{D2}$$

where the $\mathbf{v}_{l',m',1}(t)$ term indicates that determining the motion of the boundary atoms requires the fine scale displacements in *Region 2*, which are to be eliminated. Therefore, we rewrite Eq. D2 as

$$\mathbf{v}_{l,m,0_{,tt}}(t) = \sum_{l'=l-\mu}^{l+\mu}\ \sum_{m'=m-\nu}^{m+\nu}\ \sum_{n'=-1}^{0}\mathbf{M}_A^{-1}\mathbf{K}_{l-l',m-m',0-n'}\mathbf{v}_{l',m',n'}(t) + \mathbf{M}_A^{-1}\mathbf{f}_{l,m,0}^{imp}(t) \tag{D3}$$

where

$$\mathbf{f}_{l,m,0}^{imp}(t) = \sum_{l'=l-\mu}^{l+\mu}\ \sum_{m'=m-\nu}^{m+\nu}\mathbf{K}_{l-l',m-m',-1}\mathbf{v}_{l',m',1}(t) \tag{D4}$$

is the impedance boundary force to be derived, which mimics the effect of the *Region 2* fine scale degrees of freedom on the MD boundary atoms. The objective is to evaluate the impedance force $\mathbf{f}_{l,m,0}^{imp}(t)$ by solving for $\mathbf{v}_{l',m',1}(t)$ in terms of the displacements of the $n = 0$ atoms using mathematical transformation techniques introduced in Appendix C.

Note that we assume the motion of the $n = 0$ layer of atoms only depends on the displacements of those within layer $n = 0$ and their immediately neighboring layers ($n = -1$ and $n = 1$), as shown in Fig. D3a. Since the Fourier transforms can be employed only for the atoms within the harmonic region, the $n < 0$ atoms are temporarily removed from the system, and are replaced by an undetermined external force $\mathbf{f}_{l,m,0}^{ext}(t)$ that acts only upon the $n = 0$ atoms, as shown in Fig. D3b. Therefore, for the $n \geq 0$ atoms, equation D1 can be rewritten as

$$\mathbf{v}_{l,m,n_{,tt}}(t)=\sum_{l'=l-\mu}^{l+\mu}\sum_{m'=m-\nu}^{m+\nu}\sum_{n'=n-1}^{n+1}\mathbf{M}_A^{-1}\mathbf{K}_{l-l',m-m',n-n'}\mathbf{v}_{l',m',n'}(t)+\mathbf{M}_A^{-1}\mathbf{f}_{l,m,0}^{ext}(t) \tag{D5}$$

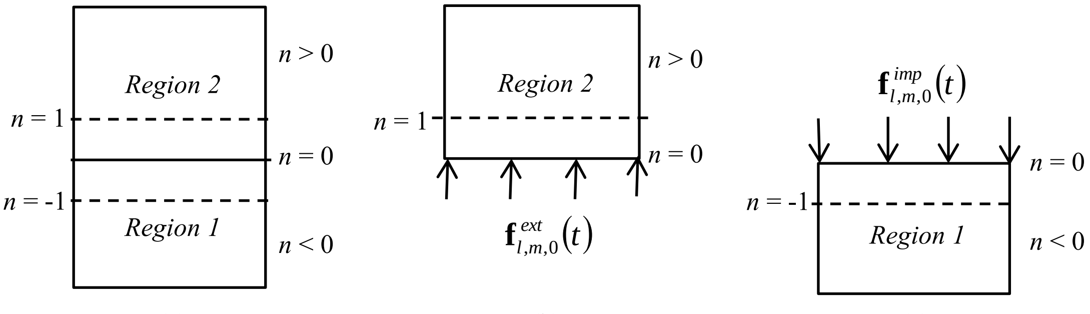

(a) (b) (c)

Figure D3 The external force that replaces the effect of the removed *n* < 0 atoms, (a) original system, (b) *n* < 0 atoms replaced with $\mathbf{f}_{l,m,0}^{ext}(t)$, and (c) *Region 2* fine scale eliminated by introducing impedance boundary force $\mathbf{f}_{l,m,0}^{imp}(t)$

Note that $\mathbf{f}_{l,m,0}^{ext}(t)$ is introduced merely to support the derivation of the impedance boundary condition, and it is *NOT* the impedance boundary force $\mathbf{f}_{l,m,0}^{imp}(t)$ (illustrated in Fig D3c) to be developed.

Taking discrete Fourier transform and Laplace transform of Eq. D5 gives

$$s^2\hat{\mathbf{V}}(p,q,r,s)-s\hat{\mathbf{v}}(p,q,r,0)-\hat{\mathbf{v}}_{,t}(p,q,r,0)=\hat{\mathbf{A}}(p,q,r)\hat{\mathbf{V}}(p,q,r,s)+\mathbf{M}_A^{-1}\hat{\mathbf{F}}_0^{ext}(p,q,s) \tag{D6}$$

where *p*, *q* and *r* correspond to the spatial indices *l*, *m* and *n* respectively. The variable *s* is introduced to indicate the Laplace transform variables. The hatted notation represents the discrete Fourier transform with respect to indices *l*, *m* and *n*. $\hat{\mathbf{A}}(p,q,r)$ is the discrete Fourier transform of $\mathbf{M}_A^{-1}\mathbf{K}_{l,m,n}$. Rearranging Eq. D6 yields

$$\hat{\mathbf{V}}(p,q,r,s)=\hat{\mathbf{G}}(p,q,r,s)\left(\mathbf{M}_A^{-1}\hat{\mathbf{F}}_0^{ext}(p,q,s)+s\hat{\mathbf{v}}(p,q,r,0)+\hat{\mathbf{v}}_{,t}(p,q,r,0)\right) \tag{D7}$$

where $\hat{\mathbf{G}}(p,q,r,s)=\left(s^2\mathbf{I}-\hat{\mathbf{A}}(p,q,r)\right)^{-1}$. Taking inverse Fourier transform of Eq. D7 in *z* direction gives

$$\tilde{\mathbf{V}}_n(p,q,s) = \tilde{\mathbf{G}}_n(p,q,s)\mathbf{M}_A^{-1}\hat{\mathbf{F}}_0^{ext}(p,q,s) + \tilde{\mathbf{R}}_n^d(p,q,s) \tag{D8}$$

where

$$\tilde{\mathbf{R}}_n^d(p,q,s) = s\sum_{n'=-N/2+1}^{N/2}\tilde{\mathbf{G}}_{n-n'}(p,q,s)\mathbf{v}_{n'}(p,q,0) + \sum_{n'=-N/2+1}^{N/2}\tilde{\mathbf{G}}_{n-n'}(p,q,s)\mathbf{v}_{n'_{,t}}(p,q,0) \tag{D9}$$

The tilde notation in Eqs. D8 and D9 denotes the mixed space-wavenumber functions in which the *z* direction is represented by spatial index *n*, and the *x* and *y* directions are expressed by wavenumber variables *p* and *q*. By writing Eq. D8 for both $n = 0$ and $n = 1$, the external force $\hat{\mathbf{F}}_0^{ext}(p,q,s)$ can be canceled out and the displacement $\tilde{\mathbf{V}}_1(p,q,s)$ can be obtained in term of $\tilde{\mathbf{V}}_0(p,q,s)$, as

$$\tilde{\mathbf{V}}_1(p,q,s) = \tilde{\mathbf{Q}}(p,q,s)\left(\tilde{\mathbf{V}}_0(p,q,s) - \tilde{\mathbf{R}}_0^d(p,q,s)\right) + \tilde{\mathbf{R}}_1^d(p,q,s) \tag{D10}$$

where $\tilde{\mathbf{Q}}(p,q,s) = \tilde{\mathbf{G}}_1(p,q,s)\tilde{\mathbf{G}}_0^{-1}(p,q,s)$. Note that $\tilde{\mathbf{R}}_n^d(p,q,s)$ is related to the initial conditions in the continuum region, and is considered to be a random displacement that represents the thermally dependent excitations exerted on the MD region by the surrounding coarse scale; in our numerical example, by assuming the temperature of the surrounding continuum to be 0K, these terms can be set to zero.

Taking inverse Fourier transform of Eq. D10 in *x* and *y* directions using the convolution property while neglecting the random terms gives

$$\mathbf{V}_{l,m,1}(s) = \sum_{l'=-L/2+1}^{L/2}\sum_{m'=-M/2+1}^{M/2}\mathbf{Q}_{l-l',m-m'}(s)\mathbf{V}_{l',m',0}(s) \tag{D11}$$

Thus, the displacements of the $n = 1$ atoms have been solved for in terms of the displacements of the $n = 0$ atoms. To obtain the expression of the impedance force, we take Laplace transform of Eq. D4, yielding

$$\mathbf{F}^{imp}_{l,m,0}(s)=\sum_{l'=l-\mu}^{l+\mu}\sum_{m'=m-\nu}^{m+\nu}\mathbf{K}_{l-l',m-m',-1}\mathbf{V}_{l',m',1}(s) \tag{D12}$$

Substituting Eq. D11 into Eq. D12 gives

$$\begin{aligned}\mathbf{F}^{imp}_{l,m,0}(s)&=\sum_{l'=l-\mu}^{l+\mu}\sum_{m'=m-\nu}^{m+\nu}\mathbf{K}_{l-l',m-m',-1}\sum_{l''=-L/2+1}^{L/2}\sum_{m''=-M/2+1}^{M/2}\mathbf{Q}_{l'-l'',m'-m''}(s)\mathbf{V}_{l'',m'',0}(s)\\&=\sum_{l''=-L/2+1}^{L/2}\sum_{m''=-M/2+1}^{M/2}\sum_{l'=l-\mu}^{l+\mu}\sum_{m'=m-\nu}^{m+\nu}\mathbf{K}_{l-l',m-m',-1}\mathbf{Q}_{l'-l'',m'-m''}(s)\mathbf{V}_{l'',m'',0}(s)\\&=\sum_{l''=-L/2+1}^{L/2}\sum_{m''=-M/2+1}^{M/2}\mathbf{\Theta}_{l-l'',m-m''}(s)\mathbf{V}_{l'',m'',0}(s)\end{aligned} \tag{D13}$$

where

$$\begin{aligned}\mathbf{\Theta}_{m-m''}(s)&=\sum_{l'=l-\mu}^{l+\mu}\sum_{m'=m-\nu}^{m+\nu}\mathbf{K}_{l-l',m-m',-1}\mathbf{Q}_{l'-l'',m'-m''}(s)\\&=\sum_{l'-l''=(l-l'')-\mu}^{(l-l'')+\mu}\sum_{m'-m''=(m-m'')-\nu}^{(m-m'')+\nu}\mathbf{K}_{l-l''-(l'-l''),m-m''-(m'-m''),-1}\mathbf{Q}_{l'-l'',m'-m''}(s)\end{aligned} \tag{D14}$$

For simplicity, rewriting Eq. D13 by replacing all l'' and m'' after the last equal sign with l' and m', giving

$$\mathbf{F}^{imp}_{l,m,0}(s)=\sum_{l'=-L/2+1}^{L/2}\sum_{m'=-M/2+1}^{M/2}\mathbf{\Theta}_{l-l',m-m'}(s)\mathbf{V}_{l',m',0}(s) \tag{D15}$$

Hence, the impedance boundary force acting upon the n = 0 atoms can be obtained by taking inverse Laplace transform of Eq. D15, as

$$\mathbf{f}^{imp}_{l,m,0}(t)=\sum_{l'=-L/2+1}^{L/2}\sum_{m'=-M/2+1}^{M/2}\int_0^t\boldsymbol{\theta}_{l-l',m-m'}(t-\tau)\mathbf{v}_{l',m',0}(\tau)d\tau \tag{D16}$$

where $\boldsymbol{\theta}_{l,m}(t)=\mathcal{L}^{-1}(\mathbf{\Theta}_{l,m}(s))$ is named the time history kernel matrix. The diagonal components of the time history kernel calculated based on the 3-D FCC lattice (Fig. D1) and the normalized LJ 6-12 potential are plotted in Fig. D4. As can be seen, $\boldsymbol{\theta}_{33}(t)$ is the most important component, while $\boldsymbol{\theta}_{11}(t)$ and $\boldsymbol{\theta}_{22}(t)$ are equal to each other due to symmetry of the lattice in *x* and *y* directions.

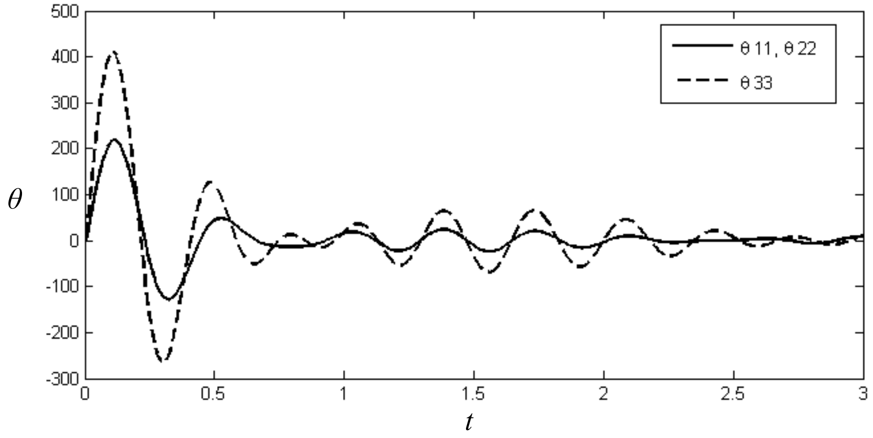

Figure D4 Diagonal components of the time history kernel matrix ***θ***

Note that for a generalized 3-D case, the coarse scale equation of motion (Eq. 3.21a) can be rewritten for the atoms at $n = 0$, as

$$\mathbf{u}_{l,m,0_{,tt}} = \mathbf{M}_A^{-1}\mathbf{f}_{l,m,0}(\mathbf{u}) \tag{D17}$$

Substituting the expression of the impedance boundary force (Eq. D16) into the fine scale equation of motion for the boundary atoms (Eq. D3) and combining the result with Eq. D17 gives

$$\mathbf{M}_A\mathbf{q}_{l,m,0_{,tt}}(t) = \mathbf{f}_{l,m,0}(\mathbf{q},\mathbf{u}) + \sum_{l'=l-l_{crit}}^{l+l_{crit}} \sum_{m'=m-m_{crit}}^{m+m_{crit}} \int_0^t \boldsymbol{\theta}_{l-l',m-m'}(t-\tau)\mathbf{v}_{l',m',0}(\tau)d\tau \tag{D18}$$

where the $\mathbf{f}_{l,m,0}(\mathbf{q},\mathbf{u})$ term implies that the motion of the MD boundary atoms depends also on the coarse scale solution **u** outside the MD area. The fine scale displacement $\mathbf{v}_{l',m',0}$ in Eq. D18 can be calculated by

$$\mathbf{v}_{l',m',0}(\tau) = \mathbf{q}_{l',m',0}(\tau) - \mathbf{u}_{l',m',0}(\tau) \tag{D19}$$

Note that in Eq. D18, l_{crit} and m_{crict} are introduced as maximum numbers of neighboring atoms that will be considered in the calculation of the boundary force. It has been proved in [23] that the biggest improvement occurs when the zeroth-order component of the time history kernel is utilized ($l_{crit} = m_{crit} = 0$). Also, it has been shown in [28] that higher order values of $\boldsymbol{\theta}(t)$ corresponding to $l_{crit} > 0$ and $m_{crit} > 0$ are at most 10% of the values shown in Fig. D4. Therefore, in this thesis, we assume that $l_{crit} = m_{crit} = 0$ when calculating the time history kernel matrix.

Finally, we show calculation of the stiffness matrices **K** used in deriving the impedance boundary condition for the 3-D FCC atomic lattice (Fig. D1) implemented in our 3-D numerical example.

According to [27], the stiffness matrices **K** can be defined in general as

$$\mathbf{K}_{l-l',m-m',n-n'} = \frac{\partial \mathbf{f}_{l,m,n}}{\partial \mathbf{r}_{l',m',n'}} \Big|_{\mathbf{r}=\mathbf{r}_{eq}} \tag{D20}$$

where **r** is a vector of current atomic locations and $\mathbf{r}_{eq}$ denotes the corresponding vector at equilibrium. For the atomic structure depicted in Fig. D1, the **K** matrices are calculated as

$$\mathbf{K}_{1,1,0} = \mathbf{K}_{-1,-1,0} = \frac{k}{2}\begin{bmatrix} 1 & 1 & 0 \\ 1 & 1 & 0 \\ 0 & 0 & 0 \end{bmatrix} \tag{D21a}$$

$$\mathbf{K}_{1,-1,0} = \mathbf{K}_{-1,1,0} = \frac{k}{2}\begin{bmatrix} 1 & -1 & 0 \\ -1 & 1 & 0 \\ 0 & 0 & 0 \end{bmatrix} \tag{D21b}$$

$$\mathbf{K}_{0,1,1} = \mathbf{K}_{0,-1,-1} = \frac{k}{2}\begin{bmatrix} 0 & 0 & 0 \\ 0 & 1 & 1 \\ 0 & 1 & 1 \end{bmatrix} \tag{D21c}$$

$$\mathbf{K}_{0,1,-1} = \mathbf{K}_{0,-1,1} = \frac{k}{2}\begin{bmatrix} 0 & 0 & 0 \\ 0 & 1 & -1 \\ 0 & -1 & 1 \end{bmatrix} \tag{D21d}$$

$$\mathbf{K}_{1,0,1} = \mathbf{K}_{-1,0,-1} = \frac{k}{2}\begin{bmatrix} 1 & 0 & 1 \\ 0 & 0 & 0 \\ 1 & 0 & 1 \end{bmatrix} \tag{D21e}$$

$$\mathbf{K}_{1,0,-1} = \mathbf{K}_{-1,0,1} = \frac{k}{2}\begin{bmatrix} 1 & 0 & -1 \\ 0 & 0 & 0 \\ -1 & 0 & 1 \end{bmatrix} \tag{D21f}$$

$$\mathbf{K}_{0,0,0} = 4k\begin{bmatrix} -1 & 0 & 0 \\ 0 & -1 & 0 \\ 0 & 0 & -1 \end{bmatrix} \tag{D21g}$$

Note that only nearest neighbor interactions are considered. All **K** matrices not listed above are zero simply because there is no atom located at positions denoted by certain pairs of indices, such as (*l*-1, *m*-1, *n*-1) and (*l*, *m*, *n*-1). The interaction coefficient *k* for the LJ 6-12 potential has been given in Eq. 3.4.

APPENDIX E

DISCRETIZATION OF REGION 2 COARSE SCALE IN THREE DIMENSIONS

This appendix presents the calculation of first Piola-Kirchoff stress and the discretization of coarse scale strain energy outside the MD region for the 3-D FCC lattice used in our numerical example.

In *Region 2*, due to the absence of atomistic information, the coarse scale forces acting on the finite element nodes are calculated by evaluating the first Piola-Kirchoff stress tensor $\mathcal{P}$ at individual quadrature points using the Cauchy-Born rule. To start with, the strain energy density and deformation gradient **F** at a given location will be determined based on nodal displacements. The stress tensor $\mathcal{P}$ can then be obtained by taking derivative of the energy density with respect to $\mathbf{F}^T$. Detailed derivations for a 2-D hexagonal lattice can be found in reference [60]. In this appendix, we focus on 3-D FCC lattice.

According to the Cauchy-Born rule, the strain energy density is related to the interatomic potential and the atomic lattice structure defined in the MD simulation. For illustration, a single atom α with its nearest neighbors within a 3-D FCC lattice is depicted in Fig. E1. The equilibrium distance between two neighboring atoms is h_a. The equilibrium atomic bonds connected with atom α can be represented by vectors; for example, the undeformed (1,1,0) bond in Fig. E1 can be written as

$$\mathbf{r}_{1,1,0eq} = \begin{bmatrix} h_a \cdot \sqrt{2}/2 \\ h_a \cdot \sqrt{2}/2 \\ 0 \end{bmatrix} \tag{E1}$$

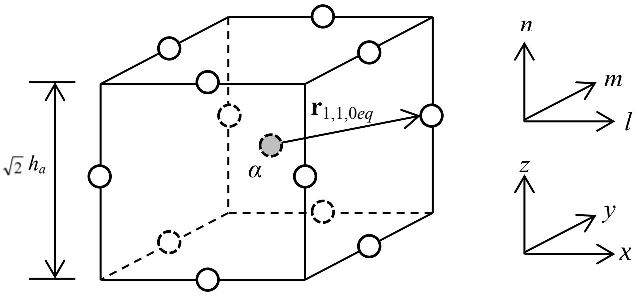

Figure E1 Undeformed FCC lattice centered at atom α

When the continuum is deformed, the (1,1,0) bond vector needs to be transformed according to the deformation gradient at the location $\mathbf{x}_\alpha$, as

$$\mathbf{r}_{1,1,0} = \begin{bmatrix} r_{1,1,0x} \\ r_{1,1,0y} \\ r_{1,1,0z} \end{bmatrix} = \mathbf{F}_\alpha \cdot \mathbf{r}_{1,1,0eq} = \mathbf{F}_\alpha \begin{bmatrix} h_a \cdot \sqrt{2}/2 \\ h_a \cdot \sqrt{2}/2 \\ 0 \end{bmatrix} \tag{E2}$$

The length change of the bond (1,1,0):

$$\Delta r_{1,1,0} = \sqrt{r_{1,1,0x}^2 + r_{1,1,0y}^2 + r_{1,1,0z}^2} - \sqrt{\left(\sqrt{2}h_a/2\right)^2 + \left(\sqrt{2}h_a/2\right)^2 + 0^2} \tag{E3}$$

can be approximated under small deformation assumption, as

$$\Delta \tilde{r}_{1,1,0} = \left(\frac{\partial \Delta r_{1,1,0}}{\partial \mathbf{r}_{1,1,0}^T} \Big|_{\mathbf{r}_{1,1,0}=\mathbf{r}_{1,1,0eq}} \right) \left(\mathbf{r}_{1,1,0} - \mathbf{r}_{1,1,0eq} \right) \tag{E4}$$

where

$$\frac{\partial \Delta r_{1,1,0}}{\partial \mathbf{r}_{1,1,0}^T} \Big|_{\mathbf{r}_{1,1,0}=\mathbf{r}_{1,1,0eq}} = \begin{bmatrix} \frac{\sqrt{2}}{2} & \frac{\sqrt{2}}{2} & 0 \end{bmatrix} \tag{E5}$$

The linearized strain energy of bond (1,1,0) due to deformation can be written as

$$\Phi_{1,1,0} = \frac{1}{2} k \Delta\tilde{r}_{1,1,0}^{2} \tag{E6}$$

where k is the interaction coefficient (Eq. 3.4) for the interatomic force at equilibrium distance. Taking derivative of $\Phi_{1,1,0}$ with respect to $\mathbf{F}_{\alpha}^{T}$ gives

$$\frac{\partial \Phi_{1,1,0}}{\partial \mathbf{F}_{\alpha}^{T}} = k\Delta\tilde{r}_{1,1,0}\frac{\partial \Delta\tilde{r}_{1,1,0}}{\partial \mathbf{F}_{\alpha}^{T}} = \frac{kh_a}{2}\begin{bmatrix} \frac{\sqrt{2}}{2} & \frac{\sqrt{2}}{2} & 0 \end{bmatrix}\left(\mathbf{F}_{\alpha}\cdot\mathbf{r}_{1,1,0eq} - \mathbf{r}_{1,1,0eq}\right)\begin{bmatrix} 1 & 1 & 0 \\ 1 & 1 & 0 \\ 0 & 0 & 0 \end{bmatrix} \tag{E7}$$

Note that the calculation from Eqs. E1 to E7 can be carried out similarly for the other eleven bonds surrounding atom α.

The strain energy density centered at $\mathbf{x}_{\alpha}$ can be written in the form

$$\begin{aligned} W_{\alpha} = \frac{1}{2}\big[&\Phi_{1,1,0} + \Phi_{-1,-1,0} + \Phi_{-1,1,0} + \Phi_{1,-1,0} + \Phi_{-1,0,-1} + \Phi_{1,0,-1} \\ &+ \Phi_{0,-1,-1} + \Phi_{0,1,-1} + \Phi_{-1,0,1} + \Phi_{1,0,1} + \Phi_{0,-1,1} + \Phi_{0,1,1}\big]/V_{\alpha} \end{aligned} \tag{E8}$$

where $V_{\alpha} = \frac{\sqrt{2}}{2} h_a^3$ is the volume occupied by each atom in an undeformed FCC lattice. The first Piola-Kirchoff stress tensor at $\mathbf{x}_{\alpha}$ can be obtained, according to the Cauchy-Born rule, by taking derivative of Eq. E8 with respect to $\mathbf{F}^{T}$, as

$$
\begin{aligned}
\mathcal{P}(\mathbf{x}_\alpha) = \frac{\partial W_\alpha}{\partial \mathbf{F}_\alpha^T} = \frac{1}{2V_\alpha}\Bigg[& \frac{\partial \Phi_{1,1,0}}{\partial \mathbf{F}_\alpha^T} + \frac{\partial \Phi_{-1,-1,0}}{\partial \mathbf{F}_\alpha^T} + \frac{\partial \Phi_{-1,1,0}}{\partial \mathbf{F}_\alpha^T} + \frac{\partial \Phi_{1,-1,0}}{\partial \mathbf{F}_\alpha^T} + \frac{\partial \Phi_{-1,0,-1}}{\partial \mathbf{F}_\alpha^T} + \frac{\partial \Phi_{1,0,-1}}{\partial \mathbf{F}_\alpha^T} \Phi_{1,1,0} \\
& + \frac{\partial \Phi_{0,-1,-1}}{\partial \mathbf{F}_\alpha^T} + \frac{\partial \Phi_{0,1,-1}}{\partial \mathbf{F}_\alpha^T} + \frac{\partial \Phi_{-1,0,1}}{\partial \mathbf{F}_\alpha^T} + \frac{\partial \Phi_{1,0,1}}{\partial \mathbf{F}_\alpha^T} + \frac{\partial \Phi_{0,-1,1}}{\partial \mathbf{F}_\alpha^T} + \frac{\partial \Phi_{0,1,1}}{\partial \mathbf{F}_\alpha^T} \Bigg] \\
= & \frac{kh_a}{2}\begin{bmatrix} \frac{\sqrt{2}}{2} & \frac{\sqrt{2}}{2} & 0 \end{bmatrix} \left(\mathbf{F}_\alpha \cdot \mathbf{r}_{1,1,0eq} - \mathbf{r}_{1,1,0eq}\right) \begin{bmatrix} 1 & 1 & 0 \\ 1 & 1 & 0 \\ 0 & 0 & 0 \end{bmatrix} \\
& + \frac{kh_a}{2}\begin{bmatrix} \frac{\sqrt{2}}{2} & -\frac{\sqrt{2}}{2} & 0 \end{bmatrix} \left(\mathbf{F}_\alpha \cdot \mathbf{r}_{1,-1,0eq} - \mathbf{r}_{1,-1,0eq}\right) \begin{bmatrix} 1 & -1 & 0 \\ -1 & 1 & 0 \\ 0 & 0 & 0 \end{bmatrix} \\
& + \frac{kh_a}{2}\begin{bmatrix} \frac{\sqrt{2}}{2} & 0 & -\frac{\sqrt{2}}{2} \end{bmatrix} \left(\mathbf{F}_\alpha \cdot \mathbf{r}_{1,0,-1eq} - \mathbf{r}_{1,0,-1eq}\right) \begin{bmatrix} 1 & 0 & -1 \\ 0 & 0 & 0 \\ -1 & 0 & 1 \end{bmatrix} \\
& + \frac{kh_a}{2}\begin{bmatrix} 0 & \frac{\sqrt{2}}{2} & \frac{\sqrt{2}}{2} \end{bmatrix} \left(\mathbf{F}_\alpha \cdot \mathbf{r}_{0,1,1eq} - \mathbf{r}_{0,1,1eq}\right) \begin{bmatrix} 0 & 0 & 0 \\ 0 & 1 & 1 \\ 0 & 1 & 1 \end{bmatrix} \\
& + \frac{kh_a}{2}\begin{bmatrix} \frac{\sqrt{2}}{2} & 0 & \frac{\sqrt{2}}{2} \end{bmatrix} \left(\mathbf{F}_\alpha \cdot \mathbf{r}_{1,0,1eq} - \mathbf{r}_{1,0,1eq}\right) \begin{bmatrix} 1 & 0 & 1 \\ 0 & 0 & 0 \\ 1 & 0 & 1 \end{bmatrix} \\
& + \frac{kh_a}{2}\begin{bmatrix} 0 & \frac{\sqrt{2}}{2} & -\frac{\sqrt{2}}{2} \end{bmatrix} \left(\mathbf{F}_\alpha \cdot \mathbf{r}_{0,1,-1eq} - \mathbf{r}_{0,1,-1eq}\right) \begin{bmatrix} 0 & 0 & 0 \\ 0 & 1 & -1 \\ 0 & -1 & 1 \end{bmatrix}
\end{aligned}
\qquad \text{(E9)}
$$

As can be observed from Eq. E9, the Piola-Kirchoff stress tensor

$$
\mathcal{P}_\alpha = \mathcal{P}(\mathbf{x}_\alpha) = \begin{bmatrix} \mathcal{P}_{\alpha 11} & \mathcal{P}_{\alpha 12} & \mathcal{P}_{\alpha 13} \\ \mathcal{P}_{\alpha 21} & \mathcal{P}_{\alpha 22} & \mathcal{P}_{\alpha 23} \\ \mathcal{P}_{\alpha 31} & \mathcal{P}_{\alpha 32} & \mathcal{P}_{\alpha 33} \end{bmatrix} \qquad \text{(E10)}
$$

is symmetric, i.e., $\mathcal{P}_{\alpha 12} = \mathcal{P}_{\alpha 21}$, due to the small deformation assumption employed in the derivations above.

To find the deformation gradient **F**, assume an eight-node hexahedral tri-linear isoparametric finite element as illustrated in Fig. E2.

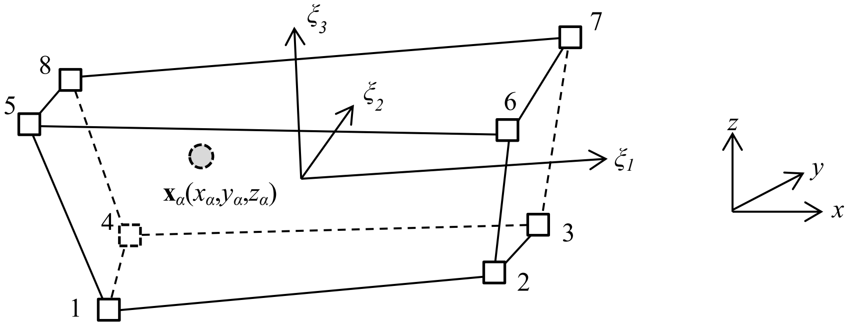

Figure E2 A hexahedral isoparametric element with eight nodes (1 ~ 8)

The deformation gradient at location $\mathbf{x}_\alpha$ within the element can be determined as

$$\mathbf{F}_\alpha = \mathbf{I} + \sum_I \mathbf{d}_I \left(\frac{\partial N_I(\mathbf{x}_\alpha)}{\partial \mathbf{x}} \right)^T = \mathbf{I} + \sum_{I=1}^{8} \begin{bmatrix} d_{Ix} \\ d_{Iy} \\ d_{Iz} \end{bmatrix} \begin{bmatrix} \dfrac{\partial N_I(\mathbf{x}_\alpha)}{\partial x} & \dfrac{\partial N_I(\mathbf{x}_\alpha)}{\partial y} & \dfrac{\partial N_I(\mathbf{x}_\alpha)}{\partial z} \end{bmatrix} \tag{E11}$$

where $N_I(\mathbf{x}_\alpha)$ is the finite element shape function of node I at location $\mathbf{x}_\alpha$. Note that for isoparametric elements, the shape functions are usually written in terms of natural coordinates ξ_1, ξ_2 and ξ_3. The relation between the natural and global (orthogonal x-y-z) reference systems is given by

$$\begin{bmatrix} \dfrac{\partial N_I(\mathbf{x}_\alpha)}{\partial x} \\ \dfrac{\partial N_I(\mathbf{x}_\alpha)}{\partial y} \\ \dfrac{\partial N_I(\mathbf{x}_\alpha)}{\partial z} \end{bmatrix} = \mathbf{J}(\mathbf{x}_\alpha)^{-1} \begin{bmatrix} \dfrac{\partial N_I(\mathbf{x}_\alpha)}{\partial \xi_1} \\ \dfrac{\partial N_I(\mathbf{x}_\alpha)}{\partial \xi_2} \\ \dfrac{\partial N_I(\mathbf{x}_\alpha)}{\partial \xi_3} \end{bmatrix} = \begin{bmatrix} J^*_{11}(\mathbf{x}_\alpha) & J^*_{12}(\mathbf{x}_\alpha) & J^*_{13}(\mathbf{x}_\alpha) \\ J^*_{21}(\mathbf{x}_\alpha) & J^*_{22}(\mathbf{x}_\alpha) & J^*_{23}(\mathbf{x}_\alpha) \\ J^*_{31}(\mathbf{x}_\alpha) & J^*_{32}(\mathbf{x}_\alpha) & J^*_{33}(\mathbf{x}_\alpha) \end{bmatrix} \begin{bmatrix} \dfrac{\partial N_I(\mathbf{x}_\alpha)}{\partial \xi_1} \\ \dfrac{\partial N_I(\mathbf{x}_\alpha)}{\partial \xi_2} \\ \dfrac{\partial N_I(\mathbf{x}_\alpha)}{\partial \xi_3} \end{bmatrix} \tag{E12}$$

where $\mathbf{J}(\mathbf{x}_\alpha)$ is known as the Jacobian matrix and can be evaluated from

$$\mathbf{J}(\mathbf{x}_\alpha) = \begin{bmatrix} \dfrac{\partial x(\mathbf{x}_\alpha)}{\partial \xi_1} & \dfrac{\partial y(\mathbf{x}_\alpha)}{\partial \xi_1} & \dfrac{\partial z(\mathbf{x}_\alpha)}{\partial \xi_1} \\ \dfrac{\partial x(\mathbf{x}_\alpha)}{\partial \xi_2} & \dfrac{\partial y(\mathbf{x}_\alpha)}{\partial \xi_2} & \dfrac{\partial z(\mathbf{x}_\alpha)}{\partial \xi_2} \\ \dfrac{\partial x(\mathbf{x}_\alpha)}{\partial \xi_3} & \dfrac{\partial y(\mathbf{x}_\alpha)}{\partial \xi_3} & \dfrac{\partial z(\mathbf{x}_\alpha)}{\partial \xi_3} \end{bmatrix} = \begin{bmatrix} \dfrac{\partial N_1(\mathbf{x}_\alpha)}{\partial \xi_1} & \cdots & \dfrac{\partial N_8(\mathbf{x}_\alpha)}{\partial \xi_1} \\ \dfrac{\partial N_1(\mathbf{x}_\alpha)}{\partial \xi_2} & \cdots & \dfrac{\partial N_8(\mathbf{x}_\alpha)}{\partial \xi_2} \\ \dfrac{\partial N_1(\mathbf{x}_\alpha)}{\partial \xi_3} & \cdots & \dfrac{\partial N_8(\mathbf{x}_\alpha)}{\partial \xi_3} \end{bmatrix} \cdot \begin{bmatrix} \mathbf{x}_{1x} & \mathbf{x}_{1y} & \mathbf{x}_{1z} \\ \mathbf{x}_{2x} & \mathbf{x}_{2y} & \mathbf{x}_{2z} \\ \vdots & \vdots & \vdots \\ \mathbf{x}_{8x} & \mathbf{x}_{8y} & \mathbf{x}_{8z} \end{bmatrix} \tag{E13}$$

Substituting Eq. E11 into Eq. E9, the stress at location $\mathbf{x}_\alpha$ can be obtained, as

$$\begin{aligned}
\boldsymbol{\sigma}(\mathbf{x}_\alpha) = \begin{bmatrix} \boldsymbol{\mathcal{P}}_{11}(\mathbf{x}_\alpha) \\ \boldsymbol{\mathcal{P}}_{22}(\mathbf{x}_\alpha) \\ \boldsymbol{\mathcal{P}}_{33}(\mathbf{x}_\alpha) \\ \boldsymbol{\mathcal{P}}_{23}(\mathbf{x}_\alpha) \\ \boldsymbol{\mathcal{P}}_{13}(\mathbf{x}_\alpha) \\ \boldsymbol{\mathcal{P}}_{12}(\mathbf{x}_\alpha) \end{bmatrix} &= \frac{\sqrt{2}k}{2h_a} \begin{bmatrix} 2 & 1 & 1 & 0 & 0 & 0 \\ 1 & 2 & 1 & 0 & 0 & 0 \\ 1 & 1 & 2 & 0 & 0 & 0 \\ 0 & 0 & 0 & 1 & 0 & 0 \\ 0 & 0 & 0 & 0 & 1 & 0 \\ 0 & 0 & 0 & 0 & 0 & 1 \end{bmatrix} \cdot \begin{bmatrix} \partial_x & 0 & 0 \\ 0 & \partial_y & 0 \\ 0 & 0 & \partial_z \\ 0 & \partial_z & \partial_y \\ \partial_z & 0 & \partial_x \\ \partial_y & \partial_x & 0 \end{bmatrix} \\
&\cdot \begin{bmatrix} N_1(\mathbf{x}_\alpha) & 0 & 0 & \cdots\cdots & N_8(\mathbf{x}_\alpha) & 0 & 0 \\ 0 & N_1(\mathbf{x}_\alpha) & 0 & \cdots\cdots & 0 & N_8(\mathbf{x}_\alpha) & 0 \\ 0 & 0 & N_1(\mathbf{x}_\alpha) & \cdots\cdots & 0 & 0 & N_8(\mathbf{x}_\alpha) \end{bmatrix} \cdot \mathbf{d} \qquad \text{(E14)} \\
&= \mathbf{E}_{6\times6}\mathbf{D}_{6\times3}\mathbf{N}_{3\times24}\mathbf{d}_{24\times1} = \mathbf{E}_{6\times6}\mathbf{B}_{6\times24}\mathbf{d}_{24\times1}
\end{aligned}$$

where

$$\mathbf{E} = \frac{\sqrt{2}k}{2h_a} \begin{bmatrix} 2 & 1 & 1 & 0 & 0 & 0 \\ 1 & 2 & 1 & 0 & 0 & 0 \\ 1 & 1 & 2 & 0 & 0 & 0 \\ 0 & 0 & 0 & 1 & 0 & 0 \\ 0 & 0 & 0 & 0 & 1 & 0 \\ 0 & 0 & 0 & 0 & 0 & 1 \end{bmatrix} \qquad \text{(E15)}$$

indicates the stress-strain relation; **D** is the operator matrix; **N** is the shape function matrix; and **B** is obtained by applying the derivatives in **D** to the shape functions in **N**.

Now assume a simple two-element coarse scale domain with twelve FE nodes (1 ~ 12) and two quadrature points (*A* and *B*), as depicted in Fig. E3. The coarse scale strain energy of this domain can be approximated by summing over the two quadrature points, as

$$\iiint_{\Omega} \bar{\boldsymbol{\varepsilon}}^T(\bar{\boldsymbol{u}})\boldsymbol{\sigma}(\boldsymbol{u})d\Omega = \sum_q \bar{\boldsymbol{\varepsilon}}^T(\mathbf{x_q})\boldsymbol{\sigma}(\mathbf{x_q})w_q$$
$$= \begin{bmatrix} \bar{\varepsilon}_{A1} & \bar{\varepsilon}_{A2} & \bar{\varepsilon}_{A3} & \bar{\gamma}_{A23} & \bar{\gamma}_{A13} & \bar{\gamma}_{A12} \end{bmatrix} \cdot \begin{bmatrix} \boldsymbol{\Phi}_{A11} \\ \boldsymbol{\Phi}_{A22} \\ \boldsymbol{\Phi}_{A33} \\ \boldsymbol{\Phi}_{A23} \\ \boldsymbol{\Phi}_{A13} \\ \boldsymbol{\Phi}_{A12} \end{bmatrix} w_A + \begin{bmatrix} \bar{\varepsilon}_{B1} & \bar{\varepsilon}_{B2} & \bar{\varepsilon}_{B3} & \bar{\gamma}_{B23} & \bar{\gamma}_{B13} & \bar{\gamma}_{B12} \end{bmatrix} \cdot \begin{bmatrix} \boldsymbol{\Phi}_{B11} \\ \boldsymbol{\Phi}_{B22} \\ \boldsymbol{\Phi}_{B33} \\ \boldsymbol{\Phi}_{B23} \\ \boldsymbol{\Phi}_{B13} \\ \boldsymbol{\Phi}_{B12} \end{bmatrix} w_B$$
$$= \begin{bmatrix} \bar{\varepsilon}_{A1} \\ \bar{\varepsilon}_{A2} \\ \vdots \\ \bar{\gamma}_{A12} \\ \bar{\varepsilon}_{B1} \\ \bar{\varepsilon}_{B2} \\ \vdots \\ \bar{\gamma}_{B12} \end{bmatrix}^T \cdot \begin{bmatrix} w_A & & & & \\ & \ddots & & & \\ & & w_A & & \\ & & & w_B & \\ & & & & \ddots \\ & & & & & w_B \end{bmatrix} \cdot \begin{bmatrix} \boldsymbol{\Phi}_{A11} \\ \boldsymbol{\Phi}_{A22} \\ \vdots \\ \boldsymbol{\Phi}_{A12} \\ \boldsymbol{\Phi}_{B11} \\ \boldsymbol{\Phi}_{B22} \\ \vdots \\ \boldsymbol{\Phi}_{B12} \end{bmatrix} \qquad \text{(E16)}$$
$$= \bar{\boldsymbol{\varepsilon}}^T \mathbf{W}_{12\times12}\boldsymbol{\Phi}_{12\times1}$$

where, for example, $\bar{\varepsilon}_{A1}$ denotes the x direction component of the virtual strain at quadrature point A. The weight of each quadrature point is related to the determinant of the its Jacobian, as

$$w_A = \frac{8}{N_{qe}}\left|\mathbf{J}(\mathbf{x}_A)\right| \qquad \text{(E17)}$$

where N_{qe} is the number of quadrature points per element.

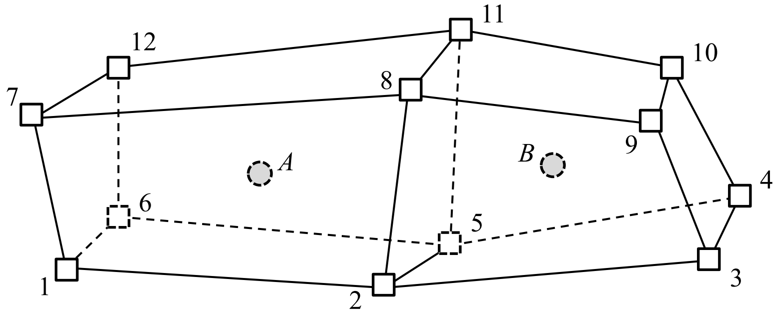

Figure E3 A two-element coarse scale domain

Further discretizing the right hand side of Eq. E16 using finite element interpolation while considering Eq. E14 yields

$$\iiint_{\Omega} \bar{\boldsymbol{\varepsilon}}^T(\bar{\boldsymbol{u}})\boldsymbol{\sigma}(\boldsymbol{u})d\Omega \overset{discretize}{=} \bar{\mathbf{d}}^T\mathbf{B}^T\mathbf{W}_{12\times12}\mathbf{E}_{12\times12}\mathbf{B}_{12\times36}\mathbf{d}_{36\times1} \tag{E18}$$

where

$$\mathbf{E}_{12\times12} = \begin{bmatrix} \mathbf{E}_{6\times6} & \\ & \mathbf{E}_{6\times6} \end{bmatrix} \tag{E19}$$

Note that the size of the matrices in Eq. E18 varies with the number of nodes and quadrature points in the domain. In Eq. E18,

$$\mathbf{B}_{12\times36} = \mathbf{D}_{12\times6}\mathbf{N}_{6\times36} = \begin{bmatrix} \mathbf{D}_{6\times3} & \\ & \mathbf{D}_{6\times3} \end{bmatrix}\mathbf{N}_{6\times36} \tag{E20}$$

where

$$\mathbf{D}_{6\times3} = \begin{bmatrix} \partial_x & 0 & 0 \\ 0 & \partial_y & 0 \\ 0 & 0 & \partial_z \\ 0 & \partial_z & \partial_y \\ \partial_z & 0 & \partial_x \\ \partial_y & \partial_x & 0 \end{bmatrix} = \begin{bmatrix} J_{11}^*\partial_{\xi_1} + J_{12}^*\partial_{\xi_2} + J_{13}^*\partial_{\xi 3} & 0 & 0 \\ 0 & J_{21}^*\partial_{\xi_1} + J_{22}^*\partial_{\xi_2} + J_{23}^*\partial_{\xi 3} & 0 \\ 0 & 0 & J_{31}^*\partial_{\xi_1} + J_{32}^*\partial_{\xi_2} + J_{33}^*\partial_{\xi 3} \\ 0 & J_{31}^*\partial_{\xi_1} + J_{32}^*\partial_{\xi_2} + J_{33}^*\partial_{\xi 3} & J_{21}^*\partial_{\xi_1} + J_{22}^*\partial_{\xi_2} + J_{23}^*\partial_{\xi 3} \\ J_{31}^*\partial_{\xi_1} + J_{32}^*\partial_{\xi_2} + J_{33}^*\partial_{\xi 3} & 0 & J_{11}^*\partial_{\xi_1} + J_{12}^*\partial_{\xi_2} + J_{13}^*\partial_{\xi 3} \\ J_{21}^*\partial_{\xi_1} + J_{22}^*\partial_{\xi_2} + J_{23}^*\partial_{\xi 3} & J_{11}^*\partial_{\xi_1} + J_{12}^*\partial_{\xi_2} + J_{13}^*\partial_{\xi 3} & 0 \end{bmatrix} \tag{E21}$$

and the size of the shape function matrix **N** can be written as $(3\times N_q)\times(3\times N_n)$, with N_q and N_n being respectively the number of quadrature points and the number of FE nodes in the domain.

Equation E18 gives the discretization of the coarse scale strain energy in *Region 2*. The coarse scale internal force acting on FE nodes in *Region 2* therefore takes the form

$$\mathbf{F}^{CB} = -\mathbf{B}^T\mathbf{WEBd} = -\mathbf{K}^{CB}\mathbf{d} \tag{E22}$$

where $\mathbf{K}^{CB}$ is the equivalent stiffness matrix for the finite element analysis in *Region 2*.

APPENDIX F

VARIATIONAL FORMULATION FOR BRIDGING SCALE METHOD

This appendix demonstrates the derivation of the energy based variational formulation for the bridging scale method. More detailed discusses regarding this topic can be found in our earlier work [35].

We start by briefly reviewing the variational method of structural systems. The total potential energy of a structural system can be defined as

$$\Pi(\mathbf{z}) = U(\mathbf{z}) - W(\mathbf{z}) \tag{F1}$$

where $U(\mathbf{z})$ is the strain energy of the structure and $W(\mathbf{z})$ is the work done by the applied conservative loads. If $\Pi(\mathbf{z})$ is differentiable at a certain displacement $\mathbf{z}$, the first variation of $\Pi(\mathbf{z})$ at $\mathbf{z}$ can be written as

$$\delta\Pi(\mathbf{z}, \bar{\mathbf{z}}) = \lim_{\tau \to 0} \frac{1}{\tau}\left[\Pi(\mathbf{z} + \tau\bar{\mathbf{z}}) - \Pi(\mathbf{z})\right] = \frac{d}{d\tau}\Pi(\mathbf{z} + \tau\bar{\mathbf{z}})\big|_{\tau=0} \tag{F2}$$

where $\bar{\mathbf{z}}$ is a small, arbitrarily chosen virtual displacement indicating the direction of the perturbation, τ is a small scalar, and $\mathbf{z} + \tau\bar{\mathbf{z}}$ represents the perturbed state.

To obtain a stationary condition of the structure, the total potential energy needs to be minimized, giving

$$\delta\Pi(\mathbf{z}, \bar{\mathbf{z}}) = \delta U(\mathbf{z}, \bar{\mathbf{z}}) - \delta W(\mathbf{z}, \bar{\mathbf{z}}) = 0 \tag{F3}$$

which is called the variational equation of the static structural problem. Note that both the solution $\mathbf{z}$ and the virtual displacement $\bar{\mathbf{z}}$ belong to the space of kinematically admissible displacements, defined as

$$Z = \left\{ \boldsymbol{z} \in \left[H^m(\Omega) \right]^3 \mid \boldsymbol{z} = 0 \,\text{on}\, \mathbf{x} \in \Gamma^h \right\} \tag{F4}$$

in which H^{m} is the Sobolev space of order m. Note that Eq. F3 can be written in another form as

$$a(\boldsymbol{z}, \bar{\boldsymbol{z}}) = \ell(\bar{\boldsymbol{z}}), \ \forall \bar{\boldsymbol{z}} \in Z \tag{F5}$$

where $a(\boldsymbol{z}, \bar{\boldsymbol{z}}) = \delta U(\boldsymbol{z}, \bar{\boldsymbol{z}})$ and $\ell(\bar{\boldsymbol{z}}) = \delta W(\boldsymbol{z}, \bar{\boldsymbol{z}})$ are known as the energy bilinear form and load linear forms, respectively. The displacement field $\boldsymbol{z} \in Z$ that satisfies Eq. F5 is the solution to the static structural problem.

In order to describe dynamic problems, Hamilton's principle needs to be introduced. If a time-dependent load is applied to the structure, the velocities of all particles within the structure generate a kinetic energy, defined as

$$T(\boldsymbol{z}_{,t}) \equiv \frac{1}{2} \iiint_\Omega \rho \boldsymbol{z}_{,t}^T \boldsymbol{z}_{,t} d\Omega \tag{F6}$$

where $\rho(\mathbf{x})$ is the mass density. Assuming that the time derivative is independent of the variation, the first variation of $T(\boldsymbol{z}_{,t})$ can be obtained for a virtual velocity $\bar{\boldsymbol{z}}_{,t}$, as

$$\delta T(\boldsymbol{z}_{,t}, \bar{\boldsymbol{z}}_{,t}) \equiv \iiint_\Omega \rho \bar{\boldsymbol{z}}_{,t}^T \boldsymbol{z}_{,t} \, d\Omega \tag{F7}$$

Note that a variational formulation is given in terms of virtual displacements, and therefore Eq. F7 is inappropriate since it involves the virtual velocity term $\bar{\boldsymbol{z}}_{,t}$. To convert Eq. F7 into its virtual displacement form, a virtual displacement $\bar{\boldsymbol{z}}$ needs to be defined to satisfy the following additional conditions:

$$\bar{\boldsymbol{z}}(\mathbf{x}, 0) = \bar{\boldsymbol{z}}(\mathbf{x}, t_T) = 0 \tag{F8}$$

where t_T is the terminal time of the dynamic problem. Integrating Eq. F7 over the time interval and using integration by part in time yields

$$\int_0^{t_T} \delta T(\boldsymbol{z}_{,t}, \bar{\boldsymbol{z}}_{,t}) dt \equiv -\int_0^{t_T} \left(\iiint_\Omega \rho \bar{\boldsymbol{z}}^T \boldsymbol{z}_{,tt} \, d\Omega \right) dt \equiv -\int_0^{t_T} d(\boldsymbol{z}_{,tt}, \bar{\boldsymbol{z}}) \, dt \tag{F9}$$

where $d(\boldsymbol{z}_{,tt}, \bar{\boldsymbol{z}})$ is called the kinetic energy bilinear form. The initial and terminal condition terms involved during the integration by part have been eliminated due to Eq. F8. Note that Eq. F9 is a general form of Hamilton's principle that is suitable for both structural analysis and design sensitivity analysis. For an elastic system subject to conservative dynamic loading, the Hamilton's principle states that the integral $\int_0^{t_T} [\Pi(\boldsymbol{z}) - T(\boldsymbol{z}_{,t})] dt$ becomes stationary; that is,

$$\delta \int_0^{t_T} [\Pi(\boldsymbol{z}) - T(\boldsymbol{z}_{,t})] \, dt = 0 \tag{F10}$$

for all times from 0 to t_T and all virtual displacements $\bar{\boldsymbol{z}} \in Z$ that also satisfy the additional condition in Eq. F8.

Equation F10 can be rewritten in terms of strain energy bilinear form, load linear form and kinetic bilinear form, as

$$\int_0^{t_T} [a(\boldsymbol{z}, \bar{\boldsymbol{z}}) - \ell(\bar{\boldsymbol{z}}) + d(\boldsymbol{z}_{,tt}, \bar{\boldsymbol{z}})] \, dt = 0 \tag{F11}$$

This general formulation provides the variational equation for structural dynamic problems.

Now we derive the variational equations for the bridging scale method. As discussed in Chapter 3, in bridging scale method, the total displacement is defined as the sum of the coarse and fine scales, as

$$\boldsymbol{z}(\mathbf{x}, t) = \boldsymbol{u}(\mathbf{x}, t) + \boldsymbol{v}(\mathbf{x}, t) \tag{F12}$$

where the displacement fields are thought to be continuous functions at first glance. In order to introduce the bridging scale, the structure domain needs to be described using atoms. Therefore, discrete functions **z**, **u** and **v**, which have values only at atomic positions, are defined to represent the atomic displacement fields. Note that the coarse scale can also be thought of as a continuous field $\boldsymbol{u}$, since it can be interpolated at points in between atoms with FE shape functions; while **u** is simply a discrete version of $\boldsymbol{u}$, with function values of $\boldsymbol{u}$ at atomic locations. All the continuous and discrete displacement fields above belong to a function space defined as

$$Z = \mathcal{Z} \cup Z \tag{F13a}$$

$$\mathcal{Z} = \left\{ \boldsymbol{z} = \boldsymbol{u} + \boldsymbol{v},\ \ \boldsymbol{u}, \boldsymbol{v} \in \left[H^m(\Omega) \right]^3 \mid \boldsymbol{u}, \boldsymbol{v} = 0 \text{ on } \mathbf{X} \in \Gamma^h \right\} \tag{F13b}$$

$$Z = \left\{ \mathbf{z} = \mathbf{u} + \mathbf{v},\ \ \mathbf{u}, \mathbf{v} \in \mathbf{R}^3 \mid \mathbf{u}, \mathbf{v} = 0 \text{ on } \mathbf{X} \in \Gamma^h \right\} \tag{F13c}$$

In bridging scale method, the strain energy $U(\mathbf{z})$ of the domain can be evaluated as the sum of the strain energy of all atomic bonds within the structure, which is a function of atomic total displacement **z**. Taking first variation of $U(\mathbf{z})$ at **z** in the direction of $\bar{\mathbf{z}} \in Z$ gives

$$\delta U(\mathbf{z}, \bar{\mathbf{z}}) = \bar{\mathbf{z}}^T \frac{\partial U(\mathbf{z})}{\partial \mathbf{z}} \tag{F14}$$

where **z** and $\bar{\mathbf{z}}$ denote vectors that consist of the displacements and virtual displacements of all atoms in the domain, respectively. Since the derivative of the strain energy *U* gives interatomic force, F14 can be rewritten as

$$a(\mathbf{z}, \bar{\mathbf{z}}) = \delta U(\mathbf{z}, \bar{\mathbf{z}}) = -\bar{\mathbf{z}}^T \mathbf{f}(\mathbf{z}) \tag{F15}$$

where $\mathbf{f}(\mathbf{z})$ represents the MD interatomic force. Due to the coarse/fine decomposition of the total displacement **z**, the strain energy *U* can be written as function of coarse scale **u** and fine scale **v**. Taking variation of $U(\mathbf{u}, \mathbf{v})$ at **u** in the direction of $\bar{\mathbf{u}}$ gives

$$\delta U(\mathbf{u},\bar{\mathbf{u}}) = \bar{\mathbf{u}}^T \frac{\partial U(\mathbf{u},\mathbf{v})}{\partial \mathbf{u}} = \bar{\mathbf{u}}^T \frac{\partial U(\mathbf{z})}{\partial \mathbf{z}} \frac{\partial \mathbf{z}}{\partial \mathbf{u}} \tag{F16}$$

where $\bar{\mathbf{u}} \in Z$, and the partial derivative of U with respect to the coarse scale displacement **u** is evaluated using a chain rule. The right hand side of Eq. F16 contains **z** since $\frac{\partial U(\mathbf{u},\mathbf{v})}{\partial \mathbf{u}}$ is a function of not only **u** but also **u** + **v**, which is equal to the total solution **z.** Substituting $\partial U(\mathbf{z})/\partial \mathbf{z} = -\mathbf{f}(\mathbf{z})$ into Eq. F16 while noting that $\partial \mathbf{z}/\partial \mathbf{u} = \mathbf{I}$ yields

$$a(\mathbf{u},\bar{\mathbf{u}}) = \delta U(\mathbf{u},\bar{\mathbf{u}}) = -\bar{\mathbf{u}}^T \mathbf{f}(\mathbf{z}) \tag{F17}$$

By repeating the derivation of Eq. F16 for the fine scale, the variation of U at **v** can also be obtained as

$$a(\mathbf{v},\bar{\mathbf{v}}) = \delta U(\mathbf{v},\bar{\mathbf{v}}) = -\bar{\mathbf{v}}^T \mathbf{f}(\mathbf{z}) \tag{F18}$$

where $\bar{\mathbf{v}} \in Z$ is a small virtual displacement of the fine scale.

The kinetic energy of the structure can be written as

$$T(\mathbf{z}_{,t}) = \frac{1}{2}\mathbf{z}_{,t}^T \mathbf{M}_A \mathbf{z}_{,t} \tag{F19}$$

where $\mathbf{M}_A$ is the atomic mass matrix. Taking variation of $T(\mathbf{z}_{,t})$ at $\mathbf{z}_{,t}$ gives

$$\delta T(\mathbf{z}_{,t},\bar{\mathbf{z}}_{,t}) = \bar{\mathbf{z}}_{,t}^T \mathbf{M}_A \mathbf{z}_{,t} \tag{F20}$$

where $\bar{\mathbf{z}}_{,t}$ represents an arbitrary virtual velocity. Similarly, based on the coarse/fine decomposition, the kinetic energy can be rewritten as a function of $\mathbf{u}_{,t}$ and $\mathbf{v}_{,t}$, as

$$T(\mathbf{u}_{,t},\mathbf{v}_{,t}) = \frac{1}{2}(\mathbf{u}_{,t} + \mathbf{v}_{,t})^T \mathbf{M}_A (\mathbf{u}_{,t} + \mathbf{v}_{,t}) = \frac{1}{2}\mathbf{u}_{,t}^T \mathbf{M}_A \mathbf{u}_{,t} + \frac{1}{2}\mathbf{v}_{,t}^T \mathbf{M}_A \mathbf{v}_{,t} \tag{F21}$$

where the cross terms of $\mathbf{u}_{,t}$ and $\mathbf{v}_{,t}$ have been eliminated due to orthogonality. For example, $\mathbf{u}_{,t}^T\mathbf{M}_A\mathbf{v}_{,t} = \mathbf{d}_{,t}^T\mathbf{N}^T\mathbf{M}_A\mathbf{Q}\mathbf{q}_{,t}$ is eliminated since

$$\begin{aligned}\mathbf{N}^T\mathbf{M}_A\mathbf{Q} &= \mathbf{N}^T\mathbf{M}_A\left(\mathbf{I}-\mathbf{N}\mathbf{M}^{-1}\mathbf{N}^T\mathbf{M}_A\right)\\ &= \mathbf{N}^T\mathbf{M}_A - \mathbf{N}^T\mathbf{M}_A\mathbf{N}\mathbf{M}^{-1}\mathbf{N}^T\mathbf{M}_A\\ &= \mathbf{N}^T\mathbf{M}_A - \mathbf{M}\mathbf{M}^{-1}\mathbf{N}^T\mathbf{M}_A\\ &= 0\end{aligned} \tag{F22}$$

For the purpose of developing a general energy formulation for the bridging scale method, Eq. F21 is rewritten by considering the coarse scale as a continuous function, giving

$$T = \frac{1}{2}\iiint_\Omega \rho \boldsymbol{u}_{,t}^T\boldsymbol{u}_{,t}\, d\Omega + \frac{1}{2}\mathbf{v}_{,t}^T\mathbf{M}_A\mathbf{v}_{,t} \tag{F23}$$

where $\boldsymbol{u}_{,t}$ is the continuous coarse scale velocity and ρ is the mass density. The first variation of T can be obtained for virtual velocities $\bar{\boldsymbol{u}}_{,t}$ and $\bar{\mathbf{v}}_{,t}$, respectively, as

$$\delta T\left(\boldsymbol{u}_{,t}, \bar{\boldsymbol{u}}_{,t}\right) = \iiint_\Omega \rho \bar{\boldsymbol{u}}_{,t}^T\boldsymbol{u}_{,t}\, d\Omega \tag{F24a}$$

$$\delta T\left(\mathbf{v}_{,t}, \bar{\mathbf{v}}_{,t}\right) = \bar{\mathbf{v}}_{,t}^T\mathbf{M}_A\mathbf{v}_{,t} \tag{F24b}$$

Following steps described in Eqs. F7 to F9, Eqs. F24a, F24b and F20 can be respectively converted into their virtual displacement forms, as

$$\int_0^{t_T} \delta T\left(\boldsymbol{u}_{,t}, \bar{\boldsymbol{u}}_{,t}\right)dt = -\int_0^{t_T} d\left(\boldsymbol{u}_{,tt}, \bar{\boldsymbol{u}}\right)dt \tag{F25a}$$

$$\int_0^{t_T} \delta T\left(\mathbf{v}_{,t}, \bar{\mathbf{v}}_{,t}\right)dt = -\int_0^{t_T} d\left(\mathbf{v}_{,tt}, \bar{\mathbf{v}}\right)dt \tag{F25b}$$

$$\int_0^{t_T} \delta T\left(\mathbf{z}_{,t}, \bar{\mathbf{z}}_{,t}\right)dt = -\int_0^{t_T} d\left(\mathbf{z}_{,tt}, \bar{\mathbf{z}}\right)dt \tag{F25c}$$

where the kinetic energy bilinear forms are defined as

$$d\left(\boldsymbol{u}_{,tt}, \bar{\boldsymbol{u}}\right) = \iiint_\Omega \rho \bar{\boldsymbol{u}}^T\boldsymbol{u}_{,tt} d\Omega \tag{F26a}$$

$$d\left(\mathbf{v}_{,tt}, \bar{\mathbf{v}}\right) = \bar{\mathbf{v}}^T \mathbf{M}_A \mathbf{v}_{,tt} \tag{F26b}$$

$$d\left(\mathbf{z}_{,tt}, \bar{\mathbf{z}}\right) = \bar{\mathbf{z}}^T \mathbf{M}_A \mathbf{z}_{,tt} \tag{F26c}$$

The virtual displacements $\bar{\boldsymbol{u}}$, $\bar{\mathbf{v}}$ and $\bar{\mathbf{z}}$ belong to the function space defined as

$$\hat{\mathrm{Z}} = \hat{\mathcal{Z}} \cup \hat{Z} \tag{F27a}$$

$$\hat{\mathcal{Z}} = \left\{ \bar{\boldsymbol{z}} = \bar{\boldsymbol{u}} + \bar{\boldsymbol{v}},\ \ \bar{\boldsymbol{u}}, \bar{\boldsymbol{v}} \in \left[H^m(\Omega)\right]^3 \mid \bar{\boldsymbol{u}}, \bar{\boldsymbol{v}} = 0 \text{ on } \mathbf{x} \in \Gamma^h ,\ \bar{\boldsymbol{u}}(\mathbf{x},0) = \bar{\boldsymbol{u}}(\mathbf{x},t_T) = \bar{\boldsymbol{v}}(\mathbf{x},0) = \bar{\boldsymbol{v}}(\mathbf{x},t_T) = 0 \right\} \tag{F27b}$$

$$\hat{Z} = \left\{ \bar{\mathbf{z}} = \bar{\mathbf{u}} + \bar{\mathbf{v}},\ \ \bar{\mathbf{u}}, \bar{\mathbf{v}} \in \mathbf{R}^3 \mid \bar{\mathbf{u}}, \bar{\mathbf{v}} = 0 \text{ on } \mathbf{x} \in \Gamma^h ,\ \bar{\mathbf{u}}(\mathbf{x},0) = \bar{\mathbf{u}}(\mathbf{x},t_T) = \bar{\mathbf{v}}(\mathbf{x},0) = \bar{\mathbf{v}}(\mathbf{x},t_T) = 0 \right\} \tag{F27c}$$

By substituting Eqs. F17, F18, F15 and Eqs. F26a, F26b, F26c into Eq. F11, the variational equations for the coarse and fine scales, as well as the total solution, can be obtained respectively, as

$$\int_0^{t_T} \iiint_\Omega \rho \bar{\boldsymbol{u}}^T \boldsymbol{u}_{,tt} \, d\Omega dt = \int_0^{t_T} \bar{\mathbf{u}}^T \mathbf{f}(\mathbf{z}) dt \tag{F28a}$$

$$\int_0^{t_T} \bar{\mathbf{v}}^T \mathbf{M}_A \mathbf{v}_{,tt} dt = \int_0^{t_T} \bar{\mathbf{v}}^T \mathbf{f}(\mathbf{z}) dt \tag{F28b}$$

$$\int_0^{t_T} \bar{\mathbf{z}}^T \mathbf{M}_A \mathbf{z}_{,tt} dt = \int_0^{t_T} \bar{\mathbf{z}}^T \mathbf{f}(\mathbf{z}) dt \tag{F28c}$$

for all $\bar{\boldsymbol{u}}, \bar{\mathbf{v}}, \bar{\mathbf{z}} \in \hat{Z}$. It is important to mention that the variational equations (Eqs. F28a ~ F28c) are derived using the energy principles instead of taking derivatives of the Lagrangian, as discussed in Chapter 3. Equations F28a and F28b, which are coupled through the interatomic force $\mathbf{f}(\mathbf{z})$, describe the energy of coarse and fine scales, respectively. Equation F28c describes the energy of the total solution. Since the MD simulation is confined into only a small area of the entire domain, Eq. F28c can be rewritten exclusively for the atoms in *Region 1* to obtain the variational equation for MD simulation; that is

$$\int_0^{t_T} \bar{\mathbf{q}}^T \mathbf{M}_A \mathbf{q}_{,tt}\, dt = \int_0^{t_T} \bar{\mathbf{q}}^T \left[\mathbf{f}(\mathbf{q},\mathbf{u}) + \mathbf{F}^{imp}\right] dt \tag{F29}$$

for all $\bar{\mathbf{q}} \in \hat{Z}$, where $\mathbf{q}$ represents the total displacements of the atoms within the MD region. The effect of the *Region 2* fine scale displacements is accounted for by $\mathbf{F}^{imp}$, which is a column vector containing the impedance forces of all *Region 1* boundary atoms.

Outside the MD region, since the *Region 2* fine scale is eliminated, the MD force $\mathbf{f}(\mathbf{z})$ in Eq. F28a is no longer available. Therefore, the strain energy of the continuum is defined using a general expression

$$U(\boldsymbol{u}) = \frac{1}{2}\iiint_{\Omega_2} \boldsymbol{\varepsilon}^T(\boldsymbol{u})\boldsymbol{\sigma}(\boldsymbol{u})d\Omega_2 \tag{F30}$$

where $\boldsymbol{\varepsilon}$ and $\boldsymbol{\sigma}$ are respectively strain and stress, which are continuous functions of the coarse scale displacement field $\boldsymbol{u}$, while Ω_2 represents the domain of *Region 2*. Taking first variation of Eq. F30 gives the energy bilinear form, as

$$a(\boldsymbol{u}, \bar{\boldsymbol{u}}) = \delta U(\boldsymbol{u}, \bar{\boldsymbol{u}}) = \iiint_{\Omega_2} \bar{\boldsymbol{\varepsilon}}^T(\bar{\boldsymbol{u}})\boldsymbol{\sigma}(\boldsymbol{u})d\Omega_2 \tag{F31}$$

A general expression describing the kinetic energy of a continuum domain can be found in Eq. F6. Replacing $\boldsymbol{z}_{,t}$ in Eq. F6 with the coarse scale velocity field $\boldsymbol{u}_{,t}$ gives

$$T(\boldsymbol{u}_{,t}) \equiv \frac{1}{2}\iiint_{\Omega} \rho \boldsymbol{u}_{,t}^T \boldsymbol{u}_{,t} d\Omega \tag{F32}$$

which is identical with the first term on the right hand side of Eq. F23. The kinetic energy bilinear form has been obtained in Eq. F26a. Substituting Eq. F26a and F31 into Eq. F11, the variational equation for *Region 2*, without considering the external forces, can be written as

$$\int_0^{t_T} \iiint_{\Omega_2} \rho \boldsymbol{u}^T \boldsymbol{u}_{,tt} d\Omega_2 dt = -\int_0^{t_T} \iiint_{\Omega_2} \bar{\boldsymbol{\varepsilon}}^T (\bar{\boldsymbol{u}}) \boldsymbol{\sigma}(\boldsymbol{u}) d\Omega_2 dt \tag{F33}$$

for all $\bar{\boldsymbol{u}} \in \hat{Z}$. By combining Eqs. F28a and F33, we obtain the variational equation for the coarse scale; that is

$$\int_0^{t_T} \iiint_{\Omega} \rho(\mathbf{x}) \bar{\boldsymbol{u}}^T \boldsymbol{u}_{,tt} d\Omega \, dt = \int_0^{t_T} \left[\bar{\mathbf{u}}^T \mathbf{f}(\mathbf{z}) - \iiint_{\Omega_2} \bar{\boldsymbol{\varepsilon}}^T (\bar{\boldsymbol{u}}) \boldsymbol{\sigma}(\boldsymbol{u}) d\Omega_2 \right] dt \tag{F34}$$

APPENDIX G

MATERIAL DERIVATIVE OF REGION 2 COARSE SCALE IN THREE DIMENSIONS

This appendix explains the material derivative of coarse scale strain energy in *Region 2*. More specifically, we demonstrate how the $\overset{\bullet}{\mathbf{F}}{}^{CB}$ term in Eq. 4.22 is evaluated.

Starting from the coarse scale energy equation (Eq. 4.7b), we taking material derivative of the strain energy in *Region 2,* giving

$$\begin{aligned}\iiint_{\Omega_2} \overset{\bullet}{\overline{\boldsymbol{\varepsilon}}{}^T(\overline{\boldsymbol{u}})\boldsymbol{\sigma}(\boldsymbol{u})} d\Omega_2 &= \iiint_{\Omega_2} \left[\overline{\boldsymbol{\varepsilon}}{}^T(\overline{\boldsymbol{u}})\boldsymbol{\sigma}(\boldsymbol{u})\right]' d\Omega_2 + \iiint_{\Omega_2} \nabla\left[\overline{\boldsymbol{\varepsilon}}{}^T(\overline{\boldsymbol{u}})\boldsymbol{\sigma}(\boldsymbol{u})\right]^T \boldsymbol{V} d\Omega_2 + \iiint_{\Omega_2} \overline{\boldsymbol{\varepsilon}}{}^T(\overline{\boldsymbol{u}})\boldsymbol{\sigma}(\boldsymbol{u}) div\boldsymbol{V} d\Omega_2 \\ &= \iiint_{\Omega_2} \left[-\overline{\boldsymbol{\varepsilon}}{}^T\left(\nabla\overline{\boldsymbol{u}}{}^T\boldsymbol{V}\right)\boldsymbol{\sigma}(\boldsymbol{u}) + \overline{\boldsymbol{\varepsilon}}{}^T(\overline{\boldsymbol{u}})\boldsymbol{\sigma}(\dot{\boldsymbol{u}}) - \overline{\boldsymbol{\varepsilon}}{}^T(\overline{\boldsymbol{u}})\boldsymbol{\sigma}\left(\nabla\overline{\boldsymbol{u}}{}^T\boldsymbol{V}\right)\right. \\ &\qquad \left. + \nabla\left(\overline{\boldsymbol{\varepsilon}}{}^T(\overline{\boldsymbol{u}})\boldsymbol{\sigma}(\boldsymbol{u})\right)^T\boldsymbol{V} + \overline{\boldsymbol{\varepsilon}}{}^T(\overline{\boldsymbol{u}})\boldsymbol{\sigma}(\boldsymbol{u}) div\boldsymbol{V}\right] d\Omega_2\end{aligned} \tag{G1}$$

where all five terms within the integral on the right hand side need to be discretized for implementation using finite element method.

The discretization process will be similar as that performed in Appendix E. The same two element domain (Fig. E3) with two quadrature points will be used for demonstration.

The first term can be discretized as:

$$\iiint_{\Omega_2}\left[-\bar{\boldsymbol{\varepsilon}}^T\left(\nabla\bar{\boldsymbol{u}}^T\boldsymbol{V}\right)\boldsymbol{\sigma}(\boldsymbol{u})\right]d\Omega_2 \overset{discretize}{=} -\begin{bmatrix}\bar{\boldsymbol{\varepsilon}}_A^T\left(\nabla\bar{\boldsymbol{u}}_A^T\boldsymbol{V}_A\right)\\ \bar{\boldsymbol{\varepsilon}}_B^T\left(\nabla\bar{\boldsymbol{u}}_B^T\boldsymbol{V}_B\right)\end{bmatrix}^T \mathbf{WEBd}$$

$$= -\bar{\mathbf{d}}^T\left\{\mathbf{D}_{12\times6}\left(\begin{bmatrix}\boldsymbol{V}_{A1} & \\ & \boldsymbol{V}_{B1}\end{bmatrix}_{6\times6}\mathbf{N}_{,1}+\begin{bmatrix}\boldsymbol{V}_{A2} & \\ & \boldsymbol{V}_{B2}\end{bmatrix}_{6\times6}\mathbf{N}_{,2}+\begin{bmatrix}\boldsymbol{V}_{A3} & \\ & \boldsymbol{V}_{B3}\end{bmatrix}_{6\times6}\mathbf{N}_{,3}\right)\right\}^T\mathbf{WEBd}$$

$$= -\bar{\mathbf{d}}^T\left\{\left(\mathbf{D}_{12\times6}\begin{bmatrix}\boldsymbol{V}_{A1} & \\ & \boldsymbol{V}_{B1}\end{bmatrix}_{6\times6}\right)\mathbf{N}_{,1}+\begin{bmatrix}\boldsymbol{V}_{A1} & \\ & \boldsymbol{V}_{B1}\end{bmatrix}_{12\times12}\mathbf{B}_{,1}+\left(\mathbf{D}_{12\times6}\begin{bmatrix}\boldsymbol{V}_{A2} & \\ & \boldsymbol{V}_{B2}\end{bmatrix}_{6\times6}\right)\mathbf{N}_{,2}+\begin{bmatrix}\boldsymbol{V}_{A2} & \\ & \boldsymbol{V}_{B2}\end{bmatrix}_{12\times12}\mathbf{B}_{,2}\right.$$

$$\left.+\left(\mathbf{D}_{12\times6}\begin{bmatrix}\boldsymbol{V}_{A3} & \\ & \boldsymbol{V}_{B3}\end{bmatrix}_{6\times6}\right)\mathbf{N}_{,3}+\begin{bmatrix}\boldsymbol{V}_{A3} & \\ & \boldsymbol{V}_{B3}\end{bmatrix}_{12\times12}\mathbf{B}_{,3}\right\}^T\mathbf{WEBd} \tag{G2}$$

where

$$\begin{bmatrix}\boldsymbol{V}_{A1} & \\ & \boldsymbol{V}_{B1}\end{bmatrix}_{6\times6} = \begin{bmatrix}V_{A1} &&&&& \\ & V_{A1} &&&& \\ && V_{A1} &&& \\ &&& V_{B1} && \\ &&&& V_{B1} & \\ &&&&& V_{B1}\end{bmatrix} \tag{G3}$$

The discretization of the remaining four terms is as follows:

$$\iiint_{\Omega_2}\left[\bar{\boldsymbol{\varepsilon}}^T(\bar{\boldsymbol{u}})\boldsymbol{\sigma}(\dot{\boldsymbol{u}})\right]d\Omega_2 \overset{discretize}{=} \bar{\mathbf{d}}^T\mathbf{B}^T\mathbf{EWB}\,\dot{\mathbf{d}} \tag{G4}$$

and

$$\iiint_{\Omega_2}\left[-\bar{\boldsymbol{\varepsilon}}^T(\bar{\boldsymbol{u}})\boldsymbol{\sigma}\left(\nabla\bar{\boldsymbol{u}}^T\boldsymbol{V}\right)\right]d\Omega_2$$

$$\overset{discretize}{=} -\bar{\mathbf{d}}^T\mathbf{B}^T\mathbf{WE}\left\{\left(\mathbf{D}_{12\times6}\begin{bmatrix}\boldsymbol{V}_{A1} & \\ & \boldsymbol{V}_{B1}\end{bmatrix}_{6\times6}\right)\mathbf{N}_{,1}+\left(\mathbf{D}_{12\times6}\begin{bmatrix}\boldsymbol{V}_{A2} & \\ & \boldsymbol{V}_{B2}\end{bmatrix}_{6\times6}\right)\mathbf{N}_{,2}+\left(\mathbf{D}_{12\times6}\begin{bmatrix}\boldsymbol{V}_{A3} & \\ & \boldsymbol{V}_{B3}\end{bmatrix}_{6\times6}\right)\mathbf{N}_{,3}\right.$$

$$\left.+\begin{bmatrix}\boldsymbol{V}_{A1} & \\ & \boldsymbol{V}_{B1}\end{bmatrix}_{12\times12}\mathbf{B}_{,1}+\begin{bmatrix}\boldsymbol{V}_{A2} & \\ & \boldsymbol{V}_{B2}\end{bmatrix}_{12\times12}\mathbf{B}_{,2}+\begin{bmatrix}\boldsymbol{V}_{A3} & \\ & \boldsymbol{V}_{B3}\end{bmatrix}_{12\times12}\mathbf{B}_{,3}\right\}\mathbf{d} \tag{G5}$$

and

$$\begin{aligned}\iiint_{\Omega_2} \nabla\left(\bar{\boldsymbol{\varepsilon}}^T(\bar{\boldsymbol{u}})\boldsymbol{\sigma}(\boldsymbol{u})\right)^T \boldsymbol{V}\, d\Omega &= \iiint_{\Omega_2} \Big[\bar{\boldsymbol{\varepsilon}}^T(\bar{\boldsymbol{u}})_{,1}\boldsymbol{\sigma}(\boldsymbol{u})V_1 + \bar{\boldsymbol{\varepsilon}}^T(\bar{\boldsymbol{u}})\boldsymbol{\sigma}(\boldsymbol{u})_{,1}V_1 \\ &\quad + \bar{\boldsymbol{\varepsilon}}^T(\bar{\boldsymbol{u}})_{,2}\boldsymbol{\sigma}(\boldsymbol{u})V_2 + \bar{\boldsymbol{\varepsilon}}^T(\bar{\boldsymbol{u}})\boldsymbol{\sigma}(\boldsymbol{u})_{,2}V_2 + \bar{\boldsymbol{\varepsilon}}^T(\bar{\boldsymbol{u}})_{,3}\boldsymbol{\sigma}(\boldsymbol{u})V_3 + \bar{\boldsymbol{\varepsilon}}^T(\bar{\boldsymbol{u}})\boldsymbol{\sigma}(\boldsymbol{u})_{,3}V_3\Big]d\Omega \\ &\overset{discretize}{=} \bar{\mathbf{d}}^T\mathbf{B}_{,1}^T\mathbf{WE}\begin{bmatrix}\boldsymbol{V}_{A1} & \\ & \boldsymbol{V}_{B1}\end{bmatrix}_{12\times12}\mathbf{Bd} + \bar{\mathbf{d}}^T\mathbf{B}^T\mathbf{WE}\begin{bmatrix}\boldsymbol{V}_{A1} & \\ & \boldsymbol{V}_{B1}\end{bmatrix}_{12\times12}\mathbf{B}_{,1}\mathbf{d} + \bar{\mathbf{d}}^T\mathbf{B}_{,2}^T\mathbf{WE}\begin{bmatrix}\boldsymbol{V}_{A2} & \\ & \boldsymbol{V}_{B2}\end{bmatrix}_{12\times12}\mathbf{Bd} \\ &\quad + \bar{\mathbf{d}}^T\mathbf{B}^T\mathbf{WE}\begin{bmatrix}\boldsymbol{V}_{A2} & \\ & \boldsymbol{V}_{B2}\end{bmatrix}_{12\times12}\mathbf{B}_{,2}\mathbf{d} + \bar{\mathbf{d}}^T\mathbf{B}_{,3}^T\mathbf{WE}\begin{bmatrix}\boldsymbol{V}_{A3} & \\ & \boldsymbol{V}_{B3}\end{bmatrix}_{12\times12}\mathbf{Bd} + \bar{\mathbf{d}}^T\mathbf{B}^T\mathbf{WE}\begin{bmatrix}\boldsymbol{V}_{A3} & \\ & \boldsymbol{V}_{B3}\end{bmatrix}_{12\times12}\mathbf{B}_{,3}\mathbf{d}\end{aligned} \tag{G6}$$

and

$$\begin{aligned}\iiint_{\Omega_2} \bar{\boldsymbol{\varepsilon}}^T(\bar{\boldsymbol{u}})\boldsymbol{\sigma}(\boldsymbol{u})\, div\boldsymbol{V}\, d\Omega &= \iiint_{\Omega_2} \Big[\bar{\boldsymbol{\varepsilon}}^T(\bar{\boldsymbol{u}})\boldsymbol{\sigma}(\boldsymbol{u})V_{1,1} + \bar{\boldsymbol{\varepsilon}}^T(\bar{\boldsymbol{u}})\boldsymbol{\sigma}(\boldsymbol{u})V_{2,2} + \bar{\boldsymbol{\varepsilon}}^T(\bar{\boldsymbol{u}})\boldsymbol{\sigma}(\boldsymbol{u})V_{3,3}\Big]d\Omega \\ &\overset{discretize}{=} \bar{\mathbf{d}}^T\mathbf{B}^T\mathbf{WE}\begin{bmatrix}\boldsymbol{V}_{A1,1} & \\ & \boldsymbol{V}_{B1,1}\end{bmatrix}_{12\times12}\mathbf{Bd} + \bar{\mathbf{d}}^T\mathbf{B}^T\mathbf{WE}\begin{bmatrix}\boldsymbol{V}_{A2,2} & \\ & \boldsymbol{V}_{B2,2}\end{bmatrix}_{12\times12}\mathbf{Bd} + \bar{\mathbf{d}}^T\mathbf{B}^T\mathbf{WE}\begin{bmatrix}\boldsymbol{V}_{A3,3} & \\ & \boldsymbol{V}_{B3,3}\end{bmatrix}_{12\times12}\mathbf{Bd}\end{aligned} \tag{G7}$$

Substituting Eqs. G2 ~ G7 into Eq. G1 gives the discretized form of the material derivative of the coarse scale strain energy of the *Region 2* domain, as

$$\begin{aligned}\iint_{\Omega_2} \overset{\bullet}{\overline{\bar{\boldsymbol{\varepsilon}}^T(\bar{\boldsymbol{u}})}}\boldsymbol{\sigma}(\boldsymbol{u})\, d\Omega_2 &\overset{discretize}{=} \bar{\mathbf{d}}^T\mathbf{B}^T\tilde{\mathbf{P}}\mathbf{WEBd} + \bar{\mathbf{d}}^T\tilde{\mathbf{Q}}\mathbf{WEBd} + \bar{\mathbf{d}}^T\mathbf{B}^T\mathbf{WE}\tilde{\mathbf{Q}}^T\mathbf{d} + \bar{\mathbf{d}}^T\mathbf{B}^T\mathbf{WEB}\dot{\mathbf{d}} \\ &= -\bar{\mathbf{d}}^T\, \overset{\bullet}{\mathbf{F}}{}^{CB}\end{aligned} \tag{G8}$$

where

$$\tilde{\mathbf{P}} = \begin{bmatrix}\boldsymbol{V}_{A1,1} + \boldsymbol{V}_{A2,2} + \boldsymbol{V}_{A3,3} & \\ & \boldsymbol{V}_{B1,1} + \boldsymbol{V}_{B2,2} + \boldsymbol{V}_{A3,3}\end{bmatrix}_{12\times12} \tag{G9}$$

and

$$\tilde{\mathbf{Q}} = -\left(\mathbf{D}_{12\times6}\begin{bmatrix}\boldsymbol{V}_{A1} & \\ & \boldsymbol{V}_{B1}\end{bmatrix}_{6\times6}\right)\mathbf{N}_{,1} - \left(\mathbf{D}_{12\times6}\begin{bmatrix}\boldsymbol{V}_{A2} & \\ & \boldsymbol{V}_{B2}\end{bmatrix}_{6\times6}\right)\mathbf{N}_{,2} - \left(\mathbf{D}_{12\times6}\begin{bmatrix}\boldsymbol{V}_{A3} & \\ & \boldsymbol{V}_{B3}\end{bmatrix}_{6\times6}\right)\mathbf{N}_{,3} \tag{G10}$$

Hence, the material derivative of the coarse scale nodal force can be written in the form

$$\overset{\bullet}{\mathbf{F}}{}^{CB} = -\overset{\bullet}{\mathbf{K}}{}^{CB}\,\mathbf{d} - \mathbf{K}^{CB}\dot{\mathbf{d}} \tag{G11}$$

where

$$\overset{\bullet}{\mathbf{K}}{}^{CB} = \mathbf{B}^T\tilde{\mathbf{P}}\mathbf{EWB} + \tilde{\mathbf{Q}}\mathbf{EWB} + \mathbf{B}^T\mathbf{EW}\tilde{\mathbf{Q}}^T \tag{G12}$$

APPENDIX H

REGRESSION ANALYSIS IN HYBRID METHOD

This appendix provides detailed steps of the regression analysis used in the hybrid method for approximating the sensitivity of crack propagation speed. We will focus on shape design variable b_2 in the nano-beam example for demonstration.

First of all, a perturbation range for regression analysis needs to be selected. As discussed in Chapter 6, we choose the perturbation range for b_2 to be $\Delta b_2 \in [0, 0.2]$, as shown in Fig. 6.6b. Note that the $S_{\tilde{V}}$ data within this range are of high accuracy compared to re-analysis results (Fig. 6.14).

Next, as shown in Fig. H1, we fit a fourth order polynomial curve to the predicted crack speed 'slope' ($S_{\tilde{V}}$) data within $\Delta b_2 \in [0, 0.2]$ using least squares method. Note that we purposely set the slope of the curve at $\Delta b_2 = 0$ to zero, so that the convergence behavior of the $S_{\tilde{V}}$ curve can be captured and the impact of noise near $\Delta b_2 = 0$ can be minimized.

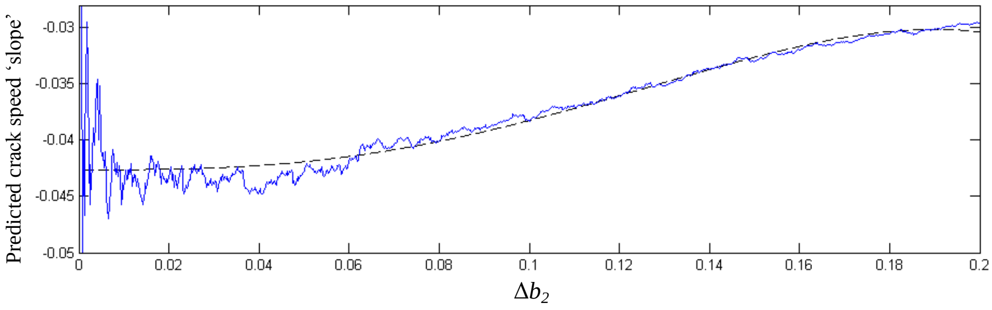

Figure H1 Polynomial curve fitted to the predicted crack speed 'slope' data (Round 1 curve fitting)

Apparently, the initial fitting curve (black dashed line in Fig. H1) is influenced by noise. Therefore, we will remove the noisy data points from the original $s_{\tilde{V}}$ data using the initial fitting curve as a reference. As shown in Figs. H2a and H2b, we first calculate the square of error for each $s_{\tilde{V}}$ data point, where the error is simply the difference between the $s_{\tilde{V}}$ curve and the fitting curve at each perturbation. Then we calculate the standard deviation of the squared error of all data from $\Delta b_2 = 0$ to $\Delta b_2 = 0.2$, and delete the data points with squared error larger than a certain multiple N_e of the standard deviation; that is

$$error(i)^2 > N_e \sqrt{\frac{1}{N_V} \sum_{j=1}^{N_V} \left(error(j)^2 - \mu \right)^2} \tag{H1}$$

where *error*(*i*) denotes the error of the *i*th data point, N_V is the number of predicted crack speed data within the range being considered, and

$$\mu = \frac{1}{N_V} \sum_{j=1}^{N_V} error(j)^2 \tag{H2}$$

is the mean value of squared error. In this example, we choose $N_e = 6$ as the threshold for eliminating the noisy data.

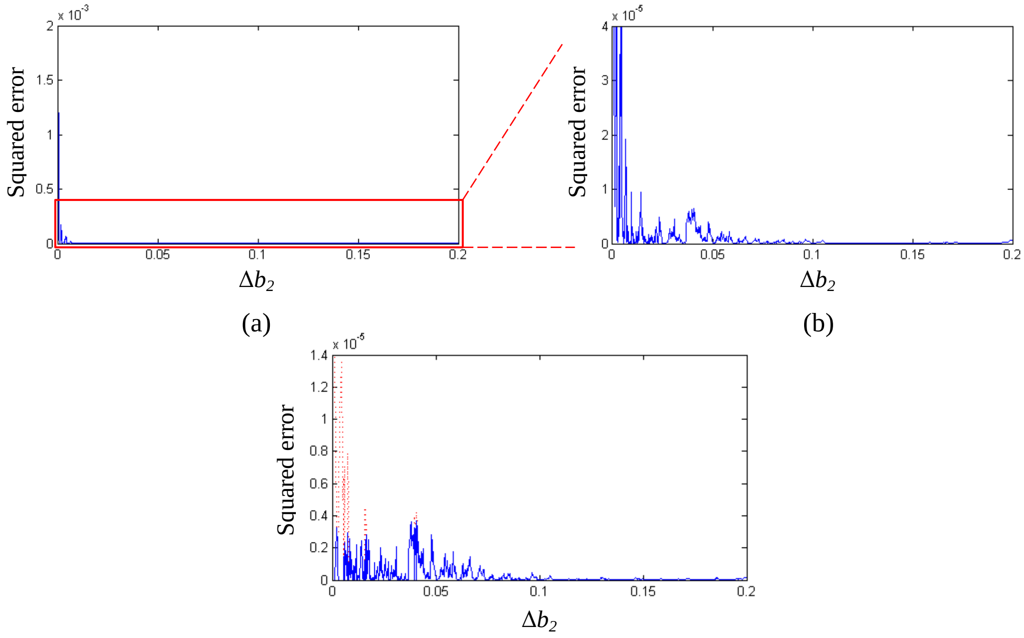

(a)

(b)

(c)

Figure H2 Removing noisy data, (a) square of error based on the original fitting curve, (b) zoomed-in view, and (c) noisy data (red dots) removed

The step above – calculating standard deviation of squared error and removing data points with large error – needs to be repeated for the remaining data points until the result converges, i.e., the deviation calculated in the current iteration is identical to that in the previous one. In Fig. H2c, the red data points are those with large error exceeding the deviation threshold and have been removed as noise. Note that this result is obtained after 5 iterations. The noise elimination result based on the original fitting curve for design variable b_2 is shown in Fig. H3. As can be seen, all $S_{\tilde{V}}$ data far away from the initial fitting curve have been removed.

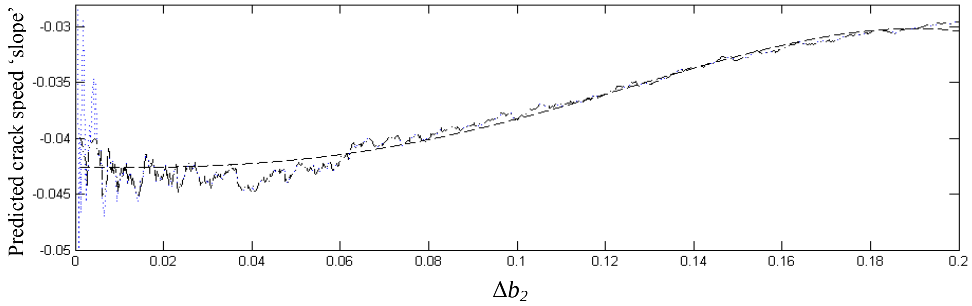

Figure H3 Result of noise elimination based on the original fitting curve. Blue dotted part of the curve is removed as noise

The next step is to repeat the curve fitting process; that is, fitting a curve to the remaining $s_{\tilde{V}}$ data shown in Fig. H3. As can be seen from Fig. H4, since some of the data points have been removed, the new fitting curve (green curve) is slightly different from the original one.

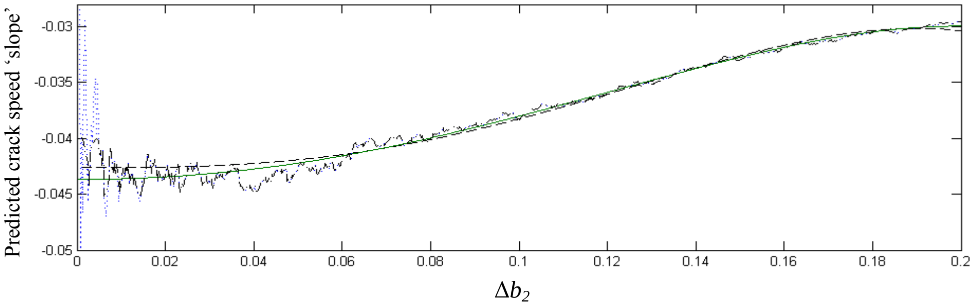

Figure H4 Polynomial curve fitted to the predicted crack speed 'slope' data remained from the first round of noise elimination (Round 2 curve fitting)

Now the noise elimination process can be performed again to remove the data that are too far away from the new fitting curve. This curve fitting and noise elimination process needs to be repeated until the difference between the vertical intercepts of the fitting curves in the current round and the previous round is smaller than 1%. Then the vertical intercept of the current fitting curve can be considered as a reasonable approximation of the sensitivity of crack speed. For design variable b_2, the crack speed sensitivity is obtained after four rounds of curve fitting, as shown in Fig. H5.

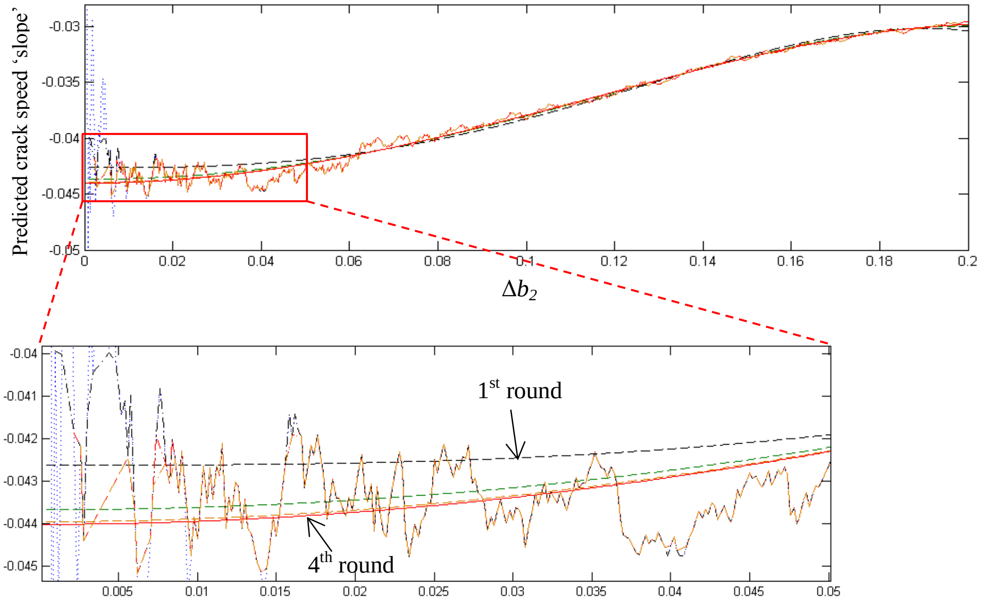

Figure H5 Regression analysis result for design variable b_2

The complete procedure of regression analysis is illustrated in the flowchart below:

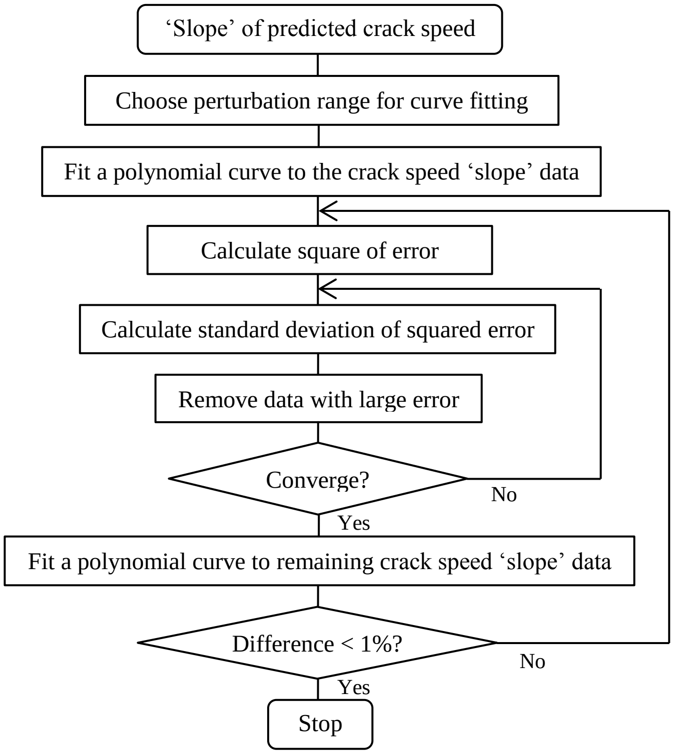

Figure H6 A flowchart of regression analysis

In our numerical example, it is found empirically that a fourth order polynomial curve will generally be adequate in fitting the data within a small perturbation range near the current design. In fact, the regression analysis result is not very sensitive to the order of the polynomial. Based on our experience, the polynomial order must be at least three to capture the trend of the $S_{\tilde{V}}$ curve, meanwhile, it should not be too large (such as eight), otherwise the vertical intercept of the fitting curve will be significantly affected by noise. Figure H7 gives the regression analysis results using polynomial curves of orders from three to five. It turns out that the difference between the crack speed sensitivities obtained is within 2%.

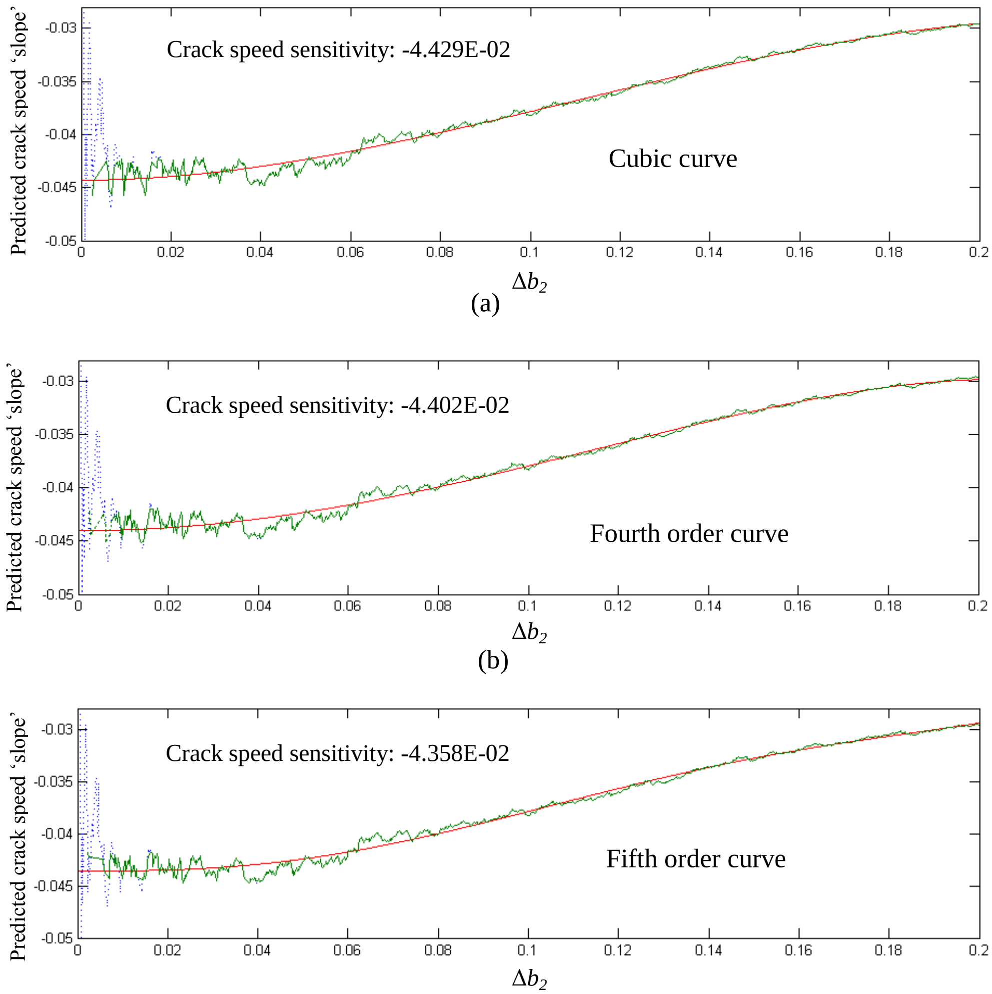

(a)

(b)

(c)

Figure H7 Regression analysis results with (a) cubic curve, (b) fourth order curve, and (c) fifth order curve

Another adjustable parameter is the multiple N_e in Eq. H1, which serves as a criterion for noise elimination. Again, the regression analysis result is not very sensitive to N_e as long as N_e is neither too large nor too small. The regression analysis results with different N_e ranging from 4 to 12 are shown in Table H1. As can be seen, the difference between calculated sensitivity coefficients is negligible (less than 2%).

Table H1 Regression analysis results with various N_e

N_e	4	6	8	10	12
Crack speed sensitivity	-4.351E-02	-4.402E-02	-4.394E-02	-4.391E-02	-4.378E-02